

Very deep spectroscopy of the bright Saturn Nebula NGC 7009 – II. Analysis of the rich optical recombination spectrum

X. Fang¹ * and X.-W. Liu^{1,2}

¹Department of Astronomy, School of Physics, Peking University, Beijing 100871, P. R. China

²Kavli Institute for Astronomy and Astrophysics at Peking University, Beijing 100871, P. R. China

Accepted . Received

ABSTRACT

In Paper I, we presented deep, long-slit spectrum of the bright Saturn nebula NGC 7009. Numerous permitted lines emitted by the C^+ , N^+ , O^+ and Ne^+ ions were detected. Gaussian profile fitting to the spectrum yielded more than 1000 lines, the majority of which are optical recombination lines (ORLs) of heavy element ions. In the current paper, we present a critical analysis of the rich optical recombination spectrum of NGC 7009, in the context of the bi-abundance nebular model proposed by Liu et al. Transitions from individual multiplets are checked carefully for potential blended lines. The observed relative intensities are compared with the theoretical predictions based on high quality effective recombination coefficients, now available for the recombination line spectrum of a number of heavy element ions.

The possibility of plasma diagnostics using the ORLs of various heavy element ions is discussed in detail. The line ratios that can be used to determine electron temperature are presented for each ion, although there is still a lack of adequate atomic data and some of the lines are still not detected in the spectrum of NGC 7009 due to weakness and/or line blending. Plasma diagnostics based on the N II and O II recombination spectra both yield electron temperatures close to 1000 K, which is lower than those derived from the collisionally excited line (CEL) ratios (e.g., the [O III] and [N II] nebular-to-auroral line ratios; see Paper I for details) by nearly one order of magnitude. The very low temperatures yielded by the O II and N II ORLs indicate that they originate from very cold regions. The C^{2+}/H^+ , N^{2+}/H^+ , O^{2+}/H^+ and Ne^{2+}/H^+ ionic abundance ratios derived from ORLs are consistently higher, by about a factor of 5, than the corresponding values derived from CELs. In calculating the ORL ionic abundance ratios, we have used the newly available high quality effective recombination coefficients, and adopted an electron temperature of ~ 1000 K, as given by the ORL diagnostics and as a consequence presumably representing the physical conditions prevailing in the regions where the heavy element ORLs arise. Measurements of the ultraviolet (UV) and infrared (IR) CELs from the literature are used to calculate CEL ionic abundance ratios when optical data are not available for the ionic species. A comparison of results of plasma diagnostics and abundance determinations for NGC 7009 points to the existence of “cold”, metal-rich (i.e., H-deficient) inclusions embedded in the hot, diffuse ionized gas, first postulated by Liu et al.

At electron temperatures yielded by the N II and O II ORLs, the predicted relative intensities of ORLs agree well with the observed values, indicating that the current quantum calculations of the recombination spectra of those two ionic species well represent the recombination processes under nebular conditions. Deviations from the LS coupling, noticed in an earlier quantitative spectroscopy by Liu et al. for the same object, are again confirmed, especially for recombination lines of the $4f-3d$ transition array. For N II, as well as for O II, the ionic abundances derived from different J -resolved transitions within a multiplet, or from the transitions belonging to different multiplets, agree with each other. This is another evidence that the new effective recombination coefficients are reliable. New calculations of the effective recombination coefficients for the Ne II lines at nebular temperatures and densities are needed.

Key words: atomic data – atomic processes – ISM: abundances – planetary nebulae: individual: NGC 7009

arXiv:1212.0005v1 [astro-ph.SR] 2 Dec 2012

1 INTRODUCTION

The bright Saturn Nebula NGC 7009 is known for its rich and prominent optical recombination lines (ORLs) of heavy element ions, especially those of O II, ever since the spectrophotographic observations of Wyse (1942), who published and analyzed deep spectra of the Orion Nebula and nine planetary nebulae (PNe), including NGC 7009. He identified and measured several dozen O II permitted lines in NGC 7009 in the wavelength range 3700 – 6750 Å, although accurate measurements of many of those O II lines were hampered by line blending. At the end of this paper Wyse (1942) expressed the desire of having more accurate measurements of the O II permitted lines. Aller & Kaler (1964) identified more than 100 O II permitted lines in the spectrum of NGC 7009. Large numbers of permitted lines of other ionic species, such as C II, N II, N III, O III, Ne II, were also detected. The majority of these permitted lines are mainly excited by recombination. Other possible excitation mechanisms, such as the dielectronic recombination, radiative charge transfer, and resonance fluorescence by starlight or by some other prominent nebular emission lines, are all by their nature selective, which means that they tend to excite lines from specific spectral terms of certain parity and multiplicity only (e.g., Grandi 1976; Liu & Danziger 1993a; Liu, Danziger & Murdin 1993). With high signal-to-noise ratio, high spectral resolution and wide wavelength-coverage spectra of PNe now available, more and more ORLs of fainter intensities from heavy element ions that arise from many different multiplets are observed and provide an opportunity to study the radiative and dielectronic recombination processes and test the accuracy of the recombination theories for non-hydrogenic ions. The first systematic study of the ORLs in NGC 7009 was carried out by Liu et al. (1995, hereafter LSBC), who analyzed dozens of O II ORLs, using effective recombination coefficients calculated in the intermediate coupling scheme for transitions from the 3d–3p and 4f–3d arrays, and coefficients calculated in the *LS* coupling scheme for transitions from the 3p – 3s array. LSBC found clear deviations from the *LS* coupling in the 3d–3p and 4f–3d transitions. Luo, Liu & Barlow (2001, hereafter LLB01) presented high-quality observations of several dozens Ne II ORLs in NGC 7009, and derived the $\text{Ne}^{2+}/\text{H}^+$ abundance ratios from them.

Along with the advance of observational techniques that have enabled the detections of many faint ORLs of heavy element ions in photoionized gaseous nebulae, the recombination theories of heavy element ions, such as C II, N II, O II, and Ne II, have seen steady improvements since early 1980s (e.g. Storey 1981; Nussbaumer & Storey 1983, 1984, 1986, 1987; Escalante & Victor 1990; Péquignot, Petitjean & Boisson 1991; Storey 1994; LSBC; Kisielius et al. 1998; Davey, Storey & Kisielius 2000; Kisielius & Storey 1999, 2002; Fang, Storey & Liu 2011). The high-quality atomic data have been widely used to reveal the physical conditions (electron temperatures and densities) under which the ORLs of heavy element ions arise, and to determine ionic and elemental abundances from them (e.g. Liu et al. 2000).

In nebular astrophysics there has been a long-standing dichotomy whereby the ionic and elemental abundances of C, N, O and Ne relative to hydrogen determined from ORLs (e.g. C II M6 $\lambda 4267$, N II M39b $\lambda 4041$, O II M1 $\lambda 4649$ and M48a $\lambda 4089$, Ne II M55e $\lambda 4392$) are systematically higher than those derived from the much brighter collisionally excited lines (CELs, often referred to as forbidden lines). With high-quality optical spectra now available, detailed studies of this problem have been carried out for several archetypal PNe (LSBC and LLB01 for NGC 7009; Liu et al. 2000

for NGC 6153; Liu et al. 2001b for M 1-42 and M 2-36; Liu et al. 2006 for Hf 2-2; Garnett & Dinerstein 2001 for NGC 6720). Several deep optical spectroscopic surveys of PNe, which allow for the analyses of nebulae based on ORLs, have been carried out during the past decade (Tsamis et al. 2003, 2004; Liu et al. 2004a,b; Robertson-Tessi & Garnett 2005; Wesson, Liu & Barlow 2005; Wang & Liu 2007). The abundance discrepancy factors (ADFs), defined as the ratio of the abundance derived from ORLs to that deduced from CELs, typically lie in the range 1–3. But for a significant number of PNe, ADF values exceeding 5, or even 10, are seen. The highest ADF value (~ 70) of all PNe is found in Hf 2-2 (Liu et al. 2006). Another dichotomy that is closely related to the problem of abundance discrepancy is that nebular electron temperatures derived from the traditional diagnostic [O III] nebular-to-auroral line ratio are generally higher than those derived from the Balmer jump (BJ) of hydrogen recombination spectrum (e.g. Peimbert 1971; Liu & Danziger 1993b). A number of postulations have been raised to explain these problems (e.g. Peimbert 1967; Rubin 1989; Viegas & Clegg 1994), but all failed to provide a consistent interpretation of all the available observations. Recently, Nicholls, Dopita & Sutherland (2012) explored the possibility that electrons in H II regions and PNe depart from a Maxwell-Boltzmann equilibrium energy distribution and suggested that a “ κ -distribution” for the electron energies, which are widely found in solar system plasmas, can explain the temperature and abundance discrepancies in H II regions and PNe. The bi-abundance nebular model proposed by Liu et al. (2000), who postulated that PNe (probably also H II regions) contain H-deficient inclusions, provides a better and natural explanation of the dichotomy. In this model, the faint ORLs of heavy element ions originate mainly from the “cold”, H-deficient inclusions, while the stronger CELs are emitted from the warmer ambient plasma with ‘normal’ chemical composition. Deep spectroscopic surveys and recombination line analysis of individual nebulae in the past decade has yielded strong evidence for the existence of such a “cold” component (see recent reviews by Liu 2003, 2006a, 2011).

This is the second of the two papers devoted to very deep spectroscopy of NGC 7009. In the previous paper (Fang & Liu 2011, hereafter Paper I), we presented high-quality spectra of NGC 7009 and tabulation of all detected lines, including their observed and dereddened intensities, many of which were obtained via careful deblending using the technique of multi-Gaussian profile fitting. We also carried out plasma diagnostics using the CEL ratios, the H I recombination spectrum (including the Balmer and Paschen decrements of the line spectrum, and the Balmer and Paschen jumps of the continuum spectrum), and the He I and He II recombination spectrum (including the He I recombination line ratios, and discontinuities of the He I and He II recombination continua). The average electron temperature yielded by CELs, $T_e(\text{CELs})$, is higher than that from the H I Balmer jump, $T_e(\text{H I BJ})$, which in turn is higher than the temperature derived from the He I recombination line ratios, $T_e(\text{He I})$. The current paper focuses on analyses of the optical recombination spectra of heavy element ions detected in the spectrum of NGC 7009. New effective recombination coefficients, including those for the N II and O II recombination spectrum that were calculated in the intermediate coupling scheme, are now available and are utilized in the analyses. Plasma diagnostics based on the ORLs of heavy element ions are carried out in Section 2, and the electron temperatures derived from the N II and O II ORL ratios agree with each other and are both close to 1200 K. Thus the general pattern of electron temperatures, $T_e(\text{CELs}) \gtrsim T_e(\text{H I BJ}) \gtrsim T_e(\text{He I}) \gtrsim T_e(\text{N II, O II ORLs})$, which was predicted by the bi-

abundance nebular model (Liu 2003) and has been seen in many PNe, is confirmed in the current analysis of NGC 7009. A comprehensive analysis of individual multiplets of the C II, N II, O II, and Ne II recombination spectra are presented in Section 3. The lines are critically examined for potential blending effects. Comparison is made for the observed and predicted relative intensities of the best observed transitions, using the latest effective recombination coefficients. Ionic and elemental abundances are derived in Section 4, where ADFs for the C, N, O, and Ne ionic abundances are calculated. The results are discussed in Section 5, followed by a summary in Section 6.

2 PLASMA DIAGNOSTICS BASED ON THE ORLS OF HEAVY ELEMENT IONS

2.1 Effective recombination coefficients

Reliable atomic data, most importantly the effective recombination coefficients of abundant heavy element ions such as C II, N II, O II, and Ne II, are key to the spectroscopic analysis of photoionized gaseous nebulae. Most of the *ab initio* calculations of heavy element ions aimed for astrophysical applications hitherto were carried out in the *LS* coupling scheme. This approximation tacitly assumes a statistical distribution in the population of the fine-structure levels of the recombining ions (i.e., 1 : 2 for the $N^{2+} \ ^2P_{1/2}^o$ and $\ ^2P_{3/2}^o$ levels in the case of N II; 1 : 3 : 5 for the $O^{2+} \ ^3P_0$, $\ ^3P_1$ and $\ ^3P_2$ levels in the case of O II). The assumption of *LS* coupling may give satisfactory results for some of the low-lying transitions such as those belonging to the 3p–3s configuration, but not for many of the transitions from the higher 3d–3p or 4f–3d configurations. In low-density objects such as H II regions and evolved PNe, the relative populations of the ground-term fine-structure levels of the recombining ion actually have density-dependence and deviate from the statistical distribution, and so do the relative emissivities of resultant recombination lines. A better treatment of the recombination and the following cascading in a proper coupling scheme is vital for probing the physical conditions in gaseous nebulae.

New *ab initio* calculation of the effective recombination coefficients for the N II recombination spectrum was presented by Fang, Storey & Liu (2011, hereafter FSL11)¹, who took into account the density dependence of effective recombination coefficients arising from the density-dependence of relative populations of the ground fine-structure levels of the recombining ion (i.e. $N^{2+} \ ^2P_{1/2}^o$ and $\ ^2P_{3/2}^o$), an elaboration that has not been attempted before for this ion. The availability of such data opens up the possibility of electron density determination via recombination line analysis. Fig. 1 (also Fig. 3 in FSL11) shows the relative populations of the $N^{2+} \ ^2P_{1/2}^o$ and $\ ^2P_{3/2}^o$ fine-structure levels as a function of electron density under typical nebular conditions. Photoionization cross-sections, bound state energies, and oscillator strengths of N II with $n \leq 11$ and $l \leq 4$ were obtained using the close-coupling R-matrix method in the intermediate coupling scheme. Photoionization data were computed using an energy mesh which accurately map out the near-threshold resonances, and were used to

derive recombination coefficients, including radiative and dielectronic recombination. Also new is the inclusion in the calculations of the effects of dielectronic recombination via high- n resonances lying between the $\ ^2P_{1/2}^o$ and $\ ^2P_{3/2}^o$ thresholds. The calculated coefficients are valid for temperatures down to an unprecedentedly low level (~ 100 K). Figs. 2, 3 and 4 (also Figs. 5, 6 and 7 in FSL11) show the theoretical relative intensities of the fine-structure components of the M3 2p3p $\ ^3D-2p3s \ ^3P^o$, M19 2p3d $\ ^3F^o-2p3p \ ^3D$ and M39 2p4f G[7/2,9/2]–2p3d $\ ^3F^o$ multiplets of N II, respectively, as a function of electron density.

So far, most calculations of the O II effective recombination coefficients have been in the *LS* coupling assumption. The first comprehensive treatment of the O II recombination at nebular temperatures and densities was by Storey (1994), who adopted the bound-bound and bound-free radiative data of O II from the Opacity Project data base (Cunto et al. 1993) and took into account cascading as well as the effects of collisions. LSBC presented partial treatment of intermediate coupling effects in transitions between the $(\ ^3P)4f$, $(\ ^3P)3d$, and $(\ ^3P)3p$ electron configurations. The most recent calculations of effective recombination coefficients for the O II recombination spectrum was carried out by P. J. Storey (private communication, hereafter PJS) in the intermediate coupling scheme. Density dependence of the relative populations of the ground-term fine-structure levels of the recombining ion was considered in the level population calculations. Fig. 5 shows the fractional populations of the recombining ion $O^{2+} \ ^3P_0$, $\ ^3P_1$ and $\ ^3P_2$ fine-structure levels as a function of electron density. The new O II recombination coefficients were calculated down to a temperature of 400 K. Figs. 6, 7 and 8 show the theoretical relative intensities of the fine-structure components of the O II M1 2p²3p $\ ^4D^o-2p^23s \ ^4P$, M10 2p²3d $\ ^4F-2p^23p \ ^4D^o$ and M48 4f G[5,4,3]^o–3d $\ ^4F$ multiplets, respectively, as a function of electron density.

The new effective recombination coefficients for the N II and O II recombination spectra provide an opportunity to construct nebular plasma diagnostics based on the ORLs of heavy element ions. With those new atomic data, we have determined electron temperatures and densities for over 100 Galactic PNe and 40 Galactic and extragalactic H II regions (McNabb et al. 2011). By comparing our results of plasma diagnostics based on the N II and O II ORLs with the electron temperatures given in literature (T_e 's derived from CELs, H I Balmer jump and the He I recombination lines), we find a temperature sequence for about 50 PNe, $T_e([O III]) \gtrsim T_e(H I BJ) \gtrsim T_e(He I) \gtrsim T_e(N II \ \& \ O II \ ORLs)$, which is consistent with predictions from the bi-abundance nebular model postulated by Liu et al. (2000).

Kisielius et al. (1998) published the Ne II effective recombination coefficients that were calculated in the *LS* coupling scheme. Only transitions between states with $l \leq 2$ were presented. Preliminary effective recombination coefficients for a few selected lines from the 4f–3d configuration are available (P. J. Storey, private communication), but only for a single temperature and density case. All the previous calculations of the Ne II recombination spectrum assumed that the three ground-term fine-structure levels of the recombining ion $Ne^{2+} \ ^3P_2$, $\ ^3P_1$ and $\ ^3P_0$, are thermalized, i.e. they are populated according to the statistical weights. However, the $\ ^3P_1$ and $\ ^3P_0$ levels have relatively large critical densities: $2.0 \times 10^5 \text{ cm}^{-3}$ for $\ ^3P_1$ and $2.9 \times 10^4 \text{ cm}^{-3}$ for $\ ^3P_0$ at 10 000 K, and these values drop to about half when the electron temperature decreases to 1000 K. At physical conditions lower than the critical densities, the $\ ^3P_1$ and $\ ^3P_0$ levels are underpopulated compared to the values under thermal equilibrium. Fig. 9 shows the fractional populations of the three Ne III levels as a function of electron den-

¹ Dr. Daniel Péquignot found some anomalies in the published data of FSL11, which were due to mislabeling of five bound-state energy levels of N II. The labeling has recently been corrected and the effective recombination coefficients for the N II lines were re-calculated. A corrigendum has been in preparation. Figs. 2, 3 and 4 in the current paper are based on the revised effective recombination coefficients of N II.

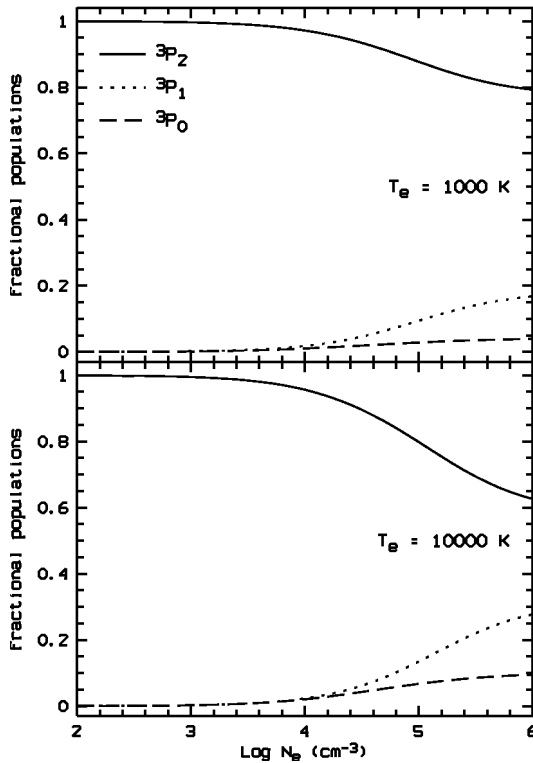


Figure 9. Fractional populations of the Ne^{2+} 3P_2 , 3P_1 and 3P_0 fine-structure levels. Two temperature cases, 1000 and 10 000 K, are shown. This figure is obtained by solving the level population equations for a five-level atomic model.

sity. The effects of the non-equilibrium level populations of Ne III on the effective recombination coefficients for the $4f - 3d$ transitions are not clear and may vary from line to line. For the strongest $4f - 3d$ lines that form exclusively from recombination of target 3P_2 plus cascades, their effective recombination coefficients will be underestimated if a thermal equilibrium of the Ne III ground levels is assumed, and that will cause a corresponding overestimation of the derived $\text{Ne}^{2+}/\text{H}^+$.

Many Ne II recombination lines from different multiplets have been observed in deep spectra of PNe and H II regions and ionic abundances derived (e.g. LLB01). However, a proper analysis of those data requires new calculations in an appropriate coupling scheme for the strongest Ne II recombination lines, especially those belonging to the $3d - 3p$ and $4f - 3d$ transition arrays.

2.2 Electron temperature from the C II recombination lines

Most C II lines detected in the spectrum of NGC 7009 are mainly excited by radiative recombination, except for a few for which dielectronic recombination dominates. Examples of the latter include the C II M28.01 $3d' ^2F^\circ - 3p' ^2D$ $\lambda 8797$ multiplet, which originates from dielectronic capture of an electron to the $2s2p(^3P_J)3d ^2F^\circ$ autoionization state that lies 0.41 eV (Moore 1993) above the first ionization threshold $2s^2 ^1S_0$ and the subsequent decay to the $2s2p(^3P_J)3p ^2D$ bound state that lies about 1.00 eV below the ionization threshold. Fig. 10 is a schematic diagram that shows the dielectronic and radiative recombination of C II.

The electron on an autoionizing state either decays to another autoionizing or bound state with the emission of radiation, or autoionizes to a true continuum state leaving an ion and a free elec-

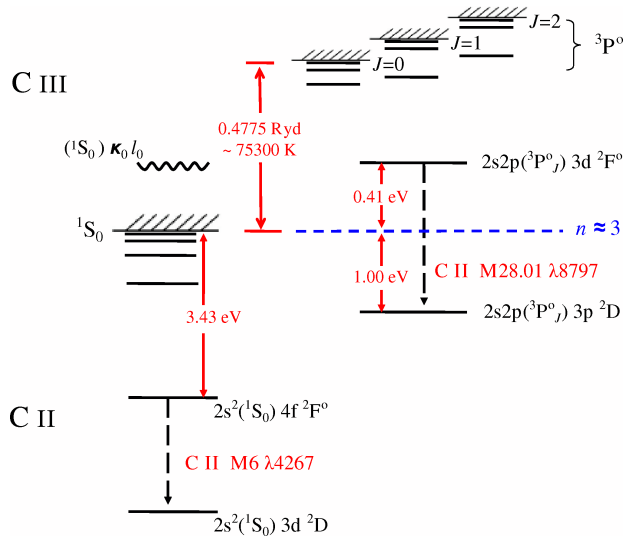


Figure 10. Schematic figure showing the dielectronic recombination of C II through the autoionizing state between the ionization thresholds $2s^2 ^1S_0$ and $2s2p(^3P_J)3d ^2F^\circ$ of C III. The electrons captured to the $2s2p(^3P_J)3d ^2F^\circ$ autoionizing state either go back to a true continuum state $2s^2(^1S_0)\kappa_0 l_0$ through autoionization, or decay to the $2s2p(^3P_J)3p ^2D$ bound state through the C II M28.01 $\lambda 8797$ transition. Also shown is the C II M6 $\lambda 4267$ radiative recombination transition between the $4f ^2F^\circ$ and the $3d ^2D$ bound states.

tron with no emission of radiation. The latter process usually dominates, and the population of autoionization states is close to that given by Saha and Boltzmann equations as in the case of the local thermodynamic equilibrium (LTE). The emissivity of a dielectronic recombination line is sensitive to electron temperature through the Boltzmann factor $\exp(-E/kT_e)$, where E is the excitation energy of the upper state relative to the ionization threshold. By comparing the strength of a dielectronic recombination line to that of an ordinary (i.e. radiative recombination dominated) recombination line, whose emissivity has a relatively weak power-law dependence on electron temperature ($\sim T_e^\alpha$, where $\alpha \sim 1$), one can determine the electron temperature. The C II dielectronic lines have been used to determine electron temperatures in stellar winds of PNe (e.g. De Marco et al. 1998). The strongest C II recombination line detected in the spectra of nebulae is the M6 $4f ^2F^\circ - 3d ^2D$ $\lambda 4267$ line, which is excited by radiative recombination only. The upper state of the $\lambda 4267$ line lies about 3.4 eV below the ionization threshold $2s^2 ^1S_0$ (see Fig. 10), and its population is far from LTE, and thus has a very different temperature-dependence from that of the upper state of the M28.01 $\lambda 8797$ transition (i.e. $3d ^2F^\circ$). We use the intensity ratio of the $\lambda 8793.80$ ($3d' ^2F^\circ_{7/2} - 3p' ^2D_{5/2}$) line, the stronger fine-structure component of the C II M28.01 multiplet, and the $\lambda 4267$ line to determine electron temperature. In NGC 7009, this line ratio yields a temperature of 3000 K, as shown in Fig. 11. The atomic data used here are the effective dielectronic and radiative recombination coefficients of Nussbaumer & Storey (1984) and Péquignot, Petitjean & Boisson (1991), respectively. Measurements of the C II M28.01 lines are presented in Section 3.1.2.

2.3 Electron temperatures and densities from the N II and O II recombination lines

In the low-density conditions in nebulae, the relative populations of the ground-term fine-structure levels of a recombining ion (e.g.,

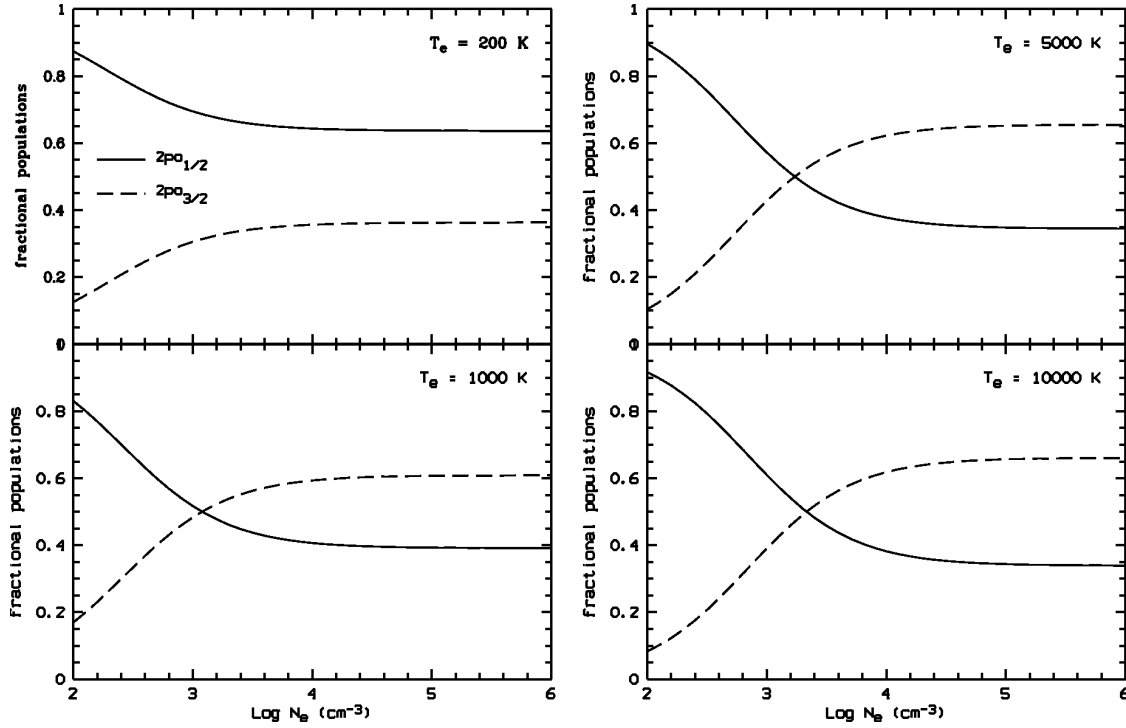


Figure 1. Fractional populations of the $N^{2+} 2P^o_{1/2}$ and $2P^o_{3/2}$ fine-structure levels. Four temperature cases, 200, 1000, 5000 and 10 000 K, are shown. This figure is obtained by solving level population equations for a five-level atomic model.

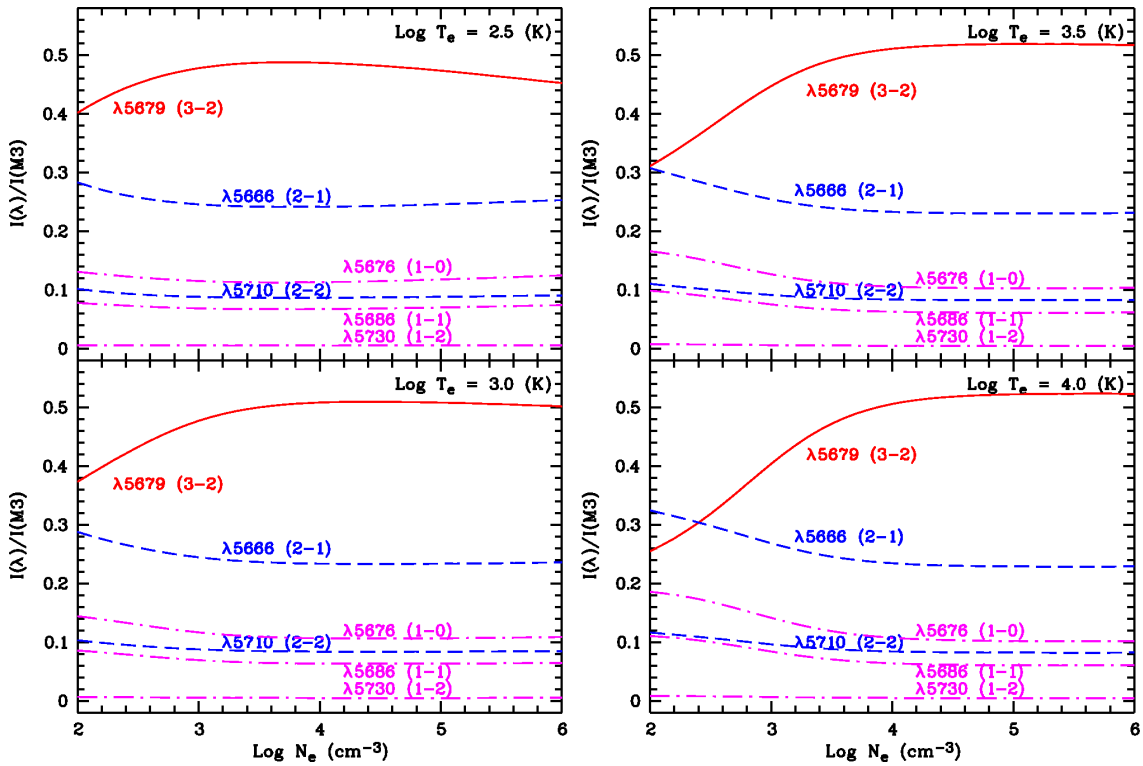


Figure 2. Fractional intensities of the $N \text{ II M3 } 2p3p \text{ } ^3D - 2p3s \text{ } ^3P^o \text{ } \lambda 5679$ multiplet as a function of electron density. The numbers in the brackets ($J_2 - J_1$) following the wavelength labels are the total angular momentum quantum numbers of the upper and lower levels, respectively. Transitions from the upper levels with the same angular momentum quantum number J_2 are represented by curves of the same color and line type. Four temperature cases, $\log T_e$ [K] = 2.5, 3.0, 3.5, and 4.0, are presented. The calculations were based on the effective recombination coefficients of FSL11.

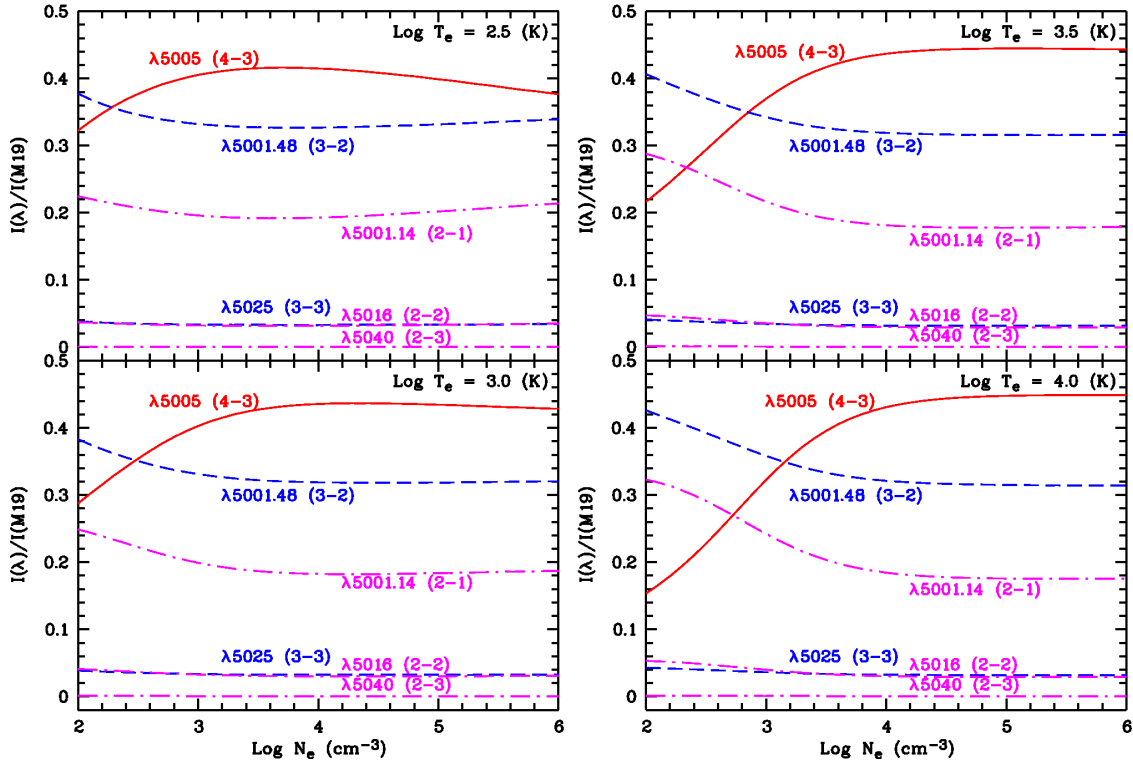


Figure 3. Same as Fig. 2 but for the fractional intensities of the N II M19 $2p3d^3F^o - 2p3p^3D$ $\lambda 5004$ multiplet.

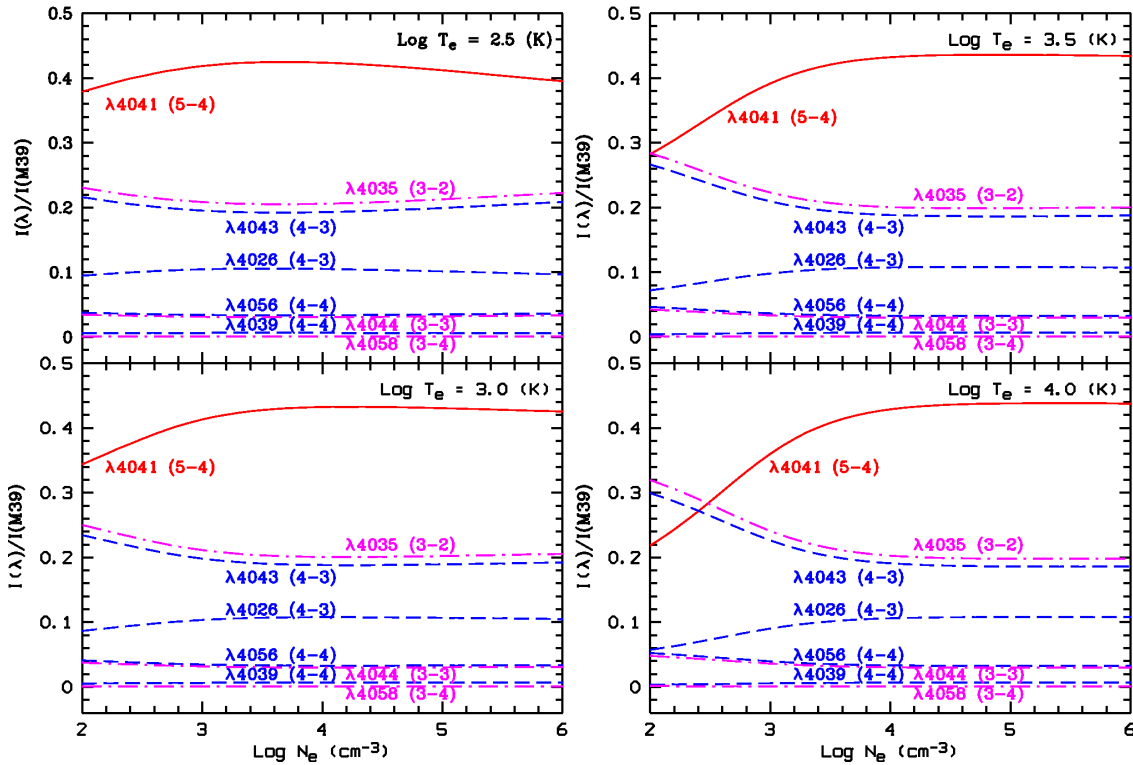


Figure 4. Same as Fig. 2 but for the fractional intensities of the N II M39 $2p4fG[7/2,9/2] - 2p3d^3F^o$ $\lambda 4041$ multiplet.

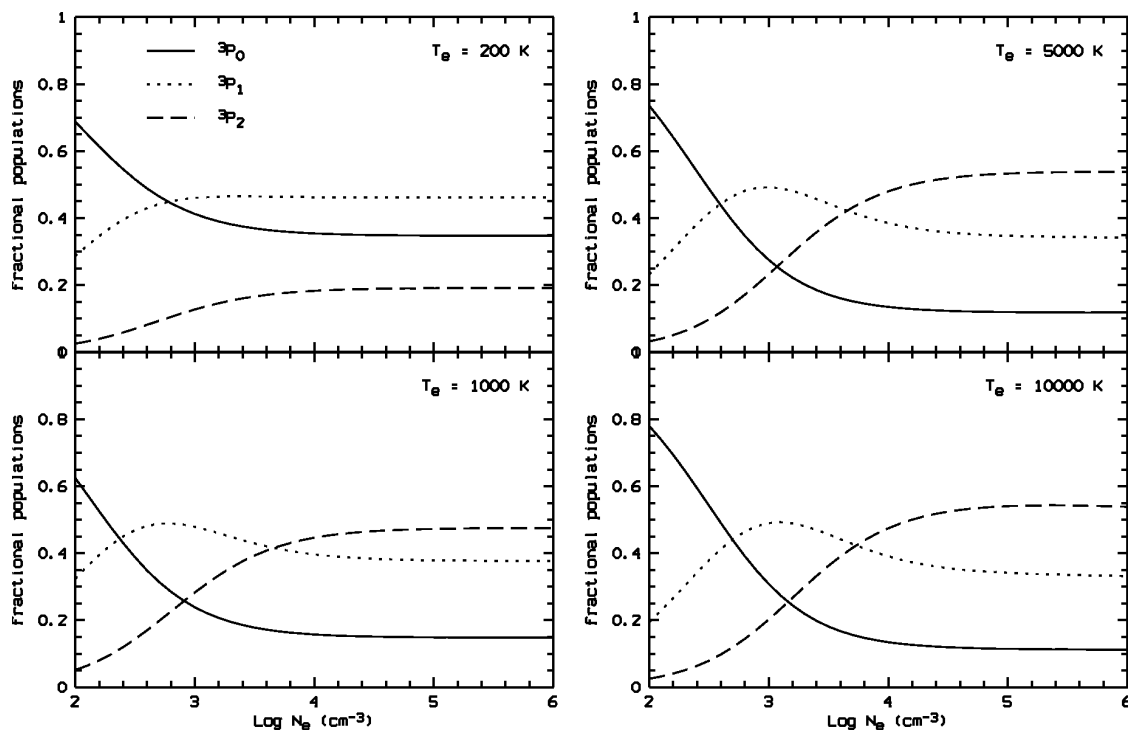


Figure 5. Fractional populations of the $O^{2+} \ ^3P_0$, $\ ^3P_1$ and $\ ^3P_2$ fine-structure levels. Four temperature cases, 200, 1000, 5000 and 10000 K, are shown. This figure is obtained by solving the level population equations for a five-level atomic model.

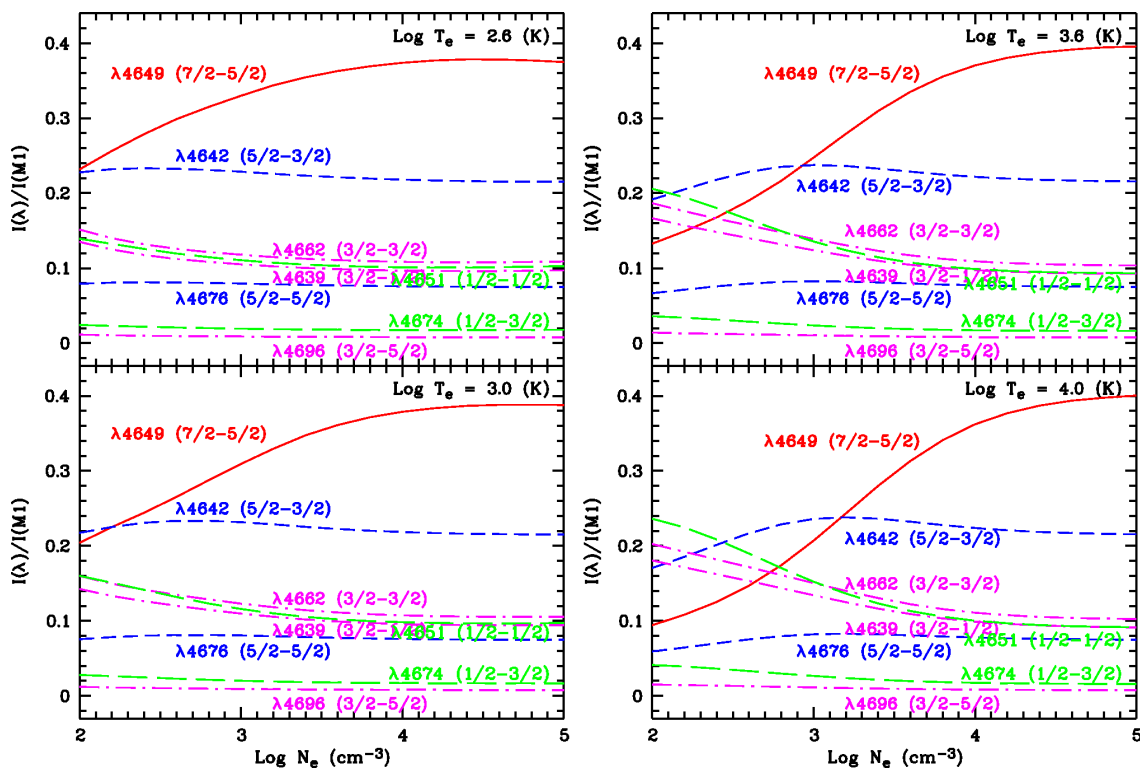


Figure 6. Same as Fig. 2 but for the fractional intensities of the $O \ II \ M1 \ 2p^2 3p^4 D^o - 2p^2 3s^4 P \ \lambda 4652$ multiplet. The calculations were based on the unpublished effective recombination coefficients of PJS.

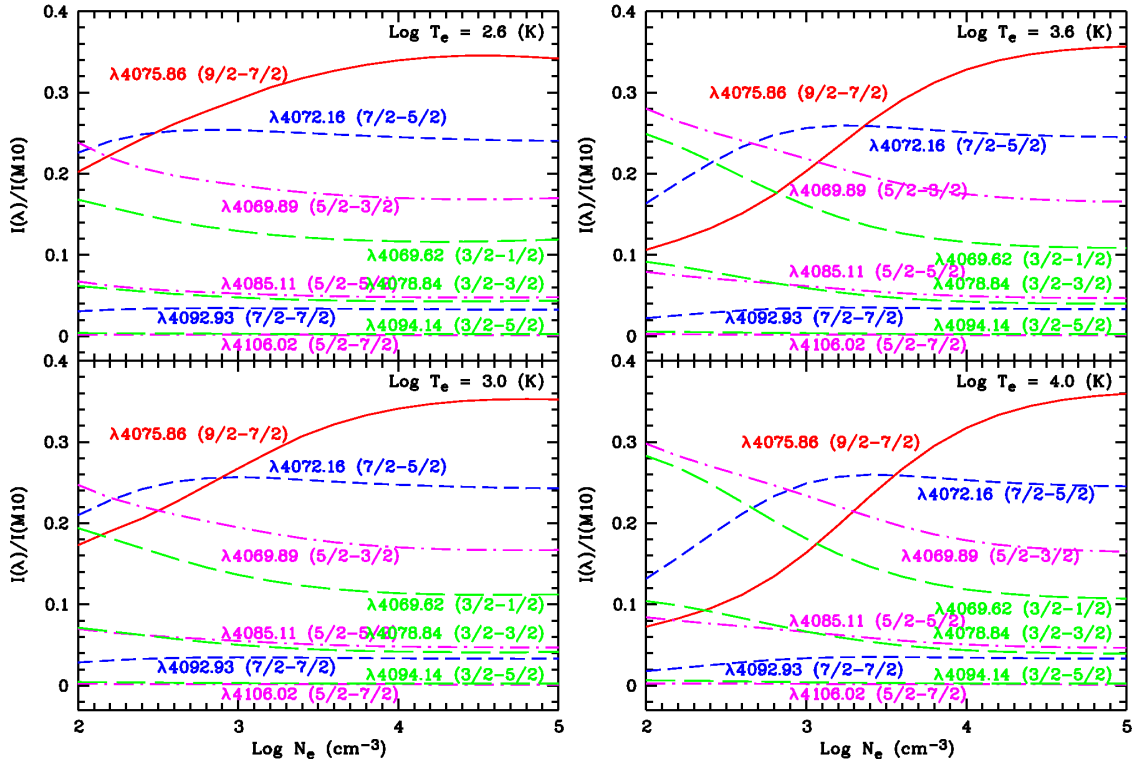


Figure 7. Same as Fig. 6 but for the fractional intensities of the O II M10 $2p^23d^4F - 2p^23p^4D^\circ$ $\lambda 4075$ multiplet.

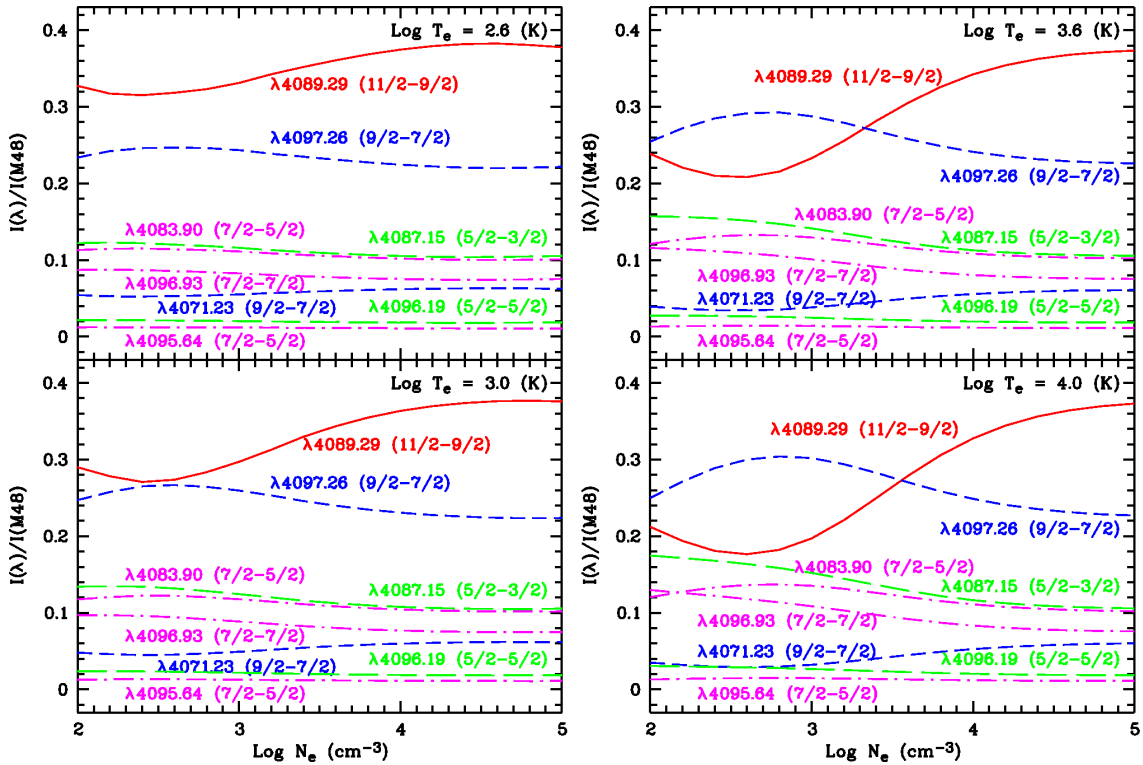


Figure 8. Same as Fig. 6 but for the fractional intensities of the O II M48 $4fG[5,4,3]^\circ - 3d^4F$ $\lambda 4089$ multiplet.

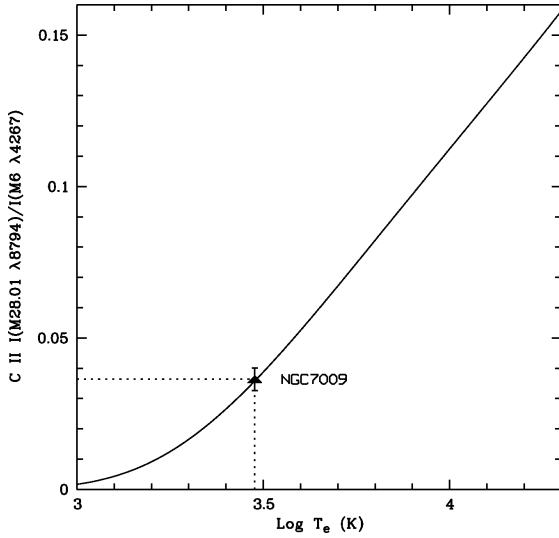


Figure 11. The C II $\lambda 8794/\lambda 4267$ ratio as a function of electron temperature. The plot is based on the effective dielectronic and radiative recombination coefficients calculated by Nussbaumer & Storey (1984) and Péquignot, Petitjean & Boisson (1991), respectively. The observed C II $\lambda 8794/\lambda 4267$ ratio in NGC 7009 yields an electron temperature of $\sim 3000 \pm 250$ K. The error bar is calculated from measurement uncertainties of the two lines.

N^{2+} $^2P_{1/2}^o$ and $^2P_{3/2}^o$ in the case of N II) vary with electron density, and this is reflected in the density dependence of the resultant emissivities (i.e. the effective recombination coefficients) of different recombination lines within a multiplet of the recombined ion. Thus by comparing the intensities of two ORLs belonging to the same multiplet but formed from different parent levels one can determine electron density. At typical nebular conditions, emissivities of heavy element recombination lines have only a weak, power-law dependence on electron temperature, $\epsilon \propto T_e^{-\alpha}$ ($\alpha \sim 1$), and in general, the line ratios depend very little on temperature. However, the temperature sensitivity still differs for recombination lines decaying from levels of different orbital angular momentum quantum number l , and this difference becomes more profound if two lines of very different l are compared. Thus the intensity ratio of two lines from multiplets of different l can be used to determine electron temperature, provided that the measurements are precise enough (e.g. Liu 2003; FSL11).

Figs. 12 and 13 show that the N II line ratio $\lambda 5679/\lambda 4041$ observed in NGC 7009 yields an electron temperature of $\sim 1200 \pm 200$ K, whereas the $\lambda 5679/\lambda 5666$ ratio yields a density of $2000 - 3000 \text{ cm}^{-3}$. The $\lambda 5679.56$ line is the strongest fine-structure component of the N II M3 $3p^3D - 3s^3P^o$ $\lambda 5679$ multiplet, and forms exclusively from the $^2P_{3/2}^o$ core capturing an electron plus cascades from higher levels, while the second strongest line $\lambda 5666.63$ can form, in addition, from recombination of the $^2P_{1/2}^o$ core. For the target N^{2+} , the population of the fine-structure level $^2P_{3/2}^o$ relative to $^2P_{1/2}^o$ increases with electron density due to collisional excitation, and this results in an increase of the $\lambda 5679.56$ intensity relative to the $\lambda 5666.63$ line with density, as shown in Fig. 2. Thus the $\lambda 5679/\lambda 5666$ ratio can be used as a density diagnostic. The $\lambda 4041.31$ line belongs to the N II M39b $4fG[9/2] - 3d^3F^o$ multiplet and is the strongest among the N II $4f - 3d$ array. It forms from recombination of the $^2P_{3/2}^o$ core plus cascades from higher levels. The intensity ratio of the $\lambda 5679.56$ and $\lambda 4041.31$ lines has a relatively strong temperature dependence, and thus can serve as a temperature diagnostic. In the spectrum of NGC 7009,

the $\lambda 5666.63$ line is free of blending and is amongst the best observed N II ORLs, while the $\lambda 5679.56$ and $\lambda 4041.31$ lines are affected by line blending. Accurate measurements of the latter two lines were obtained using multi-Gaussian profile fits (see Section 3.2). The M19 $2p3d^3F^o - 2p3p^3D$ multiplet is the strongest of the $3d - 3p$ configuration of N II. The density-dependence of the relative emissivities of the two strongest fine-structure components of M19 is noticeable (Fig. 3). The intensity ratio of those components, $\lambda 5005.15/(\lambda 5001.14 + \lambda 5001.48)$, may serve as another density diagnostic. Similarly, the intensity ratio of the $\lambda 5005.15$ and M39b $\lambda 4041.31$ lines may be used to determine electron temperature. Figs. 14 and 15 show the $\lambda 5005/\lambda 5001$ and $\lambda 5005/\lambda 4041$ ratios of N II as a function of electron density and temperature, respectively. However, accurate measurements of the N II M19 lines are essentially impossible due to the presence of the extraordinarily strong [O III] $\lambda 5007$ line, which is often strongly saturated in deep spectra.

Some N II states of parentage other than $^2P^o$ have energies even higher than the $2p(^2P^o)4fG[9/2]$ spectral term, which is the upper state of the M39b $\lambda 4041.31$ line. The intensity ratio of an N II recombination line that originates from one of those high-energy states to the M3 $\lambda 5679.56$ line can also be used as a temperature diagnostic. Possible candidates in the optical waveband for such application are, e.g. the M63 $3p^5D^o - 3s^5P$, M66 $3d^5F - 3p^5D^o$ and M72 $4f^5G^o - 3d^5F$ multiplets. According to the experimental data given by NIST², the upper state of the M63 multiplet is about 1.85 eV below the ionization threshold N III $^2P_{1/2}^o$, while the upper states of the M66 and M72 multiplets are 0.53 and 3.67 eV, respectively, above this threshold. The R-matrix calculation of the bound-state energy levels of N II in FSL11 only extends to about 0.45 eV (corresponding to $n = 11$ in the principal series of N II) below the ionization threshold. Thus only the energy levels of the $2s2p^2(^4P)3s$ and $2s2p^2(^4P)3p$ configurations (i.e., the levels of the 5P , 3P , $^3S^o$, $^5D^o$, $^5P^o$, $^3D^o$, $^5S^o$ and $^3P^o$ spectral terms, in the energy order given by NIST) are included in the R-matrix calculation and the N II recombination lines that originate from those levels are precisely calculated. In principle, the intensity ratio of the $\lambda 5679.56$ and the $\lambda 5535.36$ lines, the strongest fine-structure components of the M3 $3p^3D - 3s^3P^o$ and the M63 $3p^5D^o - 3s^5P$ multiplets of N II, respectively, can be used to determine electron temperature. Fig. 16 shows the $\lambda 5679/\lambda 5535$ ratio as a function of electron temperature, and this relation is quite insensitive to electron density in the logarithmic scale. However, accurate measurements of the $\lambda 5535.36$ line is difficult due to weakness (about 10^4 times weaker than H β). We have not detected any N II lines of the parentage other than $^2P^o$ in the deep spectrum of NGC 7009.

The $\lambda 4649.13$ line is the strongest of the O II M1 $3p^4D^o - 3s^4P$ multiplet, and forms only from recombination of the 3P_2 core plus cascades from higher energy levels, while another O II M1 line $\lambda 4661.63$ can form, in addition, from recombination of the 3P_0 and 3P_1 cores. For the recombining ion O^{2+} , the population of the fine-structure level 3P_2 relative to 3P_0 and 3P_1 increases with electron density due to collisional excitation, and so does the resultant emissivity of the $\lambda 4649.13$ line relative to the $\lambda 4661.63$ line, as is shown in Fig. 6. Thus the intensity ratio $\lambda 4649/\lambda 4662$ can serve as a density diagnostic. The $\lambda 4089.29$ line (M48a $4fG[5]_{11/2}^o - 3d^4F_{9/2}$) is the strongest amongst the O II $4f - 3d$ array, and forms from recombination of the 3P_2 core. The intensity ratio of the $\lambda 4089.29$ and

² The NIST Spectra Database

http://physics.nist.gov/PhysRefData/ASD/levels_form.html

the $\lambda 4649.13$ lines has a strong temperature dependence, and can be used to determine electron temperature. Figs. 17 and 18 show that the observed O II line ratios $\lambda 4649/\lambda 4089$ and $\lambda 4649/\lambda 4662$ in NGC 7009 yield an electron temperature of $\sim 1400 \pm 300$ K and a density of $2500 - 4000 \text{ cm}^{-3}$, respectively. Although the $\lambda 4661.63$ line is the third strongest in the O II M1 multiplet, it is free from line blending and thus best observed, while the $\lambda 4649.13$ and $\lambda 4089.29$ lines both suffer from line blending: the $\lambda 4649.13$ line is blended with another O II M1 line $\lambda 4650.84$ and the three C III M1 lines $\lambda \lambda 4647.42, 4650.25$ and 4651.47 ; the $\lambda 4089.29$ line is contaminated by the Si IV M1 $\lambda 4088.86$ ($4p^2 P_{3/2}^o - 4s^2 S_{1/2}$) line. Multi-Gaussian fitting was carried out to derive the intensities of the two O II ORLs, and both intensities are accurate to within 20 per cent. Details of spectral fits are given in Section 3.3.

The M10 $3d^4 F - 3p^4 D^o$ $\lambda 4075$ multiplet is the strongest transition of the $3d - 3p$ configuration of O II. Given the opposite trends of the fractional intensities of the $\lambda 4075.86$ and $\lambda 4069.89, 62$ lines, the three fine-structure components of M10, as a function of electron density, as shown in Fig. 7, the intensity ratio of the two lines may serve as another density diagnostic. Here the $\lambda 4075.86$ line is the strongest component of the M10 multiplet. The intensity ratio of the $\lambda 4075.86$ line and the $\lambda 4089.29$ line, the strongest fine-structure component of the M48a $4f G[5]^o - 3d^4 F$ multiplet of O II, can be used as another temperature diagnostic. Figs. 19 and 20 show the $\lambda 4076/\lambda 4089$ and $\lambda 4076/\lambda 4070$ as a function of electron temperature and density, respectively. Here the intensity of the $\lambda 4070$ line is a sum of the $\lambda 4069.89$ (M10 $3d^4 F_{5/2} - 3p^4 D_{3/2}^o$) and $\lambda 4069.62$ (M10 $3d^4 F_{3/2} - 3p^4 D_{1/2}^o$) lines. If we assume a density of about 4300 cm^{-3} , as derived from CEL ratios (Paper I), the electron temperature deduced from the O II $\lambda 4076/\lambda 4089$ ratio is 1150 ± 300 K for NGC 7009. The electron density derived from the O II $\lambda 4076/\lambda 4070$ ratio is of large uncertainty, due to the relatively large measurement uncertainties of the two lines. The $\lambda 4075.86$ line is blended with [S II] $\lambda 4076.35$ ($3p^3^2 P_{1/2}^o - 4^4 S_{3/2}^o$) line, while the $\lambda 4069.89, 62$ line is blended with the [S II] $\lambda 4068.60$ ($3p^3^2 P_{3/2}^o - 4^4 S_{3/2}^o$) line and the three C III M16 $5g^3 G - 4f^3 F^o$ lines $\lambda \lambda 4067.94, 4068.92$ and 4070.31 . Multi-Gaussian profile fitting was carried out to obtain line fluxes (c.f. Section 3.3.2).

Several O II recombination lines with parentage other than 3P have been detected in the spectrum of NGC 7009. These lines belong to the M15 $3p^2 F^o - 3s^2 D$, M36 $3d^2 G - 3p^2 F^o$, M101 $4f^2 H[5]^o - 3d^2 G$, and M105 $4f^2 P[1]^o - 3d^2 S$ multiplets of O II. According to the experimental data from NIST, the upper states of the M15 and M36 multiplets are 6.76 and 3.80 eV, respectively, below the ionization threshold O III 3P_0 , while the upper states of the M101 and M105 multiplets are about 0.89 and 0.87 eV, respectively, below this threshold. In the most recent calculation of PJS for the O II effective recombination coefficients, only the transitions between the levels with principal quantum number $n \leq 6$ (i.e. corresponding to 1.50 eV below the ionization threshold 3P_0) were presented. Thus only the effective recombination coefficients of the M15 and M36 lines are available. The strongest fine-structure components of the M15 and M36 multiplets are $\lambda 4590.97$ ($3p^2 F_{7/2}^o - 3s^2 D_{5/2}$) and $\lambda 4189.79$ ($3d^2 G_{9/2} - 3p^2 F_{7/2}^o$), respectively, and both lines are detected in the deep spectrum of NGC 7009, as shown in Figs. B1 and 31. Although the effective recombination coefficients of the M101 and M105 multiplets are not available, the strongest fine-structure component of the M101 multiplet, the $\lambda 4253.90$ ($4f^2 H[5]_{11/2}^o - 3d^2 G_{9/2}$) line, is also detected (Fig. 31). Fig. 21 shows the O II line ratios $\lambda 4649.13/\lambda 4590.97$ and $\lambda 4649.13/\lambda 4189.79$ as a function of electron temperature. The fig-

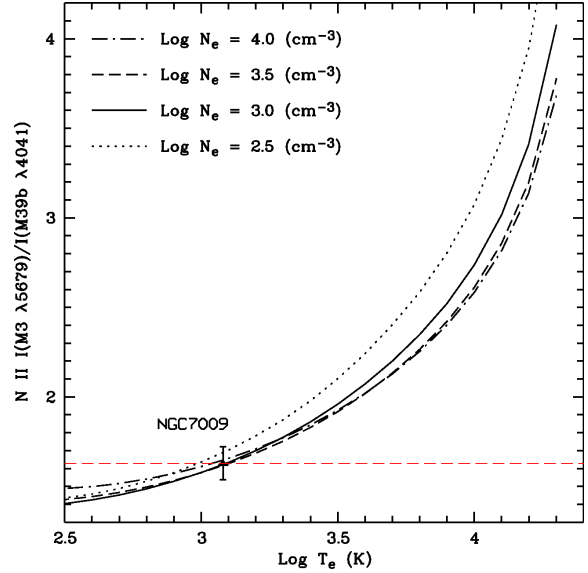


Figure 12. The N II $\lambda 5679/\lambda 4041$ ratio as a function of electron temperature. Different curves represent different density cases, and are based on the calculation of FSL11. The observed N II $\lambda 5679/\lambda 4041$ ratio in NGC 7009 yields an electron temperature of about 1200 ± 200 K. The error bar was calculated from measurement uncertainties of the two lines.

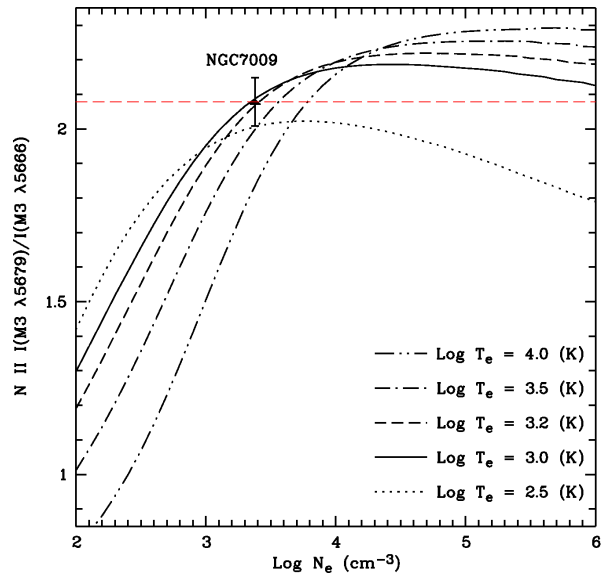


Figure 13. The N II $\lambda 5679/\lambda 5666$ ratio as a function of electron density. Different curves represent different temperature cases, and are based on the calculation of FSL11. The observed N II $\lambda 5679/\lambda 5666$ ratio in NGC 7009 yields an electron density of $2000 - 3000 \text{ cm}^{-3}$. The error bar was calculated from measurement uncertainties of the two lines.

ure also shows that the two line ratio–temperature relations are insensitive to electron density, indicating that they are good temperature diagnostics. Both line ratios detected in the spectrum of NGC 7009 yield electron temperatures close to 3600 K.

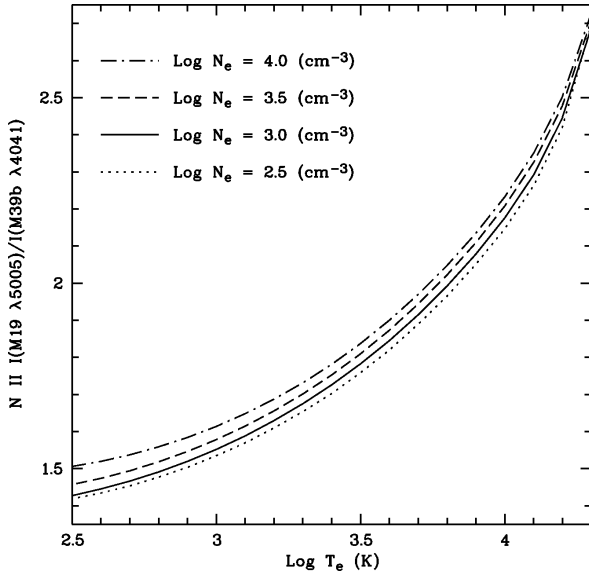


Figure 14. The N II $\lambda 5005/\lambda 4041$ ratio as a function of electron temperature. Different curves represent different density cases, and are based on the calculation of FSL11.

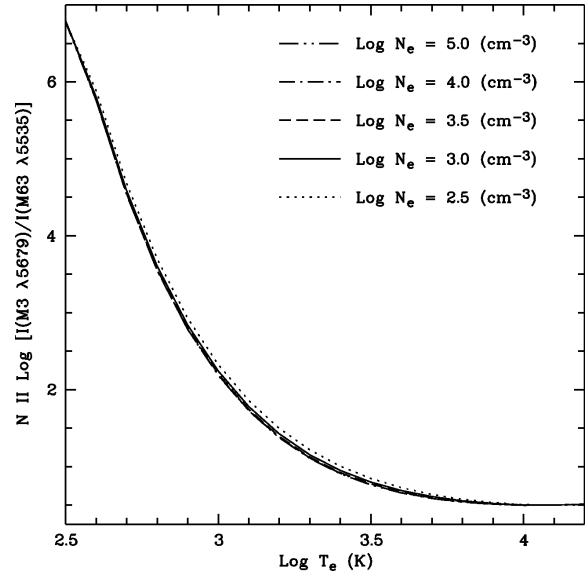


Figure 16. The N II $\lambda 5679/\lambda 5535$ ratio as a function of electron temperature. Here the intensity of the $\lambda 5535$ line is a sum of the $\lambda 5535.36$ (M63 $3p' \ ^5D_4 - 3s' \ ^5P_3$) and $\lambda 5535.36$ (M63 $3p' \ ^5D_1 - 3s' \ ^1P_3$) lines. Different curves represent different density cases, and are based on the calculation of FSL11.

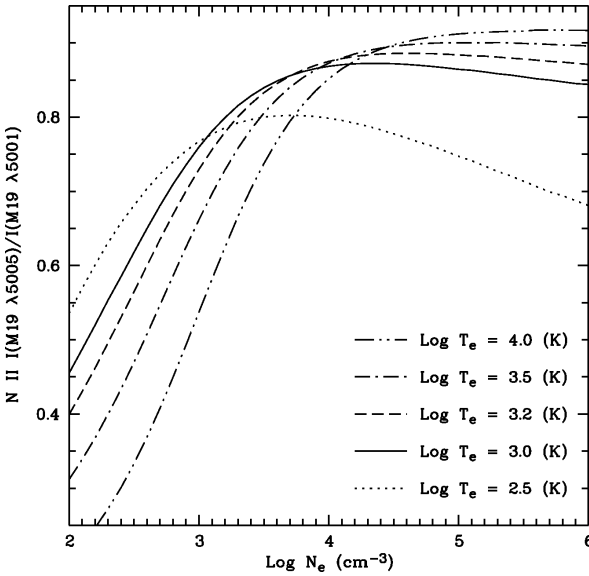


Figure 15. The N II $\lambda 5005/\lambda 5001$ ratio as a function of electron density. Here the intensity of the $\lambda 5001$ line is a sum of the $\lambda 5001.48$ (M19 $3d \ ^3F_3 - 3p \ ^3D_2$) and $\lambda 5001.14$ (M19 $3d \ ^3F_2 - 3p \ ^3D_1$) lines. Different curves represent different temperature cases, and are based on the calculation of FSL11.

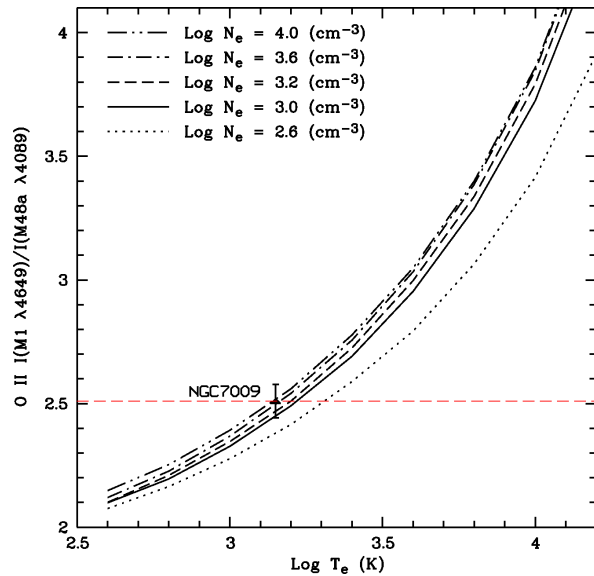


Figure 17. The O II $\lambda 4649/\lambda 4089$ ratio as a function of electron temperature. Different curves represent different density cases, and are based on the unpublished calculation of PJS. The observed O II $\lambda 4649/\lambda 4089$ ratio in NGC 7009 yields an electron temperature of about 1400 ± 300 K. The error bar was calculated from measurement uncertainties of the two lines.

2.4 The Ne II recombination lines as potential plasma diagnostics

So far no efforts have been attempted for plasma diagnostics based on the Ne II recombination spectrum, partly due to the lack of suitable effective recombination coefficients. Since all Ne II effective recombination coefficients were calculated under the *LS* coupling scheme, and relative populations of the 3P_2 , 3P_1 and 3P_0 parent levels were assumed to be proportional to the statistical weights, no density diagnostic is possible with the current available atomic data. However, the Ne II recombination line ratios may still serve as temperature diagnostics using the effective recombination co-

efficients of Kisielius et al. (1998). The M2 $3p \ ^4D^\circ - 3s \ ^4P$ $\lambda 3337$ multiplet is the strongest transition of the $3p - 3s$ configuration, and M13 $3d \ ^4F - 3p \ ^4D^\circ$ $\lambda 3220$ is the strongest multiplet of the $3d - 3p$ configuration of Ne II. The intensity ratio of the strongest fine-structure components of those two multiplets, $\lambda 3334.84/\lambda 3218.19$, may serve as a temperature diagnostic, as shown in the upper panel of Fig. 22. In order to obtain reliable electron temperature, the measurement uncertainty of the $\lambda 3334/\lambda 3218$ ratio needs to be less than 10 per cent, which is very demanding to achieve.

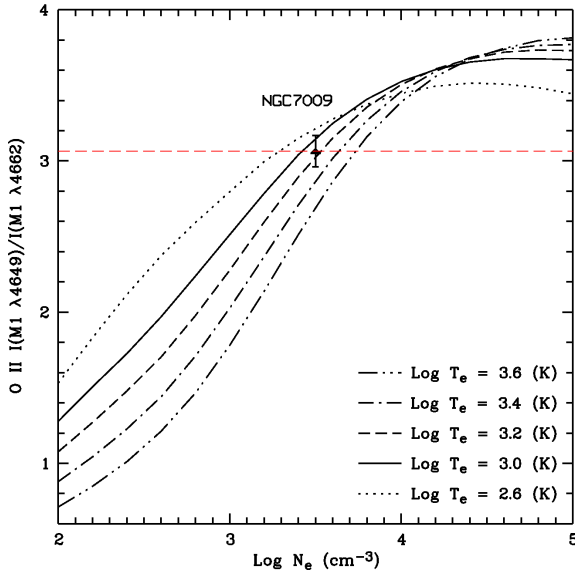


Figure 18. The O II $\lambda 4649/\lambda 4662$ ratio as a function of electron density. Different curves represent different temperature cases, and are based on the unpublished calculation of PJS. The observed O II $\lambda 4649/\lambda 4662$ ratio in NGC 7009 yields an electron density of $2500\text{--}4000\text{ cm}^{-3}$. The error bar was calculated from measurement uncertainties of the two lines.

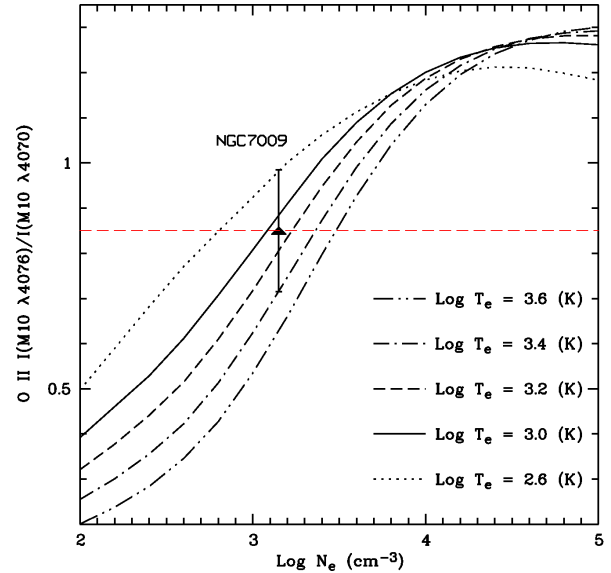


Figure 20. Same as Fig. 18 but for the O II $\lambda 4076/\lambda 4070$ ratio as a function of electron density. Here the intensity of the $\lambda 4070$ line is a sum of the $\lambda 4069.89$ (M10 $3d^4F_{5/2} - 3p^4D_{3/2}^o$) and $\lambda 4069.62$ (M10 $3d^4F_{3/2} - 3p^4D_{1/2}^o$) lines.

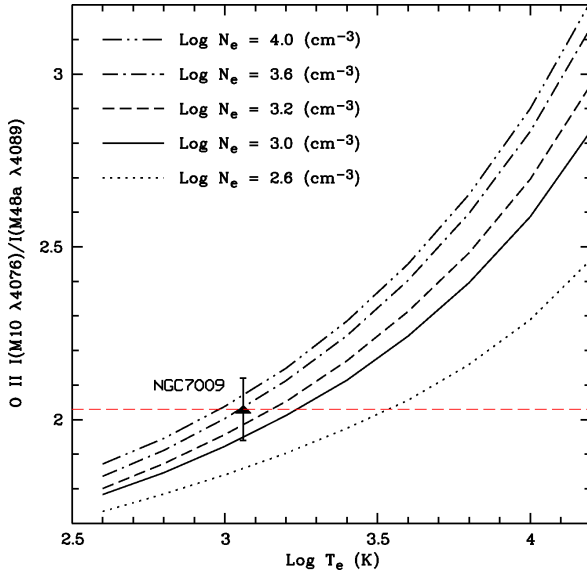


Figure 19. Same as Fig. 17 but for the O II $\lambda 4076/\lambda 4089$ ratio as a function of electron temperature.

Recombination of the $\text{Ne}^{2+} \text{ } ^1D$ core plus cascades gives rise to another series of Ne II recombination lines, and the strongest multiplet of this series is M9 $3p' \text{ } ^2F^o - 3s' \text{ } ^2D$ $\lambda 3571$. The intensity ratio of the $\lambda 3568.50$ line, the strongest fine-structure component of the M9 multiplet, and the M2 $\lambda 3334.84$ line may be used as another temperature diagnostic, as shown in the lower panel of Fig. 22. The calculation of Kisielius et al. (1998) shows that the $\lambda 3568/\lambda 3334$ ratio is only marginally sensitive to electron temperature. In order to derive reliable temperature, the line ratio (especially the $\lambda 3568$ line) needs to be measured to a very high accuracy level. Although the temperature range considered in the calculation of Kisielius et al. (1998) is from 1000 to 20 000 K, the current ana-

lytic fit to the effective recombination coefficient for the $\lambda 3568$ line is only valid for 2000–20 000 K. As a consequence, the usage of the diagnostic curve of the $\lambda 3568/\lambda 3334$ ratio in Fig. 22 outside this temperature range is not recommended. The Ne II $\lambda 3334/\lambda 3218$ and $\lambda 3568/\lambda 3334$ ratios observed in NGC 7009 are 1.86 and 0.40, respectively, both falling outside the diagnostic ranges of Fig. 22.

2.5 The C III, N III and O III recombination lines as potential temperature diagnostics

In this Section, we discuss the possibility of using the C III, N III and O III optical recombination line ratios to determine electron temperatures. Although some of those lines are detected in the spectrum of NGC 7009, they are not used for plasma diagnostics in the current paper, due to the lack of adequate atomic data. Unless otherwise specified, the effective recombination coefficients of Nussbaumer & Storey (1984) and Péquignot, Petitjean & Boisson (1991) are used to create the diagnostic curves.

The C III lines are excited by recombination only, and the ratios of the best observed lines can be used as temperature probes. The intensity ratio of the M1 $\lambda 4649$ ($3p^3P^o - 3s^3S$) and M16 $\lambda 4069$ ($5g^3G - 4f^3F^o$) multiplets of C III is sensitive to electron temperature, as shown in the upper panel of Fig. 23. The intensity ratio of the C III triplet M1 $\lambda 4649$ and singlet M18 $\lambda 4187$ ($5g^1G - 4f^1F^o$) can also be used to determine electron temperature, as shown in the lower panel of Fig. 23. However, those C III lines all suffer from line blending. The $\lambda 4187$ line is blended with the O II M36 $\lambda 4185.45$ ($3d' \text{ } ^2G_{7/2} - 3p' \text{ } ^2F_{5/2}^o$) line, but its intensity can be measured to a high accuracy using multi-Gaussian profile fitting (Fig. 31). The C III M1 $\lambda 4649$ triplets are blended with the O II M1 $3p^4D^o - 3s^4P$ lines $\lambda \lambda 4649.13$ and 4650.84 (Fig. 32), and the C III M16 $\lambda 4069$ triplets are blended with three O II M10 $3d^4F - 3p^4D^o$ lines and the [S II] $\lambda 4068.60$ line (Fig. 33). Intensities of the C III M1 and M16 multiplets are obtained from multi-Gaussian profile fitting. The intensity ratio of the fine-structure components of each multiplet was assumed to be as in *LS* coupling (Sections 3.3.1 and

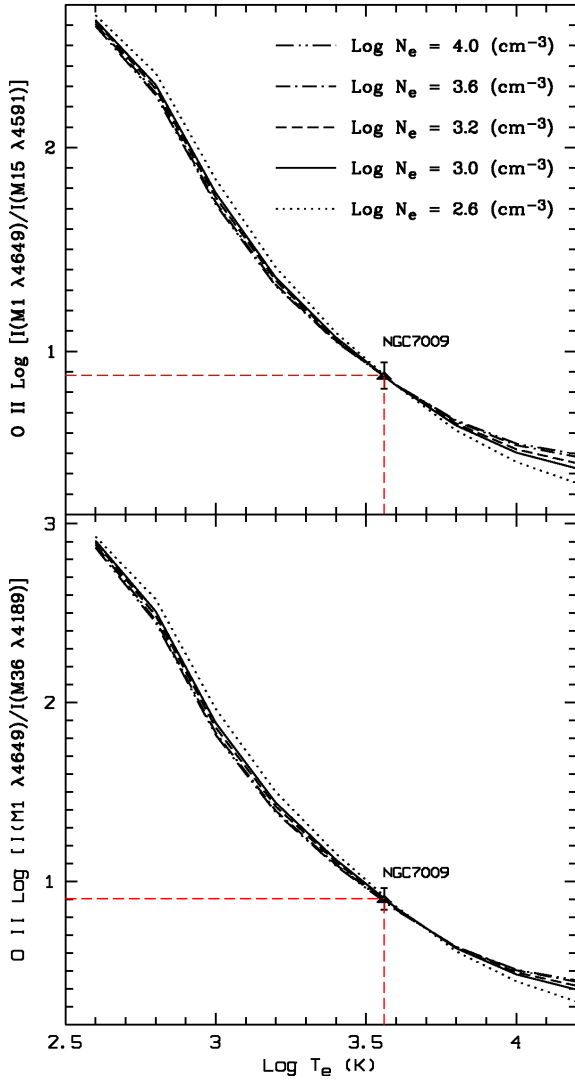


Figure 21. The O II $\lambda 4649/\lambda 4591$ (*upper*) and $\lambda 4649/\lambda 4189$ (*lower*) ratios as a function of electron temperature. Here the intensity of the $\lambda 4189$ line is a sum of the $\lambda 4189.79$ ($M36\ 3d'\ ^2G_{9/2} - 3p'\ ^2F_{7/2}^o$) and $\lambda 4189.59$ ($M36\ 3d'\ ^2G_{7/2} - 3p'\ ^2F_{7/2}^o$) lines. Different curves represent different density cases, and are based on the unpublished calculation of PJS. Both O II line ratios observed in the spectrum of NGC 7009 yield electron temperatures close to 3600 ± 500 K. The error bars were calculated from measurement uncertainties of the lines.

3.3.2). In NGC 7009, the C III $I(M1\ \lambda 4649)/I(M16\ \lambda 4069)$ and $I(M1\ \lambda 4649)/I(M18\ \lambda 4187)$ ratios are 1.05 and 3.41, respectively. Both ratios are beyond the diagnostic ranges of Fig. 23.

Fig. 23 shows that the C III $I(M1\ \lambda 4649)/I(M16\ \lambda 4069)$ and $I(M1\ \lambda 4649)/I(M18\ \lambda 4187)$ ratios increase with electron temperature below 10 000 K, but both decrease when the temperature goes beyond $\sim 12\ 600$ K ($\log T_e \sim 4.1$). In order to explain those trends, the effective radiative ($\alpha_{\text{eff}}^{\text{R}}$) and dielectronic ($\alpha_{\text{eff}}^{\text{D}}$) recombination coefficients as well as the total effective recombination coefficients ($\alpha_{\text{eff}}^{\text{Tot}}$) of the C III M1 and M16 multiplets are shown in Fig. 24 as a function of electron temperature. Below 10 000 K, the C III M16 multiplet is dominated by radiative recombination. In this temperature regime, the total effective recombination coefficient of the C III M16 multiplet decreases much faster than that of the M1 multiplet as temperature increases. When the temperature goes above

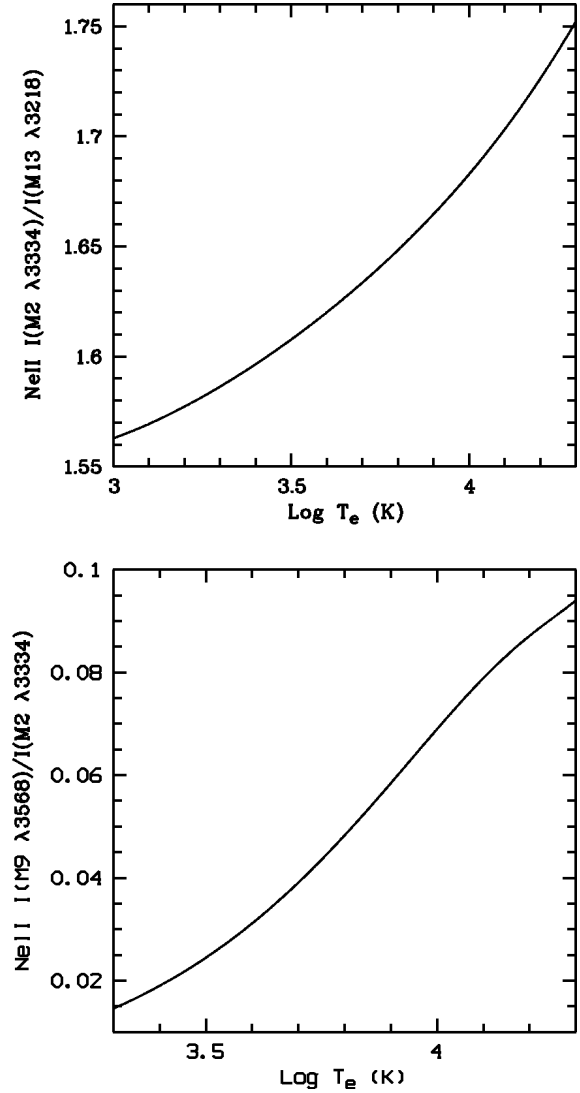


Figure 22. The Ne II recombination line ratios as a function of electron temperature. *Upper*: The $\lambda 3334/\lambda 3218$ ratio. *Lower*: The $\lambda 3568/\lambda 3334$ ratio. The plot is based on the effective recombination coefficients of Kisielius et al. (1998). Only a density case of $10\ 000\ \text{cm}^{-3}$ is presented.

10 000 K, the decreasing rate of the M16 multiplet slows down because its monotonically increasing dielectronic recombination coefficient becomes relatively significant, while that of the M1 multiplet does not change much.

The most prominent permitted transitions of N III in optical, the M1 $\lambda 4100$ ($3p\ ^2P^o - 3s\ ^2S$) and M2 $\lambda 4641$ ($3d\ ^2D - 3p\ ^2P^o$) multiplets, are affected by the Bowen fluorescence mechanism (e.g. Bowen 1934, 1935). The N III M18 $\lambda 4379.11$ ($5g\ ^2G - 4f\ ^2F^o$) line is amongst the best observed N III lines in the spectrum of NGC 7009, which are not affected by the fluorescence processes. The intensity ratio of the $\lambda 4379.11$ line and the $\lambda 4195.76$ line, which is the second strongest fine-structure component of the N III M6 $3p'\ ^2D - 3s'\ ^2P^o$ multiplet, can be used as a temperature diagnostic. Fig. 25 shows the N III $\lambda 4379/\lambda 4196$ ratio as a function of electron temperature. The dominant excitation mechanism of the N III M18 multiplet is radiative recombination, while the M6 multiplet is mainly excited by dielectronic recombination. The other two fine-structure components of the N III M6 multiplet, $\lambda\lambda 4200.10$

and 4215.77 cannot be used: the former one is blended with the He II $\lambda 4199.83$ ($11g^2G-4f^2F^\circ$) line, which is more than three times stronger, and the latter one cannot be accurately measured due to weakness ($<10^{-4}$ of the $H\beta$ intensity). Another N III multiplet, M17 $5f^2F^\circ-4d^2D$ $\lambda 4003$, when used in pair with the N III M6 $\lambda 4195.76$ line, may also be a temperature diagnostic, but its radiative recombination coefficients are unknown. The N III M17 lines are detected in the spectrum of NGC 7009 (Fig. C3).

The majority of the O III triplets of the $3d-3p$ and $3p-3s$ configurations detected in the spectrum of NGC 7009 are mainly excited by the fluorescence or charge-transfer mechanism (e.g. Liu & Danziger 1993a; Liu, Danziger & Murrin 1993). Thus those lines are not suitable for plasma diagnostics or abundance determinations. However, the O III M8 $3d^3F^\circ-3p^3D$ multiplet is unaffected by such mechanisms. The intensity of the strongest component of the O III M8 multiplet, $\lambda 3265.32$ ($3d^3F_4^\circ-3p^3D_3$), relative to the best observed O III $5g-4f$ line, can in principle be used as a temperature diagnostic. The O III M8 multiplet is mainly excited by radiative recombination at temperatures below 5000 K, and the contribution of dielectronic recombination to the total recombination rate catches up with that of the radiative recombination at about 16 000 K (Nussbaumer & Storey 1984; Péquignot, Petitjean & Boisson 1991). The O III $5g-4f$ lines are dominantly excited by radiative recombination. The upper panel of Fig. 26 shows the intensity ratio of the M46b $\lambda 4435$ ($5gH[11/2]^\circ-4fG[9/2]$) multiplet, the strongest transition of the $5g-4f$ configuration, and the M8 $\lambda 3265.32$ line as a function of electron temperature. Péquignot, Petitjean & Boisson (1991) present the radiative recombination coefficients of both the M8 and M46b multiplets of O III, while Nussbaumer & Storey (1984) only give the dielectronic recombination coefficients of M8. The lower panel of Fig. 26 shows the intensity ratio of the $\lambda 4434.60$ ($5gH[11/2]_0^\circ-4fG[9/2]_5$) line, the strongest fine-structure component of the M46b multiplet, and the M8 $\lambda 3265.32$ line as a function of electron temperature. The effective recombination coefficients of the M46b $\lambda 4434.60$ line are adopted from Kisielius & Storey (1999), whose calculations for the O III $5g-4f$ recombination spectrum were carried out in the intermediate coupling scheme and valid from 5000 to 20 000 K. Measurement of the $\lambda 4434.60$ line is of large uncertainty due to line blending. The other O III $5g-4f$ lines are not detected in the spectrum of NGC 7009.

2.6 Summary of the ORL diagnostics

We have discussed about the possibility of using various recombination line ratios of heavy element ions to determine electron temperatures and densities. The line ratios are illustrated as a function of temperature or density. For some cases, there is still a lack of adequate effective recombination coefficients or the expected lines are not detected in the spectrum of NGC 7009 due to weakness and/or line blending. The O III lines of the $5g-4f$ configuration are not detected. Fig. 26 is probably applicable once deep spectra with higher resolution are available. The effective recombination coefficients for the C III, N III and O III lines quoted from Nussbaumer & Storey (1984) and Péquignot, Petitjean & Boisson (1991) are probably inadequate, which can be inferred from the fact that the observed line ratios are all outside of the diagnostic ranges of Figs. 23 and 25.

The applicability of Figs. 14 and 15 is quite small, given that the N II M19 lines are close to the O III $\lambda 5007$ line. The N II and O II recombination lines of parentage other than the ground states of the recombining ions are good temperature diagnostics. As shown in Figs. 16 and 21, those line ratios are insensitive to elec-

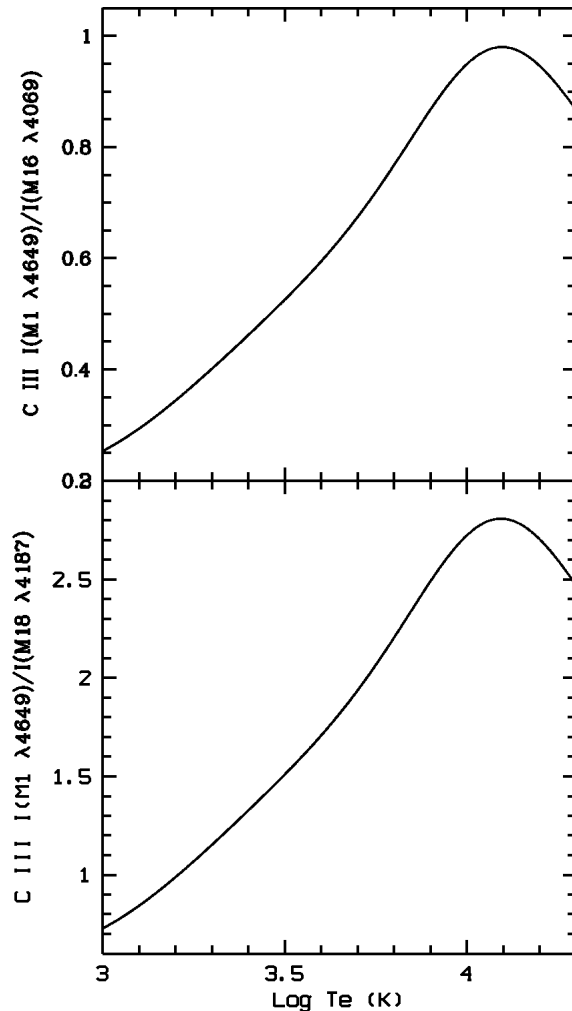


Figure 23. The C III recombination line ratios as a function of electron temperature. *Upper:* The $I(M1\ \lambda 4649)/I(M16\ \lambda 4069)$ ratio. *Lower:* The $I(M1\ \lambda 4649)/I(M18\ \lambda 4187)$ ratio. The figure is based on the effective dielectronic and radiative recombination coefficients calculated by Nussbaumer & Storey (1984) and Péquignot, Petitjean & Boisson (1991), respectively.

tron density. The electron temperatures derived from the two O II line ratios ($\lambda 4649/\lambda 4591$ and $\lambda 4649/\lambda 4189$) in Fig. 21 are consistent with each other, and are close to the temperature value yielded by the C II $\lambda 8794/\lambda 4267$ ratio as shown in Fig. 11. Although no N II lines of parentage other than $^2P^\circ$ are detected in the spectrum of NGC 7009 due to weakness, they are promising diagnostic tools in spectroscopy. The most reliable temperatures derived from the ORLs of heavy element ions are those yielded by the N II and O II lines, as shown in Figs. 12 and 17. Currently only the N II and O II recombination lines can be used to determine electron density, since the density dependence of the population distributions of the energetically lowest fine-structure levels of the recombining ions have been taken into account in the recombination calculations for those two ions (this effect was also considered by Kisielius & Storey 1999 for the calculation of the $5g-4f$ recombination lines of O III). Figs. 13, 18 and 20 all show large scatter in electron density for a given line ratio observed in NGC 7009. This is reasonable because the ORL ratios only have very weak density dependence.

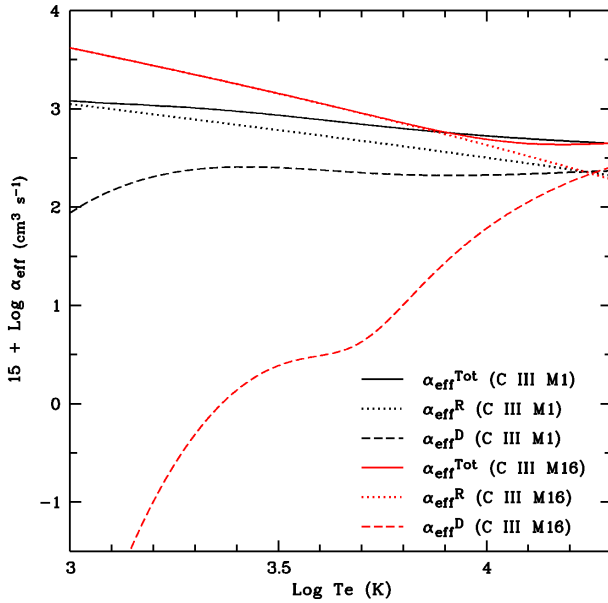


Figure 24. The effective recombination coefficients of the C III M1 $\lambda 4649$ (black curves) and M16 $\lambda 4069$ (red curves) multiplets as a function of electron temperature. Different curves of the same color represent different recombination coefficients: radiative recombination coefficient $\alpha_{\text{eff}}^{\text{R}}$ (dotted line), dielectronic recombination coefficient $\alpha_{\text{eff}}^{\text{D}}$ (dashed line), and total effective recombination coefficient $\alpha_{\text{eff}}^{\text{Tot}}$ (solid line). Data source of the plot is the same as Fig. 23.

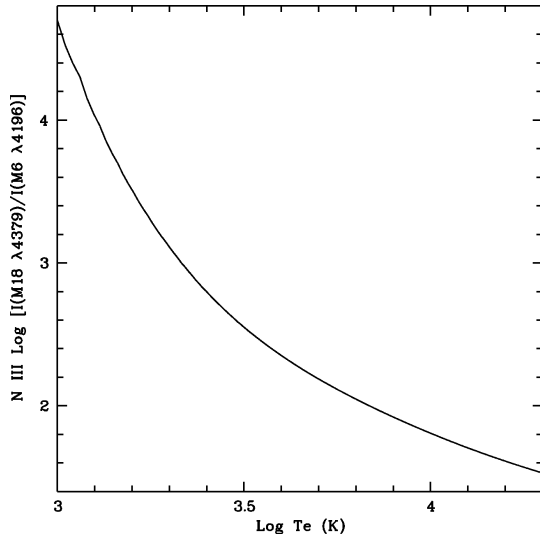


Figure 25. The N III $I(\text{M18 } \lambda 4379)/I(\text{M6 } \lambda 4196)$ ratio as a function of electron temperature. Data source of the figure is the same as Fig. 23.

New treatment of the Ne II recombination in the intermediate coupling scheme is needed.

3 THE OPTICAL RECOMBINATION SPECTRUM OF HEAVY ELEMENTS

In this section, we present a comprehensive analysis of the most significant permitted transitions of C II, N II, O II, and Ne II as well as C III, N III and O III detected in the spectrum of NGC 7009

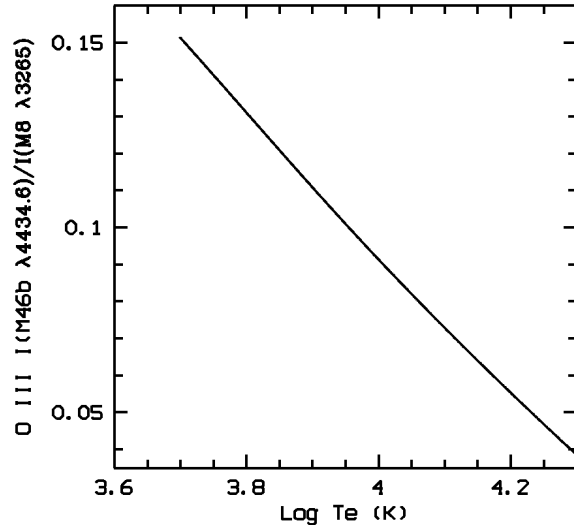
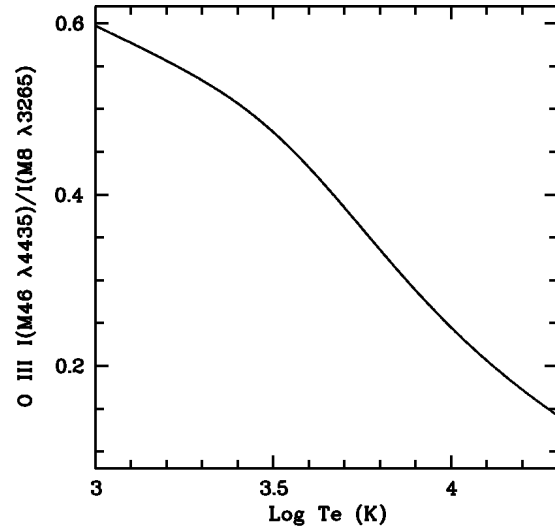


Figure 26. *Upper:* The O III $\lambda 4435/\lambda 3265$ ratio as a function of electron temperature. Here the $\lambda 4435$ line is the M46b $5g \text{ H}[11/2]^{\circ} - 4f \text{ G}[9/2]$ multiplet of O III. The figure is based on the dielectronic and radiative recombination coefficients of Nussbaumer & Storey (1984) and Péquignot, Petitjean & Boisson (1991), respectively. *Lower:* The O III $\lambda 4434.60/\lambda 3265$ ratio as a function of electron temperature. Here the $\lambda 4434.60$ line is the strongest fine-structure component of the O III M46b multiplet, and the effective recombination coefficients of this line are from Kisielius & Storey (1999), whose calculations were carried out in the intermediate coupling scheme and are valid from 5000 to 20000 K.

reported in Paper I. The lines are critically examined for potential blending effects and compared to theoretical predictions using the latest atomic data. Unless specified otherwise, all intensities quoted throughout the paper are corrected for interstellar extinction³ and in units of $I(\text{H}\beta) = 100$, and the theoretical intensities/ratios are predicted assuming an electron temperature of 1000 K as given by

³ In Paper I, we derived a mean value of 0.174 for the logarithmic extinction at $\text{H}\beta$, $c(\text{H}\beta)$, using the observed H I Balmer line ratios $\text{H}\alpha/\text{H}\beta$ and $\text{H}\gamma/\text{H}\beta$. The predicted H I line ratios in the Case B assumption were adopted from Storey & Hummer (1995), with $T_e = 10000 \text{ K}$ and $N_e = 10000 \text{ cm}^{-3}$.

the N II and O II ORL diagnostics (Figs. 12 and 17). The wavelengths of atomic transitions are adopted from the compilation of laboratory and theoretical values of Hirata & Horaguchi (1995). The extinction-corrected flux of H β , $I(\text{H}\beta)$, of NGC 7009 is derived using $\log I(\text{H}\beta) = \log F(\text{H}\beta) + c(\text{H}\beta)$, where $F(\text{H}\beta)$ is the observed H β flux (-9.80 in logarithm), which is adopted from Cahn, Kaler & Stanghellini (1992), and $c(\text{H}\beta)$ is the logarithmic extinction at H β , which was derived from the H I Balmer line ratios $\text{H}\alpha/\text{H}\beta$ and $\text{H}\gamma/\text{H}\beta$ (Paper I). The value of $c(\text{H}\beta)$ we derived for NGC 7009 is 0.174, which agrees with the value (0.17) given by Cahn, Kaler & Stanghellini (1992), who used the radio/H β flux ratio. Thus in NGC 7009 we have $I(\text{H}\beta) = 10^{-9.63} \text{ erg cm}^{-2} \text{ s}^{-1}$.

3.1 The C II optical recombination spectrum

Several dozen emission lines were identified as the permitted transitions of C II, with 41 being solid identifications (Paper I). The strongest transitions are presented in the current paper. As an example, we give principles of fits for the multiplets M6 and M28.01 in this section. The other multiplets are presented in Appendix A. The effective recombination coefficients of Davey, Storey & Kisielius (2000) are used for ORL analysis.

3.1.1 Multiplet 6, $4f^2F^\circ - 3d^2D$

C II M6 $\lambda 4267$ is the strongest C II multiplet observed in NGC 7009 (see Fig. 34). The three fine-structure components of this multiplet have close wavelengths: 4267.00, 4267.26 and 4267.26 Å. Single Gaussian profile fitting to the emission feature gives an intensity of 0.880 (normalized to a scale where H β = 100), with an uncertainty of less than 5 per cent. Here the contributions from the O II M53c $4fD[1]_{3/2}^\circ - 3d^4P_{5/2}$ $\lambda 4263.27$ and Ne II M57c $4f[3]_{7/2}^\circ - 3d^4F_{9/2}$ $\lambda 4267.38$ lines are negligible. This intensity value agrees with LSBC, whose observation yields a value of 0.838. The calculation of Bastin (2006, hereafter B06) shows that the Case A effective recombination coefficient for the C II M6 $\lambda 4267$ line differs from that in Case B by 1.5 per cent, and a similar difference is given by Davey, Storey & Kisielius (2000), indicating that this transition is case insensitive.

3.1.2 Multiplet 28.01, $3d'^2F^\circ - 3p'^2D$

This multiplet is a dielectronic transition, which is a result of cascading from the autoionization state $2s2p(^3P^\circ)3d^2F^\circ$ that lies about 0.41 eV above the first ionization threshold to the $2s2p(^3P^\circ)3p^2D$ state that lies 1.00 eV below the ionization threshold (Moore 1993). The features of the two fine-structure components, $\lambda 8793.80$ ($3d'^2F_{7/2}^\circ - 3p'^2D_{5/2}$) and $\lambda 8799.90$ ($3d'^2F_{5/2}^\circ - 3p'^2D_{3/2}$) are very broad (Fig. 27). The wings of the two lines obviously affect the weaker emission features nearby. Detailed analysis of the complex indicates that at least two more emission lines are blended with the two C II lines: one is the He II $23p^2P^\circ - 6s^2S$ $\lambda 8799.0$ line, while the other is unknown. The results of fitting to the features are shown in Fig. 27.

For each of the two C II M28.01 lines, we used a simulated Lorentz profile with an intrinsic width of 6.86 Å convolved with a Gaussian instrumental profile with a full width at half-maximum (FWHM) of 3.00 Å to fit the observed feature. The convolution of the Lorentz profile and Gaussian gives a Voigt profile with a width of 8.50 Å, which fits the observed features quite well (Fig. 27). The

intensity contribution of the blended He II $\lambda 8799$ line was estimated from the He II $4f^2F^\circ - 3d^2D$ $\lambda 4686$ line and the hydrogenic theory of Storey & Hummer (1995). An electron temperature of 10 000 K and a density of $10\,000 \text{ cm}^{-3}$ were assumed. After correcting for the contribution from the He II line, the intensity of the $\lambda 8799.90$ line is 0.022 ± 0.003 . With the assumption that the relative intensity of the two C II M28.01 lines are as in the *LS* coupling, i.e. 1.0:0.7, the intensity of the $\lambda 8793.80$ line is 0.032, which is lower than the total intensity of the broad feature at $\lambda 8793$ (see Fig. 27), indicating that there is probably unknown blending. Multiple trial fitting to the profile shows that an emission feature with an observed wavelength of 8793.20 Å best fits the feature, and its intensity is < 0.01 . The EMILI⁴ code (Sharpee et al. 2003) identified this probably blended weak line as a [Cr II] line with a laboratory wavelength of 8795.17 Å. More efforts are needed to verify this identification.

The intensity ratio of the C II $\lambda 8793.80$ line and the C II M6 $\lambda 4267$ multiplet is 0.036, and that yields an electron temperature of ~ 3000 K (Section 2.2 and Fig. 11). As discussed in Section 2.2, this temperature is questionable, due to different excitation mechanisms of the C II M28.01 $\lambda 8797$ and the M6 $\lambda 4267$ multiplets. Measurements of the C II M28.01 lines are inaccurate unless detailed modeling of the autoionization levels of C II is carried out. Besides, too many skylines in the near-red of the spectrum of NGC 7009 and the relatively poor sky subtraction in this wavelength region also makes accurate measurements of the C II lines difficult (c.f. Section 2.1 in Paper I).

3.1.3 Comments on the C II recombination spectrum

The current effective recombination coefficients used for analysis of the C II lines are mainly from Davey, Storey & Kisielius (2000) and Bastin (2006). The former calculation takes much care in the low temperature case ($T_e < 5000$ K), while the latter one mainly covers higher temperatures (5000–50 000 K) and includes the effects of high temperature dielectronic recombination, which rapidly becomes important above an electron temperature of $\sim 15\,000$ K. Both calculations were carried out in the *LS* coupling assumption and only for the transitions of the parentage 1S . In the current analysis, we adopt the calculation of Davey, Storey & Kisielius (2000), assuming a temperature of 1000 K.

The best observed (i.e. the most accurate) multiplets of C II in the spectrum of NGC 7009 are M6 ($4f^2F^\circ - 3d^2D$) and some transitions that belong to the $ng-4f$ ($n \geq 5$) array. For the transitions with parentage other than 1S , only the M28.01 ($3d'^2F^\circ - 3p'^2D$) multiplet is detected, but measurements of this multiplet could be unreliable, as mentioned in Section 3.1.2. The effective dielectronic recombination coefficients of Nussbaumer & Storey (1984) and radiative recombination coefficients of Péquignot, Petitjean & Boisson (1991) were used for the analysis of the M28.01 multiplet. A full treatment of the C II recombination in an appropriate coupling assumption (i.e. intermediate coupling), with transitions between the autoionization levels taken into account, is needed in the future.

⁴ EMILI is developed by Dr. B. Sharpee et al. and is designed to aid in the identification of weak emission lines, particularly the weak recombination lines seen in high dispersion and high signal-to-noise (S/N) spectra. URL: <http://www.pa.msu.edu/astro/software/emili>

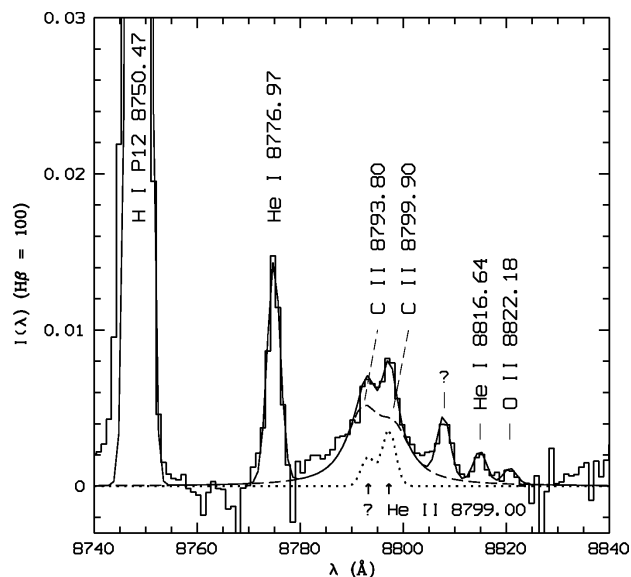


Figure 27. Spectrum of NGC 7009 from 8740 to 8840 Å showing the two C II M28.01 autoionization lines $\lambda\lambda 8793.80$ and 8799.90 . The dashed curve is the sum of Voigt profile fits to the two C II lines, which probably blend with two weaker features, He I $\lambda 8799.00$ and an unknown component, whose profiles are assumed to be Gaussian and are represented by the dotted curve. The solid continuous curve is the sum of all fits. Here a Voigt profile is the convolution of a Gaussian (~ 3.0 Å FWHM) and a Lorentz profile (~ 6.86 Å FWHM). Continuum has been subtracted and the spectrum has been normalized such that H β has an integrated flux of 100. Extinction has not been corrected for.

3.2 The N II optical recombination spectrum

In this section, we present intensities of the N II ORLs detected in the spectrum of NGC 7009, and analyze these lines using the N II effective recombination coefficients of FSL11. Unless otherwise specified, the theoretical relative intensities of the N II lines quoted in this section are all based on that calculation. Comparison of the observed and predicted relative intensities of the N II lines with accurate intensities is made to assess the new atomic data. An electron temperature of 1000 K is assumed throughout the analysis. In this section, spectral fits and discussion of results are only given for the M3 $3p^3D - 3s^3P^o$, M28 $3d^3D^o - 3p^3P$ multiplets and the strongest multiplets M39a,b of the $4f - 3d$ transition array. Discussion of other multiplets of N II are given in Appendix B.

3.2.1 Multiplet 3, $3p^3D - 3s^3P^o$

This multiplet is the strongest of N II in optical. The intensities of the N II M3 lines are presented in column 5 of Table 1 in units of $I(\lambda 5679.56) = 1.0$. Also presented are the theoretical relative intensities in the *LS* coupling assumption (column 3) and the intermediate coupling (column 4). The theoretical predictions in intermediate coupling are calculated from the N II effective recombination coefficients of FSL11. Comparisons of the observed and predicted relative intensities are in columns 6 and 7. Results of multi-Gaussian profile fitting to the wavelength range 5650–5760 Å are also presented in Fig. 28.

The strongest M3 line, $\lambda 5679.56$, is blended with $\lambda 5676.02$ of the same multiplet (Fig. 28). Two Gaussian profiles with the same width were used to fit them. The intensities of $\lambda\lambda 5679.56$ and 5676.02 are 0.135 ± 0.007 and 0.035 ± 0.004 , respectively. Thus the

Table 1. Comparison of the observed and predicted relative intensities of the N II M3 lines detected in the spectrum of NGC 7009. I_{IC} is the theoretical intensity deduced from the effective recombination coefficients of FSL11, and I_{LS} is the value in the *LS* coupling assumption. The above two symbols have the same meaning in other tables of the current paper. An electron temperature of 1000 K is assumed for the theoretical predictions I_{IC} .

Line	$J_2 - J_1$	I_{LS}	I_{IC}	I_{obs}	$\frac{I_{obs}}{I_{LS}}$	$\frac{I_{obs}}{I_{IC}}$
$\lambda 5666.63$	2–1	0.536	0.466	0.481	0.897	1.032
$\lambda 5676.02$	1–0	0.238	0.215	0.273	1.147	1.271
$\lambda 5679.56$	3–2	1.000	1.000	1.000	1.000	1.000
$\lambda 5686.21$	1–1	0.179	0.128	0.187	1.047	1.464
$\lambda 5710.77$	2–2	0.179	0.167	0.151	0.844	0.902

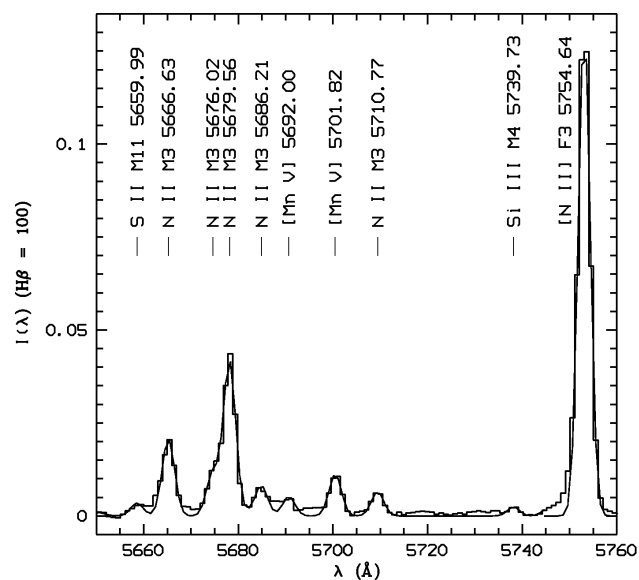


Figure 28. Spectrum of NGC 7009 from 5650 to 5760 Å showing the N II M3 lines and other emission features. The continuous curve is the sum of Gaussian profile fits. Continuum has been subtracted and the spectrum has been normalized such that H β has an integrated flux of 100. Extinction has not been corrected for.

$\lambda 5676.02/\lambda 5679.56$ ratio is 0.273, which agrees with both theoretical ratios within errors (Table 1). Another two lines, $\lambda\lambda 5666.63$ and 5710.77 , are free of line blending. The intensity of the $\lambda 5710.77$ line is 0.020 ± 0.003 , which agrees better with the intermediate coupling (Table 1). The intensity of the $\lambda 5666.63$ line is 0.065 ± 0.007 , which also agrees better with intermediate coupling (Table 1). Another M3 line $\lambda 5686.21$ is partially blended with a weaker feature, which was identified as Mn v $\lambda 5692.00$ (Fig. 28). The fitted intensity of $\lambda 5686.21$ is 0.024 ± 0.005 , which seems to agree better with *LS* coupling (Table 1). However, the intensity of this line is questionable due to weakness. The other M3 line, $\lambda 5730.65$, is not observed in our spectrum.

3.2.2 Multiplet 28, $3d^3D^o - 3p^3P$

Gaussian profile fitting to M28 $\lambda 5941.65$ ($3d^3D_3^o - 3p^3P_2$) yields an intensity of 0.030 ± 0.004 . The intensity contribution from the M28 $\lambda 5940.24$ ($3d^3D_1^o - 3p^3P_1$) line is negligible. The intensity ratio of $\lambda 5941.65$ and the N II M3 $\lambda 5679.56$ line is 0.228, which is 42 per cent lower than the theoretical ratio.

Table 2. Same as Table 1 but for a comparison of the observed and predicted relative intensities of the N II M28 lines detected in the spectrum of NGC 7009.

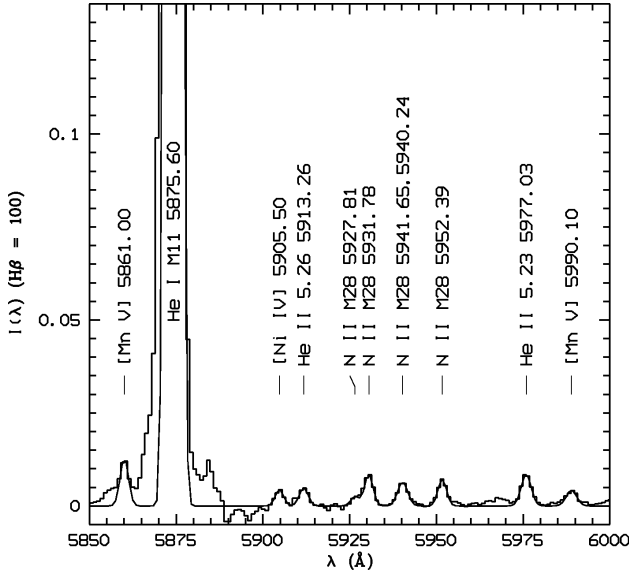
Line	$J_2 - J_1$	I_{LS}	I_{IC}	I_{obs}	$\frac{I_{obs}}{I_{LS}}$	$\frac{I_{obs}}{I_{IC}}$
$\lambda 5941.65^a$	3-2	1.000	1.000	1.000	1.000	1.000
$\lambda 5952.39^b$	2-2	0.152	0.122	0.255	1.686	2.103
$\lambda 5931.78^c$	2-1	0.455	0.412	0.471	1.037	1.143
$\lambda 5960.90^d$	1-2	0.010	0.009	-	0.000	0.000
$\lambda 5927.81$	1-0	0.202	0.219	0.317	1.570	1.448

^a Including the $\lambda 5940.24$ ($3d^3D_1^o - 3p^3P_1$) line.

^b Corrected for the contribution from the He II $\lambda 5952.93$ ($24h^2H^o - 5g^2G$) line (74 per cent).

^c Corrected for the contribution from the He II $\lambda 5931.83$ ($25h^2H^o - 5g^2G$) line (57 per cent).

^d Not detected.

**Figure 29.** Spectrum of NGC 7009 from 5850 to 6000 Å showing the N II M28 lines and other emission features. The continuous curve is the sum of Gaussian profile fits. Continuum has been subtracted and the spectrum has been normalized such that H β has an integrated flux of 100. Extinction has not been corrected for.

Another M28 line $\lambda 5927.81$ ($3d^3D_1^o - 3p^3P_0$) is blended with M28 $\lambda 5931.78$ ($3d^3D_2^o - 3p^3P_1$), which coincides in wavelength with the He II $25h^2H^o - 5g^2G$ $\lambda 5931.83$ line. Two Gaussian profiles were used to fit the complex, and the intensity of the $\lambda 5927.81$ line is 0.007, with a large uncertainty. The intensity ratio of $\lambda 5927.81$ to the $\lambda 5941.65$ line is 0.250, which agrees with the predicted ratio 0.235. Assuming that the He II $\lambda 5931.83$ line contributes 55 per cent to the total intensity of the blend at $\lambda 5932$, as estimated from the hydrogenic theory of Storey & Hummer (1995), we obtained an intensity of the $\lambda 5931.78$ line which is much higher than the theoretical prediction. Another M28 line $\lambda 5952.39$ ($3d^3D_2^o - 3p^3P_2$) is blended with the He II $24h^2H^o - 5g^2G$ $\lambda 5952.93$ line. The intensity of the $\lambda 5952.39$ line is much higher than the predicted value. The other M28 line $\lambda 5960.90$ ($3d^3D_1^o - 3p^3P_2$) is not observed.

3.2.3 4f-3d transitions

The 4f-3d transitions of N II are located in the blue side of our spectrum (<4500 Å) and suffer from line blending. Accurate measurements of most of them are difficult. Table 3 presents the observed and predicted relative intensities of those 4f-3d lines with the most reliable intensities. Figs. 30 and 31 show some of the N II lines of the 4f-3d transition array detected in the spectrum of NGC 7009. The results of multi-Gaussian profile fitting are overplotted. Only the M39a and M39b multiplets are discussed here. Discussion of other 4f-3d transitions of N II are presented in Appendix B8.

3.2.3.1 Multiplet 39a, 4f G[7/2] - 3d $^3F^o$: The $\lambda 4035.08$ ($4fG[7/2]_3 - 3d^3F_2^o$) and $\lambda 4043.53$ ($4fG[7/2]_4 - 3d^3F_3^o$) lines are shown in Fig. 30. The $\lambda 4035.08$ line is blended with the O II M50b $4fF[3]_{5/2}^o - 3d^4F_{5/2}$ $\lambda 4035.07$ line, which contributes 15 per cent to the total intensity, and the O II M50b $4fF[3]_{7/2}^o - 3d^4F_{5/2}$ $\lambda 4035.46$ line, which is negligible. The $\lambda 4035$ line has an intensity 0.037 ± 0.006 . Here the contribution from the O II $\lambda 4035.07$ line has been corrected for. This intensity agrees with the predicted relative intensity. The $\lambda 4043.53$ line is partially blended with the N II M39b $4fG[9/2]_5 - 3d^3F_4^o$ $\lambda 4041.31$ line, which is more than 2 times stronger. The intensity of the $\lambda 4043.53$ line also agrees well with the predicted value. Reliable measurements of the $\lambda 4044.78$ ($4fG[7/2]_3 - 3d^3F_3^o$) line are difficult. The other two lines $\lambda 4056.90$ ($4fG[7/2]_4 - 3d^3F_4^o$) and $\lambda 4058.16$ ($4fG[7/2]_3 - 3d^3F_4^o$) are too weak.

3.2.3.2 Multiplet 39b, 4f G[9/2] - 3d $^3F^o$: The $\lambda 4041.31$ ($4fG[9/2]_5 - 3d^3F_4^o$) line is blended with the O II M50c $4fF[2]_{5/2}^o - 3d^4F_{5/2}$ $\lambda 4041.28$ and O II M50c $4fF[2]_{3/2}^o - 3d^4F_{5/2}$ $\lambda 4041.95$ lines. The two O II lines contribute only ~ 7 per cent to the total intensity of the blend at $\lambda 4041$. The intensity of the $\lambda 4041.31$ line is 0.082 ± 0.008 . The intensity ratio of $\lambda 4041.31$ to the N II M3 $\lambda 5679.56$ line is 0.604, which agrees quite well with the predicted ratio 0.598. Another M39b line $\lambda 4026.08$ ($4fG[9/2]_4 - 3d^3F_3^o$) is blended with the He I M18 $5d^3D - 2p^3P^o$ $\lambda 4026.20$ line. The other M39b line $\lambda 4039.35$ ($4fG[9/2]_4 - 3d^3F_4^o$) is not observed.

3.2.4 Comments on the N II recombination spectrum

The effective recombination coefficients used for the analysis of the N II recombination spectrum are from FSL11, which is dedicated to low temperatures ($T_e < 10\,000$ K) and is an improvement over all previous calculations for this ion, as described Section 2.1. The best observed N II lines in our spectrum are M3 ($3p^3D - 3s^3P^o$), M12 ($3p^1D - 3s^1P^o$), and the strongest lines of the 4f-3d array, e.g. $\lambda 4041.31$ (M39b $4fG[9/2]_5 - 3d^3F_4^o$), $\lambda 4043.53$ (M39a $4fG[7/2]_4 - 3d^3F_4^o$). Those N II lines have been used for plasma diagnostics (Section 2.3). The fine-structure components of the N II multiplets M5 ($3p^3P - 3s^3P^o$), M20 ($3d^3D^o - 3p^3D$), M28 ($3d^3D^o - 3p^3P$), and M29 ($3d^3P^o - 3p^3P$) observed in our spectrum are incomplete due to line blending. Those that are detected are also blended with other lines. Although multi-Gaussian profile fitting has been carried out and effective recombination coefficients used to correct for the blended line of other ionic species, the derived intensities of those N II lines could still be questionable. Grandi (1976) shows that the strongest components of the M3, M5 and M28 multiplets are affected by the fluorescence mechanism in the Orion nebula. However, such effects is probably insignificant

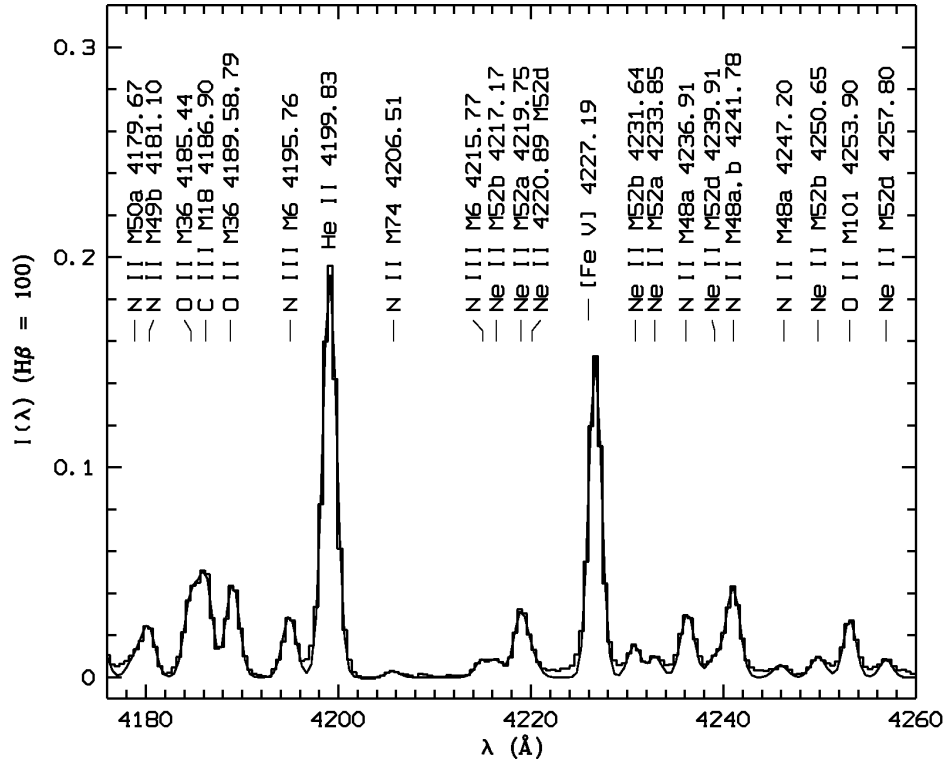


Figure 31. Spectrum of NGC 7009 from 4176 to 4260 Å showing the N II ORLs of the M48a 4fF[5/2]–3d³D^o, M48b 4fF[7/2]–3d³D^o, M49a 4fG[7/2]–3d³D^o, and M49b 4fG[9/2]–3d³D^o multiplets. The continuous curve is the sum of Gaussian profile fits. Continuum has been subtracted and the spectrum has been normalized such that Hβ has an integrated flux of 100. Extinction has not been corrected for.

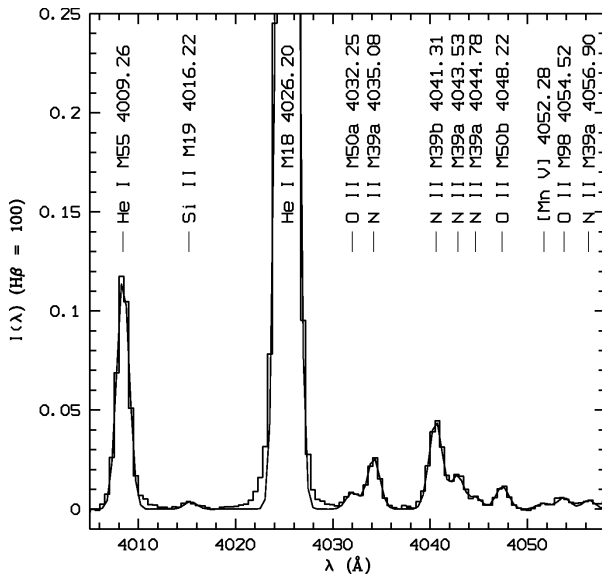


Figure 30. Spectrum of NGC 7009 from 4005 to 4058 Å showing the N II ORLs of the M39a 4fG[7/2]–3d³F^o and M39b 4fG[9/2]–3d³F^o multiplets. The strongest N II lines of the 4f–3d array, λ4041.31 (M39b 4fG[9/2]₅–3d³F^o₂) is observed. The continuous curve is the sum of Gaussian profile fits. Continuum has been subtracted and the spectrum has been normalized such that Hβ has an integrated flux of 100. Extinction has not been corrected for.

in NGC 7009 (C. Morisset, private communication). The 4f–3d transitions are almost certainly free of fluorescence enhancement because they require such high excitation energy photons that the central star of NGC 7009 cannot afford.

3.3 The O II optical recombination spectrum

LSBC observed eight multiplets of the 3–3 transition arrays and a few dozen 4f–3d lines of O II. The effective radiative recombination coefficients for the O II 3d–3p and 4f–3d transitions were calculated under the intermediate coupling scheme, and were used for spectral analysis. For the 3p_–3s transitions, the effective recombination coefficients of Storey (1994), whose calculations were carried out in the *LS* coupling scheme, were utilized. LSBC confirmed the breakdown of *LS* coupling in the O II transitions, especially those of the 4f–3d configuration. In Paper I, we presented very deep spectrum of NGC 7009. The data quality is higher than that in LSBC. In the current paper, we present the intensities of the O II ORLs, and analyze the O II recombination spectrum using the new O II effective recombination coefficients of PJS. Unless otherwise specified, the theoretical relative intensities of the O II lines quoted in this section are all based on that calculation. Comparison of the observed and predicted relative intensities of the O II lines with accurate intensities is made to assess the new atomic data. An electron temperature of 1000 K is assumed throughout the analysis. In this section, spectral fits and discussion of the results are only given for the M1 3p⁴D^o–3s⁴P, M10 3d⁴F–3p⁴D^o multiplets and the strongest multiplets M39a,b of the 4f–3d transition array. Discussion of other multiplets of O II are given in Appendix C.

Table 3. Same as Table 1 but for a comparison of the observed and predicted relative intensities of the N II 4f–3d lines detected in the spectrum of NGC 7009.

Line	$J_2 - J_1$	I_{IC}	I_{obs}	$\frac{I_{obs}}{I_{IC}}$
M39a 4f G[7/2] – 3d $^3F^o$				
$\lambda 4035.08^a$	3–2	0.477	0.540	1.132
$\lambda 4043.53$	4–3	0.436	0.432	0.992
M39b 4f G[9/2] – 3d $^3F^o$				
$\lambda 4041.31^b$	5–4	1.000	1.000	1.000
M43a 4f F[5/2] – 3d $^1D^o$				
$\lambda 4176.16^c$	3–2	0.293	0.343	1.171
M43b 4f F[7/2] – 3d $^1D^o$				
$\lambda 4171.61$	3–2	0.296	0.281	0.950
M48a 4f F[5/2] – 3d $^3D^o$				
$\lambda 4236.91^d$	2–1	0.539	0.669	1.241
M48b 4f F[7/2] – 3d $^3D^o$				
$\lambda 4241.78^e$	4–3	0.984	0.996	1.012
M55a 4f D[5/2] – 3d $^3P^o$				
$\lambda 4442.02^f$	2–1	0.130	0.242	1.859
M58a 4f G[7/2] – 3d $^1F^o$				
$\lambda 4552.53^g$	4–3	0.201	0.395	1.965
M58b 4f G[9/2] – 3d $^1F^o$				
$\lambda 4530.41^h$	4–3	0.474	0.593	1.251
M61a 4f D[5/2] – 3d $^1P^o$				
$\lambda 4694.64^i$	2–1	0.147	0.222	1.510

^a Including the contribution from the O II M50b 4f F[3] $^o_{5/2}$ – 3d 4F $_{5/2}$ $\lambda 4035.07$ line. Neglecting the O II M50b 4f F[3] $^o_{7/2}$ – 3d 4F $_{5/2}$ $\lambda 4035.46$ line.

^b Neglecting the contributions from the O II M50c 4f F[2] $^o_{5/2}$ – 3d 4F $_{5/2}$ $\lambda 4041.28$ and O II M50c 4f F[2] $^o_{3/2}$ – 3d 4F $_{5/2}$ $\lambda 4041.95$ lines.

^c Including N II M43a 4f F[5/2] $_2$ – 3d $^1D^o_2$ $\lambda 4175.66$.

^d Including N II M48b 4f F[7/2] $_3$ – 3d $^3D^o_2$ $\lambda 4237.05$.

^e Including N II M48a 4f F[5/2] $_3$ – 3d $^3D^o_2$ $\lambda 4241.78$. Neglecting N II M48a 4f F[5/2] $_2$ – 3d $^3D^o_2$ $\lambda 4241.24$ and Ne II M52c 4f 2[1] $^o_{3/2}$ – 3d $^4D_{1/2}$ $\lambda 4242.04$.

^f Including Ne II M60b 4f 1[4] $^o_{7/2}$ – 3d $^2F_{5/2}$ $\lambda 4442.69$. Neglecting O III M49b 5g F[3] o_2 , $_3$ – 4f D[3] $_2$ $\lambda 4442.02$.

^g Including Ne II M55d 4f 2[2] $^o_{5/2}$ – 3d $^4F_{3/2}$ $\lambda 4553.17$ and Si III M2 4p $^3P^o_2$ – 4s 3S_1 $\lambda 4552.62$.

^h Including N III M3 3p' $^4D_{1/2}$ – 3s' $^4P^o_{3/2}$ $\lambda 4530.86$.

ⁱ Overestimated.

3.3.1 Multiplet 1, 3p $^4D^o$ – 3s 4P

The M1 multiplet is the strongest amongst all the O II permitted transitions, and is one of the best observed multiplets. Comparisons of the observed and predicted relative intensities of the M1 fine-structure components are presented in Table 4. The results of multi-Gaussian profile fitting are shown in Fig. 32.

The strongest M1 line $\lambda 4649.13$ is blended with $\lambda 4650.84$ of the same multiplet; also blended are the three lines of C III M1 3p $^3P^o$ – 3s 3S : $\lambda\lambda 4647.42$, 4650.25 and 4651.47. Five Gaussian profiles of the same FWHM were used to fit the complex, with the laboratory wavelength differences utilized. The relative intensities of the three C III M1 lines were assumed to be as in *LS* coupling, i.e. 5 : 3 : 1, but the relative intensities of the two O II lines were not constrained. The intensity of the $\lambda 4649.13$ line is 0.667 ± 0.030 . The intensity of the $\lambda 4650.84$ line is 0.169 ± 0.008 . The intensity ratio of the $\lambda 4650.84$ and $\lambda 4649.13$ lines agrees with the theoretical ratios predicted in the intermediate coupling, but is slightly

higher than the *LS* coupling value (Table 4). Another three M1 lines, $\lambda\lambda 4661.63$, 4673.73 and 4676.24, are free of line blending. The fitted intensities of the three lines agree with the predicted values, except for $\lambda 4673.73$, whose measurement is obviously higher than both predicted values (Table 4). The measurement uncertainties of the three lines are all less than 10 per cent. Such large difference between the observed and predicted intensity of $\lambda 4673.73$ cannot be explained explicitly. $\lambda 4673.73$ coincides in wavelength with C III M5 3p' 3P_1 – 3s' $^3P^o_2$ $\lambda 4673.95$. However, as discussed in LSBC, a significant contribution from the C III $\lambda 4673.95$ line was unlikely because another C III M5 line $\lambda 4665.86$, which is expected to be much stronger than $\lambda 4673.95$, is not observed. $\lambda 4676.24$ is blended with O II M91 4f G[4] $^o_{7/2}$ – 3d $^2D_{5/2}$ $\lambda 4677.07$ and N II M61b 4f D[3/2] $_2$ – 3d $^1P^o_1$ $\lambda 4678.14$, but the contributions of these two lines are probably insignificant, as estimated from the new effective recombination coefficients.

Another two M1 lines, $\lambda\lambda 4638.86$ and 4641.81, are both blended with two N III M2 lines $\lambda\lambda 4640.64$ and 4641.85, which are excited by the Bowen fluorescence mechanism. Also blended with this feature is N II M5 3p 3P_1 – 3s $^3P^o_2$ $\lambda 4643.09$. Taking into account another N III M2 line $\lambda 4634.14$ and N II M5 3p 3P_2 – 3s $^3P^o_2$ $\lambda 4630.54$, we used six Gaussian profiles (the O II $\lambda 4641.81$ line coincides in wavelength with N III $\lambda 4641.85$, thus they were treated as a single component) to fit the complex, assuming that all the six components had the same FWHM. The results of the fitting are plotted in Fig. 32. Here the contribution of N III M2 $\lambda 4641.85$ to the total intensity of the blend at $\lambda 4642$ was estimated from N III M2 $\lambda 4634.14$, which is free of line blending. The intensity ratio of the two N III lines was assumed to be as in pure *LS* coupling, i.e. 1 : 5, considering the fact that the two lines decay from the same upper level, thus their intensity ratio depends only on the coupling scheme instead of the excitation mechanism. The relative intensity of the two O II M1 lines were not constrained. The intensity of $\lambda 4641.81$ thus obtained is 0.437 ± 0.085 . This measurement agrees well with the predicted value in the intermediate coupling (Table 4). The resultant intensity of the $\lambda 4638.86$ line is higher than the theoretical ratios (Table 4), but its intensity could be unreliable due to the strength of the N III M2 $\lambda 4640.64$ line, which is more than 10 times stronger. The C II M12.01 6d 2D – 4p $^2P^o$ lines, $\lambda\lambda 4637.63$, 4638.91 and 4639.07, may be also blended in the $\lambda 4638$ feature, but taking them into account makes the task of line deblending more difficult.

The other M1 line $\lambda 4696.35$, which is expected to be the faintest of O II M1, is observed (the inset in Fig. 32). It coincides in wavelength with O II M89a 4f D[3] $^o_{5/2}$ – 3d $^2D_{3/2}$ $\lambda 4696.35$, and is partially blended with another weak feature which was identified as N II M61a 4f D[5/2] $_2$ – 3d $^1P^o_1$ $\lambda 4694.64$. Accurate measurements of $\lambda 4696.35$ are difficult due to weakness. Assuming that the O II M89a $\lambda 4696.35$ line contributes 38 per cent to total flux of the blend at $\lambda 4696$, as estimated from the new O II effective recombination coefficients, we obtained an intensity of 0.015 for the M1 $\lambda 4696.35$ line, which agrees well with the newly predicted value (Table 4).

3.3.2 Multiplet 10, 3d 4F – 3p $^4D^o$

The observed and predicted relative intensities of O II M10 lines detected in NGC 7009 are presented in table 5. The emission features of the M10 lines and the results of Gaussian profile fitting are shown in Fig. 33 $\lambda\lambda 4069.62$ and 4069.89, are blended with [S II] 3p $^3P^o_{3/2}$ – 3p $^3S^o_{3/2}$ $\lambda 4068.60$ and the three C III M16 5g 3G

Table 6. Comparison of the observed and predicted relative intensities of the O II 4f–3d lines detected in the spectrum of NGC 7009. *LSBC* is the predicted intensities based on the effective recombination coefficients of Liu et al. (1995), and *PJS* is based on the unpublished effective recombination coefficients of P. J. Storey. An electron temperature of 1000 K is assumed for the theoretical predictions.

Line	$J_2 - J_1$	I_{pred} <i>LSBC</i>	I_{pred} <i>PJS</i>	I_{obs}	$\frac{I_{\text{obs}}}{I_{\text{pred}}}$ <i>LSBC</i>	$\frac{I_{\text{obs}}}{I_{\text{pred}}}$ <i>PJS</i>
M48a 4f G[5] ^o – 3d ⁴ F λ4089.29	11/2–9/2	1.000	1.000	1.000	1.000	1.000
M48b 4f G[4] ^o – 3d ⁴ F λ4083.90	7/2–5/2	0.285	0.316	0.326	1.141	1.032
M48c 4f G[3] ^o – 3d ⁴ F λ4087.15	5/2–3/2	0.271	0.347	0.347	1.280	1.000
M50a 4f F[4] ^o – 3d ⁴ F λ4062.94	9/2–9/2	0.125	0.126	0.137	1.096	1.087
M50b 4f F[3] ^o – 3d ⁴ F λ4048.21	7/2–7/2	0.063	0.068	0.076	1.206	1.120
M53a 4f D[3] ^o – 3d ⁴ P λ4303.83 ^a	7/2–5/2	0.413	0.522	0.534	1.293	1.022
M53b 4f D[2] ^o – 3d ⁴ P λ4294.78 ^b	5/2–3/2	0.232	0.326	0.253	1.091	0.776
M53c 4f D[1] ^o – 3d ⁴ P λ4307.23	3/2–1/2	0.105	0.118	0.108	1.031	0.919
M53c 4f D[1] ^o – 3d ⁴ P λ4288.82 ^c	3/2–1/2	0.151	0.123	0.145	0.958	1.176
M55 4f G[3] ^o – 3d ⁴ P λ4291.25 ^d	7/2–5/2	0.156	0.188	0.221	1.414	1.176
M63a 4f D[3] ^o – 3d ⁴ D λ4357.25 ^e	7/2–5/2	0.057	0.088	0.094	1.651	1.067
M67c 4f F[2] ^o – 3d ⁴ D λ4282.96 ^f	5/2–3/2	0.154	0.168	0.185	1.200	1.101
M76b 4f G[4] ^o – 3d ² F λ4371.62 ^g	9/2–7/2	0.097	0.109	0.127	1.303	1.159
M78a 4f F[4] ^o – 3d ² F λ4313.44 ^h	9/2–7/2	0.121	0.133	0.139	1.150	1.045
M78b 4f F[3] ^o – 3d ² F λ4285.69	7/2–5/2	0.189	0.264	0.229	1.208	0.869
M86a 4f D[3] ^o – 3d ² P λ4491.23	5/2–3/2	0.137	0.198	0.215	1.569	1.086
M86b 4f D[2] ^o – 3d ² P λ4489.49	3/2–1/2	0.065	0.082	0.083	1.271	1.004
M88 4f G[3] ^o – 3d ² P λ4477.90 ⁱ	5/2–3/2	0.086	0.109	0.113	1.316	1.108
M92a 4f F[4] ^o – 3d ² D λ4609.44	7/2–5/2	0.428	0.444	0.483	1.126	1.088
M92b 4f F[3] ^o – 3d ² D λ4602.13 ^j	5/2–3/2	0.171	0.194	0.195	1.139	1.003

^a Corrected for the contribution from O II M65a 4f G[5]_{9/2}^o – 3d ⁴D_{7/2} λ4303.61 (about 12 per cent). Neglecting O II M53a 4f D[3]_{5/2}^o – 3d ⁴P_{5/2} λ4304.08 (~3 per cent).

^b Including O II M53b 4f D[2]_{3/2}^o – 3d ⁴P_{3/2} λ4294.92 (~12 per cent).

^c Including O II M53c 4f D[1]_{1/2}^o – 3d ⁴P_{1/2} λ4288.82.

^d Including O II M78c 4f F[2]_{5/2}^o – 3d ²F_{5/2} λ4292.21. Neglecting O II M55 4f G[3]_{5/2}^o – 3d ⁴P_{5/2} λ4291.86 and O II M78c 4f F[2]_{3/2}^o – 3d ²F_{5/2} λ4292.95.

^e Including O II M63a 4f D[3]_{5/2}^o – 3d ⁴D_{3/2} λ4357.25. Neglecting O II M63a 4f D[3]_{5/2}^o – 3d ⁴D_{5/2} λ4357.52.

^f Including O II M67c 4f F[2]_{5/2}^o – 3d ⁴D_{5/2} λ4283.25. Neglecting O II M78a 4f F[4]_{7/2}^o – 3d ²F_{5/2} λ4282.02.

^g Neglecting O II M76b 4f G[4]_{7/2}^o – 3d ²F_{7/2} λ4371.24 (less than 2 per cent).

^h Corrected for the contribution from the O II M78a 4f F[4]_{7/2}^o – 3d ²F_{7/2} λ4312.11 line (~33 per cent).

ⁱ Neglecting O III M45a 5g H[11/2]_{5,6}^o – 4f G[9/2]₅ λ4477.91 (less than 2 per cent).

^j Corrected for the contribution from N II M5 3p ³P₂ – 3s ³P₁ λ4601.48 (26 per cent). Neglecting N II M64d 4f F[2]_{3/2}^o – 3d ⁴P_{3/2} λ4600.16.

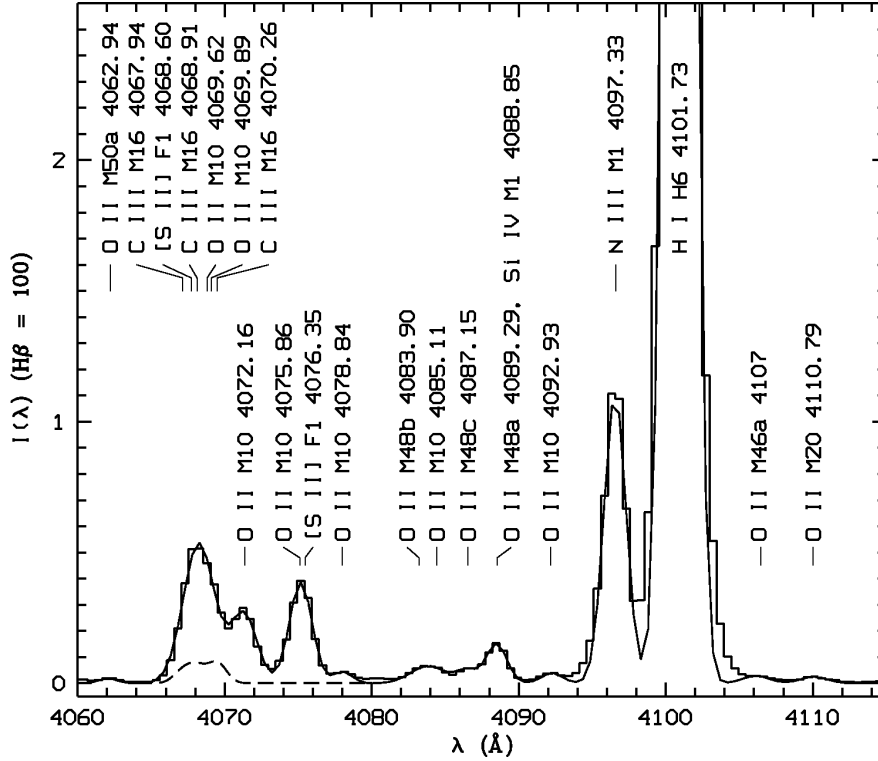


Figure 33. Spectrum of NGC 7009 from 4060 to 4115 Å showing the O II M10 lines and some O II lines from the 4f–3d configuration. The strongest O II 4f–3d line $\lambda 4089.29$ (M48a 4fG[5] $^{\circ}_{11/2}$ –3d 4 F $_{9/2}$) is observed. The solid continuous curve is the sum of Gaussian profile fits. The dashed curve is the sum of the Gaussian profiles of the three C III M16 (5g 3 G–4f 3 F $^{\circ}$) lines $\lambda\lambda 4067.94$, 4068.92 and 4070.31, whose intensity ratio is fixed to be as in LS coupling, i.e. 1.00 : 1.31 : 1.71. Continuum has been subtracted and the spectrum has been normalized such that H β has an integrated flux of 100. Extinction has not been corrected for.

Table 7. The O II optical recombination lines in NGC 7009 with parentage other than 3P_J . Line intensities measured by LSBC are also presented. All intensities are normalized such that $I(H\beta) = 100$.

Line (Å)	Mult.	Transition	Current	LSBC	
				PA=0°	PA=45°
$\lambda 4590.97$	M15	(1D)3p $^2F_{7/2}^{\circ}$ – (1D)3s $^2D_{5/2}$	0.087	0.0907	0.0752
$\lambda 4596.18^a$	M15	(1D)3p $^2F_{5/2}^{\circ}$ – (1D)3s $^2D_{3/2}$	0.062	0.0424	0.0476
$\lambda 4185.45$	M36	(1D)3d $^2G_{7/2}$ – (1D)3p $^2F_{5/2}^{\circ}$	0.070	0.0572	0.0580
$\lambda 4189.79^b$	M36	(1D)3d $^2G_{9/2}$ – (1D)3p $^2F_{7/2}^{\circ}$	0.083	0.0703	0.0747
$\lambda 4253.89^c$	M101	(1D)4f H[5] $^{\circ}_{11/2}$ – (1D)3d $^1G_{9/2}$	0.058	0.0318:	0.0249:
$\lambda 4843.37^d$	M105	(1D)4f P[1] $^{\circ}_{3/2}$ – (1D)3d $^2S_{1/2}$	0.021		

^a Including O II M15 (1D)3p $^2F_{5/2}^{\circ}$ – (1D)3s $^2D_{5/2}$ $\lambda 4595.96$.

^b Including O II M36 (1D)3d $^2G_{7/2}$ – (1D)3p $^2F_{7/2}^{\circ}$ $\lambda 4189.59$.

^c Including O II M101 (1D)4f H[5] $^{\circ}_{9/2}$ – (1D)3d $^1G_{9/2}$ $\lambda 4253.91$ and O II M101 (1D)4f H[5] $^{\circ}_{9/2}$ – (1D)3d $^1G_{7/2}$ $\lambda 4254.12$.

^d Including O II $\lambda 4843.37$ M105 (1D)4f P[1] $^{\circ}_{1/2}$ – (1D)3d $^2S_{1/2}$.

tion 2.1. The O II recombination spectrum is the richest amongst all the heavy element ions observed in NGC 7009. The best observed multiplets of the 3–3 transitions of O II are M1 ($3p^4D^{\circ}$ – $3s^4P$), M2 ($3p^4P^{\circ}$ – $3s^4P$), M10 ($3d^4F$ – $3p^4D^{\circ}$), M19 ($3d^4P$ – $3p^4P^{\circ}$), M25 ($3d^2F$ – $3p^2D^{\circ}$) and M28 ($3d^4P$ – $3p^4S^{\circ}$). Although some fine-structure components of those multiplets are blended with other lines, multi-Gaussian profile fitting gives reliable inten-

sities for most of them. The 4f–3d lines with the most reliable measurements are presented in Table 6. The O II multiplets are not affected by any other excitation mechanisms (e.g. fluorescence, charge transfer), and the strongest lines have been used for plasma diagnostics (Section 2.3). Several O II lines with the parentage 1D are detected, as presented in Table 7. Only the dielectronic recombination coefficients for the M15 and M36 multiplets are available

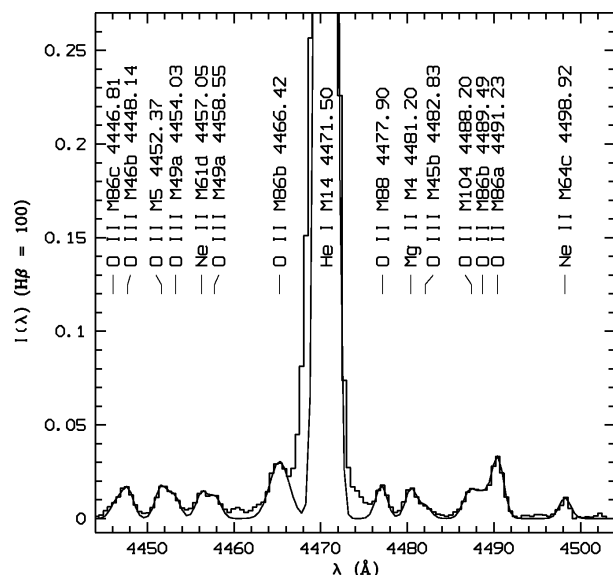


Figure 35. Spectrum of NGC 7009 from 4444 to 4504 Å showing the O II and O III ORLs. The only Mg II line detected in NGC 7009, Mg II M4 4f $^2F^\circ - 3d$ 2D λ 4481.20, is present. The continuous curve is the sum of Gaussian profile fits. Continuum has been subtracted and the spectrum has been normalized such that H β has an integrated flux of 100. Extinction has not been corrected for.

from Nussbaumer & Storey (1984). The calculation of PJS does not reach such high energy.

3.4 The Ne II optical recombination spectrum

Several dozen emission features in the spectrum of NGC 7009 were identified as the Ne II permitted lines. In this section, we present spectral fits and discussion of the results only for the M2 $3p$ $^4D^\circ - 3s$ 4P , M13 $3d$ $^4F - 3p$ $^4D^\circ$, M9 $3p'$ $^2F^\circ - 3s'$ 2D , and the M55e $4f$ $2[5]^\circ - 3d$ 4F multiplets. Discussion of other multiplets of Ne II are given in Appendix D. Line intensities measured by LLB01 are used for comparison if available. Predicted intensities that are based on the LS coupling calculations of Kisielius et al. (1998) are also used for the analysis.

3.4.1 Multiplet 2, $3p$ $^4D^\circ - 3s$ 4P

This is the strongest multiplet of Ne II. Fig. F2 shows that λ 3334.84 ($3p$ $^4D_{7/2}^\circ - 3s$ $^4P_{5/2}$) is affected by the O III fluorescence line M3 $3p$ $^3S_1 - 3s$ 3P_2 λ 3340.76, which is more than 10 times stronger. The fitted intensity of λ 3334.84 is 0.428, which is higher than LLB01 (0.345). Given that our observational data are the same as LLB01, such difference is probably due to the different reddening laws used. Besides, measurements of λ 3334.84 could be overestimated due to the O III line.

Another line λ 3355.02 ($3p$ $^4D_{5/2}^\circ - 3s$ $^4P_{3/2}$) blends with He I M8 $7p$ $^1P_1^\circ - 2s$ 1S_0 λ 3354.55 (Fig. D1), which contributes 43 per cent to the total intensity, as estimated from the calculations of Benjamin, Skillman & Smits (1999). The resultant intensity of λ 3355.02 is 0.223 ± 0.045 . The intensity ratio λ 3355.02/ λ 3334.84 agrees well with the predicted value. The intensity of another line λ 3360.60 ($3p$ $^4D_{3/2}^\circ - 3s$ $^4P_{1/2}$) is 0.040, which is unreliable (Fig. D1). The other M2 lines are not observed.

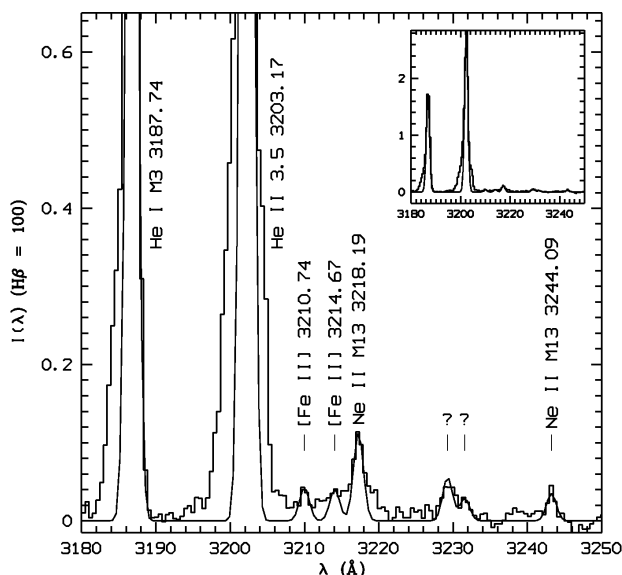


Figure 36. Spectrum of NGC 7009 from 3180 to 3250 Å showing the Ne II M13 lines and other emission features. The inset shows the profiles of the two strong lines He I M3 $4p$ $^3P^\circ - 2s$ 3S λ 3187.74 and He II $5f$ $^2F_{7/2}^\circ - 3d$ $^2D_{5/2}$ λ 3203.17. The continuous curve is the sum of Gaussian profile fits. Continuum has been subtracted and the spectrum has been normalized such that H β has an integrated flux of 100. Extinction has not been corrected for.

3.4.2 Multiplet 13, $3d$ $^4F - 3p$ $^4D^\circ$

Ne II M13 lines locate in the far-blue and they are difficult to observe due to weakness as well as the relatively poor S/N. Only λ 3218.19 ($3d$ $^4F_{9/2} - 3p$ $^4D_{7/2}^\circ$) and λ 3244.09 ($3d$ $^4F_{9/2} - 3p$ $^4D_{7/2}^\circ$) are observed, and they are shown in Fig. 36. The fitted intensity of λ 3218.19 is 0.234, which agrees well with LLB01 (0.229). Here the blended Ne II M16 $3d$ $^4P_{1/2} - 3p$ $^4D_{3/2}^\circ$ λ 3217.30 was assumed to be negligible (~ 3 per cent). The intensity ratio of λ 3218.19 to the Ne II M2 λ 3334.84 line is 0.546, which agrees with the predicted ratio 0.594. The intensity of the λ 3244.09 line is 0.074, higher than the measurement of LLB01 (0.0576).

3.4.3 Multiplet 9, $3p'$ $^2F^\circ - 3s'$ 2D

This is the only Ne II multiplet of an excited-state parentage ($2s^2 2p^4$ 1D) detected in the spectrum of NGC 7009, and shown in Fig. 37. The fitted intensity of λ 3568.50 ($3p'$ $^2F_{7/2}^\circ - 3s'$ $^2D_{5/2}$) is 0.168 ± 0.016 . The measured total intensity of the other two lines λ 3574.18, 61 is 0.053, with an uncertainty of about 10 per cent. Thus the intensity ratio $(\lambda\lambda 3574.18 + 3574.61)/\lambda$ 3568.50 is 0.32, which differs from the LS coupling value 0.75. No measurements of this multiplet are given in LLB01.

3.4.4 $4f - 3d$ transitions

Several dozen Ne II ORLs of the $4f - 3d$ configuration are detected or estimated by deblending techniques (i.e. Gaussian profile fitting). The measured intensities are 10^{-4} of H β or even lower. Table 8 presents the measured and predicted relative intensities of the $4f - 3d$ transitions with the most reliable measurements. The predicted intensities are based on the preliminary effective recombination coefficients calculated by P. J. Storey (private communication)

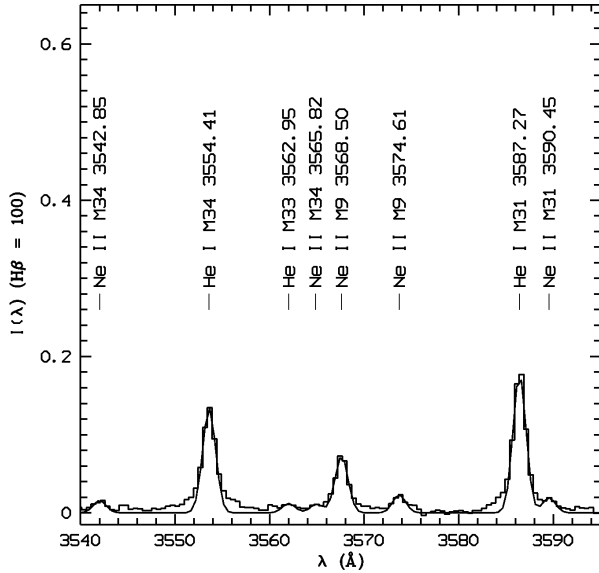


Figure 37. Spectrum of NGC 7009 from 3540 to 3595 Å showing the Ne II M9 and M34 lines as well as other emission features. The continuous curve is the sum of Gaussian profile fits. Continuum has been subtracted and the spectrum has been normalized such that H β has an integrated flux of 100. Extinction has not been corrected for.

for a few selected Ne II 4f–3d quartet lines. In this section, we only present spectral fits and results for the M55e 4f 2[5] $^{\circ}$ –3d 4 F multiplet of Ne II. Discussion of other multiplets of the 4f–3d configuration are given in Appendix D13. Some of the Ne II lines belonging to the M52a 4f 2[4] $^{\circ}$ –3d 4 D and M52b 4f 2[3] $^{\circ}$ –3d 4 D multiplets are shown in Fig 31. Fig C2 also shows many Ne II lines detected in the spectrum of NGC 7009.

The $\lambda 4391.99$ (M55e 4f 2[5] $^{\circ}_{11/2}$ –3d 4 F $_{9/2}$) line observed in NGC 7009 is shown in Fig. C2. Its intensity is 0.077 ± 0.008 , which agrees with LLB01: 0.0728 (ESO 1.52 m), 0.0779 (WHT 1996) and 0.0713 (WHT 1997). The contribution from the $\lambda 4392.00$ (4f 2[5] $^{\circ}_{9/2}$ –3d 4 F $_{9/2}$) line of the same multiplet is negligible. The other M55e line $\lambda 4409.30$ (4f 2[5] $^{\circ}_{9/2}$ –3d 4 F $_{7/2}$) is blended with the Ne II $\lambda 4409.78$ (M55b 4f 2[3] $^{\circ}_{7/2}$ –3d 4 F $_{9/2}$) line, whose intensity is negligible, and the O III $\lambda 4408.29$ (M46a 5g H[5] $^{\circ}_4$ –4f G[4] $_3$) line, which contributes about 10 per cent to the total intensity, as estimated from the effective recombination coefficients of Kisielius & Storey (1999). The resultant intensity of the $\lambda 4409.30$ line is 0.060, which agrees with LLB01: 0.0631 (ESO 1.52 m), 0.0615 (WHT 1996) and 0.0624 (WHT 1997). The intensity ratio $\lambda 4409.30/\lambda 4391.99$ observed in NGC 7009 is 20 per cent higher than the predicted value (Table 8).

3.4.5 Comments on the Ne II recombination spectrum

The Ne II effective recombination coefficients currently used are mainly from Kisielius et al. (1998). This calculation is carried out for the transitions of $l \leq 2$. Although some effective recombination coefficients for the Ne II 4f–3d transitions are available (P. J. Storey, unpublished), only a few selected Ne II lines are calculated, and the results are quite preliminary. The best observed Ne II multiplets of the 3–3 transitions is M2 (3p 4 D $^{\circ}$ –3s 4 P). For the Ne II multiplets, M12 (3d 4 D–3p 4 D $^{\circ}$), M13 (3d 4 F–3p 4 D $^{\circ}$), M20 (3d 2 F–3p 2 D $^{\circ}$), M21 (3d 2 D–3p 2 D $^{\circ}$), M28 (3d 2 P–3p 2 S $^{\circ}$) and M34 (3d 4 P–3p 4 S $^{\circ}$), only the strongest fine-structure compo-

Table 8. Comparison of the observed and predicted relative intensities of the Ne II 4f–3d lines detected in the spectrum of NGC 7009. The predicted intensities I_{pred} are based on the preliminary effective recombination coefficients for some of the strongest Ne II lines from the 4f–3d configuration (P. J. Storey, private communication).

Line	$J_2 - J_1$	I_{pred}	I_{obs}	$\frac{I_{\text{obs}}}{I_{\text{pred}}}$
M55e 4f 2[5] $^{\circ}$ –3d 4 F				
$\lambda 4391.99^a$	11/2–9/2	1.000	1.000	1.000
$\lambda 4409.30^b$	9/2–7/2	0.665	0.812	1.221
M52a 4f 2[4] $^{\circ}$ –3d 4 D				
$\lambda 4219.75^c$	9/2–7/2	0.555	0.831	1.497
$\lambda 4233.85$	7/2–5/2	0.139	0.227	1.631
M52b 4f 2[3] $^{\circ}$ –3d 4 D				
$\lambda 4231.64^d$	7/2–5/2	0.131	0.370	2.811
$\lambda 4250.65$	5/2–3/2	0.088	0.216	2.461
M57b 4f 1[4] $^{\circ}$ –3d 4 F				
$\lambda 4397.99$	7/2–5/2	0.346	0.325	0.941
M60c 4f 1[3] $^{\circ}$ –3d 2 F				
$\lambda 4428.64^e$	7/2–5/2	0.437	0.591	1.353
M61a 4f 2[4] $^{\circ}$ –3d 2 D				
$\lambda 4430.94^f$	7/2–5/2	0.283	0.452	1.598
M61d 4f 2[2] $^{\circ}$ –3d 2 D				
$\lambda 4457.05^g$	5/2–3/2	0.098	0.361	3.662
M65 4f 0[3] $^{\circ}$ –3d 4 P				
$\lambda 4413.22^h$	7/2–5/2	0.239	0.376	1.574
M66c 4f 1[3] $^{\circ}$ –3d 4 P				
$\lambda 4421.39$	5/2–3/2	0.089	0.113	1.263

^a Neglecting Ne II M55e 4f 2[5] $^{\circ}_{9/2}$ –3d 4 F $_{9/2}$ $\lambda 4392.00$.

^b Corrected for the contribution from the O III M46a 5g H[5] $^{\circ}_4$ –4f G[4] $_3$ $\lambda 4408.29$ line (~ 10 per cent). Neglecting Ne II M55b 4f 2[3] $^{\circ}_{7/2}$ –3d 4 F $_{9/2}$ $\lambda 4409.78$.

^c Including Ne II M52d 4f 2[2] $^{\circ}_{5/2}$ –3d 4 D $_{5/2}$ $\lambda 4220.89$. Neglecting Ne II M52a 4f 2[4] $^{\circ}_{7/2}$ –3d 4 D $_{7/2}$ $\lambda 4219.37$.

^d Including Ne II M52b 4f 2[3] $^{\circ}_{5/2}$ –3d 4 D $_{5/2}$ $\lambda 4231.53$.

^e Including Ne II M61b 4f 2[3] $^{\circ}_{7/2}$ –3d 2 D $_{5/2}$ $\lambda 4428.52$. Neglecting Ne II M60c 4f 1[3] $^{\circ}_{5/2}$ –3d 2 F $_{5/2}$ $\lambda 4428.52$ and Ne II M61b 4f 2[3] $^{\circ}_{5/2}$ –3d 2 D $_{5/2}$ $\lambda 4428.41$.

^f Including Ne II M57a 4f 1[2] $^{\circ}_{5/2}$ –3d 4 F $_{3/2}$ $\lambda 4430.90$ and Ne II M55a 4f 2[4] $^{\circ}_{9/2}$ –3d 4 F $_{7/2}$ $\lambda 4430.06$. Neglecting Ne II M57a 4f 1[2] $^{\circ}_{3/2}$ –3d 4 F $_{3/2}$ $\lambda 4431.11$.

^g Neglecting Ne II M61d 4f 2[2] $^{\circ}_{3/2}$ –3d 2 D $_{3/2}$ $\lambda 4457.24$ and Ne II M66c 4f 1[3] $^{\circ}_{5/2}$ –3d 4 P $_{5/2}$ $\lambda 4457.24$. Including Ne II M66c 4f 1[3] $^{\circ}_{7/2}$ –3d 4 P $_{5/2}$ $\lambda 4457.36$.

^h Neglecting Ne II M65 4f 0[3] $^{\circ}_{5/2}$ –3d 4 P $_{5/2}$ $\lambda 4413.11$. Including Ne II M57c 4f 1[3] $^{\circ}_{5/2}$ –3d 4 F $_{3/2}$ $\lambda 4413.11$.

ments are observed, and the weaker components are either blended with other lines or not detected. Measurements of the M1 (3p 4 P $^{\circ}$ –3s 4 P), M5 (3p 2 D $^{\circ}$ –3s 2 P) and M6 (3p 2 S $^{\circ}$ –3s 2 P) lines are of large uncertainties due to line blending. The M9 (3p 2 F $^{\circ}$ –3s 2 D) multiplet is the only Ne II transition observed in our spectrum of parentage other than 3 P. The effective recombination coefficients for this multiplet are available from Kisielius et al. (1998), which are probably unreliable considering that the calculation is in the LS coupling assumption. The possibility of using the Ne II lines to determine electron temperatures is discussed in Section 2.4. In NGC 7009, the effects of the fluorescence mechanism on the Ne II M1 and M2 multiplets are probably not important. Thus those lines

could be safe for plasma diagnostics and abundance determinations.

3.5 The C III permitted lines

More than 20 lines in NGC 7009 were identified as C III permitted transitions (Paper I); some identifications could be questionable. In this section, we only introduce three multiplets: M1 $3p^3P^o - 3s^3S$, M16 $5g^3G - 4f^3F^o$ and M18 $5g^1G - 4f^1F^o$. The three C III M1 lines, $\lambda\lambda 4647.42, 4650.25$ and 4651.47 , are blended with the O II M1 ($3p^4D^o - 3s^4P$) lines $\lambda\lambda 4649.13$ and 4650.84 , as shown in Fig. 32. Techniques used to obtain the total intensity of the C III M1 multiplet are illustrated in Section 3.3.1. The intensity ratio of the three lines was assumed to be as in the LS coupling, i.e. 1 : 3 : 5. The total intensity is 0.303, which is accurate to 20 per cent. This intensity agrees with the measurements of LSBC: 0.274 (PA = 45°) and 0.438 (PA = 0°).

The C III M16 lines $\lambda\lambda 4067.94, 4068.91$ and 4070.26 are blended with the [S II] $\lambda 4068$ ($3p^3^2P^o_{3/2} - 4S^o_{3/2}$) and two O II M10 ($3d^4F - 3p^4D^o$) lines $\lambda\lambda 4069.62$ and 4069.89 , as shown in Fig. 33. Details of deriving the total intensity of the C III M16 multiplet are given in Section 3.3.2. The intensity ratio of the three C III M16 lines was also assumed to be as in the LS coupling, i.e. 1.00 : 1.31 : 1.71. The total intensity is 0.288, with a large uncertainty (~ 40 per cent). The intensity ratio of the C III M16 $\lambda 4069$ and the C III M1 $\lambda 4650$ multiplets is 0.952. The predicted ratio of the two C III multiplets is 0.922, which is calculated from the radiative and dielectronic recombination coefficients of Péquignot, Petitjean & Boisson (1991) and Nussbaumer & Storey (1984), respectively.

The C III M18 $\lambda 4186.90$ ($5g^1G_4 - 4f^1F^o_3$) line is blended with the O II M36 $\lambda 4185.44$ ($3d^2G_{7/2} - 3p^2F^o_{5/2}$) line, as shown in Fig. 31. Multi-Gaussian fits yield an intensity of 0.089 ± 0.018 for the $\lambda 4186.90$ line. This intensity agrees with those given by LSBC: 0.0533 (PA = 45°) and 0.102 (PA = 0°). The intensity ratio of the C III M18 $\lambda 4187$ and the C III M1 $\lambda 4650$ multiplets is 0.293, which agrees with the predicted ratio (0.331) within errors.

3.6 The N III permitted lines

More than 30 lines were identified as the N III permitted transitions, including multiplets M1 and M2, which are mainly excited by the Bowen fluorescence mechanism. Transitions from the states with excited parentage (i.e. other than 1S) are detected. Most N III lines suffer from line blending. In this section, we only present intensity measurements and discussion for the M3 $3p^4D - 3s^4P^o$ and M18 $5g^2G - 4f^2F^o$ multiplets. Discussion of other multiplets of N III is given in Appendix E.

3.6.1 Multiplet 3, $3p^4D - 3s^4P^o$

$\lambda 4510.91$ ($3p^4D_{5/2} - 3s^4P^o_{3/2}$ and $3p^4D_{3/2} - 3s^4P^o_{1/2}$) blends with [K IV] $3p^4^1S_0 - 3p^4^1D_2$ $\lambda 4510.92$, whose intensity contribution is unknown. Another M3 line $\lambda 4514.86$ ($3p^4D_{7/2} - 3s^4P^o_{5/2}$) is partially resolved from Ne II M58a $4f 2[4]_{9/2}^o - 3d^2F_{7/2}$ $\lambda 4517.83$ (Fig. 38). Several Ne II ORLs, M58b $\lambda 4514.88$, M64d $\lambda 4516.66$ and M58a $\lambda 4517.83$, are also blended in the complex, which makes line measurements very difficult. Another line $\lambda 4518.15$ ($3p^4D_{1/2} - 3s^4P^o_{1/2}$) blends with the Ne II M58a $\lambda 4517.83$ line, which probably dominates the total intensity.

Another two lines $\lambda\lambda 4523.58$ ($3p^4D_{3/2} - 3s^4P^o_{3/2}$) and

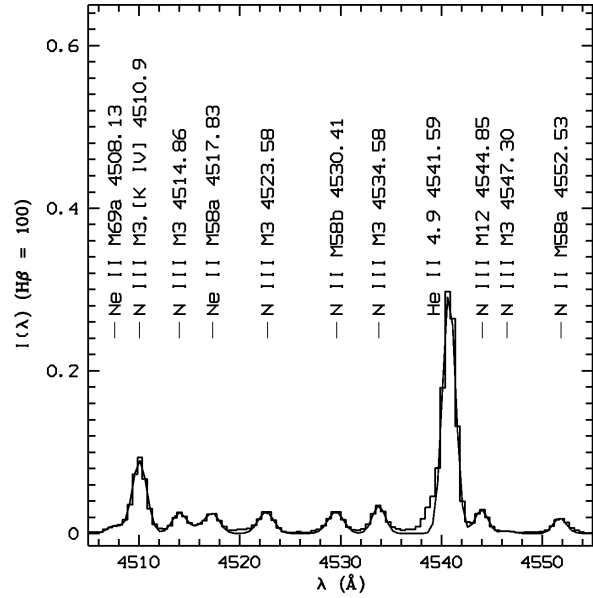


Figure 38. Spectrum of NGC 7009 from 4505 to 4555 Å showing the N III M3 lines and other emission features. The continuous curve is the sum of Gaussian profile fits. Continuum has been subtracted and the spectrum has been normalized such that H β has an integrated flux of 100. Extinction has not been corrected for.

$\lambda 4547.30$ ($3p^4D_{3/2} - 3s^4P^o_{5/2}$) decay from the same upper level, thus their intensity ratio depends only on the coupling scheme. The measured line ratio $\lambda 4547.30/\lambda 4523.58$ is 0.119, which is slightly higher than the LS coupling value 0.094. Measurements of the $\lambda 4547.30$ line could be of large error due to weakness (Fig. 38). Another M3 line $\lambda 4534.58$ ($3p^4D_{5/2} - 3s^4P^o_{5/2}$) blends with O III M48 $5g G[4]_{3,4}^o - 4f D[3]_3$ $\lambda 4534.31$ and Ne II M55b $4f 2[3]_{7/2}^o - 3d^4F_{5/2}$ $\lambda 4534.64$ as well as another three Ne II lines M55b $\lambda 4534.52$, M55c $\lambda 4535.37$, and M55c $\lambda 4535.57$, whose intensity contribution could be negligible. The other line $\lambda 4530.86$ ($3p^4D_{1/2} - 3s^4P^o_{3/2}$) blends with N II M58b $4f 2[5]_4 - 3d^1F^o_3$ $\lambda 4530.41$, which is probably more than 3 times stronger.

3.6.2 Multiplet 18, $5g^2G - 4f^2F^o$

$\lambda 4379.11$ ($5g^2G_{9/2} - 4f^2F^o_{7/2}$ and $5g^2G_{7/2} - 4f^2F^o_{7/2}$) is detected in Fig. C1. Gaussian profile fitting gives an intensity of 0.367, with an uncertainty of less than 10 per cent. Measurements for this line given by LSBC are 0.312 (PA = 45°) and 0.397 (PA = 0°). $\lambda 4379.11$ blends with Ne II M60b $4f 1[4]_{9/2}^o - 3d^2F_{7/2}$ $\lambda 4379.55$, which contributes about 10 per cent to the total intensity, and Ne II M60b $4f 1[4]_{7/2}^o - 3d^2F_{7/2}$ $\lambda 4379.40$ and O III M39c $5g G[5]_{4,5}^o - 4f F[4]_4$ $\lambda 4379.58$, both of which were assumed to be negligible. This line is used to derive N^{3+}/H^+ abundance ratio.

3.7 The O III permitted lines

In Paper I, about two dozen O III permitted transitions from the 3–3 configuration were identified, including multiplets M2 $3p^3D - 3s^3P^o$, M3 $3p^3S - 3s^3P^o$, M4 $3p^3P - 3s^3P^o$, M12 $3d^3P^o - 3p^3S$ and M15 $3d^3P^o - 3p^3P$, which are mainly excited by the Bowen fluorescence or charge-transfer (Liu & Danziger 1993a). All the O III $5g - 4f$ lines are blended with other emission features. In this section, we only present emission line measurements of the M8

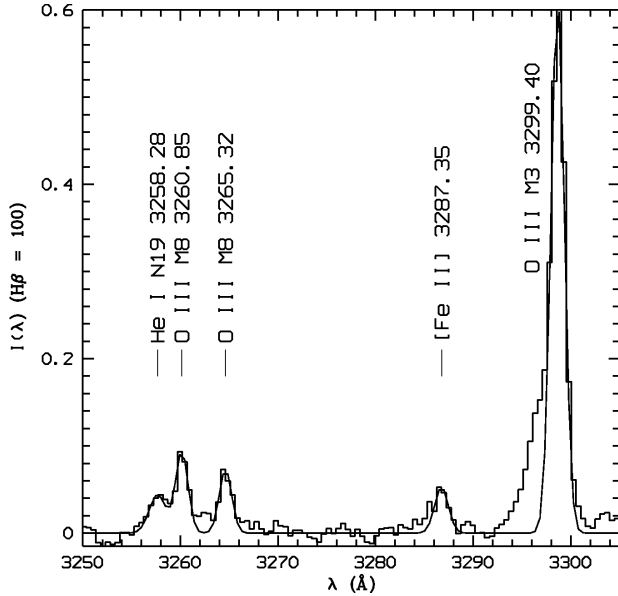


Figure 39. Spectrum of NGC 7009 from 3250 to 3305 Å showing the O III M8 lines $\lambda\lambda 3260.85$ and 3265.32 . The continuous curve is the sum of Gaussian profile fits. Continuum has been subtracted and the spectrum has been normalized such that H β has an integrated flux of 100. Extinction has not been corrected for.

$3d^3F^o - 3p^3D$ and M15 $3d^3P^o - 3p^3P$ multiplets. Measurement results of other O III multiplets are given in Appendix F. Discussion of the O III fluorescence lines is in Section 3.7.4.

3.7.1 Multiplet 8, $3d^3F^o - 3p^3D$

Only $\lambda 3260.85$ ($3d^3F_3^o - 3p^3D_2$) and $\lambda 3265.32$ ($3d^3F_4^o - 3p^3D_3$) are observed (Fig. 39). Measurements of the two lines could be of relatively large error due to poor S/N in the far blue of the spectrum. However, this multiplet cannot be excited by either the Bowen fluorescence or charge transfer, and the two lines are still used to determine the O^{3+}/H^+ abundance ratio.

3.7.2 Multiplet 15, $3d^3P^o - 3p^3P$

Fig. 40 shows the O III M15 lines detected in the spectrum of NGC 7009. Single-Gaussian profile fitting yields an intensity of 11.575 for the $\lambda 3444.06$ line, with an uncertainty of about 3 per cent. The intensity contribution from the blended He I M7 $\lambda 3447.59$ ($6p^1P_1^o - 2s^1S_0$) line is only 2 per cent. Another M15 line $\lambda 3428.62$ is blended with the $\lambda 3430.57$ line of the same multiplet, which is marginally resolved in Fig. 40. Two Gaussian profiles with the same FWHM were used to fit the feature, and the resultant intensities of the $\lambda 3428.62$ and the $\lambda 3430.57$ lines are 1.409 and 0.319, respectively, both with uncertainties of less than 10 per cent.

Another M15 line $\lambda 3415.26$ is partially resolved from the Ne II M21 $\lambda 3416.91$ ($3d^2D_{5/2} - 3p^2D_{5/2}^o$) line; the other two M15 lines, $\lambda\lambda 3405.71$ and 3408.12 are also detected in the spectrum. The three O IV M2 $3d^2D - 3p^2P^o$ lines, $\lambda\lambda 3403.52$, 3411.69 and 3413.64 , are blended among the above three O III M15 lines, as is shown in Fig. 40. Multi-Gaussian profile fitting was carried out for the complex. The intensity of the $\lambda 3415.26$ line is 0.415 ± 0.021 . The intensities of the $\lambda\lambda 3405.71$ and 3408.12 lines are 0.210 and 0.127, respectively, both with uncertainties of 10 to 15 per cent.

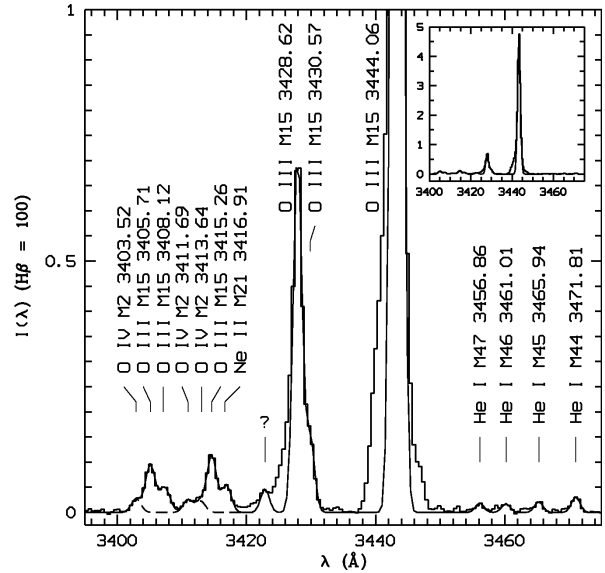


Figure 40. Spectrum of NGC 7009 from 3395 to 3475 Å showing the O III M15 lines. The profile of the O III M15 $\lambda 3444$ line shows that there is a weak component blended on its right side, which could be the He I M7 $6p^1P_1^o - 2s^1S_0$ $\lambda 3447.59$ line. Several weak He I lines from the $nd - 2p$ transition array are also detected. The solid continuous curve is the sum of Gaussian profile fits. The dashed curve is the sum of the Gaussian profiles of the three O IV M2 $3d^2D - 3p^2P^o$ lines $\lambda\lambda 3403.52$, 3411.69 and 3413.64 . Continuum has been subtracted and the spectrum has been normalized such that H β has an integrated flux of 100. Extinction has not been corrected for. The inset shows the profile of the O III M15 $\lambda 3444$ line.

Analysis of the measured intensities of the O IV M2 lines are in Section 3.8.

The observed intensity ratio $\lambda 3428.62/\lambda 3444.06$ is 0.122, lower than the theoretical prediction (0.336) given by Saraph & Seaton (1980), who assumed that the relative intensities within the O III M15 multiplet to be as in *LS* coupling, but agrees with the intermediate calculations of Kastner et al. (1983). The observed intensity ratio of the three O III M15 lines $\lambda\lambda 3405.71$, 3415.26 and 3430.57 , which have the common upper level, is 1 : 2.102 : 1.615. This ratio differs from that in the pure *LS* coupling, i.e. 1 : 0.75 : 1.25. Discussion of the intensity ratios of the O III M15 lines is presented in Section 3.7.4.

3.7.3 $5g - 4f$ transitions

The O III permitted transitions of $5g - 4f$ configuration are in the wavelength range 4300–4600 Å, where numerous ORLs of the singly-ionized ions of C, N, O and Ne are located. The typical intensities of the $5g - 4f$ lines of O III are $\sim 10^{-4} - 10^{-5}$ of H β , and accurate measurements of these lines are difficult due to line blending. The strongest O III line of the $5g - 4f$ configuration, $\lambda 4434.60$ ($M46b$ $5g H[6]_6^o - 4f G[5]_5$), is marginally detected in the spectrum of NGC 7009, as is shown in Fig. C2. Multi-Gaussian profile fitting yields an intensity of 0.024 ± 0.003 , from which we derived an O^{3+}/H^+ abundance ratio that is higher than that deduced from the O III M8 $\lambda 3265$ ($3d^3F^o - 3p^3D$) multiplet by a factor of 20. Given the relatively more accurate measurements of the O III M8 lines (see Section 3.7.1), this much higher O^{3+}/H^+ abundance ratio derived from the $\lambda 4434.60$ line is questionable. The effective recombination coefficients calculated by Kisielius & Storey (1999)

for the 5g–4f transitions of O III are utilized to estimate the intensity contributions where necessary.

3.7.4 Fluorescence of the O III permitted lines

In Table 9 we compare the observed and predicted intensity ratios for several pairs of O III Bowen fluorescence lines originating from the same upper level. The observed intensity ratios (column 2 of Table 9) are based on the measurements in NGC 7009 described in Section 3.7. The errors are estimated from the measurement errors, including Gaussian profile fit and noise level of the local continuum. The profiles of the strong O III Bowen lines deviate from the exact Gaussian due to charge transfer effect, thus we used Gaussian profiles to fit these emission lines. The error from Gaussian profile fit is 5–10 per cent for strong O III Bowen lines. These O III Bowen lines are close to the blue end of the spectrum, the uncertainties due to the poor S/N in this wavelength region are also taken into account. The errors are significant for the two ratios $\lambda 3791/\lambda 3755$ and $\lambda 3774/\lambda 3757$, because the flux errors are large for the three relatively weak lines $\lambda \lambda 3791.28$ (about 21 per cent), 3757 (about 20 per cent) and 3774 (about 32 per cent), and thus the resulting uncertainties estimated from the error propagation formula are comparable to the ratio values. The observations of Liu & Danziger (1993a) for the same object are also presented for comparison.

The radiative transition probabilities of O^{2+} have been calculated since late 1960s (Nussbaumer 1969), and later by Saraph & Seaton (1980) and Luo et al. (1989). In these approaches *LS* coupling was assumed. Calculations of the O^{2+} transition probabilities with the scheme of intermediate coupling are presented by Kastner et al. (1983) and Kastner & Bhatia (1990) for some improved values for cascading from the $2p3d\ ^3P_2^o$ level. Fischer (1994) carried out a non-relativistic configuration interaction calculation with relativistic correction and showed obvious improvement over the previous work. Simultaneously, a full relativistic configuration interaction calculation of Tong et al. (1994) gave predicted O III Bowen line ratios which were further improvement, especially for the $\lambda 3133/\lambda 3444$ ratio. Their results are in agreement with observed ratios within the accuracy of observations. A more recent variational Breit-Pauli calculation was done by Tachiev & Fischer (2001) for the carbon-like sequence. The current measurements agree better with the intermediate coupling values.

3.8 The O IV permitted lines

Measurements of the O IV lines, $\lambda \lambda 3403.52$, 3411.69 and 3413.64 of the $M2\ 3d^2D-3p^3P^o$ multiplet are of large uncertainty due to weakness and line blending (Fig. 40). The intensity of the $\lambda 3411.69$ line derived from multi-Gaussian profile fitting is 0.057 ± 0.014 . The intensity ratio of the other two O IV M2 lines $\lambda \lambda 3403.52$ and 3413.64, which share the same upper level $^2D_{3/2}$, is 1.318. This intensity ratio is significantly lower than the value in the *LS* coupling assumption, i.e. 5.0. So far the only effective recombination coefficients available for the O IV lines are the radiative recombination coefficients given by Péquignot, Petitjean & Boisson (1991) and the dielectronic recombination coefficients given by Nussbaumer & Storey (1984). Both calculations were carried out in the *LS* coupling scheme. The O IV M2 lines are the only lines detected for this ion in the spectrum of NGC 7009, but are not used in abundance determinations.

4 IONIC AND ELEMENTAL ABUNDANCES

In this section, we present the ionic abundances of helium and heavy elements derived from ORLs. For heavy element ions, the electron temperatures deduced from the N II and O II recombination line ratios are assumed (Section 2.3). For He^+/H^+ , a value of 5100 K as deduced from the He I $\lambda 7281/\lambda 6678$ ratio is adopted. For He^{2+}/H^+ , an electron temperature of 10 000 K, roughly the value deduced from the 5694 Å discontinuity of the He II recombination continuum spectrum, is assumed. The average electron temperature derived from the various optical CEL ratios is $\sim 10\,000$ K (Paper I), and is used to determine the forbidden line abundances. Given that the electron densities derived from the N II and O II ORLs are close to those from the optical CELs, and that emissivities of the heavy element ORLs are only marginally sensitive to electron density, we have assumed a constant density of 4300 cm^{-3} throughout the abundance determinations.

4.1 Ionic abundances from ORLs

Ionic abundances of He, C, N, O, Ne, Mg and Si are derived in this Section, using the extinction-corrected fluxes of ORLs given in Paper I. A critical analysis of the C II, N II, O II and Ne II permitted lines detected in the spectrum of NGC 7009 is presented in Section 3, and is used to guide the determinations of ORL abundances of heavy element ions. Again, the new effective recombination coefficients for the N II and O II recombination spectrum are utilized.

4.1.1 He^+/H^+ and He^{2+}/H^+

Numerous calculations have been dedicated to the recombination spectrum of He I (e.g. Mathis 1957; Burgess & Seaton 1960a, 1960b; Pottasch 1962; Robbins 1968, 1970; Robbins & Robinson 1971; Brocklehurst 1972; Almog & Netzer 1989; Smits 1991, 1996; Benjamin, Skillman & Smits 1999, 2002; Porter et al. 2005; Bauman et al. 2005). The recombination-cascade spectrum of He I, with no collision taken into account, was first computed by Brocklehurst (1972). A better treatment of emissivities from He I in nebular environment is that of Smits (1996), who used more accurate calculations of radiative transition rates and photoionization cross-sections, and corrected an error in Brocklehurst (1972). Benjamin, Skillman & Smits (1999) combined the detailed He I recombination model of Smits (1996) with the collisional transitions of Sawey & Berrington (1993) and calculated more accurate He I recombination line emissivities that include the effects of collisional excitation from both the $2s^3S$ and $2s^1S$ levels. Benjamin, Skillman & Smits (2002) studied the effects of the optical depth of the $2s^3S$ metastable level on the He η line intensities. The availability of these improved atomic data has made it possible to obtain secure measurements of the ionic and elemental abundances of helium, given high-quality spectroscopic data. Zhang et al. (2005a) developed the nebular plasma diagnostics based on the He I ORLs, using the theoretical emissivities of He I lines provided by Benjamin, Skillman & Smits (1999). In Paper I, we derived electron temperatures from He I line ratios using the method of Zhang et al. (2005a). In order to keep consistency, we derived ionic and elemental abundances of helium in this Section, using the atomic data of Benjamin, Skillman & Smits (1999) and assuming the temperature to be that yielded by the He I lines (~ 5000 K).

Ionic and elemental abundances of helium relative to hydrogen derived from the He I and He II ORLs are presented in Table 10.

Table 9. Comparison of the observed and predicted Bowen fluorescence line ratios.

Line Ratio	Current obs.	LD93 ^a	SS80 ^b	KBB83 ^c	FF94 ^d	TZLL94 ^e	TFF01 ^f
$\lambda 3133/\lambda 3444$	3.261±0.071	3.140±0.440	3.610	4.450	3.170	3.290	3.342
$\lambda 3299/\lambda 3341$	0.252±0.117	0.285±0.022	0.201	0.228	0.264	0.260	0.268
$\lambda 3312/\lambda 3341$	0.698±0.086	0.651±0.048	0.606	0.656	0.728	0.717	0.736
$\lambda 3428/\lambda 3444$	0.122±0.027	0.204±0.023	0.336	0.164	0.150	0.149	0.154
$\lambda 3791/\lambda 3755$	0.271±0.213	0.232±0.037	0.330	0.309	0.296	0.301	0.299
$\lambda 3774/\lambda 3757$	0.539±0.379	0.569±0.127	0.750	0.715	0.708	0.701	0.704

^a Liu & Danziger (1993a);^b Saraph & Seaton (1980);^c Kastner et al. (1983);^d Fischer (1994);^e Tong et al. (1994);^f Tachiev & Fischer (2001).

The adopted He^+/H^+ ratio (0.099) is an average of the values derived from the He I $\lambda\lambda 4471, 5876$ and 6678 lines with weights of 1 : 3 : 1, roughly proportional to their intrinsic intensities (Benjamin, Skillman & Smits 1999). Here the effective recombination coefficients were adopted from Benjamin, Skillman & Smits 1999. Case A recombination was assumed for the triplet lines and Case B for the singlet. An electron temperature of 5000 K, as derived from the He I $\lambda 7281/\lambda 6678$ ratio, and a density of $10\,000\text{ cm}^{-3}$ were assumed. Under this physical condition, the effective recombination coefficient for the $\lambda 4471$ line given by Benjamin, Skillman & Smits 1999 is 6 per cent higher than that of Brocklehurst (1972). This difference is 7 per cent when the temperature increases to 10 000 K. The differences between the calculations of Benjamin, Skillman & Smits 1999 and Brocklehurst (1972) for the other two He I lines are less than 2 per cent at 5100 K. The $\lambda 4471$ line suffers most from line blending among the three He I lines: It is blended with two O II M86c lines $\lambda\lambda 4469.46$ and 4469.48 , three O III lines M49c $\lambda\lambda 4471.02, 4475.17$ and M45b $\lambda 4476.11$, and one Ne II line M61b $\lambda 4468.91$. Both wings of the $\lambda 4471$ line are also affected by weak features (Fig. 35). All the blending brings an uncertainty of ~ 10 per cent to the intensity of the $\lambda 4471$ line. The $\lambda 4471$ line intensity adopted in the current analysis has been corrected for the contributions from the blended lines listed above, using the effective recombination coefficients available for the O II and O III lines. The intensity of the He I $\lambda 6678$ line has also been corrected for the contribution from the blended He II $\lambda 6683.20$ ($13h^2\text{H}^\circ - 5g^2\text{G}$) line, which brings an uncertainty of about 3 per cent. The measurement uncertainty of the He I $\lambda 5876$ line is less than 2 per cent.

The He^+/H^+ abundances listed in Table 10 agree with each other reasonably well, except for those yielded by the triplet line $\lambda 7065$ ($3s^3\text{S} - 2p^3\text{P}^\circ$) and the singlet line $\lambda 5016$ ($3p^1\text{P}^\circ - 2s^1\text{S}$). The former one is more than two times higher than the average abundance, while the latter is nearly half of the value. The abnormally high abundance value is probably due to the enhanced $\lambda 7065$ line as a result of self-absorption from the metastable $2s^3\text{S}$ level. By comparing the observed intensities of the He I singlet lines of the $ns^1\text{S} - 2p^1\text{P}^\circ$, $np^1\text{P}^\circ - 2s^1\text{S}$ and $nd^1\text{D} - 2p^1\text{P}^\circ$ series, relative to the $\lambda 4922$ ($4d^1\text{D}_2 - 2p^1\text{P}^\circ_1$) line, with the theoretical predictions (c.f. Section 4.5 in Paper I), we concluded that the singlet transitions of He I in NGC 7009 are close to the Case B assumption. Departure from Case B of the He I singlet lines as a result of the He I Lyman photons being destroyed by photoionization of neutral hydrogen and/or absorption by dust grains (Liu et al. (2001b)) is unlikely to be significant. Thus the low ionic abundance yielded by

the $\lambda 5016$ line in Table 10 is mainly due to self-absorption from the metastable $2s^1\text{S}$ level. The $\lambda 5016$ line is blending with the N II M19 $3d^3\text{F}^\circ_2 - 3p^3\text{D}_2$ $\lambda 5016.39$, whose contribution is negligible (< 1.0 per cent).

The $\text{He}^{2+}/\text{H}^+$ abundance ratios were derived from two He II lines $\lambda 3203$ ($5f^2\text{F}^\circ - 3d^2\text{D}$) and $\lambda 4686$ ($4f^2\text{F}^\circ - 3d^2\text{D}$). The effective recombination coefficients of the two lines were adopted from the hydrogenic calculation of Storey & Hummer (1995). Although the electron temperature ($\sim 11\,000$ K) derived from the discontinuity at $\lambda 5694\text{ \AA}$ of the He II recombination continuum is of large uncertainty due to weakness of the jump, we assumed an electron temperature of 10 000 K when deriving the $\text{He}^{2+}/\text{H}^+$ abundance ratio. The total elemental abundance of helium relative to hydrogen is 0.112, which is calculated from $\text{He}/\text{H} = \text{He}^+/\text{H}^+ + \text{He}^{2+}/\text{H}^+$. This agrees well with the value of 0.109 given by LSBC.

Several He I recombination line series have been observed in our spectrum, and relative intensities of these lines are presented in Table 11. Also presented in the Table are the theoretical predictions given by Benjamin, Skillman & Smits (1999), Brocklehurst (1972), and Smits (1996). Case A was assumed for the triplet lines and Case B for the singlet. The observed intensities of the $nd^3\text{D} - 2p^3\text{P}^\circ$ and $nd^1\text{D} - 2p^1\text{P}^\circ$ series of He I, relative to the $\lambda 4471$ line, agree well with those predicted by recombination theory. The obvious weakness of the $np^1\text{P}^\circ - 2s^1\text{S}$ series, compared with theoretical intensities, is caused by self-absorption from the metastable $2s^1\text{S}$ level. Such self-absorption should at the same time lead to the enhancement of the $ns^1\text{S} - 2p^1\text{P}^\circ$ series. However, what we observed as shown in Table 11 are opposite: The $\lambda 7281$ line seems weaker than the recent prediction. The $\lambda 3889$ ($3p^3\text{P}^\circ - 2s^3\text{S}$) line is affected by self-absorption. Enhancement of the $ns^3\text{S} - 2p^3\text{P}^\circ$ series, in particular the $\lambda 7065$ line, is clearly observed. Similar patterns in the relative intensities of the He I lines are also observed in NGC 6153 (Liu et al. 2000), M 1-42 and M 2-36 (Liu et al. 2001b).

4.1.2 C^{2+}/H^+ abundances from ORLs

The C^{2+}/H^+ abundance ratios derived from the $3-3$ and $4f-3d$ transitions as well as from the $ng-4f$ transition array are presented in Table 12. The effective recombination coefficients of Davey, Storey & Kisielius (2000) were used. Their calculation was carried out from 500 to 20 000 K. As described earlier, an electron temperature of 1000 K deduced from the N II and O II ORLs and probably prevalent in the postulated ‘‘cold’’ component where the ORLs of heavy elements arise (Liu et al. 2000), was assumed in the cal-

Table 10. Recombination line helium abundances.

He ⁱ⁺ /H ⁺	Line (Å)	Abundance
Triplet lines		
He ⁺ /H ⁺	He I λ 3187.74	0.094
He ⁺ /H ⁺	He I λ 3888.64	0.089
He ⁺ /H ⁺	He I λ 4026.20	0.103
He ⁺ /H ⁺	He I λ 4471.50	0.098
He ⁺ /H ⁺	He I λ 5875.60	0.103
He ⁺ /H ⁺	He I λ 7065.71	0.267
Singlet lines		
He ⁺ /H ⁺	He I λ 4921.93	0.099
He ⁺ /H ⁺	He I λ 5015.68	0.065
He ⁺ /H ⁺	He I λ 6678.15	0.095
He ⁺ /H ⁺	He I λ 7281.35	0.090
He ⁺ /H ⁺	Mean	0.099
He ²⁺ /H ⁺	He II λ 4685.68	0.013
He ²⁺ /H ⁺	He II λ 3203.17	0.012
He/H		0.112

culations. Transitions between doublet states were assumed to be in Case B given the ground term C II $^2P^o$. For those doublet transitions whose Case B effective recombination coefficients are not available in Davey, Storey & Kisielius (2000), the more recent calculations of Bastin (2006) were adopted. Bastin (2006) calculated the effective recombination coefficients for doublet transitions in both Case A and B from 5000 to 50 000 K. Accurately extrapolating the effective recombination coefficients of Bastin (2006) to 1000 K is difficult because the recombination coefficients are not exactly a linear function of electron temperature. The H I Balmer jump temperature 6500 K and a density of 4300 cm⁻³ were assumed when we derived the C²⁺/H⁺ abundance using the coefficients of Bastin (2006).

The C²⁺/H⁺ abundance ratio derived from the C II λ 4267 line is 5.507×10^{-4} . In the calculation of Davey, Storey & Kisielius (2000), the Case A effective recombination coefficient for the C II λ 4267 line differs from Case B by only 0.8 per cent. If a temperature of 10 000 K is assumed, the C²⁺/H⁺ ratio derived will increase to 8.432×10^{-4} , which then agrees with the abundance given by LSBC. At 10 000 K, the effective recombination coefficient for the C II λ 4267 line given by Davey, Storey & Kisielius (2000) differs from that of Bastin (2006) by only 1.4 per cent in Case B, and 1.8 per cent in Case A. Thus we expect that the C²⁺/H⁺ ratio derived from the coefficients of Bastin (2006) should agree with LSBC.

In Table 12, the C²⁺/H⁺ abundance ratios derived from the three $ng^2G-4f^2F^o$ lines (M17.02 λ 9903, M17.04 λ 6462, and M17.06 λ 5342) and the M16.04 $6f^2F^o-4d^2D$ λ 6151 line are based on the Case B effective recombination coefficients of Bastin (2006). The abundance ratios all agree with those given by LSBC. The Case B effective recombination coefficients for the C II $ng^2G-4f^2F^o$ ($n=5, 6$ and 7) transitions calculated by Bastin (2006) are almost identical to the Case A values at 6500 K; for the M16.04 $6f^2F^o-4d^2D$ λ 6151 transition, the effective recombination coefficients of the two cases differ by only 2 per cent. The C II M4 $4s^2S-3p^2P^o$ λ 3920 multiplet was not given by Davey, Storey & Kisielius (2000), and the Case B recombination coefficient of Bastin (2006) was used. The derived C²⁺/H⁺ abun-

Table 11. The He I lines observed in NGC 7009. Intensities are normalized to a scale where $I(\text{He I } \lambda 4471) = 1.0$. The theoretical predictions of Benjamin, Skillman & Smits (1999, **BSS99**), Brocklehurst (1972, **B72**) and Smits (1996, **S96**), at $T_e = 5000$ K and $N_e = 10^4$ cm⁻³, are presented for purpose of comparison. The Case A recombination is assumed for the triplets and Case B for the singlets.

λ_{lab} (Å)	n	I_{obs}	I_{pred} BSS99	I_{pred} B72	I_{pred} S96
<i>ns</i> ¹ S–2 <i>p</i> ¹ P ^o series					
3935.91	8	0.002		0.0024	
4023.99	7	0.005		0.0037	
4437.55	5	0.014	0.013	0.0124	
5047.74	4	0.033	0.031	0.030	
7281.35	3	0.106	0.118	0.108	0.113
<i>np</i> ¹ P ^o –2 <i>s</i> ¹ S series					
3354.55	7	0.036		0.034	
3447.59	6	0.042		0.054	
3613.64	5	0.060	0.094	0.097	
5015.68 ^a	3	0.312	0.498	0.512	0.486
<i>nd</i> ¹ D–2 <i>p</i> ¹ P ^o series					
3926.53	8	0.029		0.027	
4009.26	7	0.049		0.041	
4143.76	6	0.059		0.068	
4387.93	5	0.125	0.120	0.124	0.120
4921.93	4	0.245	0.269	0.275	0.269
6678.15 ^b	3	0.770	0.849	0.866	0.847
<i>ns</i> ³ S–2 <i>p</i> ³ P ^o series					
3599.32	9	0.005		0.0033	
3732.88	7	0.007		0.0076	
4120.99	5	0.054	0.028	0.0260	
4713.20	4	0.123	0.076	0.0649	0.075
7065.71	3	0.912	0.398	0.243	0.356
<i>np</i> ³ P ^o –2 <i>s</i> ³ S series					
3187.74	4	0.742	0.748	0.747	0.748
3888.64 ^c	3	1.714	1.891	1.895	1.865
<i>nd</i> ³ D–2 <i>p</i> ³ P ^o series					
3456.86	19	0.006		0.0077	
3461.01	18	0.008		0.0089	
3465.94	17	0.009		0.0105	
3471.81	16	0.011		0.0126	
3478.97	15	0.018		0.0153	
3487.72	14	0.021		0.0187	
3498.64	13	0.026		0.0234	
3512.51	12	0.034		0.0297	
3530.49	11	0.040		0.0385	
3554.41	10	0.055		0.0513	
3587.27	9	0.073		0.0707	
3634.23	8	0.112		0.101	
3705.00	7	0.187		0.154	
3819.60	6	0.275		0.251	
4026.20	5	0.504	0.452	0.459	0.451
4471.50	4	1.000	1.000	1.000	1.000
5875.60	3	3.018	2.916	3.010	2.952

^a Slightly overestimated due to the saturated [O III] λ 5007 line.

^b Corrected for the contribution from the He II λ 6683.20 (13h²H^o–5g²G) line.

^c Corrected for the contribution from the H I H8 λ 3889 line.

Table 12. Recombination line C^{2+}/H^+ abundances. Intensities are normalized such that $I(H\beta) = 100$.

Line (Å)	Mult.	I_{obs}	C^{2+}/H^+ ($\times 10^{-4}$)
4f $^2F^{\circ} - 3d \ ^2D$ $\lambda 4267$	M6	0.875	5.507
4s $^2S - 3p \ ^2P^{\circ}$ $\lambda 3918.98$ $\lambda 3920.69$ sum	M4	0.015 0.033 0.048	8.370 ^a
3d $^2D - 3p \ ^2P^{\circ}$ $\lambda 7231.32$ $\lambda 7236.42^b$ sum	M3	0.127 0.262 0.437	3.198
5g $^2G - 4f \ ^2F^{\circ}$ $\lambda 9903.46$	M17.02	0.200	8.197 ^a
6g $^2G - 4f \ ^2F^{\circ}$ $\lambda 6461.95$	M17.04	0.087	8.275 ^a
7g $^2G - 4f \ ^2F^{\circ}$ $\lambda 5342.40$	M17.06	0.037	6.771 ^a
6f $^2F^{\circ} - 4d \ ^2D$ $\lambda 6151.43$	M16.04	0.034	7.734 ^a

^a Based on the C II effective recombination coefficients of B06. An electron temperature of 6500 K, as derived from the H I Balmer jump, and a density of 4300 cm^{-3} , as derived from the CEL ratios (Paper I), are assumed.

^b Including the C II M3 $\lambda 7237.17$ line.

dance ratio agrees with those derived from the three $ng-4f$ transitions. The adopted C^{2+}/H^+ abundance ratio in the current paper is 6.865×10^{-4} , which is an average of the abundances derived from the transitions in Table 12.

4.1.3 N^{2+}/H^+ abundances from ORLs

The N^{2+}/H^+ abundance ratios derived from the N II ORLs detected in the spectrum of NGC 7009, with the most reliable measurements, are presented in Table 13. The M3 multiplet of the $3p-3s$ configuration is the best observed amongst all the $3-3$ transitions. The N II effective recombination coefficients of Kisielius & Storey (2002) are used when we derive the N^{2+}/H^+ abundance ratios from the total intensity of an N II multiplet, which is a sum of line intensities of all the fine-structure components. If some components are missing from a multiplet, i.e., not detected due to weakness or line blending, the total intensity of that multiplet is then calculated by assuming the relative intensities of the fine-structure components are as in *LS* coupling. The most recent N II effective recombination coefficients calculated by FSL11 are used when we derive the N^{2+}/H^+ abundances from the fine-structure components of each N II multiplet. The Case B recombination was assumed for the triplets and Case A for the singlets. An electron temperature of 1000 K and a density of 4300 cm^{-3} were assumed throughout the abundance determinations. Under such physical condition, the effective recombination coefficient for $H\beta$ adopted is $1.86 \times 10^{-13} \text{ cm}^3 \text{ s}^{-1}$, which is calculated from the hydrogenic theory of Storey & Hummer (1995).

The M3 $3p \ ^3D - 3s \ ^3P^{\circ}$ $\lambda 5680$ multiplet is the strongest N II permitted transition. At $T_e = 1000 \text{ K}$, the *LS* coupling effective recombination coefficient of N II M3 $\lambda 5680$ multiplet calculated by Kisielius & Storey (2002) is case-insensitive, with the Case B value being only 20 per cent higher than that for Case A. In the calculation of FSL11, the Case B effective recombination coefficient for the $\lambda 5679.56$ line, which is the strongest component of the N II M3 multiplet, is 27 per cent higher than in Case A. The Case B effective recombination coefficients for another two N II M3 lines, $\lambda \lambda 5666.63$ and 5676.02 , are higher than their corresponding Case A values by 28 and 24 per cent, respectively. The Case B coefficients of the other N II M3 lines are about 24 to 28 per cent higher than for Case A. In Table 13, the N^{2+}/H^+ abundance ratios derived from the N II M3 $\lambda 5680$ multiplet lines almost agree with the value derived from the total intensity of this multiplet. The N II singlet line $3p \ ^1D - 3s \ ^1P^{\circ}$ $\lambda 3995$ is case-insensitive, with its Case B effective recombination coefficient being only 3.6 per cent higher than for Case A. The calculation of FSL11 shows that the Case B effective recombination coefficient for the $\lambda 3995$ line is higher than the Case A value by about 5 per cent at 1000 K.

The M5 $3p \ ^3P - 3s \ ^3P^{\circ}$, M20 $3d \ ^3D^{\circ} - 3p \ ^3D$, M28 $3d \ ^3D^{\circ} - 3p \ ^3P$ and M29 $3d \ ^3P^{\circ} - 3p \ ^3P$ multiplets of N II are all case-insensitive. The Case B effective recombination coefficient for the M5 $3p \ ^3P - 3s \ ^3P^{\circ}$ $\lambda 4623$ multiplet calculated by Kisielius & Storey (2002) is higher than in Case A by a factor of 9. FSL11 shows that the Case B effective recombination coefficient for the $\lambda 4630.54$ line, which is the strongest component of the N II M5 multiplet, is higher than for Case A by a factor of 8. The Case B effective recombination coefficients for another two N II M5 lines, $\lambda \lambda 4601.48$ and 4621.39 , are 8–9 per cent higher than in Case A. For the weakest lines in the N II M5 multiplet (the $\lambda \lambda 4607.16$, 4613.87 and 4643.09 lines), their Case B effective recombination coefficients do not differ much from the Case A values. In Table 13, the N^{2+}/H^+ abundance ratios derived from the N II M5 components in the Case B assumption agree with those yielded by the case-insensitive N II M3 $\lambda 5680$ lines, which signifies Case B is a better assumption for the N II M5 multiplet.

Kisielius & Storey 2002 shows that the Case B effective recombination coefficients for the N II M20 $3d \ ^3D^{\circ} - 3p \ ^3D$ $\lambda 4794$, M28 $3d \ ^3D^{\circ} - 3p \ ^3P$ $\lambda 5939$ and M29 $3d \ ^3P^{\circ} - 3p \ ^3P$ $\lambda 5479$ multiplets are higher than those for Case A by a factor of 52, 51 and 25, respectively. FSL11 reveals that the Case B effective recombination coefficients for the strongest fine-structure components in the above three multiplets are 48, 49 and 16 times higher than those for Case A, at a given temperature of 1000 K. Given such large differences between the two cases, the N^{2+}/H^+ abundance ratios derived from the three N II multiplets (Table 13) suggest that Case B is a better assumption for the $3-3$ transitions of N II.

N^{2+}/H^+ abundances are also derived from the $4f-3d$ transitions, which are case-insensitive. The Case B effective recombination coefficient for M39b $4fG[9/2]_5 - 3d \ ^3F_4^{\circ}$ $\lambda 4041.31$, the strongest $4f-3d$ transition of N II, differs from the Case A value by only 0.25 per cent (FSL11). The N^{2+}/H^+ abundance derived from the $\lambda 4041.31$ line agrees well with that from N II M39a $4fG[7/2]_4 - 3d \ ^3F_3^{\circ}$ $\lambda 4043.53$. Most of the other N II $4f-3d$ transitions in Table 13 yield abundances close to those from the $\lambda \lambda 4041.31$ and 4043.53 lines, except for M39b $4fG[9/2]_4 - 3d \ ^3F_4^{\circ}$ $\lambda 4039.35$, which gives an abnormally high abundance value. We attribute this to the large measurement error due to weakness of this line. N II M58a $4fG[7/2]_4 - 3d \ ^1F_3^{\circ}$ $\lambda 4552.53$ also yields a relatively high abundance value, which could be due to the blended Si III M2 $4p \ ^3P_2^{\circ} - 4s \ ^3S_1$ $\lambda 4552.62$ and Ne II M55d $4f2[2]_{5/2}^{\circ} - 3d \ ^4F_{3/2}$

λ4553.17 lines. The intensity of the N II M61a 4fD[5/2]₂ – 3d¹P₁^o λ4694.64 line is probably overestimated due to unknown blend, which can be noticed from the profile of the feature. The three lines λλ4039.35, 4552.53 and 4694.64 are excluded from calculating the total intensity and the average abundance ratio. The N²⁺/H⁺ abundances derived from the λλ4041.31, 4043.53 lines agree with those from the N II M3 λλ5666.63, 5679.56 lines. The N II M3 λ5676.02 line yields a relatively high abundance. Measurements of this line could be unreliable due to the blended λ5679.56 line, which is 4 times stronger (Fig. 28). The relatively low S/N's at this wavelength region also affect the measurements.

It has been known for decades that the N II permitted lines from the low-lying 3d–3p and 3p–3s triplet arrays, whose upper levels are linked to the ground term 2p²3P by resonance lines, can be enhanced by fluorescence excitation. Grandi (1976) used photoionization models to study the excitation mechanisms of permitted transitions from common heavy element ions observed in the spectra of the Orion nebula and PNe NGC 7027 and NGC 7662, and found that while the N II M28 3d³D^o – 3p³P λ5942 multiplet is excited by both recombination and continuum fluorescence of the starlight, emission of the N II M3 3p³D – 3s³P^o λ5680, M5 3p³P – 3s³P^o λ4630 and M30 4s³P^o – 3p³P λ3838 multiplets are dominated by fluorescence excitation of the N II 4s³P₁^o level by the He I 1s8p¹p₁^o – 1s²1S₀ λ508.643 resonance line, which coincides in wavelength with the N II 2p4s³P₁^o – 2p²3P₀ λ508.668 line. Fluorescence excitation, by line or continuum, however, cannot excite the singlet transitions or transitions from the 3d–4f configuration. Escalante & Morisset (2005) analyzed the N II spectrum of the Orion nebula by using nebular and stellar atmosphere models. Their modeling shows that the intensity of most of the N II permitted lines in Orion could be explained by fluorescence of the starlight continuum. Recombination of N²⁺ contributes a minor part of the observed intensities of lines from the 3p and 3d levels connected to the ground state. They confined the effective temperature of the ionizing star to be lower than 38 000 K in order to reproduce the observed line intensities. Our current analysis shows that the N²⁺/H⁺ abundances derived from the 3p–3s transitions agree with those derived from the 4f–3d recombination lines (the values in boldface in Table 13), which are unlikely to be affected by the fluorescence mechanisms. That indicates fluorescence excitation of the N II 3p–3s lines, albeit may still exist, is probably insignificant in NGC 7009. Fluorescence enhancement of the N II lines by starlight could also be negligible, given the physical condition of NGC 7009 (C. Morisset, private communication). However, physical parameters, e.g., UV radiation field of the central star, optical depth of the resonance transition that connect the ground state 2p²3P and an excited state (e.g. 2p4s³P^o), column densities of N⁺ and N²⁺ ions, etc., are needed in order to estimate the enhancement of the N II lines due to resonance fluorescence by starlight or by other emission lines. That means consistent modeling of the central star and nebula is needed.

The average N²⁺/H⁺ abundance from the 3–3 transitions is 3.70 × 10^{−4}, which agrees with the average value (3.71 × 10^{−4}) from the 4f–3d transitions. Here the N II transitions (e.g. M29) that yield abnormally high abundances are excluded from averaging. The N²⁺/H⁺ abundance derived by co-adding the line intensities of the 4f–3d transitions is 3.42 × 10^{−4}, which agrees well with the abundance calculated from the total intensity of the M3 multiplet of N II (the values in boldface in Table 13). The abundances derived from total intensities of the 4f–3d transitions are preferred over the average values of abundances from individual lines, since strong lines are better detected with smaller (relative) flux uncertainties.

We adopt the mean value (3.45 × 10^{−4}) derived by averaging the abundances from the M3 multiplet and the total intensity of the 4f–3d transitions as the recombination line N²⁺/H⁺ abundance of NGC 7009. This value is about 10 per cent higher than 3.10 × 10^{−4} (slit position angle PA = 45°) given by LSBC, who used the N II M39b λ4041.31 and M39a λ4043.53 lines to derive the N²⁺/H⁺ abundance of NGC 7009.

4.1.4 O²⁺/H⁺ abundances from ORLs

In the spectrum of NGC 7009, O II has the most abundant optical recombination spectrum amongst all the heavy element ions detected. The most prominent multiplets of the O II transitions are presented in Section 3.3 and C. The spectrum analyzed in the current paper covers very broad wavelength range (3040–11 100 Å) and is among the deepest CCD spectra ever taken for an emission line nebula, and also has higher quality than that published by LSBC. In the wavelength ranges 3040–4048 Å and 3990–4980 Å, where the most prominent recombination lines of O II are located, our data quality is as good as that of Liu et al. (2000) for PN NGC 6153, which was observed using the same instruments mounted on the ESO 1.5 m telescope. The O²⁺/H⁺ abundance ratios derived from the O II ORLs with the most reliable measurements are presented in Tables 14 (the 3d–3p and 3p–3s transitions) and 15 (the 4f–3d transitions). The Case B effective recombination coefficients of O II calculated by PJS are adopted for the abundance determinations. An electron temperature of 1000 K is assumed. For purpose of comparison, the effective recombination coefficients of Storey (1994) for the 3p–3s transitions, and LSBC for the 3d–3p and 4f–3d transitions, are also used. Case B is assumed for the quartet transitions, and Case A for the doublets. An electron temperature of 5000 K is assumed when using the data of Storey (1994), whose calculation is valid from 5000 to 20 000 K. Since the calculation of Storey (1994) is only spectral term-resolved, we deduce the effective recombination coefficients for each fine-structure component of a multiplet with the assumption that their relative intensities are as in the LS coupling. As in the case of the N II lines (Section 4.1.3), for each multiplet in Table 14, we calculate the abundance value using the co-added intensities from all fine-structure components observed; for the O II 4f–3d transitions in Table 15, we also calculate the abundance after co-adding the intensities of all detected lines.

The O II M1 3p⁴D^o – 3s⁴P λ4650 multiplet is case-insensitive. At 5000 K, the Case B effective recombination coefficient of the M1 λ4650 multiplet given by Storey (1994) is only 3.4 per cent higher than for Case A. Péquignot, Petitjean & Boisson (1991) shows that the difference between the effective radiative recombination coefficients in the two cases for this multiplet is 2.5 per cent. The most recent calculation of PJS reveals that the difference between the effective recombination coefficients in the two cases for the strongest O II M1 line λ4649.13 is less than 5 per cent. The coefficients in the two cases for the other O II M1 fine-structure lines are of similar order. The O²⁺/H⁺ abundances derived from the individual O II M1 lines agree with each other, except for λλ4638.86 and 4673.73, which yield very high abundance values. The average O²⁺/H⁺ from O II M1 is 16.2 × 10^{−4}, which agrees well with the values derived from the recombination coefficients of Péquignot, Petitjean & Boisson (1991) and Storey (1994). The current measurements of the multiplet also agrees with LSBC, who gives 15.3 × 10^{−4} (PA = 0°) and 13.5 × 10^{−4} (PA = 45°).

Of the seven observed 3d–3p multiplets in Table 14, the intensities of those from the upper terms 2p²3d 4F and 2p²3d 4D are

Table 13. Recombination line N^{2+}/H^+ abundances. Intensities are normalized such that $H\beta = 100$. The N II effective recombination coefficients of FSL11 and Kisielius & Storey (2002, KS02) are both used for purpose of comparison.

Line (Å)	Mult.	I_{obs}	N^{2+}/H^+ ($\times 10^{-4}$)	
			FSL11	KS02
3 – 3 transitions				
$\lambda 5666.63$	M3	0.064	3.442	
$\lambda 5676.02$	M3	0.036	4.075	
$\lambda 5679.56$	M3	0.130	3.319	
$\lambda 5686.21$	M3	0.024	4.695	
$\lambda 5710.77$	M3	0.020	2.886	
M3 $3p^3D - 3s^3P^o$		0.280	3.482	3.358
$\lambda 4601.48$	M5	0.016	3.087	
$\lambda 4621.39^a$	M5	0.020	4.423	
$\lambda 4630.54$	M5	0.067	3.549	
M5 $3p^3P - 3s^3P^o$		0.102	3.598	2.242
$\lambda 3994.99$	M12	0.033	6.655	
M12 $3p^1D - 3s^1P^o$		0.033	6.655	6.776
$\lambda 4803.29$	M20	0.032	2.723	
M20 $3d^3D^o - 3p^3D$		0.078	4.412	3.464
$\lambda 5941.65^b$	M28	0.030	1.795	
M28 $3d^3D^o - 3p^3P$		0.063	3.038	2.119
$\lambda 5480.06^c$	M29	0.012	9.409	
M29 $3d^3P^o - 3p^3P$		0.061	14.949	7.590
Average			3.695	
4f – 3d transitions				
$\lambda 4035.08$	M39a	0.035	2.926	
$\lambda 4041.31^d$	M39b	0.081	3.174	
$\lambda 4043.53$	M39a	0.035	3.168	
$\lambda 4171.61$	M43b	0.023	3.033	
$\lambda 4176.16$	M43a	0.021	3.739	
$\lambda 4236.91^e$	M48a	0.036	3.727	
$\lambda 4241.78^f$	M48a	0.093	3.689	
$\lambda 4179.67$	M50a	0.010	3.508	
$\lambda 4432.74$	M55a	0.036	3.089	
$\lambda 4442.02$	M55a	0.011	3.204	
$\lambda 4552.53^g$	M58a	0.032	6.381	
$\lambda 4530.41$	M58b	0.046	3.792	
$\lambda 4678.14$	M61b	0.012	3.049	
$\lambda 4694.64$	M61a	0.020	5.393	
Sum		0.466	3.419	
Average			3.705	

^a Including O II M92c lines $4fF[2]_{5/2}^o - 3d^2D_{5/2}$ $\lambda 4621.27$. Neglecting O II M92c $4fF[2]_{3/2}^o - 3d^2D_{5/2}$ $\lambda 4622.14$.

^b Neglecting the N II M28 $3d^3D_1^o - 3p^3P_1$ $\lambda 5940.24$ line, which contributes less than 1 per cent to the total intensity.

^c Including N II M29 $3d^3P_2^o - 3p^3P_1$ $\lambda 5478.10$.

^d Corrected for the contribution from the O II M50c $4fF[2]_{5/2}^o - 3d^4F_{5/2}$ $\lambda 4041.28$ line (7 per cent).

^e Corrected for the contribution from the N II M48b $4fF[7/2]_3 - 3d^3D_2^o$ $\lambda 4237.05$ line (~ 30 per cent).

^f Including N II M48b $4fF[7/2]_4 - 3d^3D_3^o$ $\lambda 4241.78$.

^g Including the contribution from the Ne II M55d $4f2[2]_{5/2}^o - 3d^4F_{3/2}$ $\lambda 4553.17$ line. Neglecting Ne II M55d $4f2[2]_{3/2}^o - 3d^4F_{3/2}$ $\lambda 4553.40$.

almost independent of the assumption of Case A or Case B. The M2 $3p^4P^o - 3s^4P$ $\lambda 4341$, M6 $3p^2P^o - 3s^2P$ $\lambda 3967$, M10 $3d^4F - 3p^4D^o$ $\lambda 4075$, M12 $3d^4D - 3p^4D^o$ $\lambda 3867$, M20 $3d^4D - 3p^4P^o$ $\lambda 4111$ and M26 $3d^2D - 3p^2D^o$ $\lambda 4385$ multiplets of O II are case-insensitive, with their Case B or Case C⁵ effective recombination coefficients being 2.3–30 per cent higher than those for Case A (Storey 1994). The O^{2+}/H^+ abundance ratios derived from the M1 and M2 multiplets agree with those derived from the $3d-3p$ and $4f-3d$ transitions, while in LSBC and Liu et al. (2000) for NGC 6153, the abundances from those two multiplets are lower by about 40 per cent and a factor of 2, respectively. For Case C to apply to the doublets, it requires transitions to the $2p^3^2D^o$ state of the ground configuration to be optically thick, which is unlikely in the physical condition of NGC 7009. Thus the doublets (e.g. the M5 $3p^2D^o - 3s^2P$ $\lambda 4418$, M6 $3p^2P^o - 3s^2P$ $\lambda 3967$ and M25 $3d^2F - 3p^2D^o$ $\lambda 4704$ multiplets) can be regarded as case-insensitive. The M11 $3d^4P - 3p^4D^o$ $\lambda 3903$, M19 $3d^4P - 3p^4P^o$ $\lambda 4152$ and M28 $3d^4P - 3p^4S^o$ $\lambda 4913$ multiplets, which have the same upper term that can decay to the $2p^3^4S^o$ ground state of O II via resonance transitions, are expected to be very case-sensitive: their Case B effective recombination coefficients are more than 20 times higher than the Case A values.

Table 14 shows that in our current analysis, the O^{2+}/H^+ abundance ratios derived from the quartets M10, M12 and M20, all case-insensitive, are systematically higher than those derived from the case-sensitive multiplets M19 and M28, a phenomenon discovered by Liu et al. (2000) for NGC 6153. As pointed out by Liu et al. (2000), it is possible that there is a small departure from the assumed Case B towards Case A, which would increase the derived abundances for the multiplets that decay from the $2p^23d^4P$ upper term. The three doublets presented in Table 14 all yield abundance values that are consistent with those derived from the case-insensitive quartets (M10, M12 and M20), except for the M6 doublets, which yield systematically higher abundances. The O II M28 lines yield relatively lower abundance ratios, indicating that Case B might not be a good approximation for this multiplet. The O^{2+}/H^+ abundance ratios derived from the $\lambda 4132.80$ and $\lambda 4153.30$ line of the M19 multiplet of O II are obviously lower than the other O II multiplets. The observed $\lambda 4156.53$ line of M19 is too strong compared to other components of this multiplet, with the derived abundance value being higher than those deduced from other multiplets by nearly a factor of two. That was also observed in NGC 6153 (Liu et al. 2000) and by LSBC for the same object. No convincing candidates for lines which might be blended with the O II M19 $\lambda 4156.53$ line, and thus cause the discrepancy, were found by LSBC. In NGC 7009, the intensity ratio of the $\lambda 4156.53$ ($J = 3/2 - 5/2$) and $\lambda 4132.80$ ($J = 3/2 - 1/2$) lines of M19, which decay from the same upper level, is 1.06, which is about a factor of two lower than the values of 1.7 (slit position PA = 0°) and 2.1 (PA = 45°) found for the same object by LSBC, but agrees with the values of 0.6 (for the minor axis) and 1.1 (for the whole nebula) given by Liu et al. (2000) for NGC 6153. The $\lambda 4132.80$ line detected in our spectrum of NGC 7009 has an FWHM of 1.85 Å, which is broader than the $\lambda 4156.53$ line (FWHM ~ 1.60 Å). Such a line width of the $\lambda 4132.80$ line might be contributed by line blending, which results in a line ratio that is lower than the previous measurements. Be-

⁵ Defined with reference to the O II recombination spectrum. In Case B, lines terminating on the $2p^3^4S^o$ term are assumed to be optically thick and no radiative decays are permitted to this state. In Case C, radiative decays to both the $2p^3^4S^o$ and $2D^o$ terms are excluded.

sides, different data quality might also contribute to the discrepancy between LSBC and our current measurements. For the $\lambda 4156.53$ line, we still do not know which feature it is blended with.

In general, the O^{2+}/H^+ abundance ratios deduced using the Case B effective recombination coefficients of PJS are lower than those deduced using the radiative recombination coefficients of LSBC, by 30–50 per cent for the 3d–3p transitions, and by 20–30 per cent for most of the 4f–3d transitions. The O^{2+}/H^+ abundance ratios calculated, by co-adding the line intensities of each multiplet of the 3p–3s configuration, using the effective recombination coefficients of PJS, do not differ much from those deduced using the coefficients of Storey (1994). However, the abundances deduced from each fine-structure components of the 3p–3s multiplets, using the effective recombination coefficients of PJS, are systematically lower than those deduced using the coefficients of Storey (1994). This difference is more obvious for the two doublets M5 and M6, with the abundances deduced based on the coefficients of PJS being lower by about 10 per cent. If we use the Case A effective recombination coefficients of Storey (1994), the derived abundances will be lower than those deduced using the data of PJS by a factor of 7. The 4f–3d transitions are essentially case-insensitive, and the O^{2+}/H^+ abundance ratios derived from those lines using the data of PJS agree well. The abundance value calculated by co-adding the 4f–3d line intensities in Table 14 is 1.330×10^{-3} , which agrees with the average value (1.403×10^{-3}) of the 3–3 transitions. The mean O^{2+}/H^+ abundance ratios derived by averaging the values from all 3–3 multiplets (excluding the values that are abnormally high) plus the co-added 4f–3d transitions is 1.417×10^{-3} , which is slightly lower than the recombination line abundances given by LSBC: $17.0 \pm 1.0 \times 10^{-4}$ (PA = 45°) and $17.6 \pm 1.7 \times 10^{-4}$ (PA = 0°). This value is adopted as the recombination line O^{2+}/H^+ abundance in NGC 7009.

4.1.5 Ne^{2+}/H^+ abundances from ORLs

Tables 16 and 17 present the recombination line Ne^{2+}/H^+ abundances derived from the 3–3 and 4f–3d transitions, respectively. For the 3d–3p and 3p–3s transitions, the effective recombination coefficients calculated in the LS coupling assumption by Kisielius et al. (1998) are adopted. Case A is assumed for the quartet transitions and Case B for the doublets. The calculation of Kisielius et al. (1998) is valid from 1000 to 20 000 K, and four density cases, 10^2 , 10^4 , 10^5 and 10^6 cm^{-3} , were calculated. We assumed an electron density of 10^4 cm^{-3} and a temperature of 1000 K in the abundance determinations. For purpose of comparison, also presented in Tables 16 and 17 are the recombination line Ne^{2+}/H^+ abundances derived by LLB01, who used the same CCD spectrum as analyzed in the current paper but assumed an electron temperature of 7100 K, as derived from the Balmer discontinuity. In general, the Ne^{2+}/H^+ abundance ratios derived from the 3d–3p and 3p–3s transitions in the current work are lower than those given by LLB01. This is mainly due to the different temperatures adopted. For the 4f–3d transitions, the abundances derived by us are systematically lower than those given by LLB01 by about 13 per cent, except the strongest lines of this transition array, e.g. $\lambda 4391.99$ (M55e 4f 2[5] $_{11/2}^\circ$ –3d $^4F_{9/2}$) and $\lambda 4409.30$ (M55e 4f 2[5] $_{9/2}^\circ$ –3d $^4F_{7/2}$), which yield close Ne^{2+}/H^+ abundance ratios from the two analyses. The difference between the abundances given by the two analyses are partially contributed by the different extinctions used: The logarithmic extinction at $H\beta$, $c(H\beta)$, derived by LLB01 is 0.07, while ours is 0.174 (Paper I).

Table 14. Recombination line O^{2+}/H^+ abundances derived from the 3–3 transitions. Intensities are normalized such that $I(H\beta) = 100$. The effective recombination coefficients of Storey (1994) (for the 3p–3s transitions) and LSBC (for the 3d–3p and 4f–3d transitions) are also used for purpose of comparison.

Line (Å)	Mult.	I_{obs}	O^{2+}/H^+ ($\times 10^{-4}$)	
			PJS	LSBC
$\lambda 4638.86$	M1	0.335	25.002	33.581
$\lambda 4641.81$	M1	0.437	14.549	17.355
$\lambda 4649.13$	M1	0.666	13.677	13.886
$\lambda 4650.84$	M1	0.175	12.731	17.542
$\lambda 4661.63$	M1	0.217	14.490	16.946
$\lambda 4673.73$	M1	0.052	21.607	25.815
$\lambda 4676.24$	M1	0.158	15.125	14.642
$\lambda 4696.35$	M1	0.015	13.528	12.510
M1 3p $^4D^\circ$ – 3s 4P		2.056	15.241	17.369
$\lambda 4317.14$	M2	0.091	12.821	12.383
$\lambda 4319.63$	M2	0.063	14.010	7.938
$\lambda 4325.76$	M2	0.029	17.471	19.731
$\lambda 4336.86$	M2	0.053	18.008	22.536
$\lambda 4345.56$	M2	0.141	15.455	19.187
$\lambda 4349.43$	M2	0.195	15.876	10.530
$\lambda 4366.89$	M2	0.085	11.471	10.710
M2 3p $^4P^\circ$ – 3s 4P		0.657	14.589	12.577
$\lambda 4414.90$	M5	0.100	19.665	22.885
$\lambda 4416.97$	M5	0.064	17.370	26.363
$\lambda 4452.37$	M5	0.014	20.859	28.835
M5 3p $^2D^\circ$ – 3s 2P		0.178	18.855	24.440
$\lambda 3945.04$	M6	0.026	56.459	61.094
$\lambda 3954.36$	M6	0.030	31.310	35.245
$\lambda 3973.26$	M6	0.065	27.719	30.546
$\lambda 3982.71$	M6	0.010	20.411	23.497
M6 3p $^2P^\circ$ – 3s 2P		0.131	30.785	29.451
$\lambda 4069.89^a$	M10	0.635	16.777	23.914
$\lambda 4072.16^b$	M10	0.549	17.051	20.461
$\lambda 4075.86$	M10	0.687	16.687	19.241
$\lambda 4078.84$	M10	0.089	15.899	11.811
$\lambda 4085.11$	M10	0.107	16.746	23.176
$\lambda 4092.93^c$	M10	0.077	17.567	22.941
M10 3d 4F – 3p $^4D^\circ$		2.144	16.732	20.841
$\lambda 3907.45$	M11	0.010	16.364	9.291
M11 3d 4P – 3p $^4D^\circ$		0.026 ^d	15.861	8.411
$\lambda 3842.82$	M12	0.015	12.406	28.465
$\lambda 3851.03$	M12	0.017	12.351	19.397
$\lambda 3882.19^e$	M12	0.053	14.929	14.462
M12 3d 4D – 3p $^4D^\circ$		0.099	13.877	10.972
$\lambda 4129.32$	M19	0.032	21.489	45.444
$\lambda 4132.80$	M19	0.078	9.736	13.237
$\lambda 4140.70^f$	M19	0.003	45.123	23.923
$\lambda 4153.30$	M19	0.112	9.596	13.302
$\lambda 4156.53^g$	M19	0.079	35.714	59.101
$\lambda 4169.22$	M19	0.082	17.892	28.689
M19 3d 4P – 3p $^4P^\circ$		0.386	13.760	17.267
$\lambda 4110.79$	M20	0.025	14.198	9.655
M20 3d 4D – 3p $^4P^\circ$		0.259 ^d	14.162	10.973

Table 14. Continued.

Line (Å)	Mult.	I_{obs}	$\text{O}^{2+}/\text{H}^{+}$ ($\times 10^{-4}$)	
			PJS	LSBC
$\lambda 4699.22$	M25	0.024	25.809	33.771
$\lambda 4705.35$	M25	0.021	16.924	17.753
M25 3d $^2\text{F} - 3\text{p } ^2\text{D}^{\circ}$		0.046^h	20.735	24.293
$\lambda 4890.86$	M28	0.013	6.360	10.377
$\lambda 4906.83$	M28	0.046	10.907	17.114
$\lambda 4924.53$	M28	0.074	10.609	16.190
M28 3d $^4\text{P} - 3\text{p } ^4\text{S}^{\circ}$		0.133	10.049	15.311
Average			14.032	21.896

^a Including the O II M10 3d $^4\text{F}_{3/2} - 3\text{p } ^4\text{D}_{1/2}^{\circ}$ $\lambda 4069.62$ line.

^b Corrected for the contribution from the O II M48a 4f $\text{G}[5]_{9/2}^{\circ} - 3\text{d } ^4\text{F}_{7/2}$ $\lambda 4071.23$ line (~ 10 per cent). Neglecting the N II M38b 4f $\text{G}[7/2]_3 - 3\text{d } ^3\text{F}_2^{\circ}$ $\lambda 4073.05$ line (~ 2 per cent).

^c Overestimated due to N III M1 3p $^2\text{P}_{3/2}^{\circ} - 3\text{s } ^2\text{S}_{1/2}$ $\lambda 4097.33$ line which is more than 20 times stronger.

^d Assuming the relative intensities of this multiplet are the predicted values based on the effective recombination coefficients of PJS.

^e Corrected for the contribution from the O II M11 3d $^4\text{P}_{3/2} - 3\text{p } ^4\text{D}_{3/2}^{\circ}$ $\lambda 3882.45$ line (~ 17 per cent). Neglecting the O II M12 3d $^4\text{D}_{5/2} - 3\text{p } ^4\text{D}_{7/2}^{\circ}$ $\lambda 3883.13$ line (~ 2 per cent).

^f Overestimated due to the much stronger He I M53 6d $^1\text{D}_2 - 2\text{p } ^1\text{P}_1^{\circ}$ $\lambda 4143.76$ line.

^g Neglecting the N II M50b 4f $\text{D}[3/2]_2 - 3\text{d } ^3\text{D}_1^{\circ}$ $\lambda 4156.39$ and the N II M50b 4f $\text{D}[2]_1 - 3\text{d } ^3\text{D}_1^{\circ}$ $\lambda 4157.01$ lines (~ 4 per cent in total).

^h Not including the O II M25 3d $^2\text{F}_{5/2} - 3\text{p } ^2\text{D}_{5/2}^{\circ}$ $\lambda 4741.71$ line.

The Ne II M21 3d $^2\text{D}_{5/2} - 3\text{p } ^2\text{D}_{5/2}^{\circ}$ $\lambda 3416.91$ line yields relatively higher abundance, probably due to a blend of the Ne II M19 3d $^4\text{F}_{7/2} - 3\text{p } ^2\text{D}_{5/2}^{\circ}$ $\lambda 3417.69$ line. The nearby O III Bowen fluorescence line M15 3d $^3\text{P}_1^{\circ} - 3\text{p } ^3\text{P}_1$ $\lambda 3415.26$ also affects the measurement of the $\lambda 3416.91$ line (Fig. 40). The Ne II lines of the M9 3p $^2\text{F}^{\circ} - 3\text{s } ^2\text{D}$ multiplet, $\lambda 3568.50$ and 3574.61 are detected in the spectrum of NGC 7009 (Fig. 37). The $\text{Ne}^{2+}/\text{H}^{+}$ abundance derived from this multiplet is much higher than yielded by other multiplets. Similar results are also observed by LLB01 and in another two PNe, M 1-42 and M 2-36 (Liu et al. 2001b). LLB01 pointed out that the high abundance yielded by M9 is possibly due to the underestimated effective recombination coefficients for this multiplet. The 3p $^4\text{D}_{5/2}^{\circ} - 3\text{s } ^4\text{P}_{3/2}$ $\lambda 3355.02$ line of multiplet M2 is blended with the He I M8 7p $^1\text{P}_1^{\circ} - 2\text{s } ^1\text{S}_0$ $\lambda 3354.55$ line, and is also partially blended with the [Cl III] 3p $^3\text{P}_{1/2}^{\circ} - 3\text{p } ^3\text{S}_{3/2}$ $\lambda 3353.17$ line, as shown in Fig. D1. The intensity of the [Cl III] line was obtained from line fitting with two Gaussian profiles. The intensity contribution from the He I line was corrected for, as LLB01 did, using the observed intensity of the He I M6 5p $^1\text{P}_1^{\circ} - 2\text{s } ^1\text{S}_0$ $\lambda 3613.64$ line, assuming the line ratio $I(\lambda 3354.55)/I(\lambda 3613.64) = 0.35$ (in Case B assumption), as predicted by Brocklehurst (1972). Here an electron temperature of 5000 K, as derived from the He I line ratios (Paper I), and a density of $10\,000\text{ cm}^{-3}$ were assumed. The correction for the He I line amounts to 26 per cent, close to the result of LLB01 (30 per cent). The reason that we use the He I $\lambda 3613.64$ line, instead of the He I M48 4d $^1\text{D}_2 - 2\text{p } ^1\text{P}_1^{\circ}$ $\lambda 4921.93$ line, to correct for the intensity contribution from the He I $\lambda 3354.55$ line is that given the small wavelength span between the $\lambda 3354.55$, 3613.64 lines,

Table 15. Recombination line $\text{O}^{2+}/\text{H}^{+}$ abundances from the 4f–3d transitions. Intensities are normalized such that $I(\text{H}\beta) = 100$. The O II effective recombination coefficients of LSBC are also used for purpose of comparison.

Line (Å)	Mult.	I_{obs}	$\text{O}^{2+}/\text{H}^{+}$ ($\times 10^{-4}$)	
			PJS	LSBC
$\lambda 4089.29^a$	M48a	0.264	12.901	15.308
$\lambda 4083.90$	M48b	0.094	13.310	19.077
$\lambda 4087.15^b$	M48c	0.091	13.675	19.461
$\lambda 4062.94^c$	M50a	0.036	13.975	16.592
$\lambda 4048.21^d$	M50b	0.021	14.363	19.236
$\lambda 4303.83^e$	M53a	0.120	13.844	16.847
$\lambda 4294.78^f$	M53b	0.067	13.025	16.756
$\lambda 4307.23$	M53b	0.029	12.415	16.053
$\lambda 4288.82^g$	M53c	0.026	17.477	15.659
$\lambda 4282.96^h$	M67c	0.063	17.615	23.690
$\lambda 4466.42^i$	M86b	0.032	12.247	20.368
$\lambda 4489.49$	M86b	0.022	12.958	19.542
$\lambda 4491.23$	M86a	0.057	14.606	24.119
$\lambda 4609.44^j$	M92a	0.128	13.969	17.309
$\lambda 4602.13^k$	M92b	0.052	12.938	17.628
sum		1.103	13.303	17.556
Average			13.955	18.510

^a Corrected for the contribution from Si IV M1 4p $^2\text{P}_{3/2}^{\circ} - 4\text{s } ^2\text{S}_{1/2}$ $\lambda 4088.86$, which is about 15 per cent. Neglecting O II M48a 4f $\text{G}[5]_{9/2}^{\circ} - 3\text{d } ^4\text{F}_{9/2}$ $\lambda 4088.27$ (less than 2 per cent).

^b Neglecting N II M38a 4f $\text{F}[5/2]_3 - 3\text{d } ^3\text{F}_3^{\circ}$ $\lambda 4087.30$ (about 3 per cent).

^c Including Ne II M53 4f $0[3]_{7/2}^{\circ} - 3\text{d } ^4\text{D}_{5/2}$ $\lambda 4062.97$.

^d Neglecting the contribution from O II M50b 4f $\text{F}[3]_{5/2}^{\circ} - 3\text{d } ^4\text{F}_{7/2}$ $\lambda 4047.80$, which is probably 7 per cent.

^e Corrected for the contribution from O II M65a 4f $\text{G}[5]_{9/2}^{\circ} - 3\text{d } ^4\text{D}_{7/2}$ $\lambda 4303.61$, which is about 20 per cent.

^f The contribution from O II M53b 4f $\text{D}[2]_{3/2}^{\circ} - 3\text{d } ^4\text{P}_{3/2}$ $\lambda 4294.92$ to the blend at $\lambda 4295$, which is estimated to be 28 per cent, has been subtracted.

^g A blend of O II M53c 4f $\text{D}[1]_{1/2}^{\circ} - 3\text{d } ^4\text{P}_{1/2}$ $\lambda 4288.82$ and O II M53c 4f $\text{D}[1]_{3/2}^{\circ} - 3\text{d } ^4\text{P}_{1/2}$ $\lambda 4288.82$.

^h Corrected for the contributions from O II M67c 4f $\text{F}[2]_{3/2}^{\circ} - 3\text{d } ^4\text{D}_{3/2}$ $\lambda 4283.73$ (about 35 per cent) and O II M67c 4f $\text{F}[2]_{5/2}^{\circ} - 3\text{d } ^4\text{D}_{5/2}$ $\lambda 4283.25$ (about 6 per cent). Neglecting O II M78a 4f $\text{F}[4]_{7/2}^{\circ} - 3\text{d } ^2\text{F}_{5/2}$ $\lambda 4282.02$ (less than 2 per cent). Including Ne II M57c 4f $1[3]_{7/2}^{\circ} - 3\text{d } ^4\text{F}_{7/2}$ $\lambda 4283.73$, whose contribution to the total intensity is unknown due to the lack of atomic data.

ⁱ Corrected for the contribution from O II M86b 4f $\text{D}[2]_{3/2}^{\circ} - 3\text{d } ^2\text{P}_{3/2}$ $\lambda 4466.59$, which is about 20 per cent.

^j Corrected for the contribution from O II M92c 4f $\text{F}[2]_{5/2}^{\circ} - 3\text{d } ^2\text{D}_{3/2}$ $\lambda 4610.20$, which is about 20 per cent.

^k Corrected for the contribution from N II M5 3p $^3\text{P}_2 - 3\text{s } ^3\text{P}_1^{\circ}$ $\lambda 4601.48$, which is about 25 per cent.

measurements of their intensity ratio are much less sensitive to any uncertainties in reddening corrections and flux calibration.

The Ne II 4f–3d recombination lines in Table 17 are those whose preliminary effective recombination coefficients are available (P. J. Storey, private communication). The $\text{Ne}^{2+}/\text{H}^{+}$ abundances derived from the 4f–3d transitions are systematically higher than those derived from the 3–3 transitions by about 50

per cent. The difference between the abundances derived from the 3–3 and 4f–3d transitions is mainly due to the inadequacy of the Ne II effective recombination coefficients. The average $\text{Ne}^{2+}/\text{H}^+$ abundance from the 4f–3d transitions is 8.5×10^{-4} , about 0.15 dex higher than the average value deduced from the individual lines of the 3–3 transition array. Here the two abnormally high abundances yielded by the Ne II M52b $\lambda 4250.65$ ($4f 2[3]_{5/2}^{\circ} - 3d^4 D_{3/2}$) and M61d $\lambda 4457.05$ ($4f 2[2]_{5/2}^{\circ} - 3d^2 D_{3/2}$) lines are excluded from averaging. We adopt the abundance value 8.42×10^{-4} , which is calculated by co-adding the intensities of the 4f–3d transitions, as the recombination line $\text{Ne}^{2+}/\text{H}^+$ abundance of NGC 7009. The two Ne II lines $\lambda 4250.65$ and $\lambda 4457.05$ that yield abnormally high abundances are excluded from the abundance calculation.

4.1.6 ORL abundances of other ions

Table 18 presents the recombination line C^{3+}/H^+ , C^{4+}/H^+ , N^{3+}/H^+ , O^{3+}/H^+ , and O^{4+}/H^+ abundances. The C^{3+}/H^+ abundance ratios are derived from the M1 $\lambda 4650$, M16 $\lambda 4069$ and M18 $\lambda 4187$ multiplets. The abundances from the three multiplets agree with each other, and the adopted C^{3+}/H^+ ratio in NGC 7009 is an average from them. The C^{4+}/H^+ abundance ratio 2.20×10^{-5} is derived from the C IV M8 $\lambda 4658$ line, which is slightly contaminated by [Fe III] $\lambda 4658$. This abundance agrees with those given by LSBC: 0.239×10^{-4} (PA = 45°) and 0.182×10^{-4} (PA = 0°).

The N^{3+}/H^+ abundance ratio is derived from N III M18 $\lambda 4379$. The N III M17 lines, $\lambda 3998.63$ and $4003.58, 72$ are observed, but only the effective dielectronic recombination coefficients for this multiplet are available (Nussbaumer & Storey 1984). If we adopt the dielectronic data, the derived N^{3+}/H^+ abundance from the M17 multiplet will be more than one order of magnitude higher than that from the N III M18 $\lambda 4379$ line (Table 18). This indicates that the excitation of the N II M17 lines is probably dominated by radiative recombination. We adopt the N^{3+}/H^+ ratio (1.31×10^{-4}) derived from the N II M18 $\lambda 4379$ line as the abundance in NGC 7009. This N^{3+}/H^+ abundance agrees with those given by LSBC who also used the $\lambda 4379$ line: 1.34×10^{-4} (PA = 45°) and 1.71×10^{-4} (PA = 0°). We observed the N III M1 and M2 lines, which are excited by the secondary Bowen fluorescence mechanism. Also detected in the spectra of NGC 7009 are the N III transitions with the $^3\text{P}^\circ$ parentage: M3 $3p' 4D - 3s' 4P^\circ$, M6 $3p' 2D - 3s' 2P^\circ$ and M9 $3d' 4F^\circ - 3p' 4D$. Analyses of these lines are in Section 3.6.

Some strong O III lines from the 3–3 arrays are excited by the fluorescence mechanism or radiative charge-transfer reaction of O^{3+} and H^0 (Liu & Danziger 1993a; Liu, Danziger & Murrin 1993). The O III M14 $3d^3 D^\circ - 3p^3 P$ $\lambda 3713$ lines cannot be excited by fluorescence or charge-transfer reaction, but is likely to be excited only by recombination and therefore a useful abundance indicator for O^{3+}/H^+ . Unfortunately, no recombination coefficients are available for this multiplet. The O III M8 $3d^3 F^\circ - 3p^3 D$ $\lambda 3265$ lines originate from radiative and dielectronic recombination (Liu & Danziger (1993a)), and the effective dielectronic and radiative recombination coefficients for this multiplet are available from Nussbaumer & Storey (1984) and Péquignot, Petitjean & Boisson (1991), respectively. Thus the O^{3+}/H^+ abundances are derived from two of the O III M8 lines $\lambda 3260.85$ and 3265.32 , which are observed in NGC 7009 (Fig. 39). Another M8 line $\lambda 3267.20$ is blended with the $\lambda 3265.32$ line, which is expected to be the strongest in M8, but its contribution is probably negligi-

Table 16. Recombination line $\text{Ne}^{2+}/\text{H}^+$ abundances derived from the 3–3 transitions. Intensities are normalized such that $I(\text{H}\beta) = 100$. The abundances of LLB01 are presented for purpose of comparison.

Line (Å)	Mult.	I_{obs}	$\text{Ne}^{2+}/\text{H}^+$ ($\times 10^{-4}$)	
			Current	LLB01
$\lambda 3694.21$	M1	0.254	7.932	8.97
$\lambda 3709.62$	M1	0.105	8.290	8.49
$\lambda 3777.14$	M1	0.048	3.859	3.54
M1 $3p^4 P^\circ - 3s^4 P$		0.686	7.544	7.45
$\lambda 3334.84$	M2	0.414	5.847	5.14
$\lambda 3344.40$	M2	0.129	8.805	
$\lambda 3355.02^a$	M2	0.195	5.278	5.89
M2 $3p^4 D^\circ - 3s^4 P$		1.035	5.850	5.39
$\lambda 3713.08$	M5	0.297	6.141	
M5 $3p^2 D^\circ - 3s^2 P$		0.495	6.141	
$\lambda 3481.93$	M6	0.043	4.795	5.52
M6 $3p^2 S^\circ - 3s^2 P$		0.066	4.795	5.52
$\lambda 3047.56$	M8	0.120	7.720	
M8 $3d^4 D - 3p^4 P^\circ$		0.571	7.692	
$\lambda 3329.16$	M12	0.051		7.67
$\lambda 3357.82$	M12	0.020		
$\lambda 3362.94$	M12	0.026		
$\lambda 3374.06$	M12	0.014		
$\lambda 3390.55$	M12	0.016		
M12 $3d^4 D - 3p^4 D^\circ$		0.149	8.051	7.67
$\lambda 3218.19$	M13	0.227	4.836	5.45
$\lambda 3244.09$	M13	0.072	2.253	2.02
M13 $3d^4 F - 3p^4 D^\circ$		0.636	4.840	3.68
$\lambda 3367.22$	M20	0.102	2.820	3.38
M20 $3d^2 F - 3p^2 D^\circ$		0.179	2.832	3.38
$\lambda 3416.91^b$	M21	0.075	11.818	13.00
$\lambda 3453.07$	M21	0.018	4.448	4.25
M21 $3d^2 D - 3p^2 D^\circ$		0.050	3.529	4.25
$\lambda 3542.85$	M34	0.030		2.89
$\lambda 3565.82$	M34	0.024		
$\lambda 3594.16$	M34	0.011		
M34 $3d^4 P - 3p^4 S^\circ$		0.065	3.006	3.05
$\lambda 3568.50$	M9	0.168		
$\lambda 3574.61^c$	M9	0.053		
M9 $3p' 2F^\circ - 3s' 2D$		0.221	36.125	
Average			6.040	

^a Corrected for the contribution from the He I M8 $7p^1 P_1^\circ - 2s^1 S_0$ $\lambda 3354.55$ line.

^b Probably overestimated due to Ne II M19 $3d^4 F_{7/2} - 3p^2 D_{5/2}^\circ$ $\lambda 3417.69$. Excluded from calculating the average $\text{Ne}^{2+}/\text{H}^+$ abundance ratio.

^c Including the Ne II M9 $3p' 2F_{5/2}^\circ - 3s' 2D_{5/2}$ $\lambda 3574.18$ line.

Table 17. Recombination line $\text{Ne}^{2+}/\text{H}^+$ abundances from the $4f-3d$ transitions. Intensities are normalized such that $I(\text{H}\beta) = 100$. The abundances of LLB01 are presented for purpose of comparison.

Line (Å)	Mult.	I_{obs}	$\text{Ne}^{2+}/\text{H}^+$ ($\times 10^{-4}$)	
			Current	LLB01
$\lambda 4391.99^a$	M55e	0.072	7.451	7.53
$\lambda 4409.30$	M55e	0.058	9.039	9.80
$\lambda 4219.75^b$	M52a	0.049	9.135	12.60
$\lambda 4233.85$	M52a	0.011	8.230	11.40
$\lambda 4231.64$	M52b	0.009	7.084	19.20
$\lambda 4250.65^c$	M52b	0.016	18.853	19.90
$\lambda 4397.99$	M57b	0.024	7.174	6.56
$\lambda 4379.55^d$	M60b	0.050	8.367	
$\lambda 4428.64^e$	M60c	0.037	8.775	11.50
$\lambda 4430.94^f$	M61a	0.025	9.158	12.10
$\lambda 4457.05^{c,g}$	M61d	0.026	27.305	26.30
$\lambda 4413.22^h$	M65	0.021	9.099	12.90
$\lambda 4421.39$	M66c	0.008	9.723	
Sum		0.364^i	8.425	9.93
Average			8.476	9.77

^a Neglecting the contribution from Ne II M55e $4f2[5]_{9/2}^o-3d^4F_{9/2}$ $\lambda 4392.00$.

^b Neglecting the contribution from Ne II M52a $4f2[4]_{7/2}^o-3d^4D_{7/2}$ $\lambda 4219.37$.

^c Not included in calculating the total intensity or the average abundance value.

^d Neglecting the contribution from Ne II M60b $4f1[4]_{7/2}^o-3d^2F_{7/2}$ $\lambda 4379.40$.

^e Neglecting the contribution from Ne II M60c $4f1[3]_{5/2}^o-3d^2F_{5/2}$ $\lambda 4428.52$.

^f The contribution from Ne II M57a $4f1[2]_{5/2}^o-3d^4F_{3/2}$ $\lambda 4430.90$, which is about 30 per cent, has been subtracted. The contribution from Ne II M57a $4f1[2]_{3/2}^o-3d^4F_{3/2}$ $\lambda 4431.11$ is negligible.

^g Including the contribution from the three Ne II lines, M66c $4f1[3]_{5/2}^o-3d^4P_{5/2}$ $\lambda 4457.24$, M61d $4f2[2]_{3/2}^o-3d^2D_{3/2}$ $\lambda 4457.24$ and M66c $4f1[3]_{7/2}^o-3d^4P_{5/2}$ $\lambda 4457.36$.

^h Including the contribution from Ne II M57c $4f1[3]_{5/2}^o-3d^4F_{3/2}$ $\lambda 4413.11$. Neglecting Ne II M65 $4f0[3]_{5/2}^o-3d^4P_{5/2}$ $\lambda 4413.11$.

ⁱ Excluding Ne II M52b $4f2[3]_{5/2}^o-3d^4D_{3/2}$ $\lambda 4250.65$ and Ne II M61d $4f2[2]_{5/2}^o-3d^2D_{3/2}$ $\lambda 4457.05$.

ble. The O^{3+}/H^+ abundance ratio derived from O III M8 is about 6.6×10^{-5} (Table 18).

A very faint O IV line M2 $3d^2D_{5/2}-3p^2P_{3/2}$ $\lambda 3411.69$ is also observed to partially blended with O III M15 $\lambda 3415.26$ (Fig. 40). Another M2 line $\lambda 3413.64$ is blended in between. The other line $\lambda 3403.52$ is blended with O III M15 $\lambda 3405.71$ (Fig. 40), and its accurate measurements are difficult. Multi-Gaussian profile fits give an intensity of 0.0514 for the $\lambda 3411.69$ line, and 0.0567 for the $\lambda 3413.64$ line, both have an uncertainty of more than 20 per cent (Table 7 in Paper I). The intensity ratio of the two lines differ from the pure LS coupling ratio, i.e. 9 : 1. We use $\lambda 3411.69$ to derive the O^{4+}/H^+ abundance ratio because its measurement is probably more reliable. Here the effective radiative and dielectronic recombination coefficients from Péquignot, Petitjean & Boisson (1991) and Nussbaumer & Storey (1984), respectively, are used.

The adopted C, N, O and Ne ionic abundances from optical re-

Table 18. Recombination line C^{3+}/H^+ , C^{4+}/H^+ , N^{3+}/H^+ , O^{3+}/H^+ , and O^{4+}/H^+ abundances. Intensities are normalized such that $I(\text{H}\beta) = 100$.

Line (Å)	Mult.	I_{obs}	C^{3+}/H^+ ($\times 10^{-4}$)
$\lambda 4647.42$	M1	0.170	
$\lambda 4650.25$	M1	0.100	
$\lambda 4651.47$	M1	0.034	
M1 $3p^3P^o-3s^3S$		0.304	1.659
$\lambda 4067.94$	M16	0.071	
$\lambda 4068.91$	M16	0.093	
$\lambda 4070.26$	M16	0.120	
M16 $5g^3G-4f^3F^o$		0.284	1.472
M18 $5g^1G-4f^1F^o$	$\lambda 4186.90$	0.088	1.309
Wavelength (Å)	Mult.	I_{obs}	C^{4+}/H^+ ($\times 10^{-4}$)
M8 $6h^2H^o-5g^2G$	$\lambda 4658.30^a$	0.147	0.220
Wavelength (Å)	Mult.	I_{obs}	N^{3+}/H^+ ($\times 10^{-4}$)
$\lambda 3998.63$	M17	0.025	
$\lambda 4003.58^b$	M17	0.040	
M17 $5f^2F^o-4d^2D$		0.065	12.390
M18 $5g^2G-4f^2F^o$	$\lambda 4379.11$	0.310	1.313
Wavelength (Å)	Mult.	I_{obs}	O^{3+}/H^+ ($\times 10^{-4}$)
$\lambda 3260.85$	M8	0.179	
$\lambda 3265.32$	M8	0.139	
M8 $3d^3F^o-3p^3D$		0.324	0.659
Wavelength (Å)	Mult.	I_{obs}	O^{4+}/H^+ ($\times 10^{-4}$)
$\lambda 3411.69^c$	M2	0.057	
M2 $3d^2D-3p^2P^o$		0.114	0.158

^a Including [Fe III] $\lambda 4658.05$.

^b Including N III M17 $\lambda 4003.72$ ($5f^2F_{5/2}^o-4d^2D_{5/2}$).

^c Could be of large uncertainty due to line blending.

combination lines are summarized in Table 19. They are mostly averaged from the abundance ratios that are calculated by co-adding the line intensities of individual multiplets (or transition arrays). Atomic data references used for the ORL analysis are listed in Table 21.

Several permitted lines emitted by silicon ions were observed or debled (Paper I). As the first and the second ionization potentials of atomic silicon are 8.15 and 16.35 eV, respectively, we expect that the main ionization stages of silicon are doubly and triply ionized, while the amount of Si^+ is assumed to be negligible and Si^{4+} should exist but is of much lower abundance compared to Si^{2+} and Si^{3+} .

The $\text{Si}^{3+}/\text{H}^+$ abundance ratios derived from Si III M2 and M5 lines are presented in Table 20. The Si IV M1 $\lambda 4116.10$ line is also observed (Fig. C5), which means that $\lambda 4088.86$ of the same multiplet should also exist. Since only the effective dielectronic recombination coefficients for a few selected Si III transitions are available

Table 19. Adopted recombination line abundances for the C, N, O, and Ne ions.

Ion	Abundances	
	($\times 10^{-4}$)	$\log[X^{i+}/H^+]+12$
C ²⁺ /H ⁺	6.865	8.796
C ³⁺ /H ⁺	1.480	8.170
C ⁴⁺ /H ⁺	0.220	7.342
N ²⁺ /H ⁺	3.450	8.538
N ³⁺ /H ⁺	1.313	8.118
O ²⁺ /H ⁺	14.176	9.152
O ³⁺ /H ⁺	0.659	7.819
O ⁴⁺ /H ⁺	0.158	7.198
Ne ²⁺ /H ⁺	8.425	8.926

Table 20. Recombination line Si³⁺/H⁺ and Mg²⁺/H⁺ abundances. Intensities are normalized such that $I(H\beta) = 100$.

Line (Å)	Mult.	I_{obs}	Si ³⁺ /H ⁺ ($\times 10^{-5}$)
λ4552.62	M2	0.0175	
λ4567.82	M2	0.0114	
λ4574.76	M2	0.0041	
M2 4p³P^o – 4s³S		0.0325	0.770
λ3806.54	M5	0.022	
M5 4d³D – 4p³P^o		0.0396	0.438
Wavelength (Å)	Mult.	I_{obs}	Mg ²⁺ /H ⁺ ($\times 10^{-5}$)
λ4481.20 ^a	M4	0.0303	
M4 4f²F^o – 3d²D		0.0309	3.179

^a We assume that the Mg II 4f–3d λ4481 line has an effective recombination coefficient equal to that of the C II 4f–3d λ4267 line, given the similarity between the atomic structure of Mg II and C II.

from Nussbaumer & Storey (1986), we only present the Si³⁺/H⁺ abundance ratios. The averaged Si³⁺/H⁺ ratio is 6.04×10^{-6} .

The Mg II M4 λ4481 line is observed (Fig. 35), and the Mg²⁺/H⁺ abundance derived is presented in Table 20. Since the ionization potentials of neutral Mg⁰ and Mg²⁺ are 7.65 and 80.14 eV, respectively, we assume that magnesium in NGC 7009 is mainly doubly ionized. Unfortunately no effective recombination coefficients for Mg II lines are available. Given the similarity between the atomic structure of Mg II and C II, we assumed that the effective recombination coefficient of the Mg II M4 4f²F^o – 3d²D λ4481 line is equal to, or at least is close to, that of the C II M6 4f²F^o – 3d²D λ4267 transition. The effective recombination coefficient (in Case B) for the C II λ4267 line is adopted from Bastin (2006), with the assumption of $T_e = 10\,000$ K and $N_e = 10\,000$ cm⁻³. The calculation of Davey, Storey & Kisielius (2000) differs from that of Bastin (2006) by 1.5 per cent for the C II λ4267 line. The Mg²⁺/H⁺ abundance derived from the λ4481 line is 3.18×10^{-5} .

4.2 Ionic abundances from CELs

4.2.1 Ionic abundances from the optical CELs

The ionic abundances derived from optical CELs detected in the spectrum of NGC 7009 are presented in Table 22. An electron tem-

perature of 10 000 K, which is an average from different CEL diagnostic ratios (Paper I), and a constant density of 4300 cm⁻³, an average derived from a variety of optical CEL ratios, are assumed throughout the abundance determinations. In addition to the ionic abundances of N, O and Ne, abundances are also derived for the ions of F, Mg, Si, S, Cl, Ar from the CELs detected in the spectrum of NGC 7009. The atomic data references used for CEL analysis are listed in Table 23.

4.2.2 Ionic abundances from the IR and UV CELs

NGC 7009 has been observed in wavelength range other than optical: the *IUE* Short Wavelength Prime (SWP) and Long Wavelength Redundant (LWR) observations by Perinotto & Benvenuti (1981), the *IRAS* Low Resolution Spectrometer (LRS) observations by Potasch et al. (1986), the *ISO* Short Wavelength Spectrometer (SWS) and Long Wavelength Spectrometer (LWS) observations by Liu et al. (2001a), and the Kuiper Airborne Observatory (*KAO*) observations by Rubin et al. (1997). Ionic abundances derived from ten near- to far-infrared lines and seven ultraviolet lines are presented in Table 24.

The dereddened and normalized intensities of three infrared lines, the [Ne II] 12.8 μm and the [Ne III] 15.5 and 36.0 μm, are adopted from LLB01. The Ne⁺/H⁺ abundance ratio is derived from the [Ne II] 12.8 μm line, assuming a temperature of 10 020 K and a density of 4300 cm⁻³. The derived Ne⁺/H⁺ ratio is 1.32×10^{-5} , which agrees with 1.38×10^{-5} given by LLB01, as is expected. The critical densities of the [Ne III] ³P₁ and ³P₀ levels are 2.1×10^5 and 3.1×10^4 cm⁻³ (at $T_e = 10\,000$ K; Osterbrock & Ferland 2006), respectively, much larger than the average electron density. The Ne²⁺/H⁺ abundance ratios deduced from the [Ne III] 15.5 and 36 μm lines are 1.67×10^{-4} and 1.48×10^{-4} , respectively. The two ratio values agree with each other within errors. We adopt a value of 1.65×10^{-4} , which is derived from the sum of the intensities of the two [Ne III] infrared (IR) fine-structure lines, as the Ne²⁺/H⁺ ratio in NGC 7009. It agrees with the value of 1.63×10^{-4} given by LLB01. An electron temperature of 9980 K and a density of 3930 cm⁻³ were assumed in LLB01.

The observed line fluxes, in units of erg cm⁻² s⁻¹, of the [N III] 57 μm and the [O III] 52 and 88 μm fine-structure lines are adopted from Liu et al. (2001a). These fluxes were normalized using the observed total Hβ flux, $10^{-9.63}$ erg cm⁻² s⁻¹. The extinction of the three IR lines, as pointed out by Liu et al. (2001a), should be negligible. Since the critical density of the [N III] ²P_{3/2} level is 1.5×10^3 cm⁻³, comparable to the density of NGC 7009, we have assumed a density of 1260 cm⁻³, deduced from the [O III] 52 μm/88 μm line ratio, in deriving the N²⁺/H⁺ abundance ratio from the [N III] 57 μm line. Here an electron temperature of 10 020 K is again assumed. The derived N²⁺/H⁺ ratio is 4.97×10^{-5} , in close agreement with 4.91×10^{-5} given by Liu et al. (2001a).

The O²⁺/H⁺ abundance ratios derived from the [O III] 52 and 88 μm lines are 2.79×10^{-4} and 2.76×10^{-4} , respectively. Here an electron temperature of 9800 K derived from the [O III] λ4959/λ4363 ratio, and a density of 1260 cm⁻³ derived from the [O III] 52 μm/88 μm ratio, were assumed. Given that the critical densities of the [O III] ³P₁ and ³P₂ fine-structure levels are 5.1×10^2 and 3.6×10^3 cm⁻³, respectively (Osterbrock & Ferland 2006), the density value of 1260 cm⁻³ for the O III IR-line abundances is appropriate. We adopt a value of 2.99×10^{-4} , which is derived from the sum of the two [O III] IR lines, as the O²⁺/H⁺

Table 21. References for the ORL atomic data.

ion	Effec.recomb. coefficients	ORLs	Comments
H I	Storey & Hummer (1995)		Case B
He I	Benjamin, Skillman & Smits (1999) Brocklehurst (1972)		Case B; singlets Case A; triplets
He II	Storey & Hummer (1995)		Case B
C I	Escalante & Victor (1990) Escalante & Victor (1990)		Case A; singlets Case B; triplets
C II	Davey, Storey & Kisielius (2000)		Case B
C III	Péquignot, Petitjean & Boisson (1991) Nussbaumer & Storey (1984)		Case A Dielectronic recombination
C IV	Péquignot, Petitjean & Boisson (1991)		Case A
N I	Péquignot, Petitjean & Boisson (1991) Péquignot, Petitjean & Boisson (1991)		Case A; doublets Case B; quartets
N II	FSL11		Case B
N III	Péquignot, Petitjean & Boisson (1991) Nussbaumer & Storey (1984)		Case A Dielectronic recombination
O I	Péquignot, Petitjean & Boisson (1991)		Case A
O II	P. J. Storey (PJS, private communication)		Case B
O III	Péquignot, Petitjean & Boisson (1991)		Case A
O IV	Péquignot, Petitjean & Boisson (1991) Nussbaumer & Storey (1984)		Case A Dielectronic recombination
Ne II	Kisielius et al. (1998) Storey (unpublished) Nussbaumer & Storey (1987)		Case B; doublets Case A; quartets Dielectronic recombination
Mg II	Davey, Storey & Kisielius (2000) ^a		Case B
Si II	Nussbaumer & Storey (1986)		Dielectronic recombination
Si III	Nussbaumer & Storey (1986)		Dielectronic recombination

^a Given the similarity between the atomic structure of Mg II and C II, we have assumed that the Mg II M4 4f ²F^o – 3d ²D λ 4481 line has an effective recombination coefficient equal to that of the C II M6 4f ²F^o – 3d ²D λ 4267 line (Zhang et al. 2005b).

abundance ratio in NGC 7009. This abundance ratio agrees well with the value of 2.96×10^{-4} given by Liu et al. (2001a).

The flux of the [O IV] 25.9 μ m line were estimated from the $F([\text{O IV}] 25.9\mu\text{m})/F([\text{S III}] 18.7\mu\text{m})$ flux ratio given by Rubin et al. (1997), who obtained far-IR observations of the PNe NGC 7009, NGC 7027 and NGC 6210 with the Kuiper Airborne Observatory (KAO). The *ISO* SWS observations by X.-W. Liu (unpublished) during the *ISO* Orbit #344 in 1996 gives the $F([\text{O IV}] 25.9\mu\text{m})/F([\text{S III}] 18.7\mu\text{m})$ ratio that differs from that of Rubin et al. (1997) by more than 30 per cent. The O⁴⁺/H⁺ abundance ratio derived from the above two observations are given in Table 24. Here the flux of the [S III] 18.7 μ m line was adopted from Pottasch et al. (1986).

The *IRAS* fluxes (in units of erg cm⁻² s⁻¹) of the [Ne V] 14.3 μ m, the [S III] 18.7 μ m and the [S IV] 10.52 μ m lines, as well as the total flux of H β , are adopted from Pottasch et al. (1986). The Ne⁴⁺/H⁺ abundance ratio derived from the [Ne V] 14.3 μ m line is 6.11×10^{-7} . Here an electron temperature of 10 020 K is assumed. The critical densities for the [Ne V] ³P₁ and ³P₂ fine-structure levels are 6.2×10^3 and 3.5×10^4 cm⁻³ (Osterbrock & Ferland 2006), respectively. Thus the electron density of 1260 cm⁻³ from the [O III] 52 μ m/88 μ m ratio is again assumed. If we adopt a density value of 4300 cm⁻³, the derived Ne⁴⁺/H⁺ abundance ratio slightly increases to 6.87×10^{-7} .

The S²⁺/H⁺ abundance ratio derived from the [S III] 18.7 μ m line is 8.36×10^{-7} . Here an electron temperature of 10 020 K and a density of 1260 cm⁻³ are assumed. Since the critical densities of the [S III] ³P₁ and ³P₂ fine-structure levels are 1.98×10^3 and

1.54×10^4 cm⁻³, respectively, a density of 1260 cm⁻³ is reasonable. If we increase the density value to 4300 cm⁻³, the S²⁺/H⁺ ratio derived then increases to 9.93×10^{-7} . The S³⁺/H⁺ abundance ratio derived from the [S IV] 10.52 μ m line is 7.34×10^{-6} . The same temperature is assumed.

The observed fluxes (in unit of erg cm⁻² s⁻¹) for the seven ultraviolet (UV) lines in Table 24 are adopted from Perinotto & Benvenuti (1981). The fluxes are normalized using their H β flux, which should be multiplied by a factor 0.48, the fraction of the H β flux entering into the *IUE* slot in position of SWP and LWR images. Using the logarithmic reddening constant $c(\text{H}\beta) = 0.174$ derived in Paper I and the extinction curve of Howarth (1983), we derived the dereddened intensities of those UV lines. The ionic abundances are presented in Table 24. Here an electron temperature of 10 020 K and a density of 4300 cm⁻³ are assumed in the abundance calculations.

4.3 Comparison of the ORL and CEL abundances

4.3.1 Ionic abundances

In Fig. 41, the ionic abundances of C, N, O and Ne derived from ORLs are compared with the corresponding values derived from the optical, UV and far-IR CELs. Here the ionic abundances of C, N, O and Ne derived from ORLs are from Table 19, and the ionic abundances derived from CELs are from Tables 22 (optical) and 24 (UV and IR). The IR fine-structure line fluxes are adopted from the recent *ISO* observations (Liu et al. 2001a). We also make use

Table 22. Ionic abundances derived from optical CELs. Line intensities are normalized such that $I(H\beta) = 100$.

Ions	Lines Lines (Å)	I_{obs}	X^{i+}/H^+	Abundances	
				X^{i+}/H^+	$\log[X^{i+}/H^+]+12$
[C I]	$\lambda\lambda 9824.13, 9850.26$	0.035	C^0/H^+	8.483×10^{-9}	3.929
[N I]	$\lambda\lambda 5197.90, 5200.26$	0.091	N^0/H^+	8.435×10^{-8}	4.926
[O I]	$\lambda\lambda 6300.30, 6363.78$	0.740	O^0/H^+	8.395×10^{-7}	5.924
[N II]	$\lambda 5754.64$	0.390	N^+/H^+	2.876×10^{-6}	6.459
[N II]	$\lambda\lambda 6548.04, 6583.46$	20.600	N^+/H^+	2.725×10^{-6}	6.435
[O II]	$\lambda\lambda 3726.03, 3728.81$	19.971	O^+/H^+	8.779×10^{-6}	6.943
[O II]	$\lambda\lambda 7319.99, 7330.73$	2.300	O^+/H^+	1.996×10^{-5}	7.300
[O III]	$\lambda 4363.21$	7.300	O^{2+}/H^+	2.435×10^{-4}	8.387
[O III]	$\lambda 4931.23$	0.120	O^{2+}/H^+	2.455×10^{-4}	8.390
[O III]	$\lambda\lambda 4958.91, 5006.84$	1550.753	O^{2+}/H^+	3.231×10^{-4}	8.509
[F II]	$\lambda 4789.45$	0.017	F^+/F^+	2.579×10^{-8}	4.411
[F IV]	$\lambda 4059.90$	0.012	F^{3+}/F^+	4.387×10^{-9}	3.642
[Ne III]	$\lambda 3342.50$	0.755	Ne^{2+}/H^+	3.079×10^{-4}	8.488
[Ne III]	$\lambda\lambda 3868.76$	118.837	Ne^{2+}/H^+	1.296×10^{-4}	7.928
[Ne III]	$\lambda 4012.01$	0.014	Ne^{2+}/H^+	2.161×10^{-4}	8.335
[Ne IV]	$\lambda\lambda 4724.17, 4725.67$	0.042	Ne^{3+}/H^+	1.501×10^{-5}	7.176
[Ne IV]	$\lambda\lambda 4714.17, 4715.66$	0.067	Ne^{3+}/H^+	3.845×10^{-5}	7.585
[S II]	$\lambda\lambda 4068.60, 4076.35$	0.960	S^+/H^+	1.085×10^{-7}	5.035
[S II]	$\lambda\lambda 6716.44, 6730.82$	3.700	S^+/H^+	1.192×10^{-7}	5.076
[S III]	$\lambda 3721.69$	1.045	S^{2+}/H^+	2.781×10^{-6}	6.444
[S III]	$\lambda 6312.10$	1.400	S^{2+}/H^+	2.265×10^{-6}	6.355
[S III]	$\lambda\lambda 9068.60, 9530.60$	64.000	S^{2+}/H^+	1.965×10^{-6}	6.293
[Cl II]	$\lambda 6161.84$	0.006	Cl^+/H^+	3.434×10^{-8}	4.536
[Cl II]	$\lambda\lambda 8578.69, 9123.60$	0.075	Cl^+/H^+	4.994×10^{-9}	3.698
[Cl III]	$\lambda 3353.17$	0.076	Cl^{2+}/H^+	1.388×10^{-7}	5.142
[Cl III]	$\lambda\lambda 5517.72, 5537.89$	1.000	Cl^{2+}/H^+	5.513×10^{-8}	4.741
[Cl III]	$\lambda 8480.85$	0.020	Cl^{2+}/H^+	8.319×10^{-8}	4.920
[Cl IV]	$\lambda 5323.28$	0.012	Cl^{3+}/H^+	2.525×10^{-8}	4.402
[Cl IV]	$\lambda\lambda 7530.80, 8045.63$	0.990	Cl^{3+}/H^+	5.475×10^{-8}	4.738
[Ar III]	$\lambda 3109.17$	0.175	Ar^{2+}/H^+	5.956×10^{-7}	5.775
[Ar III]	$\lambda 5191.82$	0.100	Ar^{2+}/H^+	8.584×10^{-7}	5.934
[Ar III]	$\lambda\lambda 7135.80, 7751.10$	18.300	Ar^{2+}/H^+	1.027×10^{-6}	6.012
[Ar IV]	$\lambda\lambda 4711.37, 4740.17$	7.600	Ar^{3+}/H^+	5.592×10^{-7}	5.748
[Ar IV]	$\lambda\lambda 7237.40, 7262.76$	0.372	Ar^{3+}/H^+	2.713×10^{-6}	6.433
[Ar V]	$\lambda\lambda 6435.10, 7005.67$	0.065	Ar^{4+}/H^+	6.654×10^{-9}	3.823
[K IV]	$\lambda\lambda 6101.83, 6795.10$	0.196	K^{3+}/H^+	1.146×10^{-8}	4.059

of the IR line fluxes from observations of *IRAS* in the literature. The UV line fluxes from the *IUE* observations are dereddened using the extinction derived in Paper I, and they are used to derive ionic abundances for highly ionized heavy elemental ions. The recombination line C^{2+}/H^+ , N^{2+}/H^+ , O^{2+}/H^+ and Ne^{2+}/H^+ abundances are all higher than the abundance ratios derived from CELs by nearly a factor of 5 (i.e. $ADF \sim 5$), in agreement with what was observed by LSBC (for C, N and O) and LLB01 (for Ne). However, the ADF differs from 5 when the abundances derived from UV CELs are used: The N^{3+}/H^+ abundance derived from ORL is higher than the value derived from the N IV] $\lambda 1486$ UV line by a factor of 2. The recombination line O^{3+}/H^+ abundance is higher than the abundance derived from the O IV] $\lambda 1403$ UV line by only 65 per cent. This is probably mainly due to systematic difference in flux calibrations, given that the UV data are adopted from the early *IUE* observations of Perinotto & Benvenuti (1981). The ADF value of O^{3+} is close to 5 when the abundance derived from the [O IV] $25.9\mu\text{m}$ IR line is used.

4.3.2 Total elemental abundances

Elemental abundances derived from ORLs and CELs are compared in Table 25. Abundance errors (numbers in brackets) are estimated from measurement uncertainties, which is calculated by quadratically adding line flux errors from Gaussian profile fitting and the systematic uncertainties in line measurements e.g. subtraction of the continuum. Uncertainties introduced by ionization correction method, i.e. the ionization correction factors (*icf*'s), are not taken into account in error estimate. Also given in this table are the solar abundances from Asplund et al. (2009) and average abundances of the Galactic disc and bulge PNe from literature. The C/H, N/H, O/H and Ne/H elemental abundances derived from ORLs are higher than the corresponding values derived from CELs by a factor of 5.4, 6.9, 4.7 and 5.3, respectively. This result is similar to LSBC, who derived ADF values of 6.1, 4.1 and 4.7 for C, N and O respectively in NGC 7009. The Ne abundance discrepancy derived by LLB01 is about 4. In the analyses of LSBC, the elemental abundances of C and N derived from CELs were adopted from the earlier observations of Barker (1983), who first discussed the large discrepancy between the C^{2+}/H^+ abundances derived from the C II $\lambda 4267$ recombination line and from the UV CEL C III] $\lambda\lambda 1907, 1909$.

Table 23. References for the CEL atomic data.

ion	CELs	
	Transition probabilities	Collision strengths
C II	Nussbaumer & Storey (1981a)	Blum & Pradhan (1992)
C III	Keenan et al. (1992) Fleming et al. (1996)	Keenan et al. (1992)
C IV	Wiese et al. (1966)	Gau & Henry (1977)
N I	Zeippen (1982)	Berrington & Burke (1981)
N II	Nussbaumer & Rusca (1979)	Stafford et al. (1994)
O I	Baluja & Zeippen (1988)	Berrington (1988) Berrington & Burke (1981)
O II	Zeippen (1982)	Pradhan (1976)
O III	Nussbaumer & Storey (1981b)	Aggarwal (1983)
F II	Baluja & Zeippen (1988)	Butler & Zeippen (1994)
F IV	Fischer & Saha (1985)	Lennon & Burke (1994)
Ne II	Mendoza (1983)	Bayes et al. (1985)
Ne III	Mendoza (1983)	Butler & Zeippen (1994)
Ne IV	Zeippen (1982)	Giles (1981)
Ne V	Fischer & Saha (1985)	Lennon & Burke (1994)
S II	Mendoza & Zeippen (1982b) Keenan et al. (1993)	Keenan et al. (1996)
S III	Mendoza & Zeippen (1982a)	Mendoza (1983)
S IV	Storey (unpublished)	Saraph & Storey (1999)
Cl II	Mendoza (1983)	Mendoza (1983)
Cl III	Mendoza (1983)	Mendoza (1983)
Cl IV	Mendoza & Zeippen (1982b)	Butler & Zeippen (1989)
Ar II	Pelan & Berrington (1995)	Vujnovic & Wiese (1992)
Ar III	Mendoza & Zeippen (1983)	Johnson & Kingston (1990)
Ar IV	Mendoza & Zeippen (1982b)	Zeippen et al. (1987)
Ar V	Mendoza & Zeippen (1982a)	Mendoza (1983)
Fe III	Nahar & Pradhan (1996)	Zhang (1996)
Fe IV	Garstang (1958) Fischer & Rubin (2004)	Zhang & Pradhan (1997)
Fe V		Berrington (1995)
Fe VI	Nussbaumer & Storey (1978)	Nussbaumer & Storey (1978)
Fe VII	Nussbaumer & Storey (1982a)	Keenan & Norrington (1987) Berrington et al. (2000)

Whenever available, the ionization correction factors (*icf*'s) given by Kingsburg & Barlow (1994) were used. In Section 4.2.2, we have derived 16 ionic abundances from UV and IR data available from the literature (Table 24). These ionic abundances can be used as an aid to derive total elemental abundances. When they are not necessary, we can use them to check the elemental abundance values derived from *icf*'s, by adding these UV and IR abundances with the optical abundance ratios in Table 22 and compare with the ionization corrected total abundances.

The forbidden line O/H abundance ratio was calculated from the O^+/H^+ ratio derived from the [O II] $\lambda\lambda 3726$ and 3729 lines⁶ and the O^{2+}/H^+ ratio derived from the [O III] $\lambda\lambda 4959$ and 5007 lines, correcting for the unseen O^{3+} in optical using

$$\frac{O}{H} = icf(O) \times \left(\frac{O^+}{H^+} + \frac{O^{2+}}{H^+} \right) = \left[\frac{He^+ + He^{2+}}{He^+} \right]^{2/3} \times \left(\frac{O^+}{H^+} + \frac{O^{2+}}{H^+} \right). \quad (1)$$

From the He^+ and He^{2+} abundances given in Table 10, we have $icf(O) = 1.086$. Thus derived O/H ratio is 3.603×10^{-4} , close

to the value 3.716×10^{-4} , which is derived by combining the O ions from UV, IR and optical lines, $O/H = O^+/H^+ + O^{2+}/H^+ + O^{3+}/H^+$. Here the O^{3+}/H^+ is derived from the O IV] $\lambda 1403$ UV line (Section 4.2.2).

The recombination line abundance O^+/H^+ is not available, thus in order to make use of the above equation, we assume that the recombination line O^+/O^{2+} ratio is the same as that derived from the CELs. Given the small ionic concentration of O^+ (less than 10 per cent in NGC 7009), the errors introduced should be negligible. The O^{2+}/H^+ , O^{3+}/H^+ and O^{4+}/H^+ abundance ratios derived from ORLs are available from Table 19. The recombination line O/H abundance ratio thus derived is 1.667×10^{-3} .

Both C^{2+}/H^+ and C^{3+}/H^+ abundance ratios have been derived from ORLs and are presented in Table 19. The C^{4+}/H^+ abundance ratio has also been derived from the C IV M8 $\lambda 4658.30$ line, but probably is not acceptable because it blends with [Fe III] $\lambda 4658.05$. The unseen C^+/H^+ are corrected for using the equation of LSBC,

$$\frac{C}{H} = \frac{C^2 + C^3}{H^+} \times icf(C) \quad (2)$$

⁶ Recombination excitation of the [O II] $\lambda\lambda 3726$, 3729 doublet is neglected. Given the small ionic concentration of O^+ , compared to O^{2+} , the errors introduced to the total O/H elemental abundances deduced below, both from CELs and from ORLs, should be negligible.

and

Table 24. Ionic abundances derived from the UV and far-IR fine-structure CELs. Intensities are normalized such that $I(H\beta) = 100$.

Ions	Lines	I_{obs}	X^{i+}/H^+	$\log(X^{i+}/H^+)+12$	Ref.
IR Lines					
[N III]	57 μm	24.315	N^{2+}/H^+	4.974×10^{-5}	8.065 (1)
[O III]	52 μm	165.940	O^{2+}/H^+	2.792×10^{-4}	8.446 (1)
[O III]	88 μm	55.029	O^{2+}/H^+	2.762×10^{-4}	8.441 (1)
[O IV]	25.9 μm	20.29 ± 1.10	O^{3+}/H^+	1.275×10^{-5}	7.105 (2) ^a
[O IV]	25.9 μm	14.16 ± 0.76	O^{3+}/H^+	8.893×10^{-6}	6.950 (2) ^b
[Ne II]	12.8 μm	9.9 ± 3.0	Ne^+/H^+	1.322×10^{-5}	7.121 (3)
[Ne III]	15.5 μm	250 ± 12	Ne^+/H^+	1.667×10^{-4}	8.222 (3)
[Ne III]	36.0 μm	18.0 ± 1.8	Ne^{2+}/H^+	1.477×10^{-4}	8.169 (3)
[Ne V]	14.3 μm	8.696	Ne^{4+}/H^+	6.107×10^{-7}	5.786 (4)
[S III]	18.7 μm	7.826	S^{2+}/H^+	8.356×10^{-7}	5.922 (4)
[S IV]	10.52 μm	230.434	S^{3+}/H^+	7.342×10^{-6}	6.866 (4)
UV Lines (\AA)					
C II]	$\lambda 2326$	3.821	C^+/H^+	4.555×10^{-6}	5.629 (5)
C III]	$\lambda 1908$	44.832	C^{2+}/H^+	1.308×10^{-4}	8.117 (5)
N III]	$\lambda 1751$	6.959	N^{2+}/H^+	5.535×10^{-5}	7.743 (5)
N IV]	$\lambda 1486$	6.197	N^{3+}/H^+	6.151×10^{-5}	7.789 (5)
O III]	$\lambda 1663$	4.313	O^{2+}/H^+	2.387×10^{-4}	8.378 (5)
O IV]	$\lambda 1403$	0.705	O^{3+}/H^+	3.977×10^{-5}	7.600 (5)
[Ne IV]	$\lambda 2424$	7.789	Ne^{3+}/H^+	1.895×10^{-5}	7.278 (5)

(1) The observed flux is from Liu et al. (2001a).

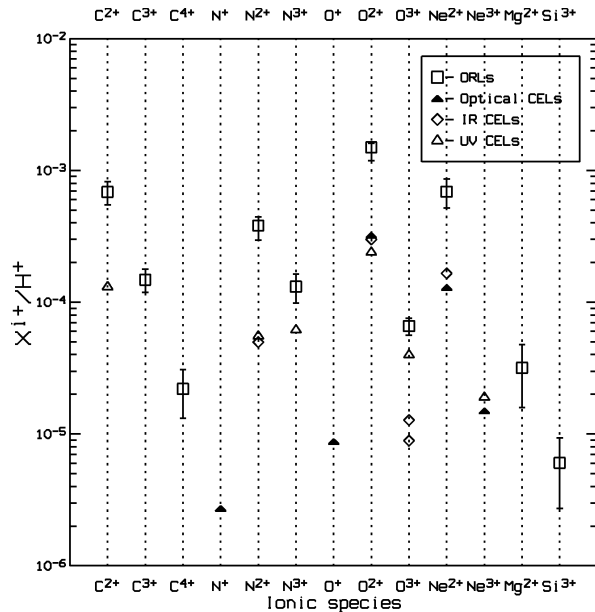
(2)^a The observed flux is estimated from the flux ratio $F([O\text{ IV}] 25.9\mu\text{m})/F([S\text{ III}] 18.7\mu\text{m})$ adopted from the ISO/LWS observations during ISO #344 Orbit in 1996 (Liu et al., unpublished), using the [S III] 18.7 μm flux adopted from Pottasch et al. (1986).

(2)^b The observed flux is estimated from the flux ratio $F([O\text{ IV}] 25.9\mu\text{m})/F([S\text{ III}] 18.7\mu\text{m})$ adopted from the KAO observations of Rubin et al. (1997), using the [S III] 18.7 μm flux adopted from Pottasch et al. (1986).

(3) The observed flux is from LLB01.

(4) The observed flux is from Pottasch et al. (1986).

(5) The observed flux is from Perinotto & Benvenuti (1981).


Figure 41. Comparison of the ionic abundances derived from ORLs and the optical, UV and IR CELs. Error bars on the ORL abundances are from the propagation calculations of the ORL measurement errors.

$$icf(C) = \left[\frac{He^+ + He^{2+}}{He^+} \right]^{1/3} \times \left[\frac{O^+ + O^{2+}}{O^{2+}} \right]. \quad (3)$$

The ionic abundances of O^+ and O^{2+} in the above equation are assumed to be those derived from the forbidden line measurements. In NGC 7009, most of the carbon should exist in the form of C^{2+} and C^{3+} , and the correction required for unobserved C^+ and C^{4+} is quite small. The Equation 3 gives $icf(C) = 1.07$. Thus derived recombination line C/H abundance ratio is 8.932×10^{-4} , which is only 3 per cent lower than the value given by LSBC.

For the collisionally excited lines, C^+/H^+ and C^{2+}/H^+ are derived from UV lines (Table 24). We assume $C^{3+}/C^{2+} = 0.216$, as given by the ORL abundance ratios. Thus the CEL ratio of carbon is $C/H = C^+/H^+ + C^{2+}/H^+ + C^{3+}/H^+$, which is 1.636×10^{-4} .

Recombination line abundances are available for the N^{2+}/H^+ and N^{3+}/H^+ ratios (Table 19) but not for N^+/H^+ . The latter is available from the collisionally excited [N II] $\lambda\lambda 6548$ and 6584 lines. The N^{2+}/H^+ ratio derived from the UV collisionally excited N III] $\lambda 1751$ line is about 10 per cent higher than that deduced from the [N III] 57 μm far-IR fine-structure line (Table 24). Given the weakness of the $\lambda 1751$ and the relative new observations of the 75 μm line, we adopt the N^{2+}/H^+ abundance ratio derived from the far-IR line. N^{2+}/H^+ from the 57 μm and N^+/H^+ from the $\lambda\lambda 6548$ and 6584 lines yield $N^+/N^{2+} = 0.0548$. We assume that this is also valid for corresponding abundances derived from ORLs. The N IV

optical recombination lines are not clearly detected in the spectrum of NGC 7009, but we detected the O IV M2 3d ²D – 3p ²P^o λ 3412 line, and the O⁴⁺/H⁺ abundance ratio is derived from it (Table 18). Given the ionization potential of N³⁺ (77.472 eV) is the same to that of O³⁺ (77.4 eV), we assume N⁴⁺/N = O⁴⁺/O. Thus the total recombination line N/H abundance is given by

$$\frac{N}{H} = (1.0548 \times \frac{N^{2+}}{H^+} + \frac{N^{3+}}{H^+}) / (1 - \frac{O^{4+}}{O}). \quad (4)$$

To obtain the forbidden-line N/H abundance, we correct for the unseen N³⁺/H⁺ assuming N³⁺/N²⁺ = 0.380, as given by ORLs. so that

$$\frac{N}{H} = \frac{N^+}{H^+} + 1.380 \times \frac{N^{2+}}{H^+}. \quad (5)$$

The total CEL N/H abundance thus derived is 7.01×10^{-5} . Here the N⁴⁺/H⁺ is neglected, given its very low abundance, if we assume that the N⁴⁺/N²⁺ ratio from CELs is the same as that given by the ORL values. If we take into account the N³⁺/H⁺ abundance ratio derived from the UV N IV] λ 1486 line (Table 24), the total CEL abundance ratio is then N/H = N⁺/H⁺ + N²⁺/H⁺ + N³⁺/H⁺ = 1.140×10^{-4} , which is 64 per cent higher than the value derived by the ionization correction Equation 5. Since the recent IR data should be more reliable, we adopt the ratio derived from Equation 5.

Ne⁺/H⁺, Ne²⁺/H⁺ and Ne³⁺/H⁺ ionic abundances are available from IR (Table 24) and optical CELs (Table 22). For the Ne²⁺/H⁺ ratio, we adopt the abundance derived from the [Ne III] λ 3868⁷ optical line, which is only about 21 per cent lower than that derived from the ISO SWS observation of the [Ne III] 15.5+36 μ m IR fine-structure lines. For the Ne³⁺/H⁺ ratio, we adopt the value derived from the [Ne IV] λ 4724.17 and 4725.67 optical lines. From the IUE observation by Perinotto & Benvenuti (1981), we also derived the Ne³⁺/H⁺ abundance ratio from their observed Ne IV] λ 2422 and 2424 lines (Table 24), which is 26 per cent higher than that from optical. Thus the CEL Ne/H ratio obtained from the equation

$$\frac{Ne}{H} = \frac{Ne^+}{H^+} + \frac{Ne^{2+}}{H^+} + \frac{Ne^{3+}}{H^+} \quad (6)$$

is 1.578×10^{-4} (Table 25). This is only 9 per cent lower than the Ne/H ratio derived by LLB01.

Only the Ne²⁺/H⁺ ratio is available from ORLs. The Ne⁺/Ne²⁺ ratio from CELs is 0.102, with and Ne³⁺/Ne²⁺ from optical CELs is 0.116. Assuming these ionization ratios from CELs are the same as given by ORLs, we obtain a recombination line Ne/H abundance ratio value of 8.398×10^{-4} by using

$$\frac{Ne}{H} = (0.102 + 1.0 + 0.116) \times \frac{Ne^{2+}}{H^+}. \quad (7)$$

This ratio value is 21 per cent higher than that given by LLB01.

CELs emitted by [F II] and [F IV] ions are detected, with the F⁺/H⁺ and F³⁺/H⁺ abundance ratios derived from the [F II] λ 4789 and [F IV] λ 4060 lines respectively (Table 22). O⁺ has ionization potential comparable to F⁺ and Ne³⁺ has that comparable

to F³⁺. Zhang & Liu (2005) suggested that F/O = F²⁺/O²⁺ for low-excitation PNe, and F/O = (F³⁺/Ne³⁺)(Ne/O) for high-excitation PNe. Here we adopt the assumption of Zhang & Liu (2005). Given that NGC 7009 is a medium excitation PN, we derive the Ne²⁺/H⁺ abundance ratio from the equation

$$\frac{F}{H} = (\frac{F^+}{H^+} + \frac{F^{3+}}{H^+}) / (1 - \frac{O^{2+}}{O}). \quad (8)$$

The derived F/H abundance ratio is 2.923×10^{-7} . The F⁴⁺/H⁺ should be negligible because the ionization potential of F³⁺ is 87 eV, which is too high. No recombination line from the fluorine ions are detected.

For the elements heavier than Ne, we detected CELs emitted by S, Cl, Ar and K ions (Table 22), and ORLs by Si and Mg ions (Table 20). Considering that the first ionization potential of silicon atom is only 8.2 eV, and the ionization potential of Si⁴⁺ is 166.8 eV, which is a huge jump from that of Si³⁺, 45 eV, we assume that the S⁺/H⁺ abundance is negligible, and the main ionization stages of Si in NGC 7009 are Si²⁺, Si³⁺ and Si⁴⁺. Several Si III multiplets and the Si IV multiplet V1 are detected from NGC 7009. Only effective dielectronic recombination coefficients for Si III multiplets are available from Nussbaumer & Storey (1984), thus only the S³⁺/H⁺ abundance ratio from S III ORLs is derived. The S³⁺/H⁺ ratio is derived from the Si III multiplets M2 4p ³P^o – 4s ³S and M5 4d ³D – 4p ³P^o (Table 20). Since the ionization potential of S⁺ (16.3 eV) is close to that of F (17.4 eV), and the ionization potential of Si³⁺ (45 eV) is comparable to that of N²⁺ (47.4 eV), we assume the relation: Si²⁺/Si = F⁺/F = O⁺/O, and Si⁴⁺/Si = N³⁺/N. Thus the total Si/H abundance ratio from ORLs can be derived from the equation

$$\frac{Si}{H} = \frac{Si^{3+}}{H^+} / (1 - \frac{O^+}{O} - \frac{N^{3+}}{N}) = \frac{Si^{3+}}{H^+} / (1 - \frac{F^+}{F} - \frac{N^{3+}}{N}). \quad (9)$$

The Si/H abundance ratio thus derived is 8.278×10^{-6} . In Equation 9, the O⁺/O ratio is from optical CELs, and the N³⁺/N ratio is from ORLs.

The Mg²⁺/H⁺ abundance ratio is derived from the Mg II M4 4f ²F^o – 3d ²D λ 4481 line. The ionization potentials of Mg⁰ and Mg²⁺ are 7.65 eV and 80.1 eV, respectively, thus we assume that magnesium in NGC 7009 are mainly doubly ionized, and Mg⁺ and Mg³⁺ are negligible. No effective recombination coefficients for Mg II lines are available. Given the similarity between the atomic structure of Mg II and C II, we assume that the Mg II λ 4481 line has an effective recombination coefficient equal to that of C II M6 λ 4267. Thus we have Mg/H = Mg²⁺/H⁺.

For S, we have S⁺/H⁺ derived from the [S II] λ 6716 and 6731 optical lines, S²⁺/H⁺ derived from the [S III] λ 6312 optical line. The S²⁺/H⁺ is also available from the [S III] 18.7 μ m IR line. S³⁺/H⁺ is derived from the [S IV] 10.5 μ m far-IR fine-structure line, which was adopted from the IRAS observations by Pottasch et al. (1986). We use the S²⁺/H⁺ ratio derived from the λ 6312 line. S⁴⁺ is not observed. Since S³⁺ has an ionization potential of 47.3 eV, very close to the value of 47.4 eV for N²⁺, we assume that S⁴⁺/S = N³⁺/N. The N³⁺/N ratio is from ORLs. Thus the S/H ratio is obtained from

$$\frac{S}{H} = (\frac{S^+}{H^+} + \frac{S^{2+}}{H^+} + \frac{S^{3+}}{H^+}) / (1 - \frac{N^{3+}}{N}). \quad (10)$$

The derived S/H ratio is 1.299×10^{-5} . If we adopt the S²⁺/H⁺ ratio derived from the [S III] 18.7 μ m IR line, then the S/H ratio is

⁷ Another [Ne III] nebular line λ 3967 is saturated in the higher resolution spectrum, and is not saturated but blended with the H I λ 3970 line in the low-resolution spectrum.

1.10×10^{-5} , about 15 per cent lower than the case when we adopt the optical value.

The Cl^+/H^+ , $\text{Cl}^{2+}/\text{H}^+$, and $\text{Cl}^{3+}/\text{H}^+$ abundances are derived from optical CELs (Table 22). Given that the ionization potential of Cl^{3+} (53.5 eV) is similar to that of He^+ (54.4 eV), and that the ionization potential of Cl^{4+} (67.7 eV) is comparable to that of Ne^{2+} (63.5 eV), we assumed $\text{Cl}^{4+}/\text{Cl} = \text{He}^{2+}/\text{He} = 0.013/0.112 = 0.116$ and $\text{Cl}^{5+}/\text{Cl} = \text{Ne}^{3+}/\text{Ne} = 0.095$. Here the Ne^{3+}/Ne ratio is from the CEL abundances. Thus the Cl/H abundance ratio can be obtained from the equation

$$\frac{\text{Cl}}{\text{H}} = \left(\frac{\text{Cl}^+}{\text{H}^+} + \frac{\text{Cl}^{2+}}{\text{H}^+} + \frac{\text{Cl}^{3+}}{\text{H}^+} \right) / \left(1 - \frac{\text{He}^{2+}}{\text{He}} - \frac{\text{Ne}^{3+}}{\text{Ne}} \right). \quad (11)$$

The derived total Cl/H abundance is 1.927×10^{-7} .

$\text{Ar}^{2+}/\text{H}^+$ is derived from the [Ar III] $\lambda\lambda 7136$ and 7751 lines, $\text{Ar}^{3+}/\text{H}^+$ is from [Ar IV] $\lambda\lambda 4711$ and 4740 , and $\text{Ar}^{4+}/\text{H}^+$ is from the [Ar V] $\lambda\lambda 6435$ and 7006 lines (Table 22). The unseen Ar^+ is corrected for assuming $\text{Ar}^+/\text{Ar} = \text{N}^+/\text{N}$, where the N^+/N is derived from optical CELs. The total Ar/H ratio can be obtained using

$$\frac{\text{Ar}}{\text{H}} = \left(\frac{\text{Ar}^{2+}}{\text{H}^+} + \frac{\text{Ar}^{3+}}{\text{H}^+} + \frac{\text{Ar}^{4+}}{\text{H}^+} \right) / \left(1 - \frac{\text{N}^+}{\text{N}} \right). \quad (12)$$

The finally derived Ar/H abundance ratio is 2.570×10^{-6} .

We have derived the K^{3+}/H^+ abundance ratio from the [K IV] $\lambda\lambda 6102$ and 6795 lines. A very faint feature, which might be the [K V] $\lambda 4163$ line is detected in the spectrum of NGC 7009, but we could not confirm that. K^+ is probably negligible in NGC 7009, judging from the very low ionization potential of K. Since the ionization potential of K^+ (31.6 eV) is comparable to that of N^+ (29.6 eV), and ionization potential of K^{3+} (60.9 eV) is comparable to that of F^{2+} (62.7 eV), we assume $\text{K}^{2+}/\text{K} = \text{N}^{2+}/\text{N}$ and $\text{K}^{4+}/\text{K} = \text{F}^{3+}/\text{F}$. Here the N^{2+}/N ratio is from the ORLs, and the F^{3+}/F ratio is from CELs. We use the following equation to correct for the unseen K^{2+} and K^{4+} ions,

$$\frac{\text{K}}{\text{H}} = \frac{\text{K}^{3+}}{\text{H}^+} / \left(1 - \frac{\text{N}^{2+}}{\text{N}} - \frac{\text{F}^{3+}}{\text{F}} \right). \quad (13)$$

The derived total K/H abundance ratio is 4.242×10^{-8} .

5 DISCUSSION

Average elemental abundances for the Galactic disc and bulge PNe taken from Kingsburg & Barlow (1994) and Exter, Barlow & Walton (2004) are presented in Table 25 for purpose of comparison. Also presented in this table are the average abundances for 23 Galactic bulge PNe of Wang & Liu (2007) plus two bulge PNe M 1-42 and M 2-36 studied by Liu et al. (2001b), and 58 Galactic disc PNe selected from Tsamis et al. (2003, 2004), Liu et al. (2004a, b) and Wesson et al. (2005). The helium abundance derived from the current analyses agrees well with the average value of the 58 disc sample, but 0.12 dex higher than the most recent solar value (Asplund et al. 2009). The recombination line C/H abundance 8.95 derived for NGC 7009 also agrees with the average value (9.03) of the disc sample, but 0.14 dex lower than the 23 bulge sample of Wang & Liu (2007). The forbidden-line C/H abundance for NGC 7009 is lower than all the values quoted from literature. The elemental N/H abundance derived from CELs for NGC 7009 agrees well with the the Sun, but lower than all other average values. Our recombination line N/H abundance is lower than the average values of

the bulge and disc samples compiled by Wang & Liu (2007), but is higher than the average value of the sample from Kingsburg & Barlow (1994) plus Exter, Barlow & Walton (2004). The forbidden-line O/H abundance for NGC 7009 is 0.13 dex low than the solar value, and lower than the average value of the disc sample of Wang & Liu (2007) by the same amount. Our C/O abundance ratio derived from CELs is 0.96, slightly lower than all other ratios from literature, indicating that NGC 7009 might be enriched in oxygen, which is consistent with the fact that the spectrum of NGC 7009 is obviously rich in oxygen emission lines. The forbidden-line neon abundance of NGC 7009 is 0.27 dex (\sim) higher than the solar value, and agrees with the average value (8.13) of the disc sample of Wang & Liu (2007). The forbidden-line Ne/O ratio observed in NGC 7009 is higher than the solar ratio by a factor of 2.5. However, Wang & Liu (2008) suggests that the solar Ne/O ratio of Asplund, Grevesse & Sauval (2005) be revised upwards by 0.22 dex, i.e. increased to 0.37. Similarly high forbidden-line Ne/O ratio (0.34–0.36) is also found in NGC 6153 by Liu et al. (2000). The sulfur and argon abundances of NGC 7009 both agree with the solar values. The Mg/H abundance of NGC 7009 agrees with the average abundance of the bulge PNe sample of Wang & Liu (2007), and is 0.1 dex lower than the solar value.

Elemental abundances derived from ORLs and CELs observed in NGC 7009 are presented in Table 25. By using the IR and UV observed line fluxes from the literature and correcting for extinction, we are able to derive elemental abundances of C, N, O, and Ne relative to hydrogen from both ORLs and CELs. The resultant ORL abundances of the above four elements are all higher than the abundance ratios derived from CELs, by a factor of 5–7. After deep spectroscopic observations of the ORLs detected in the spectrum of NGC 7009 by LSBC (for C, N and O) and LLB01 (for Ne), those heavy-element abundance discrepancy problems are again studied quantitatively, using the deepest CCD spectrum ever taken for a gaseous nebula and the new effective recombination coefficients calculated for the N II and O II recombination spectra under the nebular conditions in the intermediate coupling scheme. The analyses of the spectrum are carried out in a very consistent manner, i.e. an electron temperature of 1000 K as derived from the N II and O II ORL ratios is assumed throughout analyses of the heavy-element ORLs, while a temperature of about 10 000 K as yielded by CELs is assumed in calculating the CEL abundances. In the previous deep spectroscopy of NGC 7009 by LSBC, the electron temperature ($\sim 10 000$ K) derived from the [O III] nebular-to-auroral line ratio was adopted in calculating the ORL abundances. In the analyses of the neon abundance in NGC 7009 by LLB01, the electron temperature (7100 K) derived from the H I Balmer jump was used to calculate the recombination line neon abundance. Liu et al. (2000) assumed a temperature of 9100 K, as derived from the [O III] CEL ratio, in calculating the recombination line abundances for the C, N, O and Ne ions in NGC 6153. In the analyses of Galactic bulge PNe M 1-42 and M 2-36, Liu et al. (2001b) used the H I Balmer jump temperature (3560 K for M 1-42 and 5900 K for M 2-36) to derived the recombination line abundances. However, the recombination line abundances derived in the studies mentioned above are questionable, given that the temperatures assumed are not derived from the heavy-element ORLs. The effective recombination coefficients of the permitted transitions of heavy element ions, which are mainly excited by radiative recombination, usually decrease as the electron temperature increases, except for the dielectronic transitions (with high-lying parent), whose effective recombination coefficients increases as the temperature increases. When we use the recombination lines that are mainly excited by radiative recombina-

Table 25. Total elemental abundances derived from ORLs and CELs, in units such that $\log N(\text{H}) = 12$.

Element	X/H		log[X/H]+12		TLW ^a		TLW ^b		KB94 ^c	Solar ^d
	ORLs	CELs	ORLs	CELs	ORLs	CELs	ORLs	CELs		
He	0.112		11.049		11.02		11.06		11.06	10.93
C	$8.93(\pm 0.45) \times 10^{-4}$	$1.64(\pm 0.33) \times 10^{-4}$	8.95	8.21	9.09	8.52	9.03	8.56	8.74	8.43
N	$4.92(\pm 0.20) \times 10^{-4}$	$7.14(\pm 0.35) \times 10^{-5}$	8.69	7.85	8.94	8.17	9.14	8.34	8.38	7.83
O	$1.67(\pm 0.06) \times 10^{-3}$	$3.60(\pm 0.07) \times 10^{-4}$	9.22	8.56	9.22	8.60	9.32	8.70	8.66	8.69
F		$2.92(\pm 0.58) \times 10^{-7}$		5.47						4.56
Ne	$8.40(\pm 0.42) \times 10^{-4}$	$1.58(\pm 0.08) \times 10^{-4}$	8.92	8.20	9.06	7.99	9.07	8.13	8.06	7.93
Mg ^e	$3.18(\pm 0.16) \times 10^{-5}$		7.50		7.56		7.71			7.60
Si ^f	$8.28(\pm 0.80) \times 10^{-6}$		6.92							7.51
S		$1.30(\pm 0.11) \times 10^{-5}$		7.11		6.84		7.05	6.99	7.12
Cl		$1.93(\pm 0.21) \times 10^{-7}$		5.28		5.35		5.29		5.50
Ar		$2.57(\pm 0.38) \times 10^{-6}$		6.41		6.20		6.34	6.51	6.40
K ^g		$4.24(\pm 0.84) \times 10^{-8}$		4.63						5.03

^a Average abundances for 23 Galactic bulge PNe of Wang & Liu (2007) plus Galactic bulge PNe M 1-42 and M 2-36 analyzed by Liu et al. (2001b).

^b Average abundances given by Wang & Liu (2007) for 58 Galactic disc PNe which were selected from Tsamis et al. (2003, 2004), Liu et al. (2004a, b) and Wesson, Liu & Barlow (2005).

^c Average abundances of Galactic disc and bulge PNe (Kingsburg & Barlow 1994; Exter, Barlow & Walton 2004), all based on CEL analyses except for helium for which ORLs were used.

^d Solar values from Asplund et al. (2009).

^e Mg^+/H^+ and $\text{Mg}^{3+}/\text{H}^+$ are neglected in calculating the total ORL abundance.

^f Si^+/H^+ is neglected in calculating the total ORL abundance.

^g K^+/H^+ and K^{4+}/H^+ are neglected in calculating the total CEL abundance.

tion, such as those used by LSBC and LLB01, to calculate the ionic abundances of C, N, O and Ne, using the forbidden line temperature e.g. $T_e([\text{O III}])$ or the H I Balmer jump temperature will result in overestimated recombination line abundances, because those two temperatures are both much higher than the temperatures yielded by the heavy element ORLs as revealed in the current analyses as well as many previous studies (e.g. Liu 2011 for a recent review). Here we take the O II recombination lines as examples. When the electron temperature increases from 1000 to 10 000 K, the effective recombination coefficient for the O II M1 $\lambda 4649.13$ line decreases by a factor of 7.5 (PJS), and the effective recombination coefficient for H β decreases by a factor of 6 (Storey & Hummer 1995), as a consequence the O^{2+}/H^+ ionic abundance, which is calculated from the ratio of the effective recombination coefficients of the two lines $\alpha_{\text{eff}}(\text{H}\beta)/\alpha_{\text{eff}}(\lambda 4649)$, will increase by 22 per cent.

The ADFs observed in NGC 7009, although moderate compared with those found in PNe NGC 6153 (ADF \sim 10, Liu et al. 2000), M 1-42 (ADF \sim 20, Liu et al. 2001b), NGC 1501 (ADF \sim 30, Ercolano et al. 2004) and Hf 2-2 (ADF \sim 70, Liu et al. 2006), is high compared with most of the other Milky Way PNe so far spectroscopically studied (ADFs \sim 1.6–3.2). Ever since the observation of an ADF value of about 5 from the deep spectroscopy of NGC 7009 by LSBC, it has been wondered that possible systematic effects in the classic plasma analysis procedure based on CEL measurements might cause the observed discrepancies, if inaccuracies in the effective recombination coefficients or contamination of the recombination lines by processes such as stellar continuum resonance fluorescence as the origins of the discrepancies can be ruled out. After observations of the [O III] $\lambda 4931/\lambda 4959$ line ratio in seven Milky Way PNe and the Orion Nebula by Mathis & Liu (1999), the measurement errors in CELs as the culprit has also been ruled out. Clearly the temperature and abundance discrepancies are real, and the two categories of emission lines probably arise from regions with different physical conditions. A detailed study of

NGC 6153 by Liu et al. (2000) yielded an ADF of about 10 for that object and, based on the empirical composite models, Liu et al. (2000) proposed a bi-abundance nebular model as a possible explanation to such high abundance discrepancy.

Ever since the detection of a Balmer jump temperature as low as 3560 K for M 1-42, 5660 K lower than the [O III] forbidden line temperature for the same nebula (Liu et al. 2001b), it has become increasingly clear that PNe, at least those exhibiting large ADFs, must contain another component of previously unknown ionized gas. This component of gas mainly emits ORLs yet is essentially invisible in strong CELs because the electron temperature prevailing in the component is too low to excite any UV or optical CELs. The low temperature condition in that component is probably due to the much enhanced cooling by the IR fine-structure lines of the heavy element ions, which is a consequence of a very high metallicity (i.e. H-deficient). This physical idea is supported by detailed photoionization modeling of Péquignot et al. (2003) and Tylenda (2003) and also by direct measurements of the average electron temperatures under which various types of emission lines are emitted (c.f. Liu 2003, 2006a, b and 2011 for reviews; Zhang et al. 2004 for the plasma diagnostics based on the H I recombination spectrum and Zhang et al. 2005a for the plasma diagnostics based on the He I recombination spectrum). The discovery of a dramatically high ADF value of \sim 70 and the remarkably low Balmer jump temperature (\sim 900 K) in PN Hf 2-2 by Liu et al. (2006a) strengthens the validity of the bi-abundance nebular model. In order to reproduce the multi-waveband spectroscopic and imaging observations of NGC 6153 and investigate the nature and origin of the H-deficient inclusions, Yuan et al. (2011) constructed three-dimensional photoionization models, using the Monte Carlo photoionization code MOCASSIN developed by Ercolano et al. (2003). Modeling of NGC 6153 showed that chemically homogeneous models yielded small electron temperature fluctuations and failed to reproduce the strengths of the ORLs of heavy ele-

ment ions. In contrast, bi-abundance models incorporating a small amount of metal-rich inclusions (~ 1.3 per cent of the total nebular mass) are able to match all the observations within measurement uncertainties. The metal-rich inclusions, cooled down in a very low temperature (~ 800 K) by ionic IR fine-structure lines, dominate the emission of heavy-element ORLs, but contribute almost nil to the emission of most CELs. The current analyses of the optical recombination spectrum of NGC 7009 are carried out under the context of the bi-abundance nebular model, and the results of plasma diagnostics based on various types of emission lines and abundance determinations are consistent with that context: the temperature sequence $T_e([\text{O III}]) \gtrsim T_e(\text{H I BJ}) \gtrsim T_e(\text{He I}) \gtrsim T_e(\text{N II} \ \& \ \text{O II ORLs})$ is consistent with predictions from the bi-abundance model; the C^{2+}/H^+ , N^{2+}/H^+ , O^{2+}/H^+ and $\text{Ne}^{2+}/\text{H}^+$ ionic abundances derived from ORLs, using the new effective recombination coefficients and the electron temperature yielded by the N II and O II ORLs, are systematically higher, by about a factor of 5, than the corresponding abundances derived from CELs. It has been shown from optical observations that the ADF varies with position in several high-ADF PNe and is highest close to the central star. The “cold” inclusions should be cooled via the IR fine-structure lines of heavy element ions. Thus it is interesting to see if the IR fine-structure line fluxes relative to optical/UV CELs peak where the ADF peaks in PNe with large ADFs. Recently, Herschel and Hubble observations of NGC 7009 have been carried out and the results show that within the first ~ 5 arcsec from the central star of NGC 7009, the $[\text{O III}] \ 88\mu\text{m}/\lambda 5007$ flux ratio seems to increase towards center (R. H. Rubin, private communication). With the very deep spectrum and the high-quality atomic data now available, we can derive more precise physical properties e.g. total mass, spatial distribution of the “cold”, metal-rich inclusions in NGC 7009 through three-dimensional photoionization modeling.

Given that the ADFs found in PNe are all larger than unity, the metal-rich (H-deficient) inclusions are probably a real feature of PNe. However, the presence of those “cold” inclusions is not predicted by the current theories of stellar evolution. Iben, Kaler & Truran (1983) proposed that an evolved star undergoing a very late helium flash (the so-called ‘born-again’ PNe) may harbour H-deficient material, such as the H-deficient knots detected in the two ‘born-again’ PNe Abell 30 and Abell 58. Wesson, Liu & Barlow (2003) and Wesson et al. (2008) found that the H-deficient knots in Abell 30 and Abell 58 are O-rich, in contradiction with the expectation of the ‘born-again’ scenario. The ADFs are found to be high in the PNe with Wolf-Rayet central stars, and that can be explained by the scenario of a single post-asymptotic giant branch (post-AGB) star experiencing a late helium shell flash, but not all PNe with large ADFs have an H-deficient central star, such as the case of NGC 7009 studied in the current paper. García-Rojas, Peña & Peimbert (2009) observed the faint ORLs in Galactic PNe with [WC] nucleus and found the results that argue against the presence of H-deficient knots coming from a late thermal pulse event. De Marco (2008) suggested a binary scenario to explain the observations that are in contradiction with the theory of the single post-AGB evolution. In this respect, it is interesting to note that Abell 58 have experienced a nova-like outburst (Clayton & De Marco 1997). Lutz et al. (1998) has also found the central star of Hf 2-2, a PN with the largest ADF value (~ 70 , Liu et al. 2006a) ever found for an emission line nebulae, to be a close binary system. An alternative scenario of the origin of the H-deficient inclusions is that they evolve from metal-rich planetary material, such as icy planetesimals left over from the debris of planetary system of the progenitor star of the PN (Liu 2003, 2006a). Both high spectral- and

spatial-resolution observations in the future, in combination with detailed three-dimensional photoionization modeling as has been carried out for NGC 6153 (Yuan et al. 2011), will help to reveal the possible astrophysical origins of the H-deficient inclusions in NGC 7009.

6 SUMMARY AND CONCLUSIONS

Nearly two decades after the first analysis of the O II optical recombination spectrum of the bright PN NGC 7009 (LSBC), once again we focus on the rich ORLs of heavy element ions detected in very deep CCD spectrum of the same object. Thanks to much advance in observational techniques, which enables accurate detection of the weak ORLs of heavy element ions, and the steady improvements in atomic data, especially the recombination theories of heavy element ions in the physical conditions of photoionized nebulae, we are now clear that the long-standing dichotomy between nebular plasma diagnostics and abundance determinations using CELs on the one hand and ORLs on the other, are real rather than cause by, e.g., observational uncertainties or errors in atomic data. Unremitting efforts in nebular research of the past 40 years gradually lead to new understanding of the problems in nebular astrophysics. Various mechanisms (e.g. temperature fluctuations and/or density inhomogeneities, abundance inhomogeneities, non-Maxwell-Boltzmann equilibrium electrons e.g. the κ -distribution of electron energies) have been proposed to explain the discrepancies in plasma diagnostics and abundance determinations, and debate over these mechanisms are still going on.

In the context of bi-abundance nebular model postulated by Liu et al. (2000), we present a comprehensive and critical analysis of the rich optical recombination spectrum of NGC 7009. Transitions from individual multiplets of heavy element ions, e.g. C II, N II, O II and Ne II, are checked carefully for line blending, and accurate dereddened line fluxes of the most prominent transitions of those ions are obtained through multi-Gaussian profile fitting. In addition to the accurate observations of ORLs, we have finished new calculations of the effective recombination coefficients for the N II recombination spectrum. The new effective recombination coefficients for the nebular O II lines calculated by P. J. Storey (unpublished) help to enlarge our current atomic dataset for nebular recombination line study. Both calculations were carried out in the intermediate coupling scheme, and have taken into account the density-dependence of the relative populations of the ground fine-structure levels of recombining ions (i.e. $\text{N}^{2+} \ 2\text{P}_{1/2}^o$ and $2\text{P}_{3/2}^o$ for N II, and $\text{O}^{2+} \ 3\text{P}_0$, 3P_1 and 3P_2 for O II). The new effective recombination coefficients of N II and O II are of high quality and make nebular density diagnostics using the ORLs of heavy element ions possible for the first time.

The observed relative intensities of ORLs are compared with theoretical predictions that are based on the new effective recombination coefficients. At a given electron temperature ($T_e = 1000$ K) as yielded by the ORL ratios of N II and O II, the predicted relative intensities of ORLs agree with the observed values. Plasma diagnostics based on the best observed N II and O II ORLs (i.e. the $I(\text{M3 } \lambda 5679)/I(\text{M39b } \lambda 4041)$ ratio of N II and the $I(\text{M1 } \lambda 4649)/I(\text{M48a } \lambda 4089)$ ratio of O II) both yield electron temperatures close to 1000 K, which is lower than those derived from the CEL ratios by nearly one order of magnitude. The low temperatures yielded by the N II and O II ORLs indicate that the recombination lines of heavy element ions originate from very cold regions. The electron temperatures derived from

the intensity ratios of the O II high-excitation recombination lines M15 $\lambda 4591$ and M36 $\lambda 4189$, which are formed from recombination of excited-state parent (i.e. $O^{2+} 2p^2\ ^1D$), relative to the O II M1 $\lambda 4649$ line agree with each other (~ 3600 K), and is consistent with the fact that very cold (≤ 1000 K) inclusions probably exist in the nebula. The electron temperature (~ 3000 K) yielded by the C II $I(M28.01\ \lambda 8794)/I(M6\ \lambda 4267)$ dielectronic-to-radiative recombination line ratio also agrees with the conjecture of very cold inclusions. The C^{2+}/H^+ , N^{2+}/H^+ , O^{2+}/H^+ and Ne^{2+}/H^+ ionic abundance ratios derived from ORLs, using the new effective recombination coefficients of N II and O II, are consistently higher than the corresponding values derived from CELs, by about a factor of 5. An electron temperature of 1000 K, which is yielded by the best observed N II and O II recombination line ratios and as a consequence presumably represents the physical condition prevailing in the regions where the heavy element ORLs arise, has been assumed throughout the recombination-line abundance determinations. The results of plasma diagnostics and abundance determinations for NGC 7009 points to the existence of “cold”, metal-rich inclusions in NGC 7009, and is thus consistent with the context of the current spectral analyses, i.e. the bi-abundance nebular model.

Recombination line analysis for NGC 7009 helps to assess the new atomic data. The agreement between the observed and predicted relative intensities of the N II and O II ORLs indicates that the current calculations of the recombination spectra of those two ionic species well represent the physical processes, i.e. radiative and dielectronic recombination, under nebular conditions. Our nebular analysis also shows that the recombination lines of different multiplets, or different J -resolved fine-structure components of a multiplet yield consistent ionic abundances (e.g. N^{2+}/H^+ and O^{2+}/H^+). This is another evidence that the new effective recombination coefficients are reliable. However, the Ne^{2+}/H^+ abundance ratio derived from the total intensity of the $4f-3d$ transitions is higher, by nearly 0.2 dex, than the average value derived from the multiplets of the $3-3$ configuration. That indicates new calculations of the effective recombination coefficients for the Ne II lines are needed.

ACKNOWLEDGEMENTS

We thank Dr. P. J. Storey for making the effective recombination coefficients for the O II lines and the Ne II $4f-3d$ transitions available prior to publication. We thank Dr. R. H. Rubin for fruitful discussions. We would also like to thank Dr. O. De Marco for her valuable comments and suggestions which have greatly improved the quality of this paper. This work is supported by the Natural Science Foundation of China (No. 10933001).

REFERENCES

- Aggarwal, K. M., 1983, *ApJS*, 52, 387
 Asplund, M., Grevesse, N., Sauval, A. J., 2005, in Barnes, T. G. III, Bash, F. N., eds, *ASP Conf. Ser. Vol. 336, Cosmic Abundances as Records of Stellar Evolution and Nucleosynthesis*. Astron. Soc. Pac., San Francisco, p. 25
 Asplund, M., Grevesse, N., Sauval, A. J., Scott, P., 2009, *ARA&A*, 47, 481
 Aller, L. H., Kaler, J. B., 1964, *ApJ*, 139, 1074
 Almog, Y., Netzer, H., 1989, *MNRAS*, 238, 57
 Baluja, K. L., Zeippen, C. J., 1988, *J. Phys. B: At. Mol. Opt. Phys.*, 21, 1455
 Barker, T., 1983, *ApJ*, 267, 630
 Barker, T., 1991, *ApJ*, 371, 217
 Bastin, R. J., 2006, Ph.D. Thesis. University College London (B06)
 Burgess, A., Seaton, M. J., 1960a, *MNRAS*, 120, 121
 Burgess, A., Seaton, M. J., 1960b, *MNRAS*, 121, 471
 Barlow, M. J., Storey, P. J., 1993, in Weinberger, R., Acker, A., eds, *Proc. IAU Symp. 155, Planetary Nebulae*. Kluwer, Dordrecht, p. 92
 Bauman, R. P., Porter, R. L., Ferland, G. J., MacAdam, K. B., 2005, *ApJ*, 628, 541
 Bayes, F. A., Saraph, H. E., Seaton, M. J., 1985, *MNRAS*, 215, 85
 Benjamin, R. A., Skillman, E. D., Smits, D. P., 1999, *ApJ*, 514, 307
 Benjamin, R. A., Skillman, E. D., Smits, D. P., 2002, *ApJ*, 569, 288
 Berrington, K. A., 1988, *J. Phys. B: At. Mol. Opt. Phys.*, 21, 1083
 Berrington, K. A., 1995, *A&AS*, 109, 193
 Berrington, K. A., Burke, P. G., 1981, *Planetary and Space Science*, 29, 377
 Berrington, K. A., Nakazaki, S., Norrington, P. H., 2000, *A&AS*, 142, 313
 Berrington, K. A., Seaton, M. J., 1985, *J. Phys. B: At. Mol. Phys.*, 18, 2587
 Bowen, I. S., 1934, *PASP*, 46, 146
 Bowen, I. S., 1935, *ApJ*, 81, 1
 Blum, R. D., Pradhan, A. K., 1992, *ApJS*, 80, 425
 Brocklehurst, M., 1972, *MNRAS*, 157, 211
 Butler, K., Zeippen, C. J., 1989, *A&A*, 208, 337
 Butler, K., Zeippen, C. J., 1994, *A&AS*, 108, 1
 Cahn, J. H., Kaler, J. B., Stanghellini, L., 1992, *A&AS*, 94, 399
 Clayton, G. C., De Marco, O., 1997, *AJ*, 114, 2679
 Clegg, R. E. S., Harrington, J. P., Barlow, M. J., Walsh, J. R., 1987, *ApJ*, 314, 551
 Cunto, W., Mendoza, W., Ochsenbein, F., Zeippen, C. J., 1993, *A&A*, 275, L5
 Davey, A. R., Storey, P. J., Kisielius, R., 2000, *A&AS*, 142, 85
 De Marco, O., 2008, in Werner, K., Rauch, T., eds, *ASP Conf. Ser., Vol. 391, Hydrogen-Deficient Stars*, Astron. Soc. Pac., San Francisco, p. 209
 De Marco, O., Storey, P. J., Barlow, M. J., 1998, *MNRAS*, 297, 999
 Exter, K. M., Barlow, M. J., Walton, N. A., 2004, *MNRAS*, 349, 1291
 Escalante, V., Morisset, C., 2005, *MNRAS*, 361, 813
 Escalante, V., Victor, G. A., 1990, *ApJS*, 73, 513
 Ercolano, B., Barlow, M. J., Storey, P. J., Liu, X.-W., 2003, *MNRAS*, 340, 1136
 Ercolano, B., Wesson, R., Zhang, Y., Barlow, M. J., De Marco, O., Rauch, T., Liu, X.-W., 2004, *MNRAS*, 354, 558
 Fang, X., Liu, X.-W., 2011, *MNRAS*, 415, 181 (Paper I)
 Fang, X., Storey, P. J., Liu, X.-W., 2011, *A&A*, 530, A18 (**FSL11**)
 Ferland, G. J., 2003, *Annu. Rev. Astron. Astrophys.*, 41, 517
 Froese Fischer, C., 1994, *Phys. Scri.*, 49, 323
 Froese Fischer, C., Rubin, R. H. 2004, *MNRAS*, 355, 461
 Froese Fischer, C., Saha, H. P., 1985, *Phys. Scr.*, 32, 181
 Fleming, J., Bell, K. L., Hibbert, A., Vaecck, N., Godefroid, M. R., 1996, *MNRAS*, 279, 1289
 French, H. B., 1983, *ApJ*, 273, 214

- Garstang, R. H., 1958, MNRAS, 118, 572
- Garnett, D. R., Dinerstein, H. L., 2001, ApJ, 558, 145
- Gau, J. N., Henry, R. J. W., 1977, Phys. Rev. A, 16, 986
- Giles, K., 1981, MNRAS, 195, 63
- Grandi, S. A., 1976, ApJ, 206, 658
- García-Rojas, J., Peña, M., Peimbert, A., 2009, A&A, 496, 139
- Hummer, D. G., Storey, P. J., 1987, MNRAS, 224, 801
- Howarth, I. D., 1983, MNRAS, 203, 301
- Hummer, D. G., Berrington, K. A., Eissner, W., Pradhan, A. K., Saraph, H. E., Tully, J. A., 1993, A&A, 279, 298
- Hirata, R., Horaguchi, T., 1995, Atomic Spectral Line List
- Iben, I., Kaler, J. B., Truran, J. W., 1983, ApJ, 264, 605
- Johnson, C. T., Kingston, A. E., 1990, J. Phys. B, 23, 3393
- Kaler, J. B., 1986, ApJ, 308, 322
- Kastner, S. O., Behring, W. E., Bhatia, A. K., 1983, ApJS, 53, 129
- Kastner, S. O., Bhatia, A. K., 1990, ApJ, 362, 745
- Keenan, F. P., Aller, L. H., Bell, K. L., Hyung, S., McKenna, F. C., Ramsbottom, C. A., 1996, MNRAS, 281, 1073
- Keenan, F. P., Feibelman, W. A., Berrington, K. A., 1992, ApJ, 389, 443
- Keenan, F. P., Hibbert, A., Ojha, P. C., Conlon, E. S., 1993, Phys. Scr., 48, 129
- Keenan, F. P., Norrington, P. H., 1987, A&A, 181, 370
- Kisielius, R., Storey, P. J., 1999, A&AS, 137, 157
- Kisielius, R., Storey, P. J., 2002, A&A, 387, 1135
- Kisielius, R., Storey, P. J., Davey, A. R., Neale, L. T., 1998, A&AS, 133, 257
- Kingsburg, R. L., Barlow, M. J., 1994, MNRAS, 271, 257
- Lennon, D. J., Burke, V. M., 1994, A&AS, 103, 273
- Liu, X.-W., 2003, in Kwok, S., Dopita, M., Sutherland, R. eds, IAU Symposium #209, Planetary Nebulae: Their Evolution and Role in the Universe. Astron. Soc. Pac., San Francisco p. 339
- Liu, X.-W., Danziger, I. J., 1993a, MNRAS, 261, 465
- Liu, X.-W., Danziger, I. J., 1993b, MNRAS, 263, 256
- Liu, X.-W., Danziger, I. J., Murdin, P., 1993, MNRAS, 262, 699
- Liu, X.-W., Barlow, M. J., Cohen, M., Danziger, I. J., Luo, S.-G., Baluteau, J. P., Cox, P., Emery, R. J., Lim, T., Péquignot, D., 2001a, MNRAS, 323, 343
- Liu, X.-W., Luo, S.-G., Barlow, M. J., Danziger, I. J., Storey, P. J., 2001b, MNRAS, 327, 141
- Liu, X.-W., 2006a, in Barlow, M. J., Méndez, R. H., eds, IAU Symposium #234, Planetary Nebulae in our Galaxy and Beyond, Cambridge University Press, p. 219
- Liu, X.-W., 2006b, in Walsh, J., Stanghellini, L., Douglas, N., eds, Proceedings of the ESO Workshop on Planetary Nebulae beyond the Milky Way. Springer-Verlag, Berlin, p. 169
- Liu, X.-W., 2011, in York, D. G., Gingerich, O., Zhang, S.-N., Harper, C. L., eds, New Vision 400: Engaging Big Questions in Astronomy and Cosmology Four Hundred Years after the Invention of the Telescope. CRC Press, p. 103
- Liu, X.-W., Barlow, M. J., Zhang, Y., Bastin, R. J., Storey, P. J., 2006, MNRAS, 368, 1959
- Liu, X.-W., Storey, P. J., Barlow, M. J., Clegg, R. E. S., 1995, MNRAS, 272, 369 (LSBC)
- Liu, X.-W., Storey, P. J., Barlow, M. J., Danziger, I. J., Cohen, M., Bryce, M., 2000, MNRAS, 312, 585
- Liu, Y., Liu, X.-W., Luo, S.-G., Barlow, M. J., 2004a, MNRAS, 353, 1231
- Liu, Y., Liu, X.-W., Barlow, M. J., Luo, S.-G., 2004b, MNRAS, 353, 1251
- Luo, D., Pradhan, A. K., Saraph, H. E., Storey, P. J., Yu, Y., 1989, J. Phys. B: At. Mol. Opt. Phys., 22, 389
- Luo, S.-G., Liu, X.-W., Barlow, M. J., 2001, MNRAS, 326, 1049 (LLB01)
- Lutz, J., et al., 1998, AAS, 192, 5309
- Mathis, J. S., 1957, ApJ, 125, 318
- Mathis, J. S., Liu, X.-W., 1999, ApJ, 521, 212
- McNabb, I. A., Fang, X., Liu, X.-W., Bastin, R. J., Storey, P. J., 2012, MNRAS, accepted
- Mendoza, C. 1983, in IAU Symp. 103, Planetary Nebulae, ed. Flower, D., Reidel, Dordrecht, p.143
- Mendoza, C., Zeippen, C. J., 1982a, MNRAS, 199, 1025
- Mendoza, C., Zeippen, C. J., 1982b, MNRAS, 198, 127
- Mendoza, C., Zeippen, C. J., 1983, MNRAS, 202, 981
- Moore, C. E., 1993, In *CRC Series in Evaluated Data in Atomic Physics* : Tables of Spectra of Hydrogen, Carbon, Nitrogen, and Oxygen Atoms and Ions. Edited by Gallagher, J. w., CRC Press, Boca Raton, FL
- Nahar, S. N., 1995, ApJS, 101, 423
- Nicholls, D. C., Dopita, M. A., Sutherland, R. S., 2012, ApJ, 752, 148
- Nahar, S. N., Pradhan, A. K., 1996, A&AS, 119, 509
- Nussbaumer, H., 1969, Astrophys. Lett, 4, 183
- Nussbaumer, H., Rusca, C., 1979, A&A, 72, 129
- Nussbaumer, H., Storey, P. J., 1978, A&A, 70, 37
- Nussbaumer, H., Storey, P. J., 1981a, A&A, 96, 91
- Nussbaumer, H., Storey, P. J., 1981b, A&A, 99, 177
- Nussbaumer, H., Storey, P. J., 1982, A&A, 113, 21
- Nussbaumer, H., Storey, P. J., 1983, A&A, 126, 75
- Nussbaumer, H., Storey, P. J., 1984, A&AS, 56, 293
- Nussbaumer, H., Storey, P. J., 1986, A&AS, 64, 545
- Nussbaumer, H., Storey, P. J., 1987, A&AS, 69, 123
- Osterbrock, D. E., Ferland, G. J. (2006). Astrophysics of Gaseous Nebulae and Active Galactic Nuclei. Sausalito: University Science Books.
- Peimbert, M., 1967, ApJ, 150, 825
- Peimbert, M., 1971, Bol. Obs. Tonantzintla y Tacubaya, 6, 29
- Perinotto, M., Benvenuti, P., 1981, A&A, 101, 88
- Pelan, J., Berrington, K. A., 1995, A&AS, 110, 209
- Péquignot, D., Liu, X.-W., Barlow, M. J., Storey, P. J., Morisset, C., 2003, in Kwok, S., Dopita, M., Sutherland, R., eds, IAU Symposium #209, Planetary Nebulae: Their Evolution and Role in the Universe. Astron. Soc. Pac., San Francisco, p. 347
- Péquignot, D., Petitjean, P., Boisson, C., 1991, A&A, 251, 680
- Pottasch, S. R., 1962, ApJ, 135, 385
- Pottasch, S. R., Preite-Martinez, A., Olmon, F. M., Jing-Er, Mo, Kingma, S., 1986, A&A, 161, 363
- Porter, R. L., Bauman, R. P., Ferland, G. J., MacAdam, 2005, ApJ, 622, L73
- Pradhan, A. K., 1976, MNRAS, 177, 31
- Robertson-Tessi, M., Garnett, D. R., 2005, ApJS, 157, 371
- Robbins, R. R., 1968, ApJ, 151, 497
- Robbins, R. R., 1970, ApJ, 160, 519
- Robbins, R. R., Robinson, E. L., 1971, ApJ, 167, 249
- Rubin, R. H., 1989, ApJS, 69, 897
- Rubin, R. H., Colgan, S. W. J., Haas, M. R., Lord, S. D., Simpson, J. P., 1997, ApJ, 479, 332
- Sawey, P. M., Berrington, K. A., 1993, Atom. Data Nucl. Data Tables, 55, 81
- Saraph, H. E., Seaton, M. J., 1980, MNRAS, 193, 617
- Saraph, H. E., Storey, P. J., 1999, A&AS, 134, 369
- Seaton, M. J., 1987, J. Phys. B, 20, 6363
- Sharpee, B., Williams, R., Baldwin, J. A., van Hoof, P. A. M., 2003, ApJS, 149, 157

- Stafford, R. P., Bell, K. L., Hibbert, A., Wijesundera, W. P., 1994, MNRAS, 268, 816
- Smits, D. P., 1991, MNRAS, 251, 316
- Smits, D. P., 1996, MNRAS, 278, 683
- Storey, P. J., 1981, MNRAS, 195, 27
- Storey, P. J., 1994, A&A, 282, 999
- Storey, P. J., Hummer, D. G., 1995, MNRAS, 272, 41
- Tylenda, R., 2003, in Kwok, S., Dopita, M., Sutherland, R., eds, IAU Symposium #209, Planetary Nebulae: Their Evolution and Role in the Universe. Astron. Soc. Pac., San Francisco, p. 389
- Tachiev, G., Froese Fischer, C., 2001, Can. J. Phys. 79, 955
- Tong, X.-M., Zou, Y., Li, J.-M., Liu, X.-W., 2001, Chin. Phys. Letter, 11, 69
- Tsamis, Y. G., Barlow, M. J., Liu, X.-W., Danziger, I. J., Storey, P. J., 2003, MNRAS, 345, 186
- Tsamis, Y. G., Barlow, M. J., Liu, X.-W., Storey, P. J., Danziger, I. J., 2004, MNRAS, 353, 953
- Viegas, S. M., Clegg, R. E. S., 1994, MNRAS, 271, 993
- Vujnovic, V., Wiese, W. L., 1992, J. Phys. Chem. Ref. Data, 21, 919
- Wang, W., Liu, X.-W., 2007, MNRAS, 381, 669
- Wang, W., Liu, X.-W., 2008, MNRAS, 389, L33
- Wenåker, I., 1990, Physica Scripta, 42, 667
- Wesson, R., Barlow, M. J., Liu, X.-W., Storey, P. J., Ercolano, B., De Marco, O., 2008, MNRAS, 383, 1639
- Wesson, R., Liu, X.-W., Barlow, M. J., 2003, MNRAS, 340, 253
- Wesson, R., Liu, X.-W., Barlow, M. J., 2005, MNRAS, 362, 424
- Wiese, W. L., Smith, M. W., Glennon, B. M., 1966, NSRDS-NBS 4, US Government Printing Office, Washington DC
- Wyse, A. B., ApJ, 95, 356
- Yuan, H.-B., Liu, X.-W., Péquignot, D., Rubin, R. H., Ercolano, B., Zhang, Y., 2011, MNRAS, 411, 1035
- Zeippen, C. J., 1982, MNRAS, 198, 111
- Zeippen, C. J., Le Bourlot, J., Butler, K., 1987, A&A, 188, 251
- Zhang, H. L., 1996, A&AS, 119, 523
- Zhang, H. L., Pradhan, A. K., 1997, A&AS, 126, 373
- Zhang, Y., Liu, X.-W., Wesson, R., Storey, P. J., Liu, Y., Danziger, D., 2004, MNRAS, 351, 935
- Zhang, Y., Liu, X.-W., Liu, Y., Rubin, R. H., 2005a, MNRAS, 358, 457
- Zhang, Y., Liu, X.-W., Luo, S.-G., Péquignot, D., Barlow, M. J., 2005b, A&A, 442, 249
- Zhang, Y., Liu, X.-W., 2005, ApJ, 631, L61

APPENDIX A: THE C II OPTICAL RECOMBINATION SPECTRUM

A1 Multiplet 6, $4f^2F^\circ - 3d^2D$

See Section 3.1.1.

A2 Multiplet 3, $3d^2D - 3p^2P^\circ$

Only the $\lambda 7231.32$ ($3d^2D_{3/2} - 3p^2P_{1/2}^\circ$) line is detected; the other two components $\lambda 7236.42$ ($3d^2D_{5/2} - 3p^2P_{3/2}^\circ$) and $\lambda 7237.17$ ($3d^2D_{3/2} - 3p^2P_{3/2}^\circ$) are blended with the [Ar IV] $3p3^2P_{3/2}^\circ - 3p3^2D_{5/2}^\circ$ $\lambda 7237.40$ line. The intensity of $\lambda 7231.32$ is 0.130, with an uncertainty of less than 5 per cent. Assuming that the intensity ratios of the C II M3 lines are as in the *LS* coupling, i.e. 1 : 5 : 9, we obtain a total intensity ratio of M3 $\lambda 7235$ to C II M6 $\lambda 4267$ of 0.442, which is lower than the predicted ratio 1.204 in Case B but much higher than the Case A value (0.017). Those theoretical ratios are based on the C II effective recombination coefficients of B06. Since the calculation of B06 for the C II recombination spectrum is valid from 5000 K, here an electron temperature of 10000 K and a density of 10000 cm^{-3} were assumed. In this section, an electron temperature of 5000 or 10000 K is assumed when we use the effective recombination coefficients of B06.

The calculation of Davey, Storey & Kisielius (2000) is valid from 500 to 20000 K. Using their C II effective recombination coefficients, we derived a theoretical C II $I(\text{M3 } \lambda 7235)/I(\text{M6 } \lambda 4267)$ ratio of 0.013 in Case A and 0.907 in Case B. An electron temperature of 1000 K and a density of 10000 cm^{-3} are assumed when we use the atomic data of Davey, Storey & Kisielius (2000) in the current paper. Given that the effective recombination coefficients are insensitive to electron density at low temperature, we expect that the intensity ratio of those two C II multiplets at 10000 cm^{-3} does not differ much from that at $2000-4000 \text{ cm}^{-3}$, a density range yielded by the N II and O II recombination line diagnostics (see Figs. 12 and 17). Thus the C II $I(\text{M3 } \lambda 7235)/I(\text{M6 } \lambda 4267)$ ratio observed in NGC 7009 (0.442) lies between the two cases.

A3 Multiplet 4, $4s^2S - 3p^2P^\circ$

The $\lambda 3918.98$ ($4s^2S_{1/2} - 3p^2P_{1/2}^\circ$) component is blending with the O II M17 $3p'^2P_{1/2}^\circ - 3s'^2D_{3/2}$ $\lambda 3919.29$ and N II M17 $3d^1P_1 - 3p^1P_1$ $\lambda 3919.00$ lines, and is partially blended with the other M4 line $\lambda 3920.69$ ($4s^2S_{1/2} - 3p^2P_{3/2}^\circ$). Two Gaussian profiles were used to fit the complex. Using the O II effective recombination coefficients of PJS, we estimated that the O II line contributes 42 per cent to the total intensity of the blend at $\lambda 3919$. The contribution of the N II line is negligible according to the calculation of FSL11. The intensities of the $\lambda 3918.98$ and $\lambda 3920.69$ lines have 0.016 ± 0.003 and 0.034 ± 0.004 , respectively. Thus the intensity ratio of C II M4 $\lambda 3920$ to the C II M6 $\lambda 4267$ multiplet is 0.057, which agrees with the predicted ratio in Case B derived from the coefficients of B06, but higher than the Case A value 0.018. An electron temperature of 10000 K was assumed. At 5000 K, the lowest temperature of the calculation by B06, this C II ratio is 0.011 in Case A and 0.035 in Case B. The C II M4 multiplet is not presented in the calculation of Davey, Storey & Kisielius (2000).

A4 Multiplet 16.04, $6f^2F^\circ - 4d^2D$

All fine-structure components of this multiplet have an identical laboratory wavelength 6151.43 \AA . Single Gaussian profile fitting

to this feature gives an intensity of 0.028 ± 0.004 . The contribution from the blended N II M36 $4p^3D_2 - 3d^3F_2^\circ$ $\lambda 6150.75$ line is negligible. Thus the intensity ratio of this multiplet to C II M6 $\lambda 4267$ is 0.031, agrees with the predicted ratio 0.027 deduced from the coefficients of Davey, Storey & Kisielius (2000). The predicted ratio of the two C II multiples, based on the coefficients of B06, is 0.037. Both Davey, Storey & Kisielius (2000) and B06 show that the Case A effective recombination coefficient for the $\lambda 6151$ multiplet differs from its Case B value by only 2 per cent. For the C II transitions of large l ($l > 4$), only Case A coefficients are presented by Davey, Storey & Kisielius (2000). Thus in this section, the theoretical intensity ratios of those C II transitions relative to the M6 $\lambda 4267$ multiplet are all presented in Case A.

A5 Multiplet 17.02, $5g^2G - 4f^2F^\circ$

This multiplet ($\lambda 9903$) is free of blending, and has an intensity 0.213 ± 0.020 . The intensity ratio of M17.02 $\lambda 9903$ to the C II M6 $\lambda 4267$ multiplet is 0.234, which is slightly lower than the predicted ratio 0.302 deduced from the coefficients of Davey, Storey & Kisielius (2000). At 10000 K, the effective recombination coefficient for this multiplet given by Davey, Storey & Kisielius (2000) differs from that of B06 by only 3 per cent.

A6 Multiplet 17.04, $6g^2G - 4f^2F^\circ$

This multiplet ($\lambda 6462$) has an intensity of 0.078 ± 0.004 . The intensity ratio of $\lambda 6462$ to the C II M6 $\lambda 4267$ multiplet is 0.088, which agrees with the predicted value 0.076 (deduced from the atomic data of Davey, Storey & Kisielius (2000)) within errors.

A7 Multiplet 17.06, $7g^2G - 4f^2F^\circ$

The C II M17.06 $\lambda 5342$ multiplet is partially blending with a very weak feature, which was identified as [Kr IV] $\lambda 5346.02$ (Paper I). Two Gaussian profiles were used to fit the complex, and that gives an intensity of 0.037 ± 0.002 for $\lambda 5342$. The intensity ratio of $\lambda 5342$ to the C II M6 $\lambda 4267$ multiplet is 0.043, which agrees well with the predicted ratio 0.045 deduced from the data of Davey, Storey & Kisielius (2000).

A8 Multiplet 28.01, $3d'^2F^\circ - 3p'^2D$

See Section 3.1.2.

APPENDIX B: THE N II OPTICAL RECOMBINATION SPECTRUM

B1 Multiplet 3, $3p^3D - 3s^3P^\circ$

See Section 3.2.1.

B2 Multiplet 5, $3p^3P - 3s^3P^\circ$

The strongest component of the N II M5 multiplet, $\lambda 4630.54$ ($3p^3P_2 - 3s^3P_2^\circ$) is partially blended with the N III M2 $3d^2D_{3/2} - 3p^2P_{1/2}^\circ$ $\lambda 4634.14$ fluorescence line (Fig. 32). Gaussian profile fitting yields an intensity of 0.067 ± 0.013 for $\lambda 4630.54$. The intensity ratio of the $\lambda 4630.54$ line and the N II M3 $\lambda 5679.56$ line is 0.512, which agrees well with the predicted ratio 0.491. Another M5 line $\lambda 4601.48$ ($3p^3P_2 - 3s^3P_1^\circ$) is blended with the O II M92b

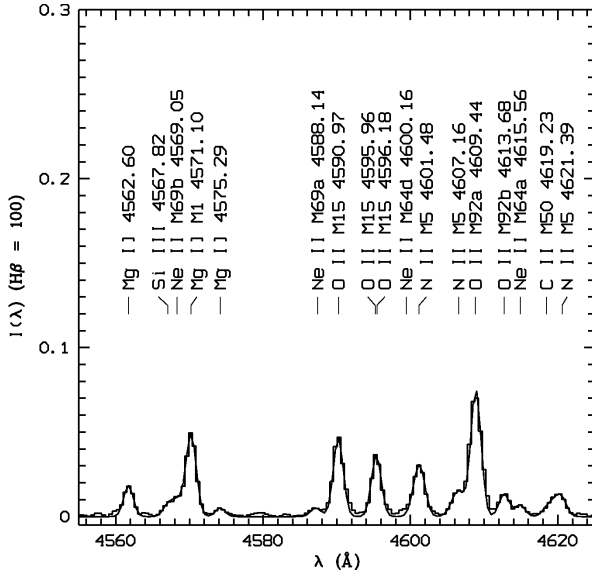


Figure B1. Spectrum of NGC 7009 from 4555 to 4625 Å showing the N II M5 lines and other emission features. Note the detection of the three Mg I lines of the $3s3p\ ^3P^{\circ} - 3s^2\ ^1S$ multiplet. The continuous curve is the sum of Gaussian profile fits. Continuum has been subtracted and the spectrum has been normalized such that H β has an integrated flux of 100. Extinction has not been corrected for.

$4f\ F[3]_{5/2}^{\circ} - 3d\ ^2D_{3/2}$ $\lambda 4602.13$ line, which contributes about 70 per cent to the total intensity, as estimated from the O II effective recombination coefficients of PJS.

The other four M5 lines all suffer from serious line blending: (1) The $\lambda 4607.16$ ($3p\ ^3P_1 - 3s\ ^3P_0^{\circ}$) line is blended with the [Fe III] $\lambda 4607.03$ line, whose contribution to the total intensity is uncertain. The blend at $\lambda 4607$ is again partially blended with a much stronger feature centered at $\lambda 4609$, which is a blend of O II M92a $4f\ F[4]_{7/2}^{\circ} - 3d\ ^2D_{5/2}$ $\lambda 4609.44$ and O II M92c $4f\ F[2]_{5/2}^{\circ} - 3d\ ^2D_{3/2}$ $\lambda 4610.20$ (Fig. B1). (2) The $\lambda 4613.87$ ($3p\ ^3P_1 - 3s\ ^3P_1^{\circ}$) line is blended with at least three lines, O II M92b $4f\ F[3]_{5/2}^{\circ} - 3d\ ^2D_{5/2}$ $\lambda 4613.14$, O II M92b $4f\ F[3]_{7/2}^{\circ} - 3d\ ^2D_{5/2}$ $\lambda 4613.68$, and Ne II M64b $4f\ F[2]_{3/2}^{\circ} - 3d\ ^4P_{5/2}$ $\lambda 4612.93$. (3) The $\lambda 4621.39$ ($3p\ ^3P_0 - 3s\ ^3P_1^{\circ}$) line is blended with at least two lines, O II M92c $4f\ F[2]_{5/2}^{\circ} - 3d\ ^2D_{5/2}$ $\lambda 4621.27$ and O II M92c $4f\ F[2]_{3/2}^{\circ} - 3d\ ^2D_{5/2}$ $\lambda 4622.14$. (4) The $\lambda 4643.09$ ($3p\ ^3P_1 - 3s\ ^3P_2^{\circ}$) line is blended with the N III M2 $\lambda\lambda 4640.64$ and 4641.85 fluorescence lines (Fig. 32). Accurate measurements of these four N II M5 lines are difficult.

B3 Multiplet 12, $3p\ ^1D - 3s\ ^1P^{\circ}$

This singlet ($\lambda 3994.99$) is shown in Fig. C3. Gaussian profile fitting yields an intensity of 0.033 ± 0.004 . The intensity ratio of the $\lambda 3994.99$ line to the N II M3 $\lambda 5679.56$ line is 0.257, which is higher than the theoretical prediction 0.123.

B4 Multiplet 19, $3d\ ^3F^{\circ} - 3p\ ^3D$

The M19 $\lambda 5004$ lines are blended with or seriously affected by the saturated [O III] $\lambda 5007$ line.

B5 Multiplet 20, $3d\ ^3D^{\circ} - 3p\ ^3D$

The M20 $\lambda 4803.29$ ($3d\ ^3D_3^{\circ} - 3p\ ^3D_3$) line is blended with the C II M17.08 $8g\ ^2G - 4f\ ^2F^{\circ}$ $\lambda 4802.70$ line, which contributes ~ 50 per cent to the total intensity of the blend at $\lambda 4803$, as estimated from the C II effective recombination coefficients of Davey, Storey & Kisielius (2000). The intensity of the $\lambda 4803.29$ line is 0.032 ± 0.016 . The intensity ratio of $\lambda 4803.29$ and the N II M3 $\lambda 5679.56$ line is 0.248, which agrees with the predicted value 0.282 within errors. The other M20 lines are not detected.

B6 Multiplet 28, $3d\ ^3D^{\circ} - 3p\ ^3P$

See Section 3.2.2.

B7 Multiplet 29, $3d\ ^3P^{\circ} - 3p\ ^3P$

Accurate measurements of this multiplet are difficult. Only the $\lambda 5454.22$ ($3d\ ^3P_0^{\circ} - 3p\ ^3P_1$) and $\lambda 5480.06$ ($3d\ ^3P_1^{\circ} - 3p\ ^3P_2$) lines are detected. The former line is blended with the S II M6 $4p\ ^4D_{7/2}^{\circ} - 4s\ ^4P_{5/2}$ $\lambda 5453.83$ line and the latter one is blended with the $\lambda 5478.10$ ($3d\ ^3P_2^{\circ} - 3p\ ^3P_1$) line of the same multiplet.

B8 $4f - 3d$ transitions

B8.1 Multiplet 39a, $4f\ G[7/2] - 3d\ ^3F^{\circ}$:

See Section 3.2.3.1.

B8.2 Multiplet 39b, $4f\ G[9/2] - 3d\ ^3F^{\circ}$:

See Section 3.2.3.2.

B8.3 Multiplet 38a, $4f\ F[5/2] - 3d\ ^3F^{\circ}$:

Accurate measurements of this multiplet are difficult. The $\lambda 4076.91$ ($4f\ F[5/2]_2 - 3d\ ^3F_2^{\circ}$) and $\lambda 4077.40$ ($4f\ F[5/2]_3 - 3d\ ^3F_2^{\circ}$) lines are blended with the [S II] $\lambda 4076.35$ ($3p\ ^2P_{1/2}^{\circ} - 3p\ ^3S_{3/2}$) line. The $\lambda 4086.83$ ($4f\ F[5/2]_2 - 3d\ ^3F_3^{\circ}$) and $\lambda 4087.30$ ($4f\ F[5/2]_3 - 3d\ ^3F_3^{\circ}$) lines are blended with the O II M48c $4f\ G[3]_{5/2}^{\circ} - 3d\ ^4F_{3/2}$ $\lambda 4087.15$ line. The other M38a line $\lambda 4100.97$ ($4f\ F[5/2]_3 - 3d\ ^3F_4^{\circ}$) line is blended with the H I $\lambda 4101$ line.

B8.4 Multiplet 38b, $4f\ F[7/2] - 3d\ ^3F^{\circ}$:

Accurate measurements of the M38b lines are difficult. The $\lambda 4073.04$ ($4f\ F[7/2]_3 - 3d\ ^3F_2^{\circ}$) line is blended with the much stronger O II M10 $\lambda 4072.16$ line. The $\lambda 4095.90$ ($4f\ F[7/2]_4 - 3d\ ^3F_4^{\circ}$) and $\lambda 4096.58$ ($4f\ F[7/2]_3 - 3d\ ^3F_4^{\circ}$) lines are blended with the N III M1 $3p\ ^2P_{3/2}^{\circ} - 3s\ ^2S_{1/2}$ $\lambda 4097.33$ fluorescence line. The other lines are not observed.

B8.5 Multiplet 43a, $4f\ F[5/2] - 3d\ ^1D^{\circ}$:

The intensity of the $\lambda 4176.16$ ($4f\ F[5/2]_3 - 3d\ ^1D_2^{\circ}$) line is 0.028 ± 0.004 , which includes the contribution from the N II M43a $4f\ F[5/2]_2 - 3d\ ^1D_2^{\circ}$ $\lambda 4175.66$ line (about 20 per cent).

B8.6 *Multiplet 43b, 4fF[7/2] – 3d¹D^o:*

The $\lambda 4171.61$ ($4fF[7/2]_3 - 3d^1D_2^o$) line is partially blended with the O II M19 $\lambda 4169.22$ line. The $\lambda 4171.61$ line has an intensity of 0.023 ± 0.003 , which agrees well with the predicted value (Table 3).

B8.7 *Multiplet 48a, 4fF[5/2] – 3d³D^o:*

The $\lambda 4241.78$ ($4fF[5/2]_3 - 3d^3D_2^o$) line coincides in wavelength with the N II M48b $4fF[7/2]_4 - 3d^3D_3^o$ $\lambda 4241.78$ line. The $\lambda 4236.91$ ($4fF[5/2]_2 - 3d^3D_1^o$) line is blended with the N II M48b $4fF[7/2]_3 - 3d^3D_2^o$ $\lambda 4237.05$ line (Fig. 31). Gaussian profile fitting yields an intensity of 0.055 ± 0.011 for the $\lambda 4236.91$ line, which includes the contribution from the N II M48b $\lambda 4237.05$ line (~ 30 per cent). The $\lambda 4236.91$ line intensity is 24 per cent higher than what is predicted (Table 3). Measurements of the other two M48a lines, $\lambda 4246.71$ ($4fF[5/2]_2 - 3d^3D_3^o$) and $\lambda 4247.20$ ($4fF[5/2]_3 - 3d^3D_3^o$) are difficult.

B8.8 *Multiplet 48b, 4fF[7/2] – 3d³D^o:*

The $\lambda 4241.78$ ($4fF[7/2]_4 - 3d^3D_3^o$) line coincides in wavelength with the N II M48a $4fF[5/2]_3 - 3d^3D_2^o$ $\lambda 4241.78$ line. The total intensity of the $\lambda 4242$ line agrees well with the predicted value (Table 3). The contribution from the blended Ne II M52c $4f2[1]_{3/2}^o - 3d^4D_{1/2}$ $\lambda 4242.04$ line (~ 10 – 15 per cent) is included. The contributions from the N II M48a $4fF[5/2]_2 - 3d^3D_2^o$ $\lambda 4241.24$ and M48b $\lambda 4242.49$ ($4fF[7/2]_3 - 3d^3D^o$) lines are negligible. The other M48b line $\lambda 4237.05$ ($4fF[7/2]_3 - 3d^3D_2^o$) is blended with the N II M48a $4fF[5/2]_2 - 3d^3D_1^o$ $\lambda 4236.91$ line, which contributes ~ 70 per cent to the total intensity.

B8.9 *Multiplet 49a, 4fG[7/2] – 3d³D^o:*

The $\lambda 4195.97$ ($4fG[7/2]_3 - 3d^3D_2^o$) line is blended with the N III M6 $3p'2D_{3/2} - 3s'2P_{1/2}$ $\lambda 4195.76$ line (Fig. 31), and contributes 8 per cent to the total intensity. The other two M49a lines, $\lambda 4199.98$ ($4fG[7/2]_4 - 3d^3D_3^o$) and $\lambda 4201.35$ ($4fG[7/2]_3 - 3d^3D_3^o$) are blended with the much stronger He II $11g^2G - 4f^2F^o$ $\lambda 4199.83$ line.

B8.10 *Multiplet 49b, 4fG[9/2] – 3d³D^o:*

The $\lambda 4181.10$ ($4fG[9/2]_4 - 3d^3D_3^o$) line is blended with the N II M50a $\lambda 4178.86$ ($4fD[5/2]_2 - 3d^3D_3^o$) and M50a $\lambda 4179.67$ ($4fD[5/2]_3 - 3d^3D_3^o$) lines, whose intensity contribution is less than 40 per cent. [Fe V] $\lambda 4180.60$ is probably also blended (Fig. 31), but its intensity is uncertain.

B8.11 *Multiplet 50a, 4fD[5/2] – 3d³D^o:*

The $\lambda 4169.38$ ($4fD[5/2]_2 - 3d^3D_1^o$) line is blended with the O II M19 $\lambda 4169.22$ line, which contributes ~ 70 per cent to the total intensity. The $\lambda 4178.86$ ($4fD[5/2]_2 - 3d^3D_3^o$) and $\lambda 4179.67$ ($4fD[5/2]_3 - 3d^3D_3^o$) lines are blended with the N II M49b $4f2[5]_4 - 3d^3D_3^o$ $\lambda 4181.10$ line, which contributes more than 60 per cent to total intensity. The other two M50a lines $\lambda 4173.57$ ($4fD[5/2]_2 - 3d^3D_2^o$) and $\lambda 4174.38$ ($4fD[5/2]_3 - 3d^3D_2^o$) are not observed.

B8.12 *Multiplet 50b, 4fD[3/2] – 3d³D^o:*

The $\lambda 4156.39$ ($4fD[3/2]_2 - 3d^3D_1^o$) and $\lambda 4157.01$ ($4fD[3/2]_1 - 3d^3D_1^o$) lines are blended with the O II M19 $\lambda 4156.53$ ($3d^4P_{3/2} - 3p^4P_{5/2}^o$) line, which contributes ~ 75 per cent to the total intensity of the blend at $\lambda 4157$. The other M50b lines are not observed.

B8.13 *Multiplet 55a, 4fD[5/2] – 3d³P^o:*

The $\lambda 4442.02$ ($4fD[5/2]_2 - 3d^3P_1^o$) line is blended with the Ne II M60b $4f1[4]_{7/2}^o - 3d^2F_{5/2}$ $\lambda 4442.69$ and O III M49b $5gF[3]_{2,3}^o - 4fD[3]_2$ $\lambda 4442.02$ lines. The Ne II line contributes ~ 40 – 50 per cent to the total intensity of the blend at $\lambda 4442$, while the contribution of the O III line is negligible. The corrected intensity of the $\lambda 4442.02$ line is higher than the theoretical prediction (Table 3). The other two M55a lines, $\lambda 4431.82$ ($4fD[5/2]_2 - 3d^3P_2^o$) and $\lambda 4432.74$ ($4fD[5/2]_3 - 3d^3P_2^o$) are blended with several weak Ne II line of the $4f-3d$ transition array, whose effective recombination coefficients are unavailable.

B8.14 *Multiplet 58a, 4fG[7/2] – 3d¹F^o:*

The $\lambda 4552.53$ ($4fG[7/2]_4 - 3d^1F_3^o$) line is blended with the Ne II M55d $4f2[2]_{5/2}^o - 3d^4F_{3/2}$ $\lambda 4553.17$ and Si III M2 $4p^3P_2^o - 4s^3S_1$ $\lambda 4552.62$ lines, whose intensities are unknown. The other M58a line $\lambda 4554.10$ ($4fG[7/2]_3 - 3d^1F_3^o$) is not observed.

B8.15 *Multiplet 58b, 4fG[9/2] – 3d¹F^o:*

The $\lambda 4530.41$ ($4fG[9/2]_4 - 3d^1F_3^o$) line is blended with the N III M3 $3p'4D_{1/2} - 3s'4P_{3/2}$ $\lambda 4530.86$ (Fig. 38), which contributes ~ 12 per cent to the total intensity. The intensity of the $\lambda 4530.41$ line is 0.049 ± 0.007 , which agrees with the theoretical prediction (Table 3).

B8.16 *Multiplet 61a, 4fD[5/2] – 3d¹P^o:*

The $\lambda 4694.64$ ($4fD[5/2]_2 - 3d^1P_1^o$) line is partially blended with the weak O II M1 $\lambda 4696.35$ ($3p^4D_{3/2} - 3s^4P_{5/2}$) line. The $\lambda 4694.64$ line has an intensity that is 50 per cent higher than what is predicted (Table 3). The intensity of this line is unreliable due to the weakness.

APPENDIX C: THE O II OPTICAL RECOMBINATION SPECTRUM

C1 *Multiplet 1, 3p⁴D^o – 3s⁴P*

See Section 3.3.1.

C2 *Multiplet 2, 3p⁴P^o – 3s⁴P*

The observed and predicted relative intensities of O II M2 lines with most reliable measurements are presented in Table C1. The features of these lines as well as results of Gaussian profile fitting are shown in Fig. C1. $\lambda 4349.43$ is clearly observed. A single Gaussian profile fit to the feature of $\lambda 4349.43$ gives an intensity of 0.195 ± 0.029 . The intensity ratio of the $\lambda 4349.43$ line to the O II M1 $\lambda 4649.13$ line is 0.292, slightly higher than the predicted value 0.274. The intensity of the $\lambda 4349.43$ line could be overestimated due to the saturated H I $\lambda 4340$ line (Fig. C1). The O II

Table C1. Comparison of the observed and predicted relative intensities of the O II M2 lines detected in the spectrum of NGC 7009. Only lines with the most reliable measurements are presented. Here an electron temperature of 1000 K and a density of 4300 cm^{-3} are assumed for the theoretical intensities I_{IC} .

Line	$J_2 - J_1$	I_{LS}	I_{IC}	I_{obs}	$\frac{I_{obs}}{I_{LS}}$	$\frac{I_{obs}}{I_{IC}}$
$\lambda 4317.14^a$	3/2–1/2	0.397	0.553	0.551	1.388	0.996
$\lambda 4319.63$	5/2–3/2	0.429	0.365	0.322	0.750	0.882
$\lambda 4325.76$	1/2–1/2	0.079	0.119	0.147	1.861	1.235
$\lambda 4349.43$	5/2–5/2	1.000	1.000	1.000	1.000	1.000
$\lambda 4366.89$	3/2–5/2	0.429	0.578	0.640	1.492	1.107

^a Corrected for the contribution from O II M53a $4f D[3]_{5/2}^o - 3d \ ^4P_{3/2}$ $\lambda 4317.70$, which is about 15 per cent.

M16 $3p' \ ^2D_{5/2}^o - 3s' \ ^2D_{5/2}$ $\lambda 4351.26$ and $3p' \ ^2D_{5/2}^o - 3s' \ ^2D_{3/2}$ $\lambda 4351.45$ lines are also blended with the $\lambda 4349.43$ line, but their contributions are probably insignificant.

Another three M2 lines, $\lambda\lambda 4317.14$, 4319.63 and 4325.76 , are less affected by the saturated H I $\lambda 4340$ line. $\lambda 4317.14$ blends with O II M53a $4f D[3]_{5/2}^o - 3d \ ^4P_{3/2}$ $\lambda 4317.70$, and this blended feature is partially resolved from $\lambda 4319.63$ (Fig. C1). Three O II M63c and two O II M78b lines are blended with the left wing of $\lambda 4317.14$, and we treated these five O II lines as a single component since they are all weak and have close wavelengths. Three Gaussian profiles were used to fit the complex. The resultant intensities of $\lambda 4317.14$ and $\lambda 4319.63$ both agree better with the newly predicted values (Table C1). The intensity contribution of the blended O II M53a $\lambda 4317.70$ line was estimated from the most recent effective recombination coefficients and was subtracted. $\lambda 4325.76$ is free of blend, and its fitted intensity (with an uncertainty of 10–20 per cent) also agrees better with the intermediate coupling prediction. The main source of uncertainties in the $\lambda 4325.76$ intensity is due to the saturated H I $\lambda 4340$ line, while those in $\lambda\lambda 4317.14$ and 4319.63 are mainly due to blending.

Measurements of the remaining three M2 lines, $\lambda\lambda 4336.86$, 4345.56 and 4366.89 , are difficult: the former two are blended with the saturated H I $\lambda 4340$ line, and the latter one is affected by [O III] $\lambda 4363$ (Fig. C1). The measurement of $\lambda 4366.89$ seems to agree with the predicted intensity (Table C1). The fitting error of the $\lambda 4363$ intensity is 12 per cent, but the actual uncertainty could be even larger. The contributions of O III M39a $5g G[4]_{3,4}^o - 4f F[3]_3$ $\lambda 4366.99$ and O II M75a $4f D[3]_{7/2}^o - 3d \ 2F_{5/2}$ $\lambda 4366.53$ were assumed to be negligible.

C3 Multiplet 5, $3p \ ^2D^o - 3s \ ^2P$

Accurate measurements of the three M5 lines are difficult. $\lambda 4414.90$ ($3p \ ^2D_{5/2}^o - 3s \ ^2P_{3/2}$) is partially resolved from another M5 line $\lambda 4416.97$ ($3p \ ^2D_{3/2}^o - 3s \ ^2P_{1/2}$), as is shown in Fig. C2. $\lambda 4414.90$ coincides in wavelength O III M46a $5g H[5]_5^o - 4f G[4]_4$ $\lambda 4414.85$, whose contribution to the total flux of the blend at $\lambda 4415$ was estimated from the effective recombination coefficients of Kisielius & Storey (1999). $\lambda 4414.90$ is also affected by at least three weak Ne II lines from the $4f-3d$ configuration, and for most these Ne II lines, the effective recombination coefficients are not available. The $\lambda 4416.97$ line is blended with N II M55b $4f D[3/2]_2 - 3d \ ^3P_2^o$ $\lambda 4417.07$, N II M55b $4f D[3/2]_1 - 3d \ ^3P_2^o$ $\lambda 4417.82$, Ne II M61d $4f 2[2]_{5/2}^o - 3d \ ^2D_{5/2}$ $\lambda 4416.76$ and Ne II M61d $4f 2[2]_{3/2}^o - 3d \ ^2D_{5/2}$ $\lambda 4416.77$. The contributions of the

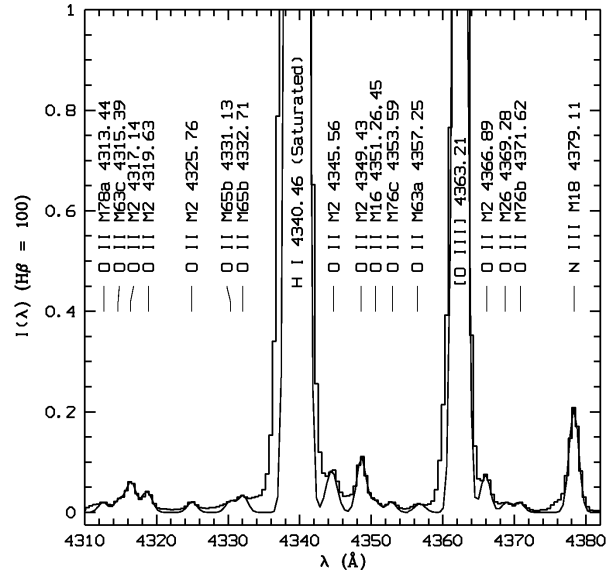


Figure C1. Spectrum of NGC 7009 from 4310 to 4382 Å showing the O II M2 lines and other O II ORLs. The continuous curve, which is the sum of Gaussian profiles, only shows the positions and possible profiles of some weak O II lines whose accurate measurements are difficult due to the strong [O III] $\lambda 4363$ and the saturated H I $\lambda 4340$ lines, both of which are assumed to be Gaussian. Global continuum has been subtracted and the spectrum has been normalized such that H β has an integrated flux of 100. Extinction has not been corrected for.

two N II lines to the total flux of the blend at $\lambda 4417$ were estimated from the new N II effective recombination coefficients, while those of the two Ne II lines could be negligible. The other line $\lambda 4452.37$ ($3p \ ^2D_{3/2}^o - 3s \ ^2P_{3/2}$) is blended with O III M49a $5g F[4]_{3,4}^o - 4f D[3]_3$ $\lambda 4454.03$ and [Fe II] $\lambda 4452.10$ (Fig. C2). The contribution from the O III $\lambda 4454.03$ line was estimated from the effective recombination coefficients of Kisielius & Storey (1999), but that of the [Fe II] line is uncertain.

C4 Multiplet 6, $3p \ ^2P^o - 3s \ ^2P$

The strongest M6 line $\lambda 3973.26$ ($3p \ ^2P_{3/2}^o - 3s \ ^2P_{3/2}$) is blended with the saturated H I $\lambda 3970$ line (Fig. C3). $\lambda\lambda 3945.04$ ($3p \ ^2P_{3/2}^o - 3s \ ^2P_{1/2}$) and 3954.36 ($3p \ ^2P_{1/2}^o - 3s \ ^2P_{1/2}$) are free of blend, but are affected by the saturated [Ne III] $\lambda 3967$ line (Fig. C3). The measured intensities of $\lambda 3945.04$ and $\lambda 3954.36$ are higher than the predicted values (in IC) by 45 and 83 per cent, respectively. Their measurements are of large uncertainties ($\gtrsim 30$ per cent).

Accurate measurements of the other M6 line $\lambda 3982.71$ ($3p \ ^2P_{1/2}^o - 3s \ ^2P_{3/2}$) are difficult due to the saturated H I $\lambda 3970$ line. It is also partially resolved from a weak feature that was identified as O III M43 $3d' \ ^3D_1 - 4d \ ^3P_1^o$ $\lambda 3985.55$. If this identification is correct, $\lambda 3982.71$ should blend with another O III M43 line $\lambda 3983.73$. Unfortunately no effective recombination coefficients for O III M43 are available for us to confirm the conjecture.

C5 Multiplet 10, $3d \ ^4F - 3p \ ^4D^o$

See Section 3.3.2.

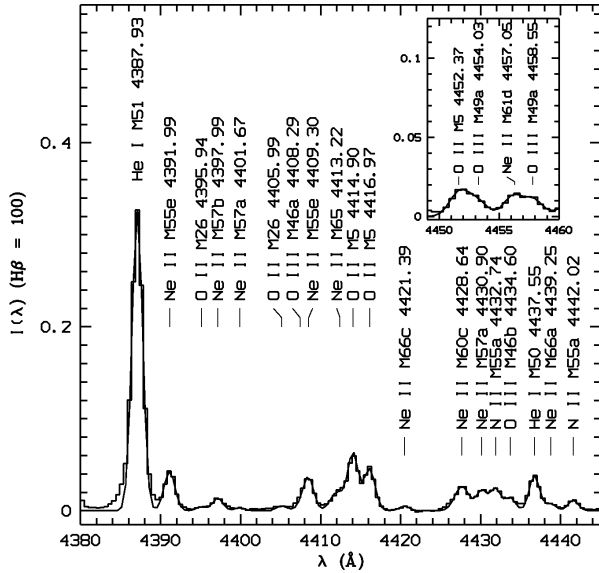


Figure C2. Spectrum of NGC 7009 from 4380 to 4445 Å showing the O II M5 lines and other emission features. Many Ne II lines of the 4f – 3d configuration are also detected. The inset shows the spectral region 4449–4460 Å, where the O II M5 $\lambda 4452.37$ line is located. The continuous curve is the sum of Gaussian profile fits. Continuum has been subtracted and the spectrum has been normalized such that H β has an integrated flux of 100. Extinction has not been corrected for.

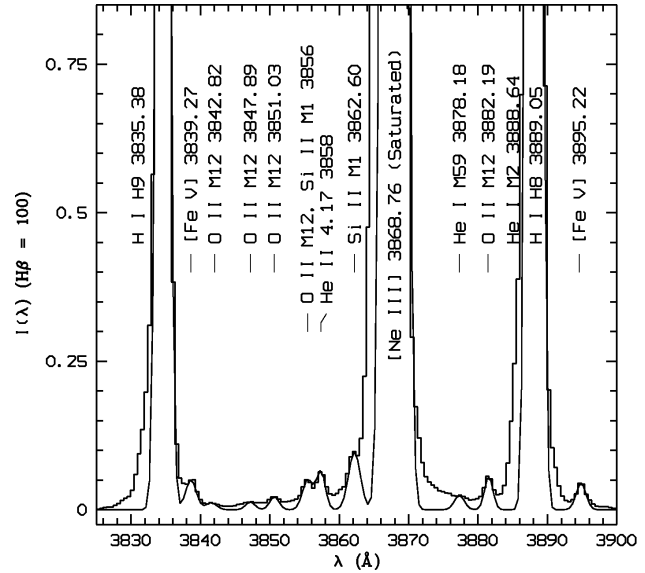


Figure C4. Spectrum of NGC 7009 from 3825 to 3900 Å showing the O II M12 features. The continuous curve, which is the sum of Gaussian profiles, only shows the positions and possible profiles of the weak lines whose accurate measurements are difficult due to the strong H I $\lambda 3889$ and the saturated [Ne III] $\lambda 3869$ lines. Global continuum has been subtracted and the spectrum has been normalized such that H β has an integrated flux of 100. Extinction has not been corrected for.

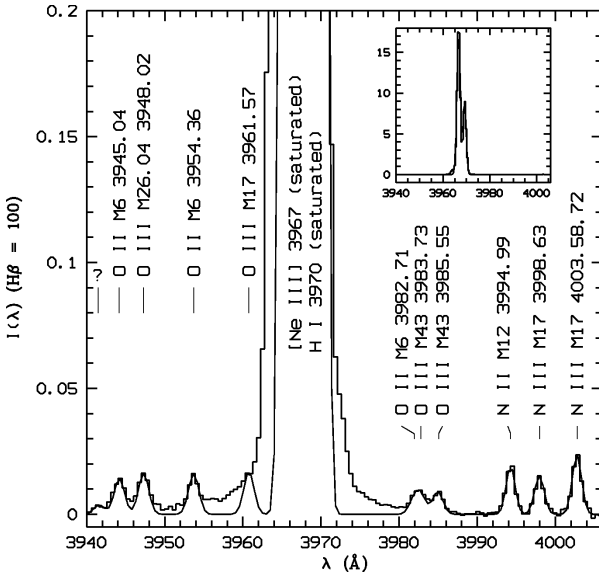


Figure C3. Spectrum of NGC 7009 from 3940 to 4006 Å showing the O II M6 lines and other emission features. The continuous curve is the sum of Gaussian profile fits. The profile of the O II M17 $\lambda 3961.57$ line, whose accurate measurement is impossible due to the saturated [Ne III] $\lambda 3967$ line, is only an estimate. The inset shows the profiles of the [Ne III] $\lambda 3967$ and H I $\lambda 3970$ lines, both of which are saturated but assumed to be Gaussian. Continuum has been subtracted and the spectrum has been normalized such that H β has an integrated flux of 100. Extinction has not been corrected for.

C6 Multiplet 12, 3d ⁴D – 3p ⁴D^o

The features of O II M12 lines are shown in Fig. C4. $\lambda 3882.19$ ($3d^4D_{7/2} - 3p^4D_{7/2}^o$) is close to H I $\lambda 3889$, which may affect its measurement. A single-Gaussian profile fit yields an intensity value of 0.084 ± 0.005 for the $\lambda 3882.19$ line. The intensity of the $\lambda 3882$ line, which is more than 50 per cent higher than the predicted value, is overestimated due to the saturated [Ne III] $\lambda 3868$. The other M12 lines are either much affected by the saturated [Ne III] line or are not observed due to weakness.

C7 Multiplet 19, 3d ⁴P – 3p ⁴P^o

The O II M19 lines are observed in Fig. C5, and the observed and predicted relative intensities are presented in Table C2. $\lambda 4169.22$ blends with He I M52 $6s^1S_0 - 2p^1P_1^o$ $\lambda 4168.97$ and N II M50a $4f^2[3]_2 - 3d^3D_1^o$ $\lambda 4169.38$. The He I $\lambda 4168.97$ line contributes 30 per cent to the total intensity, which was estimated from the theoretical He I line intensities of Benjamin, Skillman & Smits 1999, while the N II line was assumed to be negligible. The resultant intensity of the $\lambda 4169.22$ line is 0.082 ± 0.008 . The predicted intensity of this line is 0.090, which is derived from the most recent O II effective recombination coefficients (the measured intensity of O II M1 $\lambda 4649.13$ was used). The measured intensity ratio of $\lambda 4153.30$ to $\lambda 4169.22$ is much higher than the predicted value. No explanation can be given for this large discrepancy except there is unknown blend.

Although the measured intensity of $\lambda 4156.53$ is also higher than theory, its actual intensity should agree well with the predicted value, given the fact that it is blended with N II M50b $4f D[3/2]_2 - 3d^3D_1^o$ $\lambda 4156.39$ and N II M50b $4f D[3/2]_1 - 3d^3D_1^o$ $\lambda 4157.01$, which contribute about 25 per cent to the total flux of the blend at $\lambda 4156$. The measurements of another two M19 lines $\lambda \lambda 4129.32$ and 4132.80 both agree with the newly predicted intensities. These

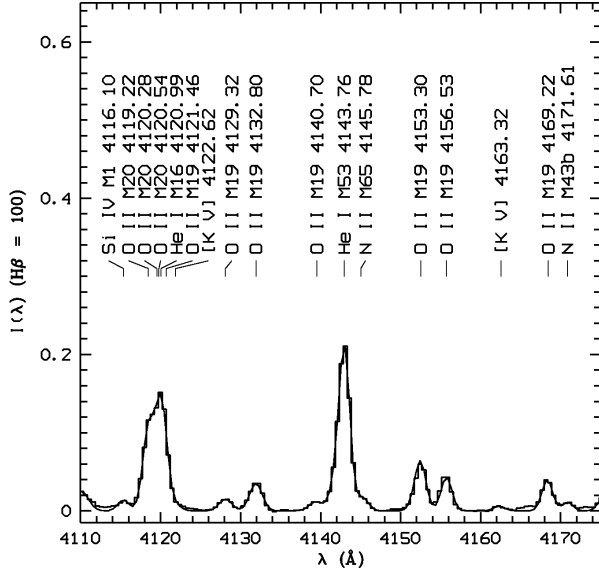


Figure C5. Spectrum of NGC 7009 from 4110 to 4175 Å showing the O II M19 lines and other emission features. The continuous curve is the sum of Gaussian profile fits. Continuum has been subtracted and the spectrum has been normalized such that H β has an integrated flux of 100. Extinction has not been corrected for.

Table C2. Same as Table C1 but for the O II M1 lines detected in the spectrum of NGC 7009.

Line	$J_2 - J_1$	I_{LS}	I_{IC}	I_{obs}	$\frac{I_{obs}}{I_{LS}}$	$\frac{I_{obs}}{I_{IC}}$
$\lambda 4129.32$	1/2–3/2	0.397	0.335	0.389	0.981	1.162
$\lambda 4132.80^a$	3/2–1/2	0.397	0.768	0.918	2.311	1.195
$\lambda 4140.70^b$	3/2–3/2	0.127	0.028	0.040	0.316	1.415
$\lambda 4153.30$	5/2–3/2	0.429	0.909	1.363	3.180	1.500
$\lambda 4156.53^c$	3/2–5/2	0.429	0.474	0.688	2.229	2.017
$\lambda 4169.22$	5/2–5/2	1.000	1.000	1.000	1.000	1.000

^a Probably including unknown blend.

^b Overestimated due to He I M53 He I M53 6d $^1D_2 - 2p \ ^1P_1^\circ$ $\lambda 4143.76$, which is stronger by early two orders of magnitude.

^c Neglecting N II M50b 4f D[3/2]₂ – 3d $^3D_1^\circ$ $\lambda 4156.39$ and N II M50b 4f D[2]₁ – 3d $^3D_1^\circ$ $\lambda 4157.01$, which contribute about 4 per cent to the total intensity.

two lines blend with three Si II M3 4f $^2F^\circ - 3d \ ^2D$ lines $\lambda\lambda 4128.07$, 4130.87 and 4130.89, whose contributions to the total flux are negligible. $\lambda 4140.70$ is overestimated due to the strength of He I M53 6d $^1D_2 - 2p \ ^1P_1^\circ$ $\lambda 4143.76$, which is more than 20 times stronger. Accurate measurements of the other line $\lambda 4121.46$ is impossible because it blends with He I M16 5s $^3S - 2p \ ^3P^\circ$ $\lambda 4120.99$ and three O II M20 lines (Fig. C5).

C8 Multiplet 20, 3d $^4D - 3p \ ^4P^\circ$

Three O II M20 lines $\lambda\lambda 4119.22$, 4120.28 and 4120.54 blend with He I M16 5s $^3S - 2p \ ^3P^\circ$ $\lambda 4120.99$ and O II M19 $\lambda 4121.46$. Accurate measurements of the lines are difficult. Three Gaussian profiles (the He I $\lambda 4120.99$ and O II M19 $\lambda 4121.46$ lines are treated as a single component, and the two O II $\lambda 4120$ lines are treated as another one) were used to fit the feature. The intensity ratio of the three O II M20 lines ($\lambda 4120.28 + \lambda 4120.54$)/ $\lambda 4119.22$ were as-

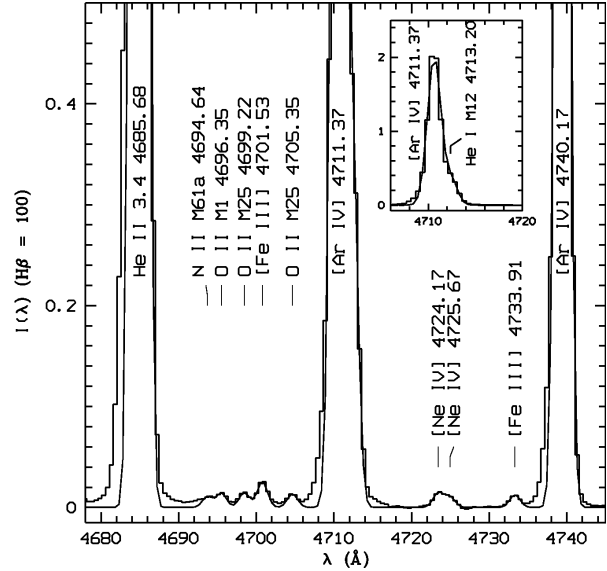


Figure C6. Spectrum of NGC 7009 from 4678 to 4745 Å showing the O II M25 lines and other emission features. The inset shows the [Ar IV] $\lambda 4711$ line blends with He I M12 $\lambda 4713.20$, which is 6 times fainter. The continuous curve is the sum of Gaussian profile fits. Continuum has been subtracted and the spectrum has been normalized such that H β has an integrated flux of 100. Extinction has not been corrected for.

sumed to be the predicted value (0.278), and the intensity of the He I $\lambda 4120.99$ line was estimated from the atomic data of Benjamin, Skillman & Smits (1999). The fitting results agree well with the observed spectrum, as is shown in Fig. C5. Accurate measurements of $\lambda 4110.79$ are also difficult due to the strong H I $\lambda 4101$ (Fig. 33). The other M20 lines are not observed.

C9 Multiplet 25, 3d $^2F - 3p \ ^2D^\circ$

Fig. C6 shows two O II M25 lines $\lambda\lambda 4699.22$ (5/2 – 3/2) and 4705.35 (7/2 – 5/2). $\lambda 4699.22$ is partially resolved from [Fe III] $\lambda 4701.53$, and it also blends with O II M40 3d' $^2F_{7/2} - 3p \ ^2D_{5/2}^\circ$ $\lambda 4699.00$ which contributes about 30 per cent to the total flux of the blend at $\lambda 4699$. $\lambda 4705.35$ is affected by the much stronger [Ar IV] $\lambda 4711$. The measured intensity ratio $\lambda 4699.22 : \lambda 4705.35$ is 0.779:1.00, which agrees with the newly predicted ratio 0.765:1, and differs from the value in pure LS coupling, i.e. 0.7:1.0. Here the contribution of the blended O II M40 $\lambda 4699.00$ line has been subtracted.

C10 Multiplet 28, 3d $^4P - 3p \ ^4S^\circ$

The three M28 lines are shown in Fig. C7. $\lambda 4924.53$ (5/2 – 3/2) is partially resolved from He I M48 4d $^1D_2 - 2p \ ^1P_1^\circ$ $\lambda 4921.93$, and the other two $\lambda 4890.86$ (1/2 – 3/2) and $\lambda 4906.83$ (3/2 – 3/2) are free of blend. The observed relative intensity of the three lines is 1.0:3.52:5.73, which deviates from the pure LS coupling ratio 1:2:3, and also differs from the newly predicted ratio in the intermediate coupling scheme is 3.49:2.09:1.0.

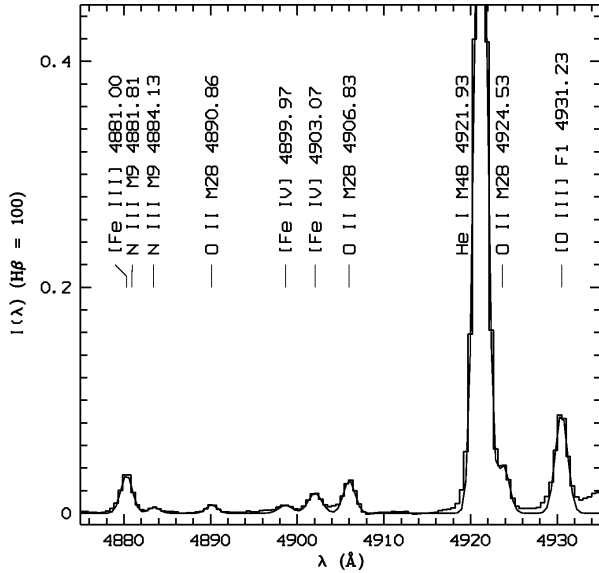


Figure C7. Spectrum of NGC 7009 from 4875 to 4935 Å showing the O II M28 lines and other emission features. The continuous curve is the sum of Gaussian profile fits. Continuum has been subtracted and the spectrum has been normalized such that H β has an integrated flux of 100. Extinction has not been corrected for.

C11 4f – 3d transitions

C11.1 Multiplet 48a, 4fG[5]^o – 3d⁴F

See Section 3.3.3.

C11.2 Multiplet 48b, 4fG[4]^o – 3d⁴F

$\lambda 4083.90$ (4f G[4]_{7/2}^o – 3d⁴F_{5/2}) blends with O II M10 3d⁴F_{5/2} – 3p⁴D_{5/2}^o $\lambda 4085.11$, which contributes more than 50 per cent to the total intensity. The other lines are not observed.

C11.3 Multiplet 48c, 4fG[3]^o – 3d⁴F

$\lambda 4087.15$ (4f G[3]_{5/1}^o – 3d⁴F_{3/2}) lies between the features of O II M48a $\lambda 4089.29$ and O II M10 $\lambda 4085.11$. Its intensity given by the fit agrees with the predicted value (Table 6), while the measurement uncertainty is large due to weakness. Here the contributions of the blended N II M38a 4f F[5/2]₂ – 3d³F₃^o $\lambda 4086.83$ and N II M38a 4f F[5/2]₃ – 3d³F₃^o $\lambda 4087.30$ lines were assumed to be negligible. The other M48c lines are not observed.

C11.4 Multiplet 50a, 4fF[4]^o – 3d⁴F

Only $\lambda 4062.94$ (4f F[4]_{9/2}^o – 3d⁴F_{9/2}) is observed, but its measurements are quite uncertain due to weakness.

C11.5 Multiplet 50b, 4fF[3]^o – 3d⁴F

Only $\lambda 4048.21$ (4f F[3]_{7/2}^o – 3d⁴F_{7/2}) is observed. $\lambda 4048.21$ blends with $\lambda 4047.80$ (4f F[3]_{5/2}^o – 3d⁴F_{7/2}), whose intensity was assumed to be negligible. The measured intensity of $\lambda 4048.21$ is slightly higher than the current prediction, but its uncertainty could be large due to weakness. $\lambda 4035.07$ (4f F[3]_{5/2}^o – 3d⁴F_{5/2}) and $\lambda 4035.46$ (4f F[3]_{7/2}^o – 3d⁴F_{5/2}) blend with N II M39a 4f G[7/2]₃

– 3d³F₂^o $\lambda 4035.08$ (Section 3.2.3.1), which contributes more than 80 per cent to the total intensity of the blend at $\lambda 4035$.

C11.6 Multiplet 50c, 4fF[2]^o – 3d⁴F

$\lambda 4032.48$ (4f F[2]_{5/2}^o – 3d⁴F_{3/2}) and $\lambda 4033.16$ (4f F[2]_{3/2}^o – 3d⁴F_{3/2}) blend with O II M50a 4f F[4]_{7/2}^o – 3d⁴F_{5/2} $\lambda 4032.25$, and measurements are difficult. $\lambda 4041.28$ (4f F[2]_{5/2}^o – 3d⁴F_{5/2}) and $\lambda 4041.95$ (4f F[2]_{3/2}^o – 3d⁴F_{5/2}) blended with N II M39b 4f G[9/2]₅ – 3d³F₄^o $\lambda 4041.31$, which contributes more than 90 per cent to the total intensity of the blend at $\lambda 4041$. The other line $\lambda 4054.08$ (4f F[2]_{5/2}^o – 3d⁴F_{7/2}) is not observed.

C11.7 Multiplet 53a, 4fD[3]^o – 3d⁴P

Only $\lambda 4303.82$ (4f D[3]_{7/2}^o – 3d⁴P_{5/2}) is observed, which is shown in Fig. 34. It blends with another M53a line $\lambda 4304.08$ (4f D[3]_{5/2}^o – 3d⁴P_{5/2}) and O II M65a 4f G[5]_{9/2}^o – 3d⁴D_{7/2} $\lambda 4303.61$, whose total intensity contribution to the blend amounts to about 15 per cent. The resultant measured intensity of $\lambda 4303.83$ agrees well with the most recent predicted value (Table 6). The other line $\lambda 4317.70$ (4f D[3]_{5/2}^o – 3d⁴P_{3/2}) is blended with O II M2 3p⁴P_{3/2}^o – 3s⁴P_{1/2} $\lambda 4317.14$ which is 5–6 times stronger.

C11.8 Multiplet 53b, 4fD[2]^o – 3d⁴P

$\lambda 4294.78$ (4f D[2]_{5/2}^o – 3d⁴P_{3/2}) coincides in wavelength with $\lambda 4294.92$ (4f D[2]_{3/2}^o – 3d⁴P_{3/2}) which contributes about 12 per cent to the total intensity of the feature at $\lambda 4295$. The total intensity of the two $\lambda 4295$ lines agrees with the new prediction. Another line $\lambda 4307.23$ (4f D[2]_{3/2}^o – 3d⁴P_{1/2}) is too weak to perform accurate measurements although it is observed (Fig. 34). The other M53b lines are not observed.

C11.9 Multiplet 53c, 4fD[1]^o – 3d⁴P

$\lambda 4288.82$ is a blend of two M53c lines (4f D[1]_{3/2}^o – 3d⁴P_{1/2} and 4f D[1]_{1/2}^o – 3d⁴P_{1/2}). The measured intensity of $\lambda 4288.82$ agrees with the newly predicted value, but is much lower than the one predicted based on the previous calculations (Table 6). The other lines are not observed.

C11.10 Multiplet 55, 4fG[3]^o – 3d⁴P

$\lambda 4291.25$ (4f G[3]_{7/2}^o – 3d⁴P_{5/2}) blends with O II M78c 4f F[2]_{9/2}^o – 3d²F_{5/2} $\lambda 4292.21$, which contributes about 38 per cent to the total intensity. The contribution from O II $\lambda 4291.86$ (4f G[3]_{5/2}^o – 3d⁴P_{5/2}) was assumed to be negligible. The other line $\lambda 4305.39$ is not observed.

C11.11 Multiplet 63a, 4fD[3]^o – 3d⁴D

Measurements of $\lambda 4357.25$ (4f D[3]_{7/2}^o – 3d⁴D_{5/2} and 4f D[3]_{5/2}^o – 3d⁴D_{3/2}) are affected by [O III] $\lambda 4363$, as well as the saturated H I $\lambda 4340$ line (Fig. C1). The other M63a lines are not observed.

C11.12 Multiplet 65a, 4fG[5]^o – 3d⁴D

$\lambda 4303.61$ (4f G[5]_{9/2}^o – 3d⁴D_{7/2}) blends with O II M53a 4f D[3]_{7/2}^o – 3d⁴P_{5/2} $\lambda 4303.82$, which is about 7–8 times stronger, and O II M53a 4f D[3]_{5/2}^o – 3d⁴P_{5/2} $\lambda 4304.08$, which contributes about 3 per cent to the total intensity of the blend at $\lambda 4304$.

C11.13 Multiplet 65b, 4fG[4]^o – 3d⁴D

Measurements of this multiplet are difficult due to the saturated H I $\lambda 4340$ line.

C11.14 Multiplet 65c, 4fG[3]^o – 3d⁴D

Measurements of this multiplet are difficult due to the saturated H I $\lambda 4340$ line.

C11.15 Multiplet 67a, 4fF[4]^o – 3d⁴D

In Fig. 34, the three lines of this multiplet blend with several O II ORLs of the 4f – 3d transition array. Using the effective recombination coefficients of PJS, we estimated that O II M67a $\lambda 4275.55$ contributes about 35 per cent to the broad feature at $\lambda 4275$, which is formed by more than 10 O II ORLs from the 4f – 3d configuration. The other two M67a lines contribute very little.

C11.16 Multiplet 67b, 4fF[3]^o – 3d⁴D

Measurements of this multiplet are difficult due to the reason given in Section C11.15. Using the new O II effective recombination coefficients, we estimated that the $\lambda 4276.75$ (4f F[3]_{7/2}^o – 3d⁴D_{5/2}) line, which is the strongest in O II M67b, contributes about 17 per cent to the total intensity of the feature at $\lambda 4275$.

C11.17 Multiplet 67c, 4fF[2]^o – 3d⁴D

Measurements of this multiplet are difficult due to blending.

C11.18 Multiplet 76b, 4fG[4]^o – 3d²F

$\lambda 4371.62$ (4f G[4]_{9/2}^o – 3d²F_{7/2}) blends with $\lambda 4371.24$ (4f G[4]_{7/2}^o – 3d²F_{7/2}) whose intensity contribution was assumed to be negligible. The measurement of $\lambda 4371.62$ agrees with the predicted intensity, but this intensity could be of large uncertainty due to weakness as well as the strength of [O III] $\lambda 4363$.

C11.19 Multiplet 76c, 4fG[3]^o – 3d²F

Only $\lambda 4353.59$ (4f G[3]_{7/2}^o – 3d²F_{5/2}) is observed, which is shown in Fig. C1. Its fitted intensity is higher than the newly predicted value. This measurement is overestimated due to the saturated H γ . The intensity contribution from $\lambda 4354.18$ (4f G[3]_{5/2}^o – 3d²F_{5/2}) was assumed to be negligible (only about 6 per cent). The other two M76c lines $\lambda 4384.70$ and $\lambda 4385.32$ are blended with He I M51 5d¹D₂ – 2p¹P₁^o $\lambda 4387.93$ (Fig. C2).

C11.20 Multiplet 78a, 4fF[4]^o – 3d²F

The measured intensity of $\lambda 4313.44$ (4f F[4]_{9/2}^o – 3d²F_{7/2}) agrees with the most recent prediction, but is probably of large uncertainty due to weakness. Here the contribution from $\lambda 4312.11$ (4f F[4]_{7/2}^o – 3d²F_{7/2}), which is about 32 per cent, has been corrected for. The other line $\lambda 4282.01$ (4f F[4]_{7/2}^o – 3d²F_{5/2}) is not observed.

C11.21 Multiplet 78b, 4fF[3]^o – 3d²F

$\lambda 4285.69$ (4f F[3]_{7/2}^o – 3d²F_{5/2}) blends with $\lambda 4285.21$ (4f F[3]_{5/2}^o – 3d²F_{5/2}) which contributes only about 1 per cent to the total intensity. It is also partially resolved from a feature at $\lambda 4283$, which is a blend of O II M67c 4f F[2]_{5/2}^o – 3d⁴D_{3/2} $\lambda 4282.96$ and Ne II M57c 4f 1[3]_{7/2}^o – 3d⁴F_{7/2} $\lambda 4283.73$. The fitted intensity of $\lambda 4285.69$ agrees with predicted value. The other lines are not observed.

C11.22 Multiplet 86a, 4fD[3]^o – 3d²P

In Fig. 35, $\lambda 4491.23$ (4f D[3]_{5/2}^o – 3d²P_{3/2}) is partially resolved from a feature at $\lambda 4488$ which is a blend of the O II M104 4f' D[2]_{3/2}^o – 3d'²P_{1/2} lines ($\lambda 4487.72$ 3/2 – 1/2, and $\lambda 4488.20$ 5/2 – 3/2 and 3/2 – 3/2) and O II M86b 4f D[2]_{3/2}^o – 3d²P_{1/2} $\lambda 4489.49$. Four Gaussian profiles were used to fit the complex. Since the effective recombination coefficients for the O II M104 lines are not available, we assumed that their relative intensities are as in pure LS coupling, i.e. 5 : 9 : 1. The resultant intensity of $\lambda 4491.23$ agrees well with the most recent theoretical value.

C11.23 Multiplet 86b, 4fD[2]^o – 3d²P

$\lambda 4489.49$ (4f D[2]_{3/2}^o – 3d²P_{1/2}) blends with O II M104 $\lambda 4488.20$ and O II M86a $\lambda 4491.23$. The fitted intensity of $\lambda 4489.49$ agrees with the newly predicted value quite well. Details of line fits are given in Section C11.22. Accurate measurements of $\lambda 4466.41$, 59 are difficult due to He I $\lambda 4471$, which is stronger by more than two orders of magnitude.

C11.24 Multiplet 88, 4fG[3]^o – 3d²P

$\lambda 4477.90$ (4f G[3]_{5/2}^o – 3d²P_{3/2}) is observed in Fig. 35. It is blended with O III M45a 5g H[11/2]_{5,6}^o – 4f G[9/2]₅ $\lambda 4477.91$, which contributes about 1–2 per cent to the total intensity and thus is negligible (an estimate based on the effective recombination coefficients for the O III 5g – 4f recombination spectrum given by Kisielius & Storey 1999). The measured intensity of $\lambda 4477.90$ agrees well with the newly predicted value (Table 6).

C11.25 Multiplet 92a, 4fF[4]^o – 3d²D

$\lambda 4609.44$ (4f F[4]_{7/2}^o – 3d²D_{5/2}) is observed in Fig. B1. It blends with O II M92c 4f F[2]_{5/2}^o – 3d²D_{3/2} $\lambda 4610.20$ and O II M92c 4f F[2]_{3/2}^o – 3d²D_{3/2} $\lambda 4611.07$, which contribute about 20 per cent to the total intensity. After subtracting the blend, the resultant intensity of $\lambda 4609.44$ agrees well with the new prediction (Table 6).

C11.26 Multiplet 92b, $4fF[3]^\circ - 3d^2D$

$\lambda 4602.13$ ($4fF[3]_{5/2}^\circ - 3d^2D_{3/2}$) is observed in Fig. B1. It blends with N II M5 $3p^3P_2 - 3s^3P_1^\circ$ $\lambda 4601.48$, which contributes about 26 per cent to the total intensity. Subtraction of the blend gives an intensity of $\lambda 4602.13$ that agrees well with the most recent prediction. The contribution from Ne II M64d $4f2[2]_{5/2}^\circ - 3d^4P_{5/2}$ $\lambda 4600.16$ was assumed to be negligible. Fig. B1 also shows the weak feature of $\lambda 4613.14$ ($4fF[3]_{5/2}^\circ - 3d^2D_{5/2}$) which blends with $\lambda 4613.68$ ($4fF[3]_{7/2}^\circ - 3d^2D_{5/2}$). The total measured intensity of the two lines agrees with both of the predicted values (Table 6). Correction has been made for the contribution from N II M5 $3p^1P_1 - 3s^3P_1^\circ$ $\lambda 4613.87$, which is about 7 per cent, and the contribution from Ne II M64b $4f2[3]_{7/2}^\circ - 3d^4P_{5/2}$ $\lambda 4612.93$ was assumed to be negligible.

APPENDIX D: THE NE II OPTICAL RECOMBINATION SPECTRUM

D1 Multiplet 1, $3p^4P^\circ - 3s^4P$

Fig. F5 shows that $\lambda 3694.21$ ($3p^4P_{5/2}^\circ - 3s^4P_{5/2}$) lies between the two H I lines H18 $\lambda 3691.55$ and H17 $\lambda 3697.15$. The fitted intensity of $\lambda 3694.21$ is 0.254 ± 0.026 . This measurement agrees with the values of LLB01: 0.294 (ESO 1.52 m) and 0.224 (WHT). Another M1 line $\lambda 3777.14$ ($3p^4P_{3/2}^\circ - 3s^4P_{1/2}$) is observed in Fig. F1. Its measured intensity is 0.050, with an uncertainty of about 20 to 25 per cent, and also agrees with LLB01: 0.045 (ESO 1.52 m) and 0.059 (WHT). The intensity ratio $\lambda 3777.14/\lambda 3694.21$ is 0.195, lower than the *LS* coupling ratio 0.397. The other lines are not observed.

D2 Multiplet 2, $3p^4D^\circ - 3s^4P$

See Section 3.4.1.

D3 Multiplet 5, $3p^2D^\circ - 3s^2P$

Fig. F5 shows that $\lambda 3713.08$ ($3p^2D_{5/2}^\circ - 3s^2P_{3/2}$) is blended with H I H15 $\lambda 3711.97$, which is more than 5 times stronger. Also blended here is O III M3 $3d^3D_3^\circ - 3p^3P_2$ $\lambda 3715.08$. Three Gaussian profiles were used to fit the complex, and the fitted intensity of $\lambda 3713.08$ is 0.306, which could be of large uncertainty (over 50 per cent). The intensity ratio of $\lambda 3713.08$ to Ne II M2 $\lambda 3334.84$ agrees with the *LS* coupling ratio. The other M2 lines are not observed.

D4 Multiplet 6, $3p^2S^\circ - 3s^2P$

$\lambda 3481.93$ ($3p^2S_{1/2}^\circ - 3s^2P_{3/2}$) is partially resolved from He I M43 $15d^3D - 2p^3P^\circ$ $\lambda 3478.97$, which is about 2 times stronger. The fitted intensity of $\lambda 3481.93$ is 0.043, which is slightly lower than LLB01 (0.051). The other line $\lambda 3557.81$ is not observed.

D5 Multiplet 8, $3d^4D - 3p^4P^\circ$

The wavelengths of the Ne II M8 lines are in the range 3017–3054 Å. The blue cutoff of our spectrum is around 3040 Å, and only three lines have the wavelengths longer than this cutoff. Measurements of these lines are difficult: The $\lambda\lambda 3045.56$ and 3047.56 lines

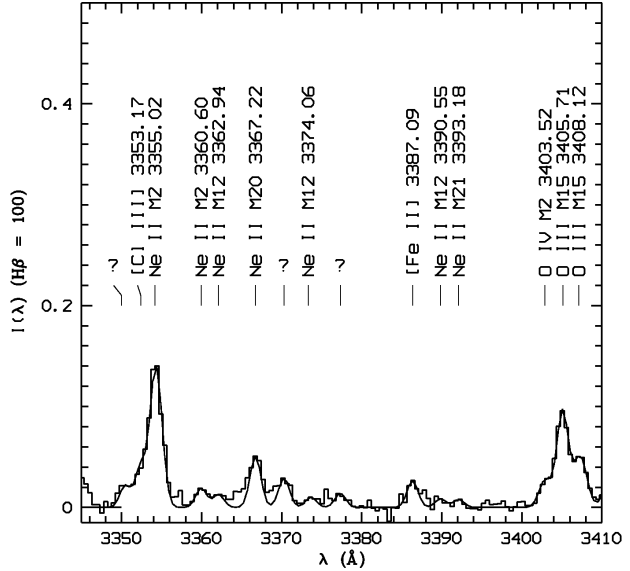


Figure D1. Spectrum of NGC 7009 from 3345 to 3410 Å showing the Ne II M12 $3d^4D - 3p^4D^\circ$ lines. Also detected in this region are the Ne II lines of the M2 $3p^4D^\circ - 3s^4P$, M20 $3d^2F - 3p^2D^\circ$ and M21 $3d^2D - 3p^2D^\circ$ multiplets. The continuous curve is the sum of Gaussian profile fits. Continuum has been subtracted and the spectrum has been normalized such that H β has an integrated flux of 100. Extinction has not been corrected for.

are blended with the much stronger O III M4 $\lambda 3047.12$ ($3p^3P_2 - 3s^3P_2^\circ$) line, which is affected by the Bowen fluorescence mechanism; the $\lambda 3054.67$ line is not observed.

D6 Multiplet 12, $3d^4D - 3p^4D^\circ$

The intensity of $\lambda 3329.16$ is 0.053, which is slightly higher than that of LLB01 (0.0464). This measurement is of large uncertainty due to weakness of the line, as is shown in Fig. F2. Another M12 line $\lambda 3366.98$ blends with Ne II M20 $3d^2F_{7/2} - 3p^2D_{5/2}^\circ$ $\lambda 3367.22$ (Fig. D1), which contributes more than 90 per cent to the total intensity. The other M12 lines are not observed.

D7 Multiplet 13, $3d^4F - 3p^4D^\circ$

See Section 3.4.2.

D8 Multiplet 20, $3d^2F - 3p^2D^\circ$

$\lambda 3367.22$ ($3d^2F_{7/2} - 3p^2D_{5/2}^\circ$) blends with Ne II M12 $3d^4D_{7/2} - 3p^4D_{5/2}^\circ$ $\lambda 3366.98$, whose intensity contribution is negligible (Section D6). The fitted intensity of $\lambda 3367.22$ is 0.106 ± 0.016 , which agrees with that of LLB01 (0.110). The other M20 lines are not observed.

D9 Multiplet 21, $3d^2D - 3p^2D^\circ$

Fig. 40 shows that $\lambda 3416.91$ ($3d^2D_{5/2} - 3p^2D_{5/2}^\circ$) is partially resolved from O III M15 $3d^3P_1 - 3p^3P_1$ $\lambda 3415.26$, which is excited by the Bowen fluorescence mechanism. It also blends with Ne II M19 $3d^4F_{7/2} - 3p^2D_{5/2}^\circ$ $\lambda 3417.69$, whose intensity contribution is unknown due to the lack of atomic data. The total intensity of the feature at $\lambda 3417$ given by fit is 0.114, higher than the measurement of LLB01 (0.0825). The other M21 lines are not observed.

D10 Multiplet 28, $3d^2P - 3p^2S^\circ$

The fitted intensity of $\lambda 3456.61$ ($3d^2P_{3/2} - 3p^2S_{1/2}^\circ$) is 0.031, which is slightly lower than the intensity value 0.0334 given by LLB01. Here the contribution from He I $19d^3D - 2p^3P^\circ$ $\lambda 3456.86$ was assumed to be negligible. The other line $\lambda 3503.58$ is not observed.

D11 Multiplet 34, $3d^4P - 3p^4S^\circ$

The measured intensity of $\lambda 3542.85$ ($3d^4P_{5/2} - 3p^4S_{3/2}^\circ$) and is 0.031, which agrees with the measurement given by LLB01 (0.0325). Fig. 37 shows that $\lambda 3565.82$ ($3d^4P_{3/2} - 3p^4S_{3/2}^\circ$) is partially resolved from Ne II M9 $3p^2F_{7/2}^\circ - 3s^2D_5$ $\lambda 3568.50$, which is about 7 times stronger. The fitted intensity of $\lambda 3565.82$ is 0.025, with a relatively large uncertainty due to the weakness. This measurement also agrees with that of LLB01 (0.0243). The intensity ratio of these two M34 lines is thus 1.24:1.0, which differs from the LS coupling value 1.5:1. The other line $\lambda 3594.16$ is not observed.

D12 Multiplet 9, $3p^2F^\circ - 3s^2D$

See Section 3.4.3.

D13 4f – 3d transitions*D13.1 Multiplet 55e, $4f2[5]^\circ - 3d^4F$*

See Section 3.4.4.

D13.2 Multiplet 52a, $4f2[4]^\circ - 3d^4D$

$\lambda 4219.75$ ($4f 2[4]_{9/2}^\circ - 3d^4D_{7/2}$) blends with Ne II M52a $4f 2[4]_{7/2}^\circ - 3d^4D_{7/2}$ $\lambda 4219.37$ and Ne II M52d $4f 2[2]_{5/2}^\circ - 3d^4D_{5/2}$ $\lambda 4220.89$ (Fig. 31). The intensity contribution of $\lambda 4219.37$ (a few per cent) could be negligible. The fitted intensity of $\lambda 4219.75$ is 0.064, which agrees with the measurements given by LLB01: 0.0674 (ESO 1.52 m), 0.0699 (WHT 1996) and 0.0616 (WHT 1997). This measurement is higher than the predicted value (Table 8). The measured intensity of the other line $\lambda 4233.85$ agrees well with LLB01, but is higher than the predicted value. This measurement is probably unreliable due to weakness of the $\lambda 4233.85$ line.

D13.3 Multiplet 52b, $4f2[3]^\circ - 3d^4D$

The measured intensity of $\lambda 4231.64$ ($4f 2[3]_{7/2}^\circ - 3d^4D_{5/2}$) is 0.027, which agrees with the measurements of LLB01: 0.0244 (ESO 1.52m), 0.0328 (WHT 1996) and 0.0237 (WHT 1997). Here the contribution of $\lambda 4231.53$ ($4f 2[3]_{5/2}^\circ - 3d^4D_{5/2}$) is included. The intensity of another M52b line $\lambda 4250.65$ is 0.016, and it also agrees with those of LLB01: 0.0169 (ESO 1.52 m) and 0.0154 (WHT 1996), and 0.0121 (WHT 1997). Both measurements are higher than the predicted values (Table 8), thus $\lambda 4231.64$ and $\lambda 4250.65$ are not used for abundance determinations. The other two lines $\lambda 4217.17$ and $\lambda 4217.15$ are too faint to measure accurately.

D13.4 Multiplet 57b, $4f1[4]^\circ - 3d^4F$

Only $\lambda 4397.99$ ($4f 1[4]_{7/2}^\circ - 3d^4F_{5/2}$) is observed (Fig. C2). Its fitted intensity is 0.024 ± 0.004 . This intensity value is slightly higher than those given by LLB01: 0.0219 (ESO 1.52 m), 0.0184 (WHT 1996) and 0.0185 (WHT 1997), but agrees with the predicted value within errors (Table 8). The other M57b lines are not observed.

D13.5 Multiplet 60c, $4f1[3]^\circ - 3d^2F$

Only $\lambda 4428.64$ ($4f 1[3]_{7/2}^\circ - 3d^2F_{5/2}$) is observed, and its fitted intensity is 0.044, which agrees with the measurements given by LLB01: 0.0483 (ESO 1.52 m), 0.0451 (WHT 1996) and 0.0479 (WHT 1997). Here the contribution from Ne II M61b $4f 2[3]_{7/2}^\circ - 3d^2D_{5/2}$ $\lambda 4428.52$ is included, but the other two blended lines Ne II M60c $4f 1[3]_{5/2}^\circ - 3d^2F_{5/2}$ $\lambda 4428.52$ and Ne II M61b $4f 2[3]_{5/2}^\circ - 3d^2D_{5/2}$ $\lambda 4428.41$ were assumed to be negligible.

D13.6 Multiplet 61a, $4f2[4]^\circ - 3d^2D$

The measured intensity of $\lambda 4430.94$ ($4f 2[4]_{7/2}^\circ - 3d^2D_{5/2}$) is 0.040, which is higher than the observations of LLB01: 0.0331 (ESO 1.52 m), 0.0340 (WHT 1996) and 0.0317 (WHT 1997). This measurement is of large uncertainty due to blending. The contribution from Ne II M57a $4f 1[2]_{5/2}^\circ - 3d^4F_{3/2}$ $\lambda 4430.90$ and Ne II M55a $4f 2[4]_{9/2}^\circ - 3d^4F_{7/2}$ $\lambda 4430.06$ are included, but Ne II M57a $4f 1[2]_{3/2}^\circ - 3d^4F_{3/2}$ $\lambda 4431.11$ was assumed to be negligible.

D13.7 Multiplet 61d, $4f2[2]^\circ - 3d^2D$

$\lambda 4457.05$ ($4f 2[2]_{5/2}^\circ - 3d^2D_{3/2}$) is partially resolved from O III M49a $5g F[4]_3^\circ - 4f D[3]_2$ $\lambda 4458.55$ (Fig. 35). The fitted intensity of $\lambda 4457.05$ is 0.026, with an uncertainty of about 20 per cent. Here the contribution from Ne II M66c $4f 1[3]_{7/2}^\circ - 3d^4P_{5/2}$ $\lambda 4457.36$ is included, but the other two blended lines Ne II M61d $4f 2[2]_{3/2}^\circ - 3d^2D_{3/2}$ $\lambda 4457.24$ and Ne II M66c $4f 1[3]_{5/2}^\circ - 3d^4P_{5/2}$ $\lambda 4457.24$ were assumed to be negligible. This measurement agrees with those of LLB01: 0.0250 (ESO 1.52 m), 0.0247 (WHT 1996) and 0.0211 (WHT 1997), but is much higher than the predicted value (Table 8). The other M61d lines are not observed.

D13.8 Multiplet 65, $4f0[3]^\circ - 3d^4P$

$\lambda 4413.22$ ($4f 0[3]_{7/2}^\circ - 3d^4P_{5/2}$) blends with O II M5 $3p^2D_{5/2}^\circ - 3s^2P_{3/2}$ $\lambda 4414.90$ (Fig. C2). The fitted intensity of $\lambda 4413.22$ is 0.028, which agrees with the measurements of LLB01: 0.0296 (ESO 1.52 m), 0.0243 (WHT 1996) and 0.0271 (WHT 1997), but is higher than the predicted value (Table 8). Here the contribution from Ne II M65 $4f 0[3]_{5/2}^\circ - 3d^4P_{5/2}$ $\lambda 4413.11$ was assumed to be negligible, but Ne II M57c $4f 1[3]_{5/2}^\circ - 3d^4F_{3/2}$ $\lambda 4413.11$ is included. The other line $\lambda 4377.98$ blends with N III M18 $\lambda 4379$.

D13.9 Multiplet 66c, $4f1[3]^\circ - 3d^4P$

$\lambda 4421.39$ ($4f 1[3]_{5/2}^\circ - 3d^4P_{3/2}$) is observed in Fig. C2. Its fitted intensity is 0.0084. The uncertainty of this measurement could be large due to weakness of this line. The other two M66c lines $\lambda 4457.24$ and $\lambda 4457.36$ blend with Ne II M61d $4f 2[2]_{5/2}^\circ - 3d^2D_{3/2}$ $\lambda 4457.05$.

APPENDIX E: THE N III PERMITTED LINES
E1 Multiplet 1, $3p^2P^{\circ} - 3s^2S$

$\lambda 4097.33$ is partially resolved from H I $\lambda 4101$ (Fig. 33). Its fitted intensity is 2.246 ± 0.112 . Several O II and N II ORLs are blended with $\lambda 4097.33$, and they contribute about 15–20 per cent to the total intensity. The other line $\lambda 4103.39$ blends with H I $\lambda 4101$, and contributes less than 1 per cent to the total intensity.

E2 Multiplet 2, $3d^2D - 3p^2P^{\circ}$

Measurements of this multiplet are presented in Section 3.3.1. Here the ratio of the two lines $\lambda \lambda 4634.14$ and 4641.85 were assumed to be as in *LS* coupling. The resultant intensities of the $\lambda \lambda 4634.14$, 4640.64 and 4641.85 lines are 1.133, 2.262 and 0.226, respectively, and the uncertainties are all less than 10 per cent. Thus the intensity ratio of $\lambda 4640.64$ to $\lambda 4641.85$ is 10:1, which differs from the pure *LS* coupling ratio, i.e. 9:1.

E3 Multiplet 3, $3p^4D - 3s^4P^{\circ}$

See Section 3.6.1.

E4 Multiplet 6, $3p^2D - 3s^2P^{\circ}$

$\lambda 4195.76$ ($3p^2D_{3/2} - 3s^2P^{\circ}_{1/2}$) is observed in Fig. 31. Its measured intensity is 0.046 ± 0.008 . Here the intensity contribution from N II M49a $4f^2[4]_3 - 3d^3D^{\circ}_2$ $\lambda 4195.97$, which is about 8 per cent, has been corrected for. Another line $\lambda 4215.77$ ($3p^2D_{3/2} - 3s^2P^{\circ}_{3/2}$) is partially resolved from Ne II M52b $4f^2[3]_{7/2} - 3d^4D_{7/2}$ $\lambda 4217.17$. Two Gaussian profiles were used to fit the complex, and the fitted intensity of $\lambda 4215.77$ is 0.0086, with an uncertainty of more than 20 per cent. Thus the ratio $\lambda 4195.76/\lambda 4215.77$ is 0.185, slightly higher than the *LS* coupling value (0.20). This is interesting because these two lines decay from the same upper level, thus their intensity ratio depends only on the coupling scheme. The other line $\lambda 4200.10$ ($3p^2D_{5/2} - 3s^2P^{\circ}_{3/2}$) blends with He II 11g $^2G - 4f^2F^{\circ}$ $\lambda 4199.83$ which is probably about 4 times stronger.

E5 Multiplet 9, $3d^4F^{\circ} - 3p^4D$

Only $\lambda 4881.81$ ($3d^4F^{\circ}_{3/2} - 3p^4D_{5/2}$) and $\lambda 4884.13$ ($3d^4F^{\circ}_{7/2} - 3p^4D_{7/2}$) are observed (Fig. C7). $\lambda 4881.81$ blends with [Fe III] $\lambda 4881.00$, whose intensity contribution is unknown. Measurements of $\lambda 4884.13$ are of large uncertainty due to weakness of the line.

E6 Multiplet 12, $5s^2S - 4p^2P^{\circ}$

Measurements of $\lambda 4544.85$ ($5s^2S_{1/2} - 4p^2P^{\circ}_{3/2}$) could be overestimated due to the strength of He II 9g $^2G - 4f^2F^{\circ}$ $\lambda 4541.59$ (Fig. 38), which is more than 10 times stronger. The other line $\lambda 4539.71$ is blended with He II $\lambda 4541.59$.

E7 Multiplet 17, $5f^2F^{\circ} - 4d^2D$

$\lambda 3998.63$ ($5f^2F^{\circ}_{5/2} - 4d^2D_{3/2}$) is detected in Fig. C3. Its fitted intensity is 0.025 ± 0.005 . The other two lines $\lambda \lambda 4003.58$ and 4003.72 are blending together. The measured intensity ratio ($\lambda 4003.58 + \lambda 4003.72$)/ $\lambda 3998.63$ is 1.54, which agrees with the value in *LS* coupling, i.e. 1.50.

Table F1. Comparison of the observed and predicted (in the *LS* coupling assumption) relative intensities of O III M2 lines in NGC 7009.

Line	$J_2 - J_1$	I_{LS}	I_{obs}	$\frac{I_{obs}}{I_{LS}}$
$\lambda 3754.69$	2–1	0.536	0.361	0.673
$\lambda 3757.24$	1–0	0.238	0.196	0.823
$\lambda 3759.87$	3–2	1.000	1.000	1.000
$\lambda 3774.02$	1–1	0.179	0.092	0.516
$\lambda 3791.27$	2–2	0.179	0.098	0.548

E8 Multiplet 18, $5g^2G - 4f^2F^{\circ}$

See Section 3.6.2.

APPENDIX F: THE O III PERMITTED LINES
F1 Multiplet 2, $3p^3D - 3s^3P^{\circ}$

Table F1 presents the observed and predicted relative intensities of the O III M2 lines detected in NGC 7009. Fig. F1 shows the observed M2 lines. $\lambda 3757.24$ is partially resolved from $\lambda 3754.69$ and $\lambda 3759.87$. Three Gaussian profile fits were used to fit the complex, and resultant relative intensities deviate from *LS* coupling. The uncertainty of the $\lambda 3757.24$ intensity is the largest among the three (over 30 per cent), because it also blends with He I M66 $14d^1D_2 - 2p^1P^{\circ}_1$ $\lambda 3756.10$, whose contribution is unknown, and He II $23g^2G - 4f^2F^{\circ}$ $\lambda 3758.15$, which contributes less than 10 per cent to the total intensity (an estimate based on the hydrogenic theory of Storey & Hummer 1995). The uncertainties of $\lambda \lambda 3754.69$ and 3759.87 are both less than 5 per cent. Measurements of $\lambda 3774.02$ is probably of large error due to the strength of H I H11 $\lambda 3770.63$, which is more than 20 times stronger. Another line $\lambda 3791.27$ is free of blend, but its fitted intensity is 45 per cent lower than the value in pure *LS* coupling. The other line $\lambda 3810.99$ is not observed. Both of the line ratios $\lambda 3791.27/\lambda 3754.69$ and $\lambda 3774.02/\lambda 3757.24$, where the two lines of each of the ratios decay from the same upper levels, differ from the *LS* coupling assumption, and agree with the measurements given by Liu et al. (1993a) for NGC 7009. Discussion of these line ratios is in Section 3.7.4.

F2 Multiplet 3, $3p^3S - 3s^3P^{\circ}$

Fig. F2 shows the observed O III M3 lines in NGC 7009. $\lambda 3340.76$ blends with the [Ne III] auroral line $2p^4^1S_0 - 2p^4^1D_2$ $\lambda 3342.50$ and Ne II M2 $3p^4D^{\circ}_{1/2} - 3s^4P_{1/2}$ $\lambda 3344.40$. The intensity of [Ne III] $\lambda 3342.50$ was estimated from the theoretical nebular-to-auroral line ratio ($\lambda \lambda 3868.76 + 3967.47$)/ $\lambda 3342.50$ which was calculated by solving the population equations for a five-level atomic model at a particular N_e and T_e . We estimated that [Ne III] $\lambda 3342.50$ contributes about 12 per cent to the total intensity of the blend at $\lambda 3341$. The contribution from Ne II M2 $\lambda 3344.40$ is negligible. The resultant $\lambda 3299.40/\lambda 3340.76$ and $\lambda 3312.32/\lambda 3340.76$ ratios are discussed in Section 3.7.4.

F3 Multiplet 4, $3p^3P - 3s^3P^{\circ}$

Only $\lambda 3047.12$ and $\lambda 3059.30$ are observed in the near-UV, but their measurements are quite unreliable due to poor S/N.

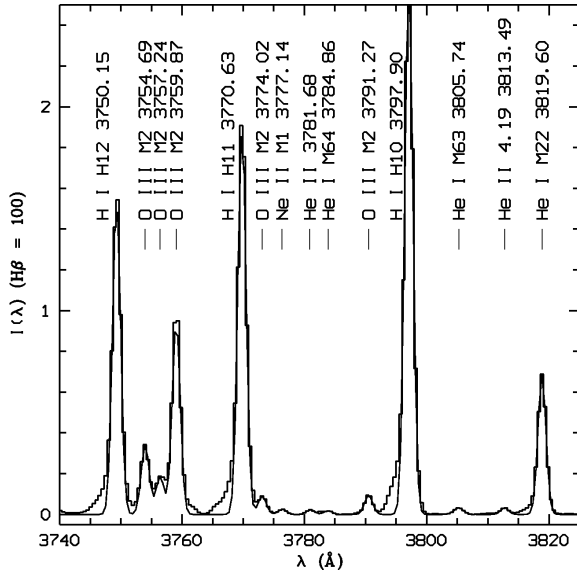


Figure F1. Spectrum of NGC 7009 from 3740 to 3825 Å showing the O III M2 lines and other emission features. The continuous curve is the sum of Gaussian profile fits. Continuum has been subtracted and the spectrum has been normalized such that H β has an integrated flux of 100. Extinction has not been corrected for.

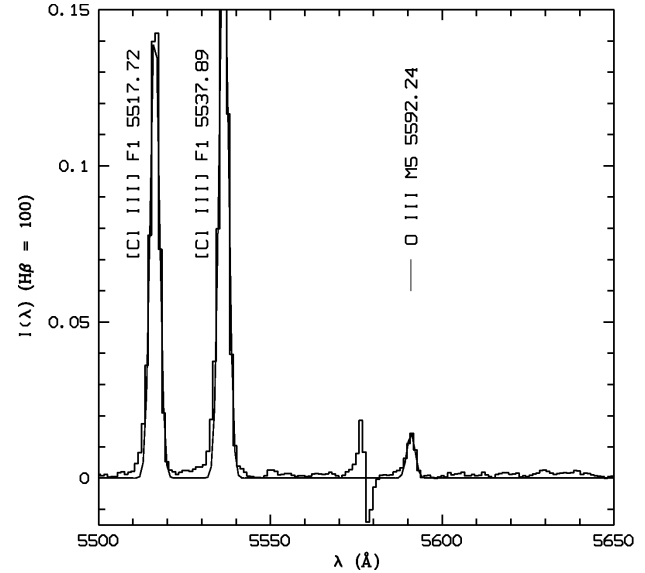


Figure F3. Spectrum of NGC 7009 from 5500 to 5650 Å showing the O III M5 λ 5592.24 line. The [Cl III] λ 5517, 5537 doublet lines are also detected. Note the residual of [O I] λ 5577 due to poor sky subtraction. The continuous curve is the sum of Gaussian profile fits. Continuum has been subtracted and the spectrum has been normalized such that H β has an integrated flux of 100. Extinction has not been corrected for.

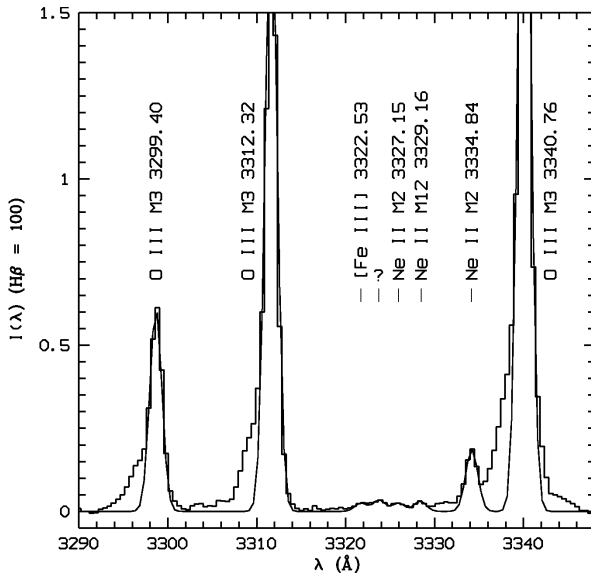


Figure F2. Spectrum of NGC 7009 from 3290 to 3348 Å showing the O III M3 lines and other emission features. The continuous curve is the sum of Gaussian profile fits. Continuum has been subtracted and the spectrum has been normalized such that H β has an integrated flux of 100. Extinction has not been corrected for.

F4 Multiplet 5, $3p^1P - 3s^1P^o$

λ 5592.24 is observed in Fig. F3. Its fitted intensity is 0.047, which is slightly lower than the observation of Liu & Danziger (1993a): 0.0510 ± 0.0031 . The uncertainty of the current measurement is about 10 per cent.

F5 Multiplet 8, $3d^3F^o - 3p^3D$

See Section 3.7.1.

F6 Multiplet 12, $3d^3P^o - 3p^3S$

The O II M12 lines are shown in Fig. F4. The fitted intensity of λ 3132.79 is 37.81, with an uncertainty of about 7 per cent. Our measurement is lower than that of Liu & Danziger (1993a): 43.4 ± 4.3 . The measured intensity ratio of the three lines λ 3115.68 : λ 3121.64 : λ 3132.79 is 1 : 13 : 343, which differs significantly from the ratio in the pure *LS* coupling assumption, i.e. 1 : 3 : 5. That is because this multiplet is mainly excited by the Bowen fluorescence mechanism.

F7 Multiplet 14, $3d^3D^o - 3p^3P$

λ 3715.08 ($3d^3D_3^o - 3p^3P_2$) is partially blended with H I H15 λ 3711.97 (Fig. F5). Also blended here are λ 3714.03 ($3d^3D_1^o - 3p^3P_1$), Ne II M5 $3p^2D_{5/2}^o - 3s^2P_{3/2}$ λ 3713.08 and He II 29g $2G - 4f^2F^o$ λ 3715.16. Reliable measurements of the two M14 lines are difficult. Accurate measurements of another line λ 3707.25 are also difficult due to weakness. The other lines are not observed.

F8 Multiplet 15, $3d^3P^o - 3p^3P$

See Section 3.7.2.

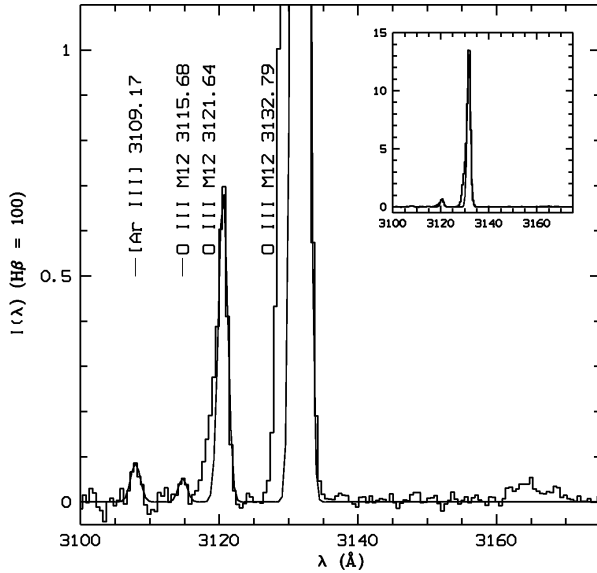


Figure F4. Spectrum of NGC 7009 from 3100 to 3175 Å showing the O III M12 lines. The continuous curve is the sum of Gaussian profile fit. Continuum has been subtracted and the spectrum has been normalized such that Hβ has an integrated flux of 100. Extinction has not been corrected for.

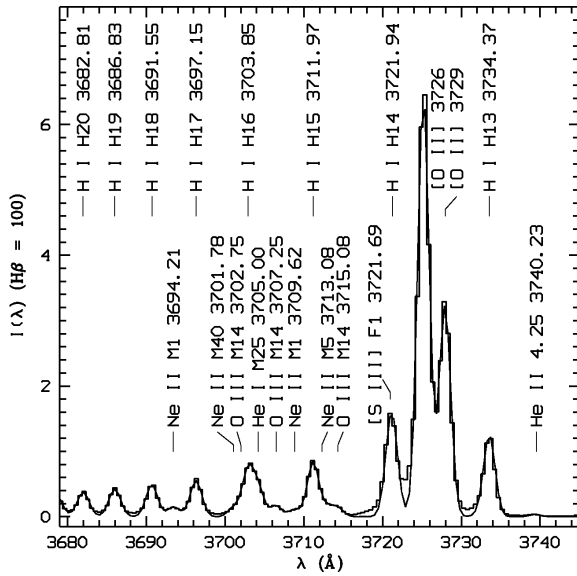


Figure F5. Spectrum of NGC 7009 from 3680 to 3745 Å showing the O III M14 lines and other emission lines. The H I Balmer series are marked on top of the figure. The Ne II M1 line $\lambda 3694.21$ ($3p\ ^4P_{5/2}^o - 3s\ ^4P_{5/2}$) is also detected. The continuous curve is the sum of Gaussian profile fits. Continuum has been subtracted and the spectrum has been normalized such that Hβ has an integrated flux of 100. Extinction has not been corrected for.